Modélisation multi-échelles du comportement électrique et élasto-plastique de fils composites Cu-Nb nanostructurés et architecturés

Tang Gu

2017-ENAM-0017

École doctorale n° 432 : Science des Métiers de l'ingénieur

Doctorat ParisTech

T H È S E

pour obtenir le grade de docteur délivré par

l'École Nationale Supérieure d'Arts et Métiers

Spécialité "Mécanique - Matériaux"

présentée et soutenue publiquement par

Tang GU

le 19 avril 2017

Modélisation multi-échelle du comportement électrique et élasto-plastique de fils composites Cu-Nb nanostructurés et architecturés

Directeur de thèse : **Olivier CASTELNAU**
Co-encadrement de la thèse : **Samuel FOREST, Henry PROUDHON, Eveline HERVE-LUANCO**

Jury

M. Roland LOGE, Professeur associé, École Polytechnique Fédérale de Lausanne	Président
Mme Irene J. BEYERLEIN, Professeur, University of California, Santa Barbara	Rapporteur
M. Yann MONERIE, Professeur, LMGC, Université de Montpellier	Rapporteur
M. Ludovic THILLY, Professeur, Pprime, Université de Poitiers	Examinateur
M. Olivier CASTELNAU, Directeur de recherche, PIMM, Arts et Métiers ParisTech	Examinateur
M. Samuel FOREST, Directeur de recherche, Centre des Matériaux, MINES Paristech	Examinateur
Mme Eveline HERVE-LUANCO, Professeur, Université de Versailles	Examinateur
M. Henry PROUDHON, Chargé de recherche, Centre des Matériaux, MINES Paristech	Invité

T H È S E

Arts et Métiers ParisTech - Campus de Paris
Procédés et Ingénierie en Mécanique et Matériaux – UMR CNRS 8006

Remerciements

En un premier temps, je tiens à remercier mes directeurs et co-directeurs de thèse M. Olivier Castelnau, M. Samuel Forest, M. Henry Proudhon et Mme Eveline Hervé-Luanco. Leur disponibilité et leur patience, leurs compétences scientifiques à la fois profondes et étendues, et leurs conseils constructifs m'ont permis de réaliser cette thèse sur un sujet difficile mais très intéressant. Grâce à eux, j'ai beaucoup appris. J'ai acquis non seulement des connaissances et des compétences scientifiques mais aussi une bonne attitude dans la recherche scientifique, qui me servira certainement tout au long de ma vie.

Je remercie Mme Irene J. Beyerlein et M. Yann Monerie qui ont accepté d'être rapporteurs de ma thèse. Merci pour leur relecture profonde d'un manuscrit pas toujours facile à lire. Je remercie aussi M. Roland Logé (président de ma soutenance) et M. Ludovic Thilly qui ont accepté d'être membres de mon jury. J'ai beaucoup apprécié leurs questions précises et constructives.

Je remercie les directeurs du laboratoire PIMM (Procédés et Ingénierie en Mécanique et Matériaux) ENSAM ParisTech : M. Gilles Régnier, M. Frédéric Vales et les directeurs successifs du laboratoire CdM (Centre des Matériaux) Mines ParisTech : M. Jacques Besson, M. Jérôme Crépin. Ils m'ont fortement aidé, pour commencer et pour terminer cette thèse. Je remercie M. Christophe Canu, Mme Claude Roy, Mme Florence Dumard, Mme Catherine Rouil, M. Ziradjoudine Akber, Mme Véronique Matos, Mme Françoise Di Rienzo, Mme Konaly Sar, Mme Odile Adam, ... pour leurs aides administratives indispensables.

Je remercie M. Ludovic Thilly qui a piloté le projet ANR METAFORES (ANR-12-BS09-0002). Je remercie toutes les personnes associées au projet ANR METAFORES pour les excellentes présentations et les discussions très constructives pendant ma thèse : Mme Florence Lecouturier, M. Pierre-Olivier Renault, M. Patrick Villechaise, M. Kedjar Bouzid, M. Vincent Klosek, ... Notamment un grand merci à Jean-Rony Medy pour nos passionnantes discussions et les données expérimentales générées pendant sa thèse. Je remercie aussi M. Fabien Volpi qui nous a beaucoup aidés grâce à ses mesures complémentaires de conductivité électrique.

Je remercie Florent Coudon : sans le développement d'une nouvelle version de la règle en β pendant sa thèse, je n'aurais pas pu effectuer les nombreux calculs élasto-plastiques. Je remercie les ingénieurs informatiques et les docteurs de CdM : Chao Ling, M. Djamel Missoum-Benziane, M. Grégory Sainte-Luce, M. Nikolay Osipov, Yang Zhang, ... qui m'ont beaucoup aidé pour l'installation et l'optimisation des codes numériques (Zset/ZéBuLoN, Python, C/C++, ...) et pour l'utilisation de clusters de calcul parallèle.

Je remercie les ingénieurs de recherche pour m'avoir offert la possibilité d'effectuer les essais mécaniques, la corrélation d'image, EBSD, MEB, ... : M. Jean-Christophe Teissedre, Mme Julie Heurtel, Mme Anne Laurent, M. Fabrice Gaslain, Mme Stéphanie Dang, Mme Sarah Baiz, Mme Maria Betbeder, ... Ils m'ont fait découvrir le monde passionnant de la recherche expérimentale particulièrement intéressant et enrichissant.

Je remercie Mme Katell Derrien, Mme Véronique Favier, M. Vladimir Esin et M. Matthieu Mazière avec qui j'ai eu l'occasion d'enseigner à l'ENSAM ParisTech et de piloter les stages/mini-projets aux Mines ParisTech.

Je remercier les enseignants-chercheurs du PIMM et du CdM : M. André Pineau, M. Justin Dirrenberger, M. Yazid Madi, M. Georges Cailletaud, M. Vladislav A. Yastrebov, M. Lucien Laiarinandrasana, Mme Anne-Francoise Gourgues-Lorenzon, M. Sébastien Joannès, M. Gilles Rousselier, ... et bien sûr les chercheurs postdoctoraux, les docteurs/-doctorants et les ingénieurs dans les deux laboratoires : Chao Ling, Florent Coudon, Yang Zhang, Yi Zhang, Erembert Nizery, Arina Marchenko, Yin Cheng, Jia Li, FengGuo Zhang, Ming Lui, Taylan Ors, Jean-Baptiste Marijon, SiCong Ren, Takahiro Sakimoto, Vincent Michel, Victor de Rancourt, Raphaël Cusset, Yahya Zahra, Nicolas Gueninchault, ... pour pleins de discussions enrichissantes et leur soutien tout au long de ma thèse. Je remercie aussi tous ceux et celles qui m'ont aidé et que j'ai connus aux laboratoires et sur les campus et qui ne sont pas dans cette liste.

Finalement, je remercie très sincèrement mes parents, qui sont en Chine, pour leur soutien et leurs sacrifices. Sans eux, je n'aurais pas pu aller si loin.

Contents

Abbreviations and notations

Abbreviations:

ADB	Accumulative Drawing and Bundling
SSC	Standard Self-Consistent
GSC	Generalized Self-Consistent
FEM	Finite Element Method
PH	Periodic Homogenization
BCC	Body-Centered Cubic
FCC	Face-Centered Cubic
CCA	Composite Cylinders Assembly
RVE	Representative Volume Element
HEM	Homogeneous Equivalent Medium
CRSS	Critical Resolved Shear Stress
OFHC Cu	Oxygen-Free High Conductivity Cu
PD	Percentage Difference

Abbreviations in French:

ACS (i.e. SSC)	schéma Auto-Cohérent Standard
ACG (i.e. GSC)	schéma Auto-Cohérent Généralisé
MEF (i.e. FEM)	Méthode des Éléments Finis
HP (i.e. PH)	Homogénéisation Périodique

Notations:

x	scalars
$\underline{\boldsymbol{x}}$	vectors
$\underset{\sim}{\boldsymbol{x}}$	2nd-order tensors
$\underset{\approx}{\boldsymbol{x}}$	4th-order tensors
$\cdot$	single contraction
:	double contraction
$\otimes$	tensor product
$\widetilde{x}$	effective (or homogenized) property
$\bar{x} = \langle x \rangle$	volume average

Chapter 1

Introduction

1.1 Introduction in English

In recent years, there has been an increasing demand for next-generation structural nano-materials that exhibit extraordinarily high strength, electrical conductivity, hardness, ductility, thermal stability and radiation damage tolerance. Two types of filamentary and multilayered nano-composites composed of copper and niobium (i.e. Cu-Nb nano-composite wires and laminates) have been highlighted among them (Misra and Thilly, 2010). These two Cu-Nb nano-composites are fabricated respectively by two different severe plastic deformation techniques: Accumulative Drawing and Bundling (i.e. ADB, see the detailed description in Section 2.1) (Dupouy et al., 1996; Vital, 2006) and Accumulated Roll Bonding (Lim and Rollett, 2009; Beyerlein et al., 2014).

To continue to improve the material properties, the main challenge remains in the understanding of the complex interaction between the different material phases and the architecture, in particular when the Cu-Nb composite is fabricated by severe plastic deformations where the elementary physical deformation mechanisms are modified by grain sizes. In this field, combining material characterization and multiscale modeling is mandatory. The previous studies on the Cu-Nb nano-composite wires and laminates dealt with textures and their evolution (Lim and Rollett, 2009; Dubois, 2010; Lee et al., 2012; Hansen et al., 2013; Medy, 2016), yield criterion (Misra and Hoagland, 2007; Thilly et al., 2009), plasticity mechanisms (Thilly et al., 2001; Misra and Hoagland, 2007; Mayeur et al., 2015), Bauschinger effect (Thilly et al., 2007; Badinier et al., 2014), hardness (Thilly et al., 2002a), Ultimate Tensile Strength (Vidal et al., 2007), Cu-Nb interfaces (Mayeur et al., 2013; Beyerlein et al., 2014; Mayeur et al., 2015), thermal stability and internal stresses (Dubois et al., 2010; Beyerlein et al., 2014), and electrical conductivity (Thilly, 2000; Dubois, 2010; Gu et al., 2015).

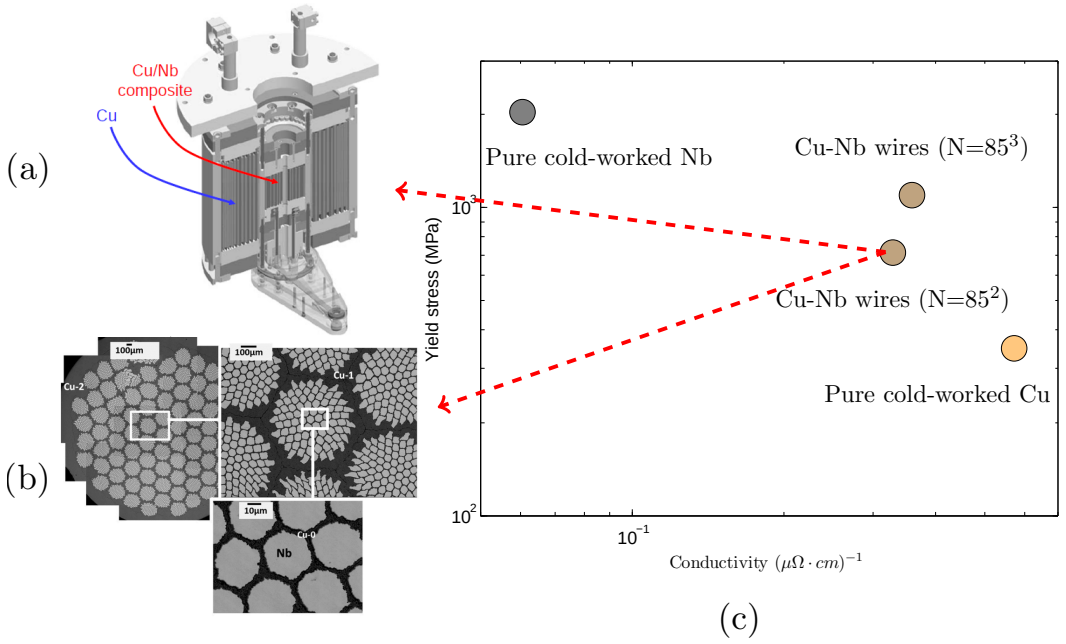

FIGURE 1.1: General introduction to Cu-Nb wires: (a) winding coil for producing high magnetic fields up to ∼90T; (b) cross-section views of the Cu-Nb nano-composite wires (N=85^2); (c) Cu-Nb wires combine both high mechanical strength and high electrical conductivity (material property at 293 K); Refer to Section 3.2.1 for the notation of N=85^2 and 85^3 Cu-Nb filamentary wires.

According to (Spencer et al., 2004; Béard et al., 2013; Halperin et al., 2013; Frydman, 2014), high magnetic fields are becoming essential experimental tools (e.g. for the condensed matter physics and the atomic physics) and industrial tools (e.g. for the nuclear fusion of hydrogen, the nuclear magnetic resonance and the maglev). To generate high magnetic field with long pulse duration, both very high strength and high electrical conductivity are required for the conductors in the winding coils. In other words, to generate a field ∼100 T, the conductors with a conductivity of ∼2 $\mu\Omega^{-1}\text{cm}^{-1}$ at 77 K have to bear a tensile load up to ∼2 GPa (Thilly, 2000). It is now very well established that copper-based nano-composite wires are good candidates to meet these special properties (Thilly, 2000; Vital, 2006; Dubois, 2010). The Cu-Nb nano-composite wires studied in this thesis are fabricated for the winding coils, as shown Fig. 1.1(a), to generate high magnetic field >90 T.

A typical cross-section of a Cu-Nb nano-composite wire is illustrated in Fig. 1.1(b), referred to as "Filamentary" structure in Thilly (2000); Thilly et al. (2002a): a multiscale Cu matrix embedding parallel Nb nano-filaments. According to Thilly (2000); Vidal et al. (2007), the filamentary conductor presenting an Ultimate Tensile Strength as large as 1.9 GPa (yield stress ∼1.5 GPa) at 77K is obtained together with an electrical conductivity of 1.72 $\mu\Omega^{-1}\text{cm}^{-1}$. On the other hand, pure cold-worked Cu is good conductor with a conductivity of 3.85 $\mu\Omega^{-1}\text{cm}^{-1}$ (at 77K) while its yield stress is "only" about 350 MPa. Furthermore, Nb long fibers in Cu-Nb wires exhibits a high yield stress (typically, > 2 GPa), however its conductivity is about ten times smaller than Cu. It

should be noted that yield stress of cold-worked bulk Nb is ∼1.4 GPa (Dupouy et al., 1995), nano-fibers of Nb display a higher yield stress due to size effect (Dubois et al., 2012). Such an excellent property of Cu-Nb wires is obtained not only thanks to the property of Cu and Nb but also due to the specific microstructure and architecture (Thilly et al., 2009; Gu et al., 2015). Experimental conductivity and yield stress at 293 K (Thilly, 2000; Medy, 2016) of pure Cu/Nb and Cu-Nb wires are shown on the Ashby graph in Fig. 1.1(c).

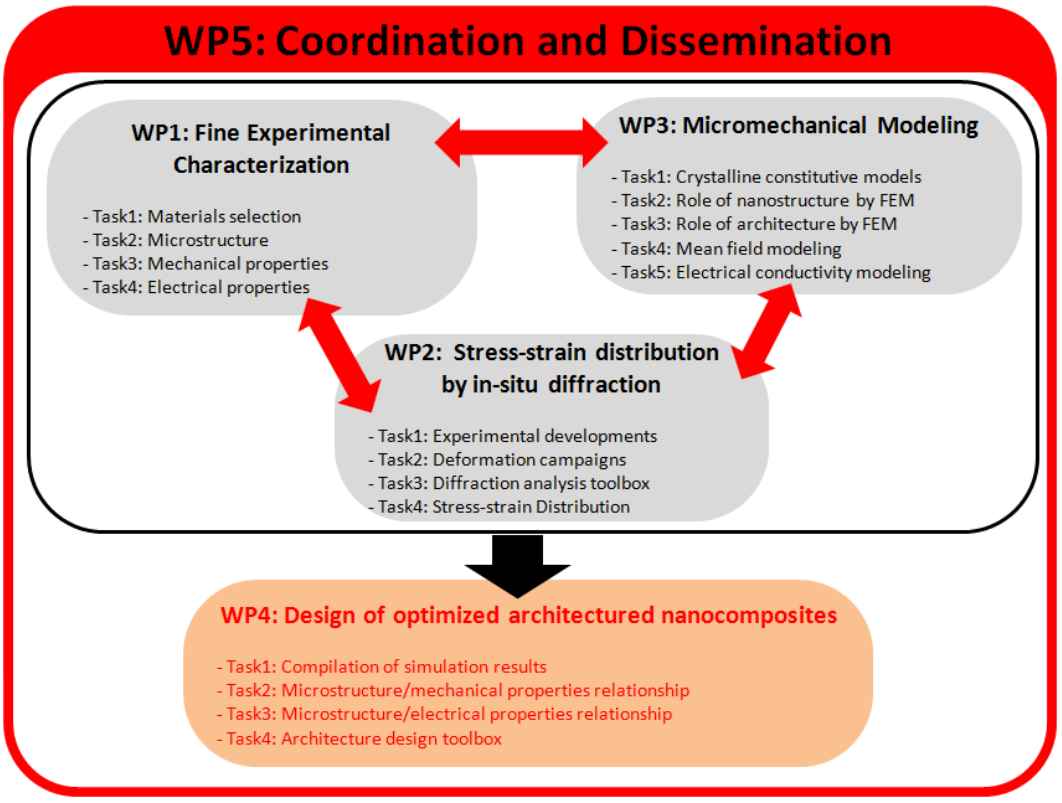

FIGURE 1.2: METAFORES project organization

The ANR **METAFORES** project (ANR-12-BS09-0002, Materials with Elementary Tailored Architecture for Functional Optimized Response: from Experiments to Simulations) is focusing on opening the access to generate intense pulsed magnetic fields up to 100 T. This project is funded by the French agency ANR, and its duration was about four years and a half from November 2012 to April 2017. In order to investigate the origin of the property of Cu-Nb wires, only advanced experimental tools coupled with simulation can help understanding the exact role of architecture (versus size effect) in the macroscopic electrical and mechanical response. Therefore, five partner laboratories were invited to this project for various experimental/modeling research aspects. The main participants list is as follows:

- CNRS-UP-ENSMA Institut Pprime (Pprime)
  - L. Thilly

  - P.-O. Renault
  - P. Villechaise
  - K. Bouzid
  - J.-R. Medy
- CNRS-INSA-UPS-UJF Laboratoire National des Champs Magnétiques Intenses (LNCMI)
  - F. Lecouturier
- Laboratoire Léon Brillouin CEA (LLB)
  - V. Klosek
- CNRS-ENSAM-PIMM Procédés et Ingénierie en Mécanique et Matériaux (PIMM)
  - O. Castelnau
  - T. Gu
- Centre des Matériaux de Mines ParisTech (CdM)
  - S. Forest
  - E. Hervé-Luanco
  - H. Proudhon

Moreover, F. Volpi of the laboratory "Science Ingénierie des Matériaux et Procédés" (SIMaP) was asked for additional measurements of electrical conductivity during this project. METAFORES project relied on four Work Packages (WP), as shown in Fig. 1.2:

- WP1: fine characterizations of microstructures and anisotropic electrical properties
- WP2: advanced strain distribution measurements by in-situ diffraction
- WP3: multiscale modeling
- WP4: design of optimized architectured nanocomposites

The WP1 (Pprime, LNCMI and SIMaP participants) aimed at providing accurate and statistically relevant data on grain geometry, texture and misorientation to ensure accurate representation of the microstructure. In addition, the anisotropic electrical property of Cu-Nb wires was characterized. The WP2 (LLB participant) dealt with advanced experimental in-situ deformation experiments to monitor the non-uniform distribution of strain within the composites upon loading. Since diffraction offers a unique non-destructive tool for the measurement of internal strains into individual structural phases

of the nanocomposites, in-situ loading strain measurements were performed using a small tensile machine mounted on the 6T1 thermal neutron diffractometer.

The experimental data of WP1 allow feeding multiscale modeling in WP3 (PIMM and CdM participants) which estimate the effective electrical and mechanical property of Cu-Nb wires. Therefore, computational homogenization methods recently developed at CdM were implemented to compute the full-fields and the effective response of multiphase crystalline microstructures, including size-dependent models: such novel approaches have been applied to investigate microstructure and architecture effects. Besides the full-field theories, the mean-field approaches (e.g. self-consistent scheme) were proposed, in order to save CPU time and carry out scale transition steps. Finally in WP4, all the experimental and simulation results were combined to assess the roles of microstructure versus architecture in order to define design criteria for Cu-Nb wires from their geometry (microstructure and shape).

Two PhD thesis were launched in the frame of METAFORES project. In the first thesis (Medy, 2016), material properties have been characterized (WP1), and the stress-strain distribution by in-situ experiments has been determined (WP2). This thesis was successfully defended on December 2016. In the second thesis of METAFORES project which is presented in this manuscript, multiscale modeling (WP3) is proposed, and theories are compared to experiments (WP4) to demonstrate predictive capabilities of models. Finally, a numerical material design tool was developed, in order to continue to improve the yield stress and electrical conductivity of Cu-Nb wires. The working time of this thesis was shared between PIMM and CdM laboratories (50% each).

Multi-scale modeling of the (1) electrical, (2) elastic and (3) elasto-plastic behavior of architectured and nanostructured Cu-Nb composite wires is proposed in this work. Thus the thesis is organized as follows. In Chapter 2, material processing and scale conventions are briefly described. In Chapter 3, the anisotropic electrical property of Cu-Nb wires are investigated by homogenization methods. Chapter 4 and Chapter 5 present the multiscale modeling strategies for effective elastic and elasto-plastic behavior of Cu-Nb wires respectively. Throughout this work, mean-field theories are systematically compared with the full-field approaches, and theories are validated by available experimental data.

Chapter 4 is a paper published in the journal "International Journal of Solids and Structures", cited as Gu et al. (2017). Chapter 3 and Chapter 5 are another two papers to be submitted hopefully soon to "Acta Materialia" and "International Journal of Plasticity", respectively. In addition, Appendix A is an another paper Gu et al. (2015) (written in French) dealing with the homogenization of the electrical conductivity of Cu-Nb wires, which was published in "Matériaux & Thechniques". The manuscripts have been slightly corrected for the thesis format.

1.2 Introduction en Français

Au cours des dernières années, il y a eu une demande croissante pour la génération de nouveaux nano-matériaux architecturés présentant une résistance, une conductivité électrique, une dureté, une ductilité, une stabilité thermique et une tolérance aux rayonnements extraordinairement élevées. Deux types de nano-composites filamentaires ou multicouches composés de cuivre et de niobium offrent des propriétés intéressantes (Misra and Thilly, 2010). Ces deux nano-composites Cu-Nb sont fabriqués respectivement par deux techniques différentes de déformation plastique sévère : "Accumulative Drawing and Bundling" (ADB, voir la description détaillée dans Section 2.1 ou Vital (2006)) et "Accumulated Roll Bonding" (Lim and Rollett, 2009; Beyerlein et al., 2014).

Pour continuer à améliorer les propriétés du matériau, le principal défi reste la compréhension de l'interaction mécanique complexe entre les phases du matériel et le rôle des différentes architectures, en particulier lorsque le composite Cu-Nb est fabriqué par déformations plastiques sévères où les mécanismes élémentaires de déformation physique sont modifiés par la taille des grains. Dans ce domaine, il est nécessaire de combiner une caractérisation expérimentale du matériau avec une approche de modélisation multi-échelle. Les études précédentes sur les fils et les microstructures laminées nano-composites Cu-Nb portaient essentiellement sur : les textures cristallographiques et leurs évolutions (Lim and Rollett, 2009; Dubois, 2010; Lee et al., 2012; Hansen et al., 2013; Medy, 2016), le critère de limite d'élasticité (Misra and Hoagland, 2007; Thilly et al., 2009), les mécanismes de plasticité (Thilly et al., 2001; Misra and Hoagland, 2007; Mayeur et al., 2015), l'effet Bauschinger (Thilly et al., 2007; Badinier et al., 2014), la dureté (Thilly et al., 2002a), la résistance ultime à la traction (Vidal et al., 2007), les interfaces Cu/Nb (Mayeur et al., 2013; Beyerlein et al., 2014; Mayeur et al., 2015), la stabilité thermique et les contraintes internes (Dubois et al., 2010; Beyerlein et al., 2014), et la conductivité électrique (Thilly, 2000; Dubois, 2010; Gu et al., 2015).

Selon (Spencer et al., 2004; Béard et al., 2013; Halperin et al., 2013; Frydman, 2014), les champs magnétiques intenses deviennent des outils expérimentaux essentiels (par exemple, pour la physique de la matière condensée et la physique atomique) et des outils industriels (par exemple, pour la fusion nucléaire d'hydrogène, la résonance magnétique nucléaire et le train à sustentation magnétique). Pour générer d'un champ magnétique intense avec une longue durée d'impulsion, les conducteurs dans les bobines ont besoin à la fois d'une limite d'élasticité et d'une conductivité électrique élevées. Par exemple, pour générer d'un champ de 100 T, les conducteurs avec une conductivité de $\sim 2\ \mu\Omega^{-1}\mathrm{cm}^{-1}$ à 77 K doivent supporter une contrainte de traction jusqu'à ~ 2 GPa (Thilly, 2000). Il est maintenant très bien établi que les fils nano-composites à base de cuivre sont de bons candidats pour répondre à ces propriétés spéciales (Thilly, 2000; Vital, 2006; Dubois, 2010). Les fils nano-composites Cu-Nb étudiés dans cette thèse sont élaborés pour les

bobines qui gérèrent des champs magnétiques intenses >90 T, comme illustré dans Fig. 1.1(a).

Une coupe transversale typique d'un fil nano-composite Cu-Nb est illustrée dans la Fig. 1.1(b), appelée structure "Filamentaire" dans Thilly (2000); Thilly et al. (2002a): une matrice du Cu multi-échelles intégrant des nano-filaments du Nb parallèles. Selon Thilly (2000); Vidal et al. (2007), le conducteur filamentaire présentant une "résistance ultime à la traction" de 1, 9 GPa (limite d'élasticité ∼1.5 GPa) à 77K est obtenu avec une conductivité électrique de $1,72\,\mu\Omega^{-1}\text{cm}^{-1}$. D'autre part, le Cu pur travaillé à froid est un bon conducteur avec une conductivité de $3,85\,\mu\Omega^{-1}\text{cm}^{-1}$ à 77K alors que sa limite d'élasticité "n'est que" environ 350 MPa. En outre, les fibres longues du Nb dans les fils de Cu-Nb présentent une haute limite d'élasticité (généralement > 2 GPa), par contre, sa conductivité est environ dix fois plus petite que celle de Cu. Il est important de noter que la limite d'élasticité des échantillons massifs du Nb travaillé à froid est de ∼1,4 GPa (Dupouy et al., 1995), les nano-fibres du Nb présentent une limite d'élasticité plus élevée en raison de l'effet de taille (Dubois et al., 2012). Une telle propriété de fils Cu-Nb est obtenue non seulement grâce à la propriété de Cu et de Nb, mais aussi en raison de la microstructure et de l'architecture spécifique (Thilly et al., 2009; Gu et al., 2015). Les données expérimentales de la conductivité et de la limite d'élasticité à 293 K (Thilly, 2000; Medy, 2016) des échantillons massifs du Cu/Nb pure et de fils Cu-Nb sont tracées sur le graphie d'Ashby dans la Fig. 1.1(c).

Le projet ANR **METAFORES** (ANR-12-BS09-0002, "Materials with Elementary Tailored Architecture for Functional Optimized Response: from Experiments to Simulations") se concentre sur l'amélioration des fils de bobinage pour la génération de champs magnétiques pulsés intenses jusqu'à 100T. Ce projet est financé par l'Agence Française pour la Recherche ANR, et sa durée était d'environ quatre ans et demi de novembre 2012 à avril 2017. Afin d'étudier les propriétés des fils Cu-Nb, les outils expérimentaux avancés associés aux modélisations et simulations peuvent aider à comprendre le rôle exact de l'architecture (conduisant à l'effet de taille) dans le comportement mécanique et électrique macroscopique. Par conséquent, les partenaires de cinq laboratoires ont été invités à ce projet sur les différents aspects scientifiques abordés. La liste des principaux participants est la suivante :

- CNRS-UP-ENSMA Institut Pprime (Pprime)
  - L. Thilly
  - P.-O. Renault
  - P. Villechaise
  - K. Bouzid
  - J.-R. Medy

- CNRS-INSA-UPS-UJF Laboratoire National des Champs Magnétiques Intenses (LNCMI)

  - F. Lecouturier

- Laboratoire Léon Brillouin CEA (LLB)

  - V. Klosek

- CNRS-ENSAM-PIMM Procédés et Ingénierie en Mécanique et Matériaux (PIMM)

  - O. Castelnau

  - T. Gu

- Centre des Matériaux de Mines ParisTech (CdM)

  - S. Forest

  - E. Hervé-Luanco

  - H. Proudhon

En outre, F. Volpi du laboratoire "Science Ingénierie des Matériaux et Procédés" (SIMaP) a été sollicité pour des mesures complémentaires de conductivité électrique au cours de ce projet. Le projet METAFORES s'appuie sur quatre "Work Packages" (i.e. WP), comme illustré dans Fig. 1.2 :

- WP1 : caractérisation fine de la microstructure et des propriétés électriques anisotropes

  participants : Pprime, LNCMI et SIMaP

- WP2 : mesures avancées de la répartition des déformations par diffraction in-situ

  participants : LLB

- WP3 : modélisation multi-échelle

  participants : PIMM et CdM

- WP4 : conception d'architecture nano-composite optimisée

  participants : Pprime, LNCMI, PIMM et CdM

Le WP1 a pour but de fournir des données précises et statistiquement pertinentes sur la géométrie des grains, les textures cristallographiques et les désorientations afin d'assurer une représentation précise de la microstructure. En outre, les propriétés électriques anisotropes de fils Cu-Nb ont été caractérisées. Le WP2 a pour but la réalisation d'expériences en déformation in-situ pour caractériser l'hétérogénéité des déformations dans les composites lors du chargement. Étant donné que la diffraction offre un outil non destructif unique pour la mesure des déformations pour chaque phase individuelle

des nanocomposites, les expériences ont été réalisées à l'aide d'une machine de traction in-situ montée sur le diffractomètre à neutrons thermiques 6T1, au LLB.

Les données expérimentales de WP1 permettent d'alimenter la modélisation multi-échelle dans le WP3 en vue d'estimer le lien entre la microstructure et les propriétés électriques et mécaniques effectives de fils Cu-Nb. Des méthodes d'homogénéisation numérique récemment développées aux CdM ont été mises en place pour calculer les champs complets et la réponse effective des microstructures cristallines multiphases, y compris les modèles dépendants de la taille. Ces méthodes ont été appliquées pour étudier les effets de la microstructure et de l'architecture. Outre les méthodes en champs complets, les approches en champs moyens (par exemple, le schéma auto-cohérent) ont été proposées, afin de réduire le temps de calcul et de réaliser les transitions d'échelle successives. Enfin, dans WP4, tous les résultats expérimentaux et de simulation ont été comparés pour évaluer le rôle respectif de la microstructure et de l'architecture afin de définir les critères de conception de fils Cu-Nb à partir de leur géométrie.

Deux thèses ont été réalisées dans le cadre du projet METAFORES. Dans la première thèse (Medy, 2016), les propriétés du matériau ont été caractérisées (WP1), et la distribution des contraintes-déformations a été déterminée par des expériences in-situ (WP2). Cette thèse a été défendue avec succès en décembre 2016. Dans la deuxième thèse du projet METAFORES présentée dans ce manuscrit, on propose une modélisation multi-échelle (WP3) et les théories sont comparées aux expériences (WP4) pour démontrer les capacités prédictives des modèles. Enfin, un outil numérique de conception de matériaux a été développé afin de continuer à améliorer la limite d'élasticité et la conductivité électrique de fils Cu-Nb. Le temps de travail de cette thèse a été partagé entre les laboratoires PIMM et CdM (50% chacun).

La modélisation multi-échelle du comportement (1) électrique, (2) élastique et (3) élasto-plastique de fils composites Cu-Nb nanostructurés et architecturés est proposée dans ce travail. Ainsi, la thèse est organisée comme suit. Dans le chapitre 2, l'élaboration du matériau et les conventions d'échelle sont décrites brièvement. Dans le chapitre 3, les propriétés électriques anisotropes (i.e. conductivités longitudinale et transversale) de fils Cu-Nb est étudiée à l'aide de méthodes d'homogénéisation. Chapitre 4 et Chapitre 5 présentent les stratégies de modélisation multi-échelle pour les comportements élastique et élasto-plastique. Tout au long de ce travail, les théories en champs moyens sont systématiquement comparées aux approches en champs complets et les résultats sont validées par les données expérimentales disponibles.

Chapitre 4 est un article publié dans la revue "International Journal of Solids and Structures", cité comme Gu et al. (2017). Chapitre 3 et Chapitre 5 sont deux autres articles qui devraient être soumis bientôt dans "Acta Materialia" et "International Journal of Plasticity", respectivement. En outre, Annexe A est un autre article Gu et al. (2015) (rédigé en français) traitant de l'homogénéisation de la conductivité électrique pour les

fils Cu-Nb, qui a été publiée dans “Matériaux & Thechniques”. Le format de ces derniers chapitres ont été légèrement corrigé pour être en phase avec le format du manuscrit de thèse.

Chapter 2

General material description of architectured and nanostructured Cu-Nb composite wires

2.1 Material processing

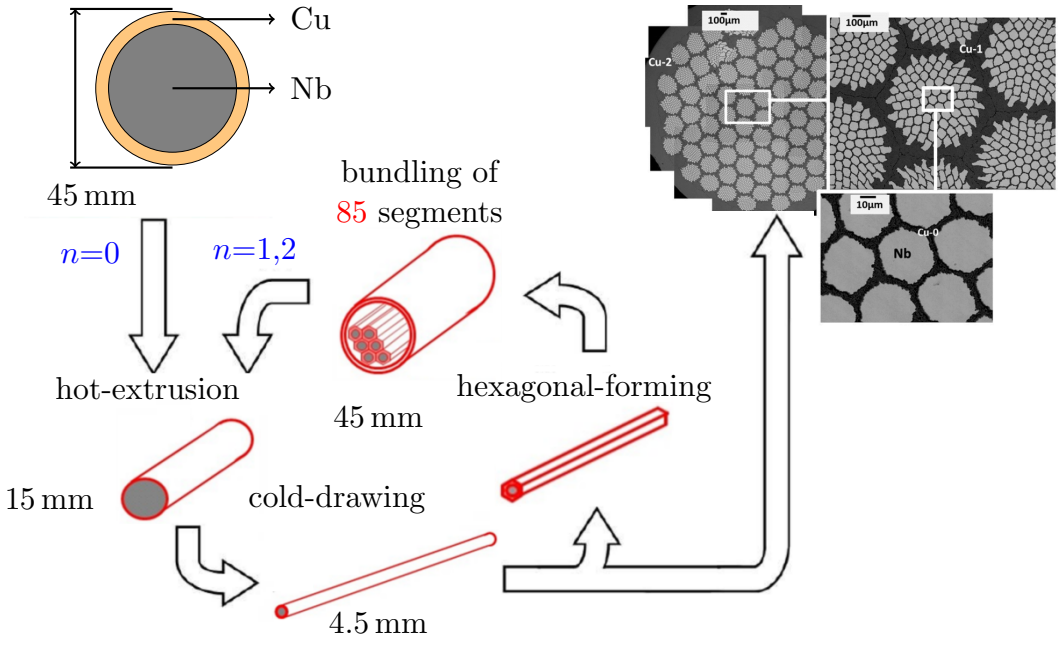

FIGURE 2.1: Schematic diagram of the material processing of Cu-Nb Filamentary wires: Accumulative Drawing and Bundling (ADB) (Vital, 2006).

According to Dupouy et al. (1996); Vital (2006); Dubois (2010), Cu-Nb nano-composite wires are fabricated via a severe plastic deformation process, based on ADB (series of hot extrusion, cold drawing and bundling stages), as shown in Fig. 2.1. The most recent ADB processing (Dubois, 2010), is as follows:

- *Hot-extrusion*: A Nb wire is initially inserted into a Cu tube, forming a rod with a diameter of 45 mm. Before hot-extrusion, these rods are degassed for 2h at 200 °C. They are then brought to extrusion at the temperature of 700 °C for a period of 2h. A direct extrusion press with a capacity of 575 tons is used. The diameter of Nb/Cu rods is reduced to 15 mm. Hot-extrusions are performed at the Laboratoire des Technologies des Matériaux Extrêmes at CEA Saclay.
- *Cold-drawing* are performed (a traction of 10 tons maximum) at room temperature obtaining the nano-composite wires with a length of 16 m. Total sample diameter is reduced again up to 4.5 mm. These operations are carried out at LNCMI.
- *Bundling*: The structure is then cut into 85 smaller pieces with hexagonal cross section. These pieces are then bundled together and inserted into a new Cu tube.

The new composite structure is again extruded and drawn. And so on. The used Cu is OFHC (Oxygen-Free High Conductivity). In Fig. 2.1, ADB is repeated two times, leading to copper based architectured and nanostructured composite wires which are composed of a multi-scale Cu matrix embedding 85^2 Nb nanofibers (so-called N=85^2 type of Cu-Nb "Filamentary" wires): Nb fibers are separated by the finest Cu-0 copper channels; groups of 85 Nb/Cu-0 elementary long fibers are then separated by Cu-1 copper channels; the group of 85^2 elementary patterns is finally embedded in an external Cu-2 copper jacket. If the ADB is repeated three times, a Cu-Nb composite wire containing N=85^3 elementary fibers will be obtained (see Fig. 3.1(b)).

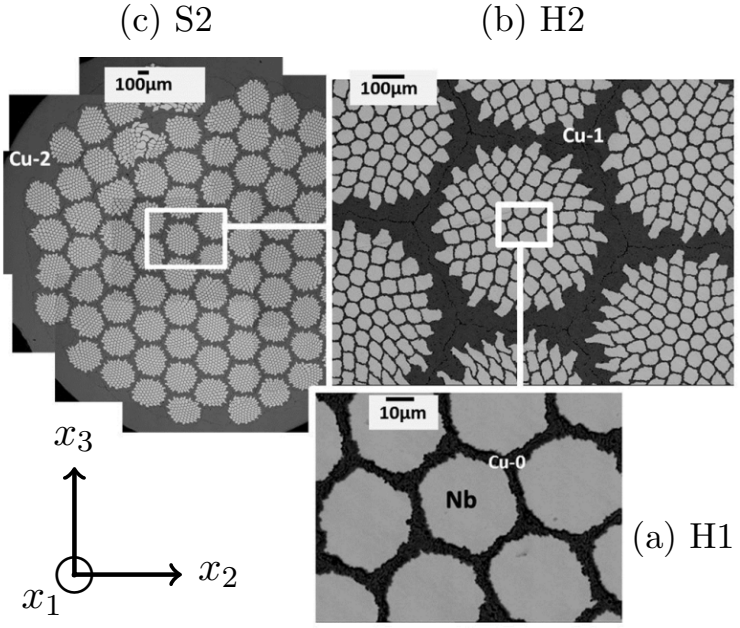

FIGURE 2.2: Successive cross-section views of the Cu-Nb nano-composite Filamentary wires containing 85^2 elementary Cu/Nb long fibers.

It is noted that, unlike Cu, Nb wires are introduced only at the very first fabrication stage. Therefore, Nb wires (i.e. Nb in Fig. 2.2(a)) are all deformed together during the

iterative ADB process, and they exhibit the same microstructure and similar characteristic sizes. The Cu-0 region (Fig. 2.2(a)) are introduced at the beginning of the process, while the Cu-1, Cu-2 (Fig. 2.2(b)(c)) are introduced successively during the two steps of ADB; different microstructure are thus expected for the different Cu-i regions (i = 0, 1, and 2).

The volume fractions and dimensions of Nb/Cu-i components in Cu-Nb wires are detailed in Section 3.2. Furthermore, the severe plastic deformations in ADB leads to specific crystallographic/morphological textures, yield stresses and initial residual stresses. This will be presented in Sections 5.2.1, 5.2.2, 5.2.3 respectively. These microstructural features are taken into account in the multiscale modeling approaches developed in this thesis.

2.2 Scale conventions

For multiscale modeling of the effective elasto-plastic behavior of these Cu-Nb wires, the following scale conventions will be used:

1. homogenization at the highest magnification scale, looking directly at each individual polycrystalline Cu or Nb phase, is labeled as H0 (Homogenization 0);
2. then, homogenization of the bundle unit of 85^1 elementary Nb/Cu-0 long fibers is labeled as H1 (Homogenization 1);
3. iterative homogenization of the effective Cu-Nb composite zone of H1 embedded in the Cu-1 matrix (see in Fig. 2.2(b)), is labeled as H2 (Homogenization 2), i.e. H2 provides the effective behavior of an assembly of 85^2 elementary patterns;
4. finally, the scale S2 (see Fig. 2.2(c)) is defined here as a single cylinder-shaped structure with two layers: effective Cu-Nb composite zone of H2 (containing 85^2 elementary patterns) surrounded by the external Cu-2 jacket.

Let the effective material behavior (i.e. homogenized stress-strain relation) denote $(\overline{\underset{\sim}{\boldsymbol{\sigma}}}\text{-}\overline{\underset{\sim}{\boldsymbol{\varepsilon}}})_{\mathrm{H0}}$ at the scale H0 of polycrystalline aggregates, corresponding to individual Cu/Nb polycrystals. Those denoted $(\overline{\underset{\sim}{\boldsymbol{\sigma}}}\text{-}\overline{\underset{\sim}{\boldsymbol{\varepsilon}}})_{\mathrm{Hi}}$ (i=1, 2) at scales Hi correspond to the effective behavior of the bundle unit of 85^{i} (i=1, 2) elementary long fibers. The structural problem S2 will be solved to compute the macroscopic behavior $(\overline{\underset{\sim}{\boldsymbol{\sigma}}}\text{-}\overline{\underset{\sim}{\boldsymbol{\varepsilon}}})_{\mathrm{S2}}$. Then, this effective behavior will be compared with the available experimental data. In addition, the effective elastic tensor are noted as $(\widetilde{\underset{\sim}{\boldsymbol{C}}})_{\mathrm{Hi/S2}}$ at scales Hi (i=0,1,2) or S2 respectively. It is worth noting that, $\underset{\sim}{\boldsymbol{\sigma}}$ denotes electrical conductivity in Chapter 3 for electrical property, while it denotes the stress tensor in Chapter 4 and Chapter 5 for mechanical behavior.

Chapter 3

Multiscale modeling of the anisotropic electrical conductivity and experimental comparison

Abstract

This chapter presents a comprehensive multiscale study to predict the anisotropic effective electrical conductivity based on material nanostructure and architecture. Two homogenization methods are applied: a mean-field theory and a full-field approach. The size effect associated with the microstructure refinement is taken into account in the definition of the conductivity of each component in the composites. The multiscale character of the material is accounted through an iterative process. The excellent agreement among both model responses allows further comparisons with experimental data, obtained by the four-point probe method. Then the model predictions are validated by experiments for the first time. Finally, the quantitative understanding provided by these models demonstrates that the microstructure of Cu-Nb wires has a significant effect on the electrical conductivity.

It should be noted that, in this chapter, the Cu-Nb wires containing 85^2 (see Fig. 2.2) and 85^3 Nb/Cu elementary long fibers[1] will be studied. In Appendix A, the effective electrical conductivity of another type of Cu-Nb wires with more complex microstructures and architectures will be predicted, i.e. co-cylindrical Cu-Nb wires with 85^3 Cu/Nb/Cu wires (see Fig. 4.1). The good agreements between experimental data and model predictions for various types of Cu-Nb wires demonstrate that multiscale modeling proposed in this work can be used for different multi-coated fiber-reinforced materials.

[1] so-called Filamentary wires

3.1 Introduction

Multiscale modeling of the electrical conductivity of composite materials is a complex topic, particularly if microstructural features lead to a size effect in electronic conduction and create an anisotropy (Heringhaus et al., 2003; Mallick, 2007; Behzad and Sain, 2007). The conductivity of Cu/Nb single crystal is isotropic, as both Cu and Nb exhibit a cubic crystal structure (Face-Centered Cubic, i.e. FCC, for Cu and Body-Centered Cubic, i.e. BCC, for Nb) (Schulgasser, 1976b; Sivardière, 2008). However, Cu/Nb grains display highly elongated shapes in Cu-Nb wires due to material processing (Medy, 2016), leading to an anisotropic grain boundary density. Thus, the influence of grain boundary in electrical conductivity need to be considered for polycrystalline materials (Lu et al., 2004). Furthermore, due to size effect, additional scattering of conduction electrons occurs at internal interfaces of many composites (e.g. Cu-Nb wires). In analogy to scattering at the surface in an infinite long fiber with a small diameter, the size effect can be modeled and confirmed by experiments, according to Fuchs (1938); Dingle (1950); Sambles et al. (1982); Sondheimer (2001); Steinhögl et al. (2002, 2005); Huang et al. (2008). Based on the Dingle's model (Dingle, 1950), Thilly (2000) takes the temperature, dislocation density and size effect into account for predicting the conductivity of Cu-Nb wires along the wire direction (denoted *longitudinal* direction in this work and corresponding to the x_1-axis).

In order to predict the *anisotropic* effective conductivity with considering the particular morphology of fiber-reinforced composites (such as Cu-Nb wires at different scales in Fig. 3.1), several homogenization models have been proposed. The homogenization models for composites can be separated into two types: mean-field analytical methods (Schulgasser, 1976a; Hasselman and Johnson, 1987; Tavman and Akinci, 2000; Hervé-Luanco and Joannès, 2016) and full-field ones (Islam and Pramila, 1999; Behzad and Sain, 2007). Among the analytical mean-field models, the Generalized Self-Consistent scheme (denoted GSC hereafter) has been found to be very efficient to estimate the electrical conductivity of Cu-Nb wires (Gu et al., 2015). The GSC scheme has been initially developed to study the elastic behavior of the fiber-reinforced composites (Hervé and Zaoui, 1995). According to Hervé (2002); Hervé-Luanco and Joannès (2016); Joannès and Hervé-Luanco (2016), this model has been modified for diffusion phenomena, such as electrical conductivity, assuming a random distribution of composite cylinders. As for the full-field method, Gu et al. (2015) proposed a Finite Element Method (FEM) method with periodic boundary conditions (denoted PH, for Periodic Homogenization). FEM PH is adopted to the case of periodic fiber distribution, as observed experimentally (see Fig. 3.1), but it will cost more CPU time compared with GSC scheme.

Finally, the theoretical studies of electrical conductivity need to be validated by experimental data. To measure electrical conductivity of materials with microstructure size ranging nanometer to millimeter, the four-point probe method has been developed using

separate pairs of current-carrying and voltage-sensing electrodes to make more accurate measurements compared with other methods (NormeInternationale, 1974; Chan, 1994). This method is available for different sample geometries, e.g. nano-wires (Huang et al., 2008; Kitaoka et al., 2009) and thin films (Smits, 1958; Liu et al., 2001). Making use of the four-point probe method, Thilly (2000); Dubois (2010) have reported the conductivity of the bulk highly hardened Cu/Nb separately and Cu-Nb wires along the wire direction (i.e. longitudinal conductivity).

Despite a wealth of literature works on the electrical conductivity of composites, we have found that the following two points are still missing: 1. no hierarchical homogenization strategy to predict the *anisotropic* electrical conductivity of recent Cu-Nb wires, taking into account the complex architectures (i.e. the multi-scaled fiber-reinforced microstructure) and the size effect; 2. no experiments to determine the *anisotropic* electrical properties of Cu-Nb wires, particularly the properties in the *transverse* direction (i.e. perpendicular to the wire direction x_1), in order to validate the theoretical predictions.

Therefore, the objectives of this chapter are twofold: 1. provide a multiscale homogenization procedure to predict the electrical conductivity of architectured and nanostructured Cu-Nb composite wires; 2. validate homogenization models by comparing with experimental data in both longitudinal and transverse directions. The outline of the chapter is as follows. The architecture and nano-structure of Cu-Nb composite wires are described in Section 3.2. Experimental methods for the anisotropic electrical property characterization are briefly presented in Section 3.3. In order to reproduce the effective behavior of this material, two multiscale methods (i.e. GSC and PH) and an iterative scale transition strategy are presented in Section 3.4. In Section 3.5, anisotropic model responses are compared with experimental data. Finally, the relation between the effective material behavior and its microstructure is discussed quantitatively.

3.2 Material description

3.2.1 Volume fraction and channel width

In the present chapter, ADB (see Chapter 2.1) is repeated two or three times, leading to copper based architectured and nanostructured composite wires which are composed of 85^2 (Fig. 3.1(a-c)) and 85^3 (Fig. 3.1(d-g)) Nb nanofibers respectively (so-called N=85^2 and N=85^3 type of Cu-Nb "Filamentary" wires (Medy, 2016)).

In this work, two types of Cu-Nb conductor are studied by experiments and multiscale modeling with different diameters d [2]: $d \in [0.25, 2.10]$ mm for N=85^2 and $d \in [0.55, 2.10]$ mm for 85^3. The volume fraction $f^{(i)}$ of each type of conductor is not

[2]Following (Thilly et al., 2002a; Medy, 2016), all dimensions are given in the x_2-x_3 cross-section, i.e. perpendicular to the wire axis x_1, see Fig. 3.1 for the coordinate system.

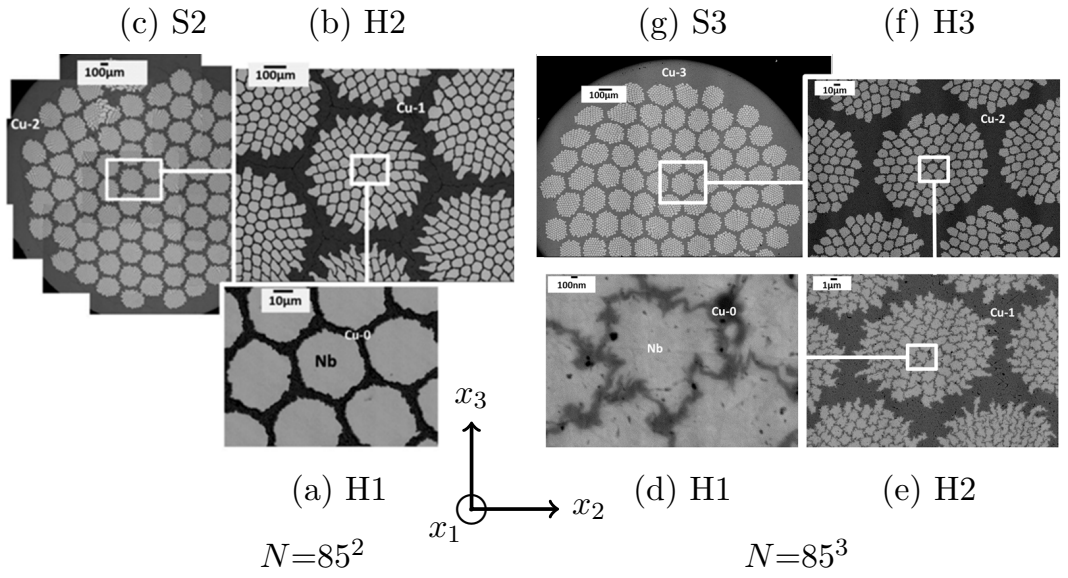

FIGURE 3.1: Successive cross-section views of the Cu/Nb nano-composite wires containing (a-c) 85^2 and (d-g) 85^3 elementary Cu/Nb long fibers (so-called N=85^2 and N=85^3 type of conductor). The diameters of the specimen of (c) and (g) are 4.50 mm and 2.10 mm respectively. The diameter of specimen (c) for N=85^2 and (g) 85^3 are reduced to a series of thinner ones ranging [0.25, 2.10] mm and [0.55, 2.10] mm respectively by supplementary cold drawing.

changed by hot-extrusion and cold-drawing and they can be determined by the initial dimensions of Nb cylinder and Cu jacket. The theoretical value of channel width, $\delta^{(i)}$, can be estimated by supposing that all the perfect and concentric components (i.e. Nb cylinder and Cu tube) are deformed in a homothetic way during material processing (Vital, 2006). Table 3.1 indicates the volume fraction $f^{(i)}$ and theoretical channel width $\delta^{(i)}$ in the two extreme diameter cases (i.e. d=0.25 and 2.10 mm for N=85^2; d=0.55 and 2.10 mm for 85^3).

phase i	$f^{(i)}$	$\delta^{(i)}$	$\sigma^{(i)}$	$\delta^{(i)}$	$\sigma^{(i)}$
N=85^2		d=0.25 mm		d=2.10 mm	
Nb	44.7%	1.67 µm	0.060	13.74 µm	0.060
Cu-0	15.2%	0.27 µm	0.508	2.19 µm	0.561
Cu-1	17.5%	2.67 µm	0.562	21.97 µm	0.568
Cu-2	22.6%	15.14 µm	0.567	124.48 µm	0.568
N=85^3		d=0.55 mm		d=2.10 mm	
Nb	34.5%	323.8 nm	0.060	1.22 µm	0.060
Cu-0	11.8%	50.9 nm	0.327	192.2 nm	0.485
Cu-1	13.6%	511.8 nm	0.537	1.93 µm	0.560
Cu-2	17.5%	5.82 µm	0.565	21.97 µm	0.568
Cu-3	22.6%	32.99 µm	0.568	124.48 µm	0.568
bulk Cu		∞	0.568	∞	0.568
bulk Nb		∞	0.060	∞	0.060

TABLE 3.1: Volume fraction $f^{(i)}$ and theoretical dimensions $\delta^{(i)}$ of each component i in the case of conductor diameter d=0.25, 2.10 mm for N=85^2 and d=0.55, 2.10 mm for N=85^3, with the corresponding conductivity $\sigma^{(i)}$ (µΩ^{-1}cm^{-1}) at 293 K.

3.2.2 Conductivity of individual components

The Cu-Nb wires are made of FCC Cu and BCC Nb polycrystalline components, i.e. Nb, Cu-0, Cu-1, Cu-2 and Cu-3. In addition, the Cu/Nb grains exhibit highly elongated shapes due to material processing (Medy, 2016), leading to an anisotropic grain boundary density (grain boundary density along $x_{2,3}$ is higher than the one along x_1). Electrical conductivity in a single BCC/FCC grain is isotropic due to its cubic crystal structure (Schulgasser, 1976b; Sivardière, 2008). Furthermore, Lu et al. (2004) has found that the influence of grain boundary is rather small on the electrical conductivity of the polycrystalline Cu with the grain size varying from 100 nm to 1 µm (similar to the Cu grain size in Cu-Nb wires (Medy, 2016)). Therefore, the effective conductivity of individual polycrystalline Cu component in Cu-Nb wires is considered to be isotropic. For the sake of simplicity, conductivity of polycrystalline Nb is also supposed to be isotropic disregarding the grain boundary effect. It will be shown that these approximations are sufficient to predict the anisotropic electrical conductivity for Cu-Nb wires based on experimental comparisons.

Developed from the Dingle's model (Dingle, 1950), Thilly (2000) takes the temperature T, dislocation density and size effect (i.e. channel width δ) into account for predicting the electrical conductivity of individual component in the Cu-Nb wires. The conductivity of bulk specimen of highly hardened Cu and Nb has also been measured (Thilly, 2000): $\sigma_{\text{bulk}} = 0.568\,\mu\Omega^{-1}\text{cm}^{-1}$ and $0.060\,\mu\Omega^{-1}\text{cm}^{-1}$ for Cu and Nb respectively at 293 K (reported in Table 3.1). It is worth noting that the highly hardened bulk specimen exhibit extreme high dislocation density, probably almost saturating. This corresponds to the dislocation density case of the Cu/Nb components in Cu-Nb wires despite various conductor diameters $d \in (0.2, 2.5)$ mm (Gu et al., 2015).

Concerning the size effect, the expression of Ashcroft and Mermin (2010); Thilly (2000) is used for associating material conductivity with mean free path ℓ of electrons:

$$\ell_{\text{Cu}}(T) = 66\ \sigma_{\text{bulk-Cu}}(T) \tag{3.1a}$$

$$\ell_{\text{Nb}}(T) = 87\ \sigma_{\text{bulk-Nb}}(T) \tag{3.1b}$$

(with σ_{bulk} in $\mu\Omega^{-1}\text{cm}^{-1}$ and ℓ in nm). Here, both σ_{bulk} and ℓ depend on the temperature T. And the mean free path ℓ of electrons is defined as the average distance traveled by a moving electron between successive collisions. The Dingle's model (Dingle, 1950) has been initially developed to predict the conductivity of an infinite long fiber with a small diameter δ. In this case, the conductivity of the long fiber is strongly affected by the transverse dimension due to electron scattering at surfaces/interfaces. Thilly (2000)

proposed the following equations based on this model in terms of the ratio δ/ℓ:

$$\frac{\sigma}{\sigma_{\text{bulk}}} = \frac{\delta}{\ell} - \frac{3}{8}\left(\frac{\delta}{\ell}\right)^2 \left[\ln(\frac{\ell}{\delta}) + 1.059\right] \quad \text{for } \delta < 0.467\ell\,, \tag{3.2a}$$

$$\frac{\sigma}{\sigma_{\text{bulk}}} = \left(1 + \frac{\ell}{\delta}\right)^{-1} \quad \text{for } \delta \in [0.467\ell, 3\ell[\,, \tag{3.2b}$$

$$\frac{\sigma}{\sigma_{\text{bulk}}} = 1 - \frac{3}{4}\frac{\ell}{\delta} \quad \text{for } \delta > 3\ell\,. \tag{3.2c}$$

The conductivity $\sigma^{(i)}$ of individual component i is determined by the choice of one of the three above equations which are expressed in terms of the theoretical channel width $\delta^{(i)}$ of this component. Table 3.1 reports the conductivity $\sigma^{(i)}$ calculated by Equations (3.1) and (3.2) of each individual component with the corresponding channel width $\delta^{(i)}$ at 293 K.

3.3 Experimental methods

At first, the macroscopic *longitudinal* conductivities have been obtained by J.-R. Medy (Medy, 2016) at LNCMI. A series of N=85[2] and 85[3] Filamentary samples were used with a length of 40 cm and a variable diameter d (see Section 3.2.1). The conductivity of these samples were measured by the four-point probe method at 293 K (NormeInternationale, 1974): the two outer current-carrying probes were placed at the ends of the wire, then the two inner voltage-sensing ones were placed between them; the distances between the outer probes and inner probes were 39 cm and L=36.8 cm respectively. A current I=0.1 A was injected by the outer pair and the potential difference ΔU was measured by the inner pair leading to the following experimental longitudinal conductivity σ_{L}:

$$\sigma_{\text{L}} = \frac{I}{\Delta U} . \frac{L}{S} \tag{3.3}$$

where the ratio $I/\Delta U$, L and S are the electrical conductance, the distance between the voltage-sensing probes and the sectional area respectively. The uncertainties of measurement were estimated on the order of 5% (Thilly, 2000; Medy, 2016).

Due to ADB processing, the architecture of Cu-Nb wires is quasi-axisymmetric with respect to x_1. As a result, the effective material behavior is expected to be *transverse isotropic* (Gu et al., 2015, 2017). For the conductivity along the *transverse* direction x_2 or x_3, a more delicate measurement was needed due to the small sample size, compared with the measurement of longitudinal conductivity. In addition, the specific structure which is composed of Cu-Nb composite zone and a Cu jacket (e.g. Fig. 3.1(c)) should be considered during experiments. The *transverse* measurements have been done by J.-R. Medy at SIMaP with the help of F. Volpi (Medy, 2016).

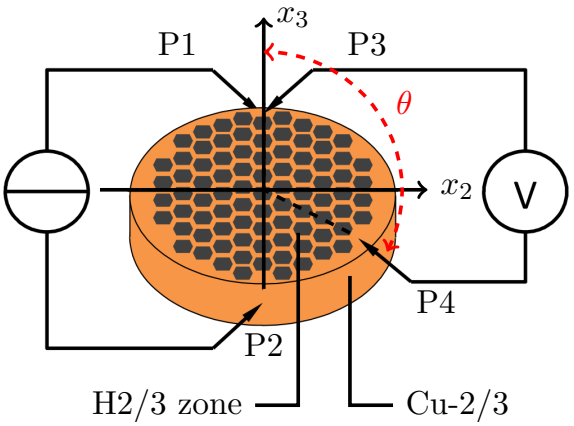

FIGURE 3.2: Schematic of Cu-Nb sample for the measurement of transverse electrical conductance.

This measurement was also performed with the four-point probe for both N=85^2 and 85^3 Cu-Nb wires with a diameter of d=2.10mm at 293 K. The cylinder-shaped S2/S3 samples have been mechanically polished on two parallel sides (denoted upper and lower surfaces hereafter) which are perpendicular to x_1 (Fig. 3.2). The samples were then thinned down to $218 \pm 5\,\mu$m and $190 \pm 5\,\mu$m for N=85^2 and 85^3 respectively. The two fixed current-carrying probes P1 and P2 were placed along the diameter x_3 outside the Cu-2/Cu-3 jacket, on the side walls of the samples (i.e. x_2=0, x_3=$\pm$1.05 mm for P1 and P2), as illustrated in Fig. 3.2. The two voltage-probes P3 and P4 were placed on the upper surface. P3 was fixed in the middle of Cu-2/Cu-3 ring along the diameter x_3. In order to investigate the electrical conductance of the whole sample, the mobile probe P4 was positioned on the upper surface along two different paths: (i) along a diameter (i.e. along x_3 axis with $x_3 \in (-1.05, 1.05)$ mm); (ii) along the middle line of Cu-2/Cu-3 ring (i.e. position described by an angle θ in a cylindrical coordinate system with $\theta \in (0, 180)\,^\circ$), as shown in Fig. 3.2.

The injected current $I(t)$ at P1 and P2 was scanned from -0.1 A to 0.1 A with a Keithley 6221 power source. Then the electric potential difference $\Delta U(t)$=$U_{\mathrm{P3}}(t)$-$U_{\mathrm{P4}}(t)$ was measured between the fixed P3 and the mobile P4 with a nanovoltmeter Agilent 34420. The uncertainties of the measured apparent conductance was estimated as small as $\pm 0.1\,\mathrm{m}\Omega^{-1}$ (fit uncertainty of the $I(t)/\Delta U(t)$ data set). On the other hand, the position uncertainties of mobile P4 were estimated as $\pm$0.1 mm and $\pm 9\,^\circ$ for P4 position along the x_3 diameter and along the Cu-2/Cu-3 ring respectively due to the small sample sizes. The experimental data will be shown and compared with model predictions, in the longitudinal (Section 3.5.1) and transverse directions (Section 3.5.2).

3.4 Hierarchical homogenization strategy

In this section, we will predict the effective electrical conductivity of Cu-Nb wires taking the specific multi-scaled fiber-reinforced material architecture into account. At the effective scale H1, (i.e. Fig. 3.1(a) and Fig. 3.1(d)), the elementary patterns appear with two layers: Nb cylinder and Cu-0 tube. In order to homogenize the assembly of these 85[1] Nb/Cu-0 fibers, a mean-field homogenization method and a full-field FEM approach will be presented in Section 3.4.1 and Section 3.4.2 respectively. As the specimens exhibit many characteristic scales (i.e. H1, H2, H3), a hierarchical homogenization strategy will be proposed in Section 3.4.3.

3.4.1 Mean-field generalized self-consistent scheme

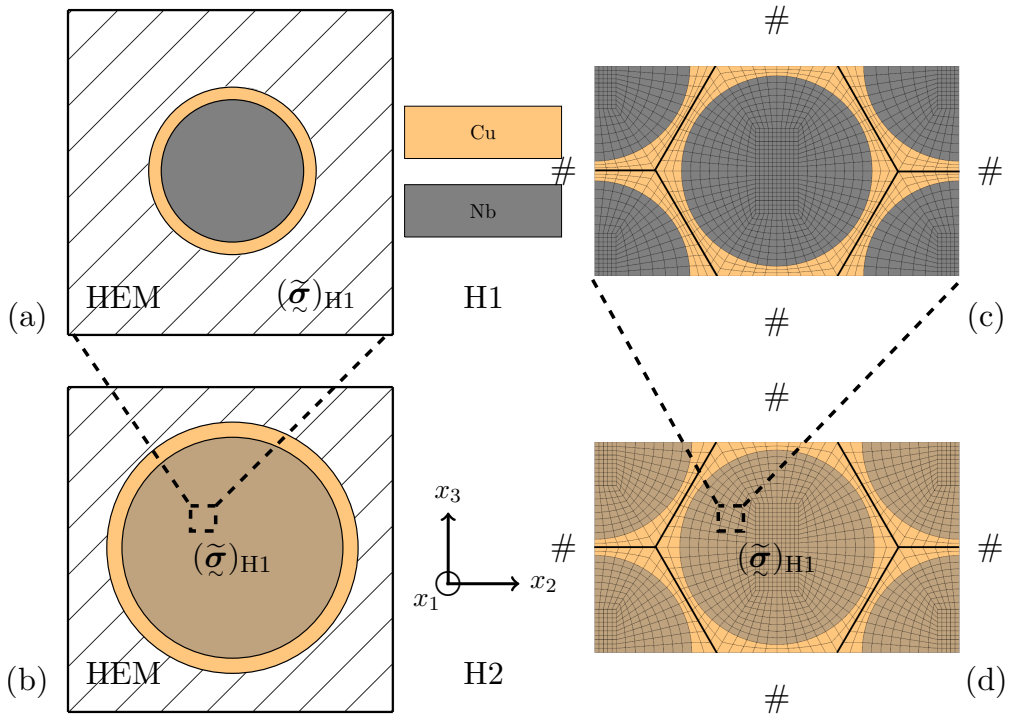

FIGURE 3.3: Multiscale modeling of the effective conductivity from the H1 (a and c) to the H2 (b and d). (a-b): The iterative process by the GSC scheme; (c-d): PH with the meshes by FEM. Periodic boundary conditions in PH, denoted #, are considered. Yellow stands for Cu, gray for Nb and brown for Cu-Nb composite.

The GSC scheme (Gu et al., 2015; Hervé-Luanco and Joannès, 2016) is developed in the following way: (i) (n+1)-layered cylindrical problem and (ii) n-layered problem embedded in the HEM (Homogeneous Equivalent Medium) where the effective electrical conductivity $\widetilde{\boldsymbol{\sigma}}$ is determined by self-consistent scheme (Christensen and Lo, 1979; Hervé, 2002) (as illustrated in Fig. 3.3(a)). When applied to estimate the effective electrical conductivity of H1, this scheme assumes that the elementary Nb/Cu-0 fibers are distributed randomly.

As in Hervé and Zaoui (1995), the component 1 constitutes the central core and component i lies within the shell limited by the two concentric cylinders with the radii R_{i-1} and R_i (R_0=0). Each component is assumed to be homogeneous and to exhibit a transverse isotropic behavior with the axis of symmetry along the wire direction x_1. We denote the longitudinal and transverse electrical conductivity by $\sigma_{\mathrm{L}}^{(i)}$ and $\sigma_{\mathrm{T}}^{(i)}$ respectively in the component i. The transverse isotropic conductivity is expressed as a second order tensor: $\underset{\sim}{\boldsymbol{\sigma}}^{(i)} = \sigma_{\mathrm{T}}^{(i)}\,(\underline{\boldsymbol{e}}_2 \otimes \underline{\boldsymbol{e}}_2 + \underline{\boldsymbol{e}}_3 \otimes \underline{\boldsymbol{e}}_3) + \sigma_{\mathrm{L}}^{(i)}\,\underline{\boldsymbol{e}}_1 \otimes \underline{\boldsymbol{e}}_1$ where $\otimes$ denotes the tensor product. Each component i obeys the Ohm's law:

$$\underline{\boldsymbol{j}}^{(i)} = -\underset{\sim}{\boldsymbol{\sigma}}^{(i)} . \boldsymbol{\nabla} U^{(i)} = \underset{\sim}{\boldsymbol{\sigma}}^{(i)} \underline{\boldsymbol{E}}^{(i)} \tag{3.4}$$

where U, $\underline{\boldsymbol{j}}$ and $\underline{\boldsymbol{E}}$ denote the electric potential (μV), current density (A mm^{-2}) and the electric field (μV mm^{-1}) respectively. Furthermore, in each individual Cu/Nb component i of this work, the conductivity is isotropic leading to $\sigma_{\mathrm{L}}^{(i)}$=$\sigma_{\mathrm{T}}^{(i)}$, as mentioned in Section 3.2.2. On the other hand, the assembly of long fibers at H1 exhibit a transverse isotropic effective conductivity (Gu et al., 2015).

The detailed GSC derivation of the effective conductivity $\widetilde{\underset{\sim}{\boldsymbol{\sigma}}}$ of the n-layered elementary fibers can be found in Gu et al. (2015); Hervé-Luanco and Joannès (2016). In the present work, the specific Cu-Nb Filamentary wires which consisted of two cylindrical layers at H1 (i.e. n=2) are studied. In this particular case, the effective *transverse* conductivity reads (Hervé-Luanco and Joannès, 2016):

$$\widetilde{\sigma}_{\mathrm{T}} = \frac{\sigma_{\mathrm{T}}^{(2)}[R_2^2(\sigma_{\mathrm{T}}^{(2)} + \sigma_{\mathrm{T}}^{(1)}) - R_1^2(\sigma_{\mathrm{T}}^{(2)} - \sigma_{\mathrm{T}}^{(1)})]}{R_2^2(\sigma_{\mathrm{T}}^{(2)} + \sigma_{\mathrm{T}}^{(1)}) + R_1^2(\sigma_{\mathrm{T}}^{(2)} - \sigma_{\mathrm{T}}^{(1)})]} \tag{3.5}$$

where component 1 and 2 indicate here Nb and Cu-0 respectively and R_1 and R_2 denote the radius of Nb cylinder and the external radius of Cu-0 tube respectively. In the case of effective *longitudinal* conductivity $\widetilde{\sigma}_{\mathrm{L}}$, GSC scheme leads to the following expression:

$$\widetilde{\sigma}_{\mathrm{L}} = \sum f^{(i)}\,\sigma_{\mathrm{L}}^{(i)} \tag{3.6}$$

with $f^{(i)}$ denotes the volume fraction of component i. It should be noted that Eq. (3.6) is nothing else but the rule of mixture for conductivity. It is the exact solution of the longitudinal conductivity for all the microstructures formed by parallel long fibers despite their distributions (Mallick, 2007). Thus, this solution does not depend on homogenization method used.

3.4.2 Full-field periodic model

The mean-field GSC scheme, presented in the previous section, assumes a random distribution of long fibers. In order to take into account the quasi-periodic fiber distribution

observed experimentally (Fig. 3.1) due to material processing and to investigate the effect of this particular distribution, a periodic problem needs to be solved. As mentioned in Kanit et al. (2003); Besson et al. (2009); Gu et al. (2015, 2017), a unit cell subjected to periodic boundary conditions was considered and this problem was solved using the FEM (i.e. so-called PH for Periodic Homogenization). The periodicity of unit cell and boundary conditions allow us to determine the effective conductivity $\widetilde{\underset{\sim}{\boldsymbol{\sigma}}}$ in a periodic and infinite HEM.

The section views of the unit cell of H1 and H2, with their FE meshes (c3d20 elements[3]), are respectively indicated in Fig. 3.3(c) and Fig. 3.3(d). Zébulon software [4] is used to perform the FE simulations of PH model. The unit cell contains all the information about the morphological RVE (Representative Volume Element) at the effective scales H1 and H2. These meshes are composed of two equivalent long fibers (1+4×1/4 fibers) which are arranged in an hexagonal lattice, and they represent the (idealized) multi-scaled experimental microstructure of Cu-Nb wires. It should be noted that the real architecture of Cu-Nb wires at all scales contains only a finite number (i.e. 85) of long fibers. We have verified with the help of a larger hexagonal structure without periodic boundary conditions that the assumed infinity does not significantly affect our results. The mesh density has also been checked to ensure adapted numerical accuracy.

In periodic boundary conditions, the electric potential U in the elementary volume V takes the following form:

$$U = \langle \boldsymbol{\nabla} U \rangle \cdot \underline{\boldsymbol{x}} + t\,, \quad \forall \underline{\boldsymbol{x}} \in V \tag{3.7}$$

where $\langle \boldsymbol{\nabla} U \rangle$ indicates the volume average of the electric field of V. In Eq. (3.7), the fluctuation t is periodic, i.e. it takes the same values at two homologous points on opposite faces of V. Furthermore, the scalar of current density $\underline{\boldsymbol{j}} \cdot \underline{\boldsymbol{n}}$ takes opposite values at the two homologous points on opposite faces of V ($\underline{\boldsymbol{n}}$ is the outwards normal vector to ∂V at $\underline{\boldsymbol{x}} \in V$). In order to determine the two components of effective conductivity (i.e. $\widetilde{\sigma}_{\mathrm{L}}$ and $\widetilde{\sigma}_{\mathrm{T}}$), the electric field $\underline{\boldsymbol{E}}$ is subjected successively to V as a boundary condition: $\langle \boldsymbol{\nabla} U \rangle = E_0 \underline{\boldsymbol{e_1}}$ for the longitudinal conductivity $\widetilde{\sigma}_{\mathrm{L}}$ and $\langle \boldsymbol{\nabla} U \rangle = E_0 \underline{\boldsymbol{e_2}}$ (or $E_0 \underline{\boldsymbol{e_3}}$) for the transverse one $\widetilde{\sigma}_{\mathrm{T}}$. Then the average current density $\langle \underline{\boldsymbol{j}} \rangle$ is determined by numerical homogenization leading to the effective conductivity $\widetilde{\underset{\sim}{\boldsymbol{\sigma}}}$ of PH by using the following equation:

$$\langle \underline{\boldsymbol{j}} \rangle = -\widetilde{\underset{\sim}{\boldsymbol{\sigma}}} \cdot \langle \boldsymbol{\nabla} U \rangle \,. \tag{3.8}$$

3.4.3 Scale transition strategy

Both GSC scheme and FEM PH are applied at the effective scale H1 taking the size effect into account by the definition of $\underset{\sim}{\boldsymbol{\sigma}}^{(i)}$ of each individual Cu/Nb component (see

[3] c3d20: quadratic hexahedrons with 20 nodes per element
[4] Software for finite element method - http://www.zset-software.com/products/zebulon/

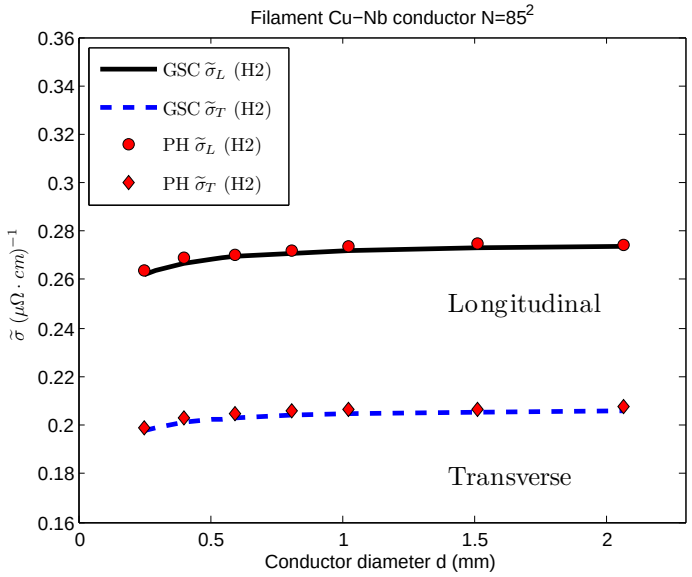

(a)

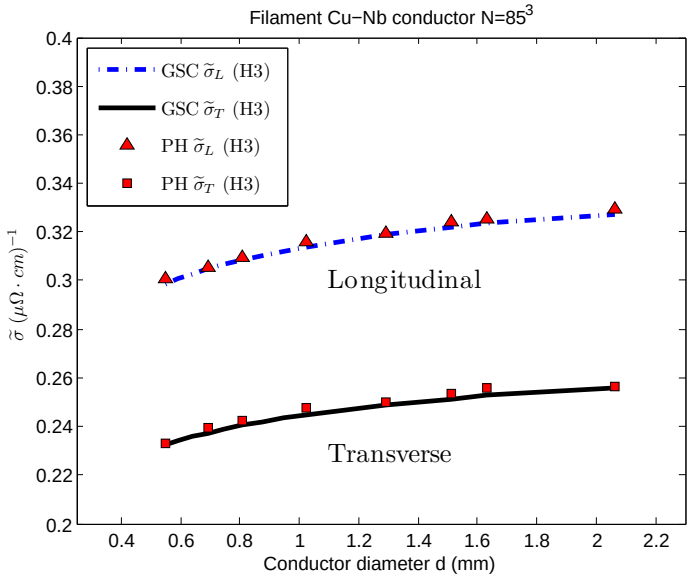

(b)

FIGURE 3.4: Effective longitudinal and transverse conductivity of (a) H2 for N=85^2 and (b) H3 for 85^3 with respect to the conductor diameter d. The curves are obtained by the Generalized Self-Consistent model (GSC) and the points by Periodic Homogenization (PH).

Table 3.1). It is found that the effective electrical conductivity $(\widetilde{\underset{\sim}{\sigma}})_{\mathrm{H1}}$ obtained by the two models are in a very good agreement (PD [5] ∼1.0%). This result allows an accurate prediction of the effective conductivity at larger scales (i.e. H2/H3 scale).

At H2 scale (Fig. 3.1(b)(e)), these effective long fibers consists of two layers: (1) the nano-composite Cu-Nb zones containing 85^1 parallel elementary fibers (i.e. H1 zones) and (2) the Cu-1 matrix. As illustrated in Fig. 3.3, an iterative process is proposed. The electrical conductivity of the inner layer at scale H2, $(\underset{\sim}{\sigma}^{(1)})_{\mathrm{H2}}$, is given by the effective tensor $(\widetilde{\underset{\sim}{\sigma}})_{\mathrm{H1}}$ at H1. On the other hand, $(\underset{\sim}{\sigma}^{(2)})_{\mathrm{H2}}$ of the second layer for H2 is associated with the conductivity of Cu-1 $(\underset{\sim}{\sigma})_{\mathrm{Cu\text{-}1}}$. The scale transition is then performed by GSC and PH approaches, leading to the effective conductivity $(\widetilde{\underset{\sim}{\sigma}})_{\mathrm{H2}}$ for the assembly of 85^2 elementary long fibers. The same iterative process will be repeated up to H3 for N=85^3 conductors using the same models, allowing to estimate $(\widetilde{\underset{\sim}{\sigma}})_{\mathrm{H3}}$.

The transverse isotropic effective conductivity $(\widetilde{\underset{\sim}{\sigma}})_{\mathrm{H2}}$ (for N=85^2) and $(\widetilde{\underset{\sim}{\sigma}})_{\mathrm{H3}}$ (for N=85^3) at 293 K are shown in Fig. 3.4(a) and Fig. 3.4(b) respectively. The decrease in conductivity $\widetilde{\underset{\sim}{\sigma}}$ with the diameter d reduction is due to the channel width δ reduction associated with drawing (i.e. due to size effect).

It is remarkable that the GSC scheme and PH provide very close results for all the diameters d of N=$85^2/85^3$ conductors. The PD between the predictions of these two models is always ∼1%. According to Gu et al. (2015), this good match between model responses is likely due to (i) the relatively small electrical contrast between Cu and Nb electrical conductivities and (ii) both models take into account the presence of a component playing the role of a matrix. Furthermore, similar predictions of GSC and PH demonstrate a limited influence of fiber distribution on conductivity, as these two models assume respectively a random or a periodic distribution.

3.5 Experimental comparison and discussion

3.5.1 Experimental comparison for longitudinal conductivity

In Section 3.3, we have determined the experimental macroscopic longitudinal conductivity by four-point probing at 293K. Then the anisotropic effective conductivity $(\widetilde{\underset{\sim}{\sigma}})_{\mathrm{H2}}$ of N=85^2 (also for $(\widetilde{\underset{\sim}{\sigma}})_{\mathrm{H3}}$ of N=85^3) has been determined by the GSC scheme and the FEM PH method with a scale transition iterative process in Section 3.4.3.

In this section, at first, the model predictions of the effective macroscopic longitudinal conductivities (i.e. $(\widetilde{\sigma}_{\mathrm{L}})_{\mathrm{S2}}/(\widetilde{\sigma}_{\mathrm{L}})_{\mathrm{S3}}$ for N=$85^2/85^3$ respectively) are calculated by the rule of mixture (Eq. (3.6)). These results are then compared with experimental data, as illustrated in Fig. 3.5. The uncertainty of the conductivity measurement is on the

[5] Percentage Difference (PD in %): the absolute difference between two values divided by their average.

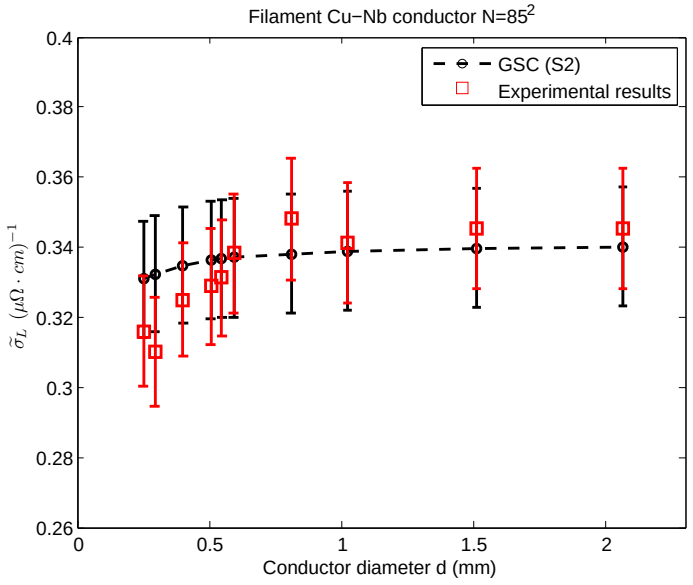

(a)

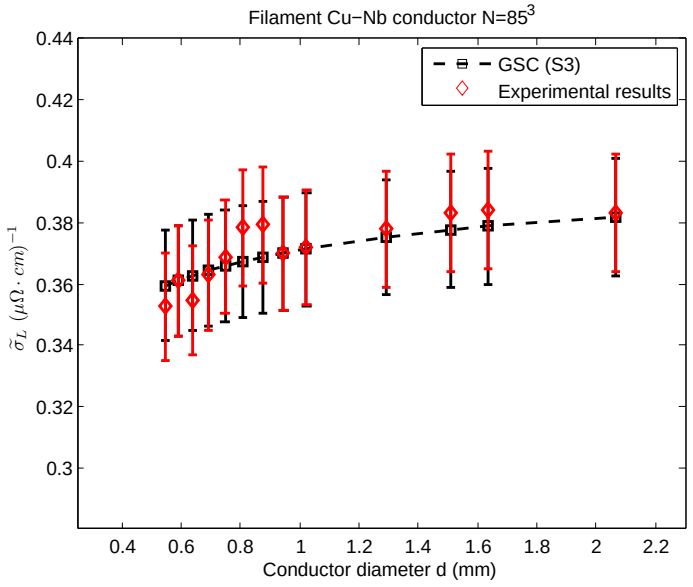

(b)

FIGURE 3.5: Experimental data for macroscopic longitudinal conductivity compared with modeling results with various diameters d for: (a) N=85^2; (b) N=85^3.

order of ±5% for $(\widetilde{\sigma}_{\mathrm{L}})_{\mathrm{S2/3}}$ of Cu-Nb composite specimens (Medy, 2016) and for the σ_{bulk} of bulk specimens (Thilly, 2000). The model results depend directly on σ_{bulk} for each Cu/Nb component, the uncertainty of σ_{bulk} leads to an uncertainty of a similar magnitude on model results (i.e. ±5%) (Gu et al., 2015).

A good agreement (PD< 5%) is found between experiment and theory for macroscopic longitudinal conductivity of both N=85^2 and 85^3 Cu-Nb wires with various conductor diameters. The longitudinal model predictions depend on the conductivity of each Cu/Nb component $(\boldsymbol{\sigma})_{\mathrm{Nb/Cu\text{-}i}}$ (i=0,1,2,3) and the scale transition strategy (i.e. the rule of mixture). The general good agreement between the model predictions and the experimental data proves that the Dingle's model (Equations (3.1) and (3.2)) correctly takes into account the size effect on the conductivity. The deviations between experiment and theory could be caused by: (i) dislocation density of highly hardened bulk Cu/Nb specimen (see Section 3.2.2)) dose not always correspond to the density in Cu-Nb wires, especially for the wires with smaller sample diameters. (ii) geometrical heterogeneity (i.e. fluctuations around the cylinders of Nb/effective cylinders of Hi zone (i=0,1,2,3) due to material processing, as observed in Fig. 3.1) is not considered by our models.

3.5.2 Experimental comparison for transverse conductance

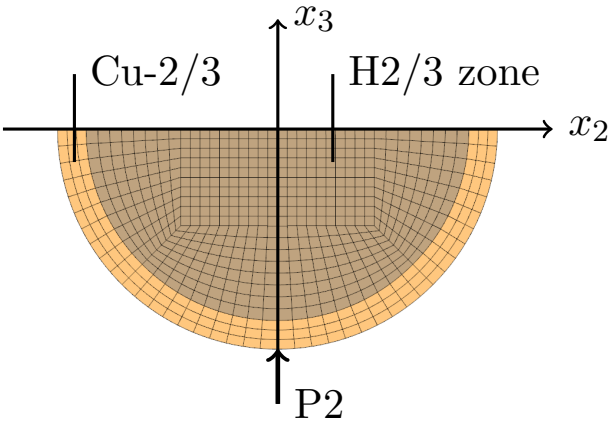

FIGURE 3.6: Section view of the FE mesh at S2/3 scale for N=85^2 and N=85^3 respectively.

In Section 3.3, the transverse electrical conductances $I/\Delta U$ of the cylinder-shaped samples have been measured by four-point probing at macro-scale (i.e. S2/S3 scale for N=85^2/85^3 respectively). These data are shown in Fig. 3.7 with respect to the positions of mobile P4. Unlike the uncertainties of P4 positions, the uncertainties of the conductance measurement is non-zero but rather small. For the sake of simplicity, only error-bars of the positions of P4 are plotted in Fig. 3.7. It should be noted that the transverse electrical *conductivity* σ_{T} cannot be calculated easily by an analytical approach from the measured *conductance* due to the irregular cylinder-shaped sample geometry

(Chan, 1994). In order to compare experimental data with model predictions, structural problems (i.e. S2 and S3) are proposed and they will be solved by FEM.

The FE mesh (c3d20) with real dimensions of the S2/S3 sample for computing the apparent electrical conductance is indicated in Fig. 3.6. In order to improve the computational efficiency for the S2/S3 mesh, only half of the Cu-Nb sample is simulated. Symmetric boundary conditions (i.e. electric potential U=0) are imposed on the appropriate x_3=0 surface. For N=85^2 Cu-Nb wires (similarly for 85^3), the electrical conductivity of the inner Cu-Nb composite zone of H2 and the external Cu-2 jacket are assigned to $(\widetilde{\boldsymbol{\sigma}})_{\text{H2}}$ determined in Section 3.4.3 and $(\widetilde{\boldsymbol{\sigma}})_{\text{Cu-2}}$ (Table 3.1) respectively. In analogy to experiments, the boundary conditions can be applied to the S2/S3 mesh as follows: prescribing electric current I at P1 and P2 and computing potential U at P3 and P4 lead to the electrical conductance (as illustrated in Fig. 3.2). In addition, the uncertainties of the conductivity measurement for bulk specimens σ_{bulk} and of the S2/S3 sample thickness are considered, obtaining an uncertainty of conductance on the order of $\pm 0.6\,\text{m}\Omega^{-1}$.

From the experimental comparison of Fig. 3.7, it follows that the S2/S3 model predicts the correct transverse electric conductance for both N=85^2 and 85^3 Cu-Nb Filamentary wires. Furthermore, the transverse conductance depends directly on the homogenized electrical conductivity $(\widetilde{\sigma}_{\text{T}})_{\text{H2/H3}}$. In other words, the proposed GSC scheme, PH and scale transition iterative process are validated for the first time by experimental data, especially in the transverse direction for the fiber-reinforced materials.

3.5.3 Current density distribution in the Cu-Nb composites

The anisotropic effective electrical conductivity $\widetilde{\boldsymbol{\sigma}}$ was predicted by multiscale modeling (Section 3.4.3) which are validated by experimental data in both longitudinal direction (Section 3.5.1) and transverse direction (Section 3.5.2). As shown in Fig. 3.4, it is found that the effective longitudinal conductivity is always larger than the transverse one $\widetilde{\sigma}_{\text{L}} > \widetilde{\sigma}_{\text{T}}$ ($\widetilde{\sigma}_{\text{L}}/\widetilde{\sigma}_{\text{T}} \approx 1.3$). In this section, our models will provide a quantitative understanding of this anisotropy by exploring the current density distribution at all scales.

The N=85^2 conductor with a diameter of 2.10 mm is chosen here. The transverse current density $j_{\text{T}} = \sqrt{j_2^2 + j_3^2}$ is investigated when the FE mesh at S2 is subjected to a current I=0.1 A at P2 (mentioned in Section 3.5.2). Fig. 3.8(a) indicates j_{T} distribution at S2 scale. A rectangular area corresponding to the H2 RVE size is chosen and its average current density $\langle \underline{\boldsymbol{j}} \rangle$ is determined which is then injected to the mesh at H2. This localization is carried out successively at H1. The j_{T} distributions at H2 and H1 are shown in Fig. 3.8(b) and Fig. 3.8(c) respectively using the same color scale.

It is found that the current density j_{T} displays a non-uniform distribution: about 50% of the Cu channel exhibits a higher j_{T} than the other part due to the fiber-reinforced microstructure, while j_{T} in Nb fibers is negligible compared with Cu matrix. Thus,

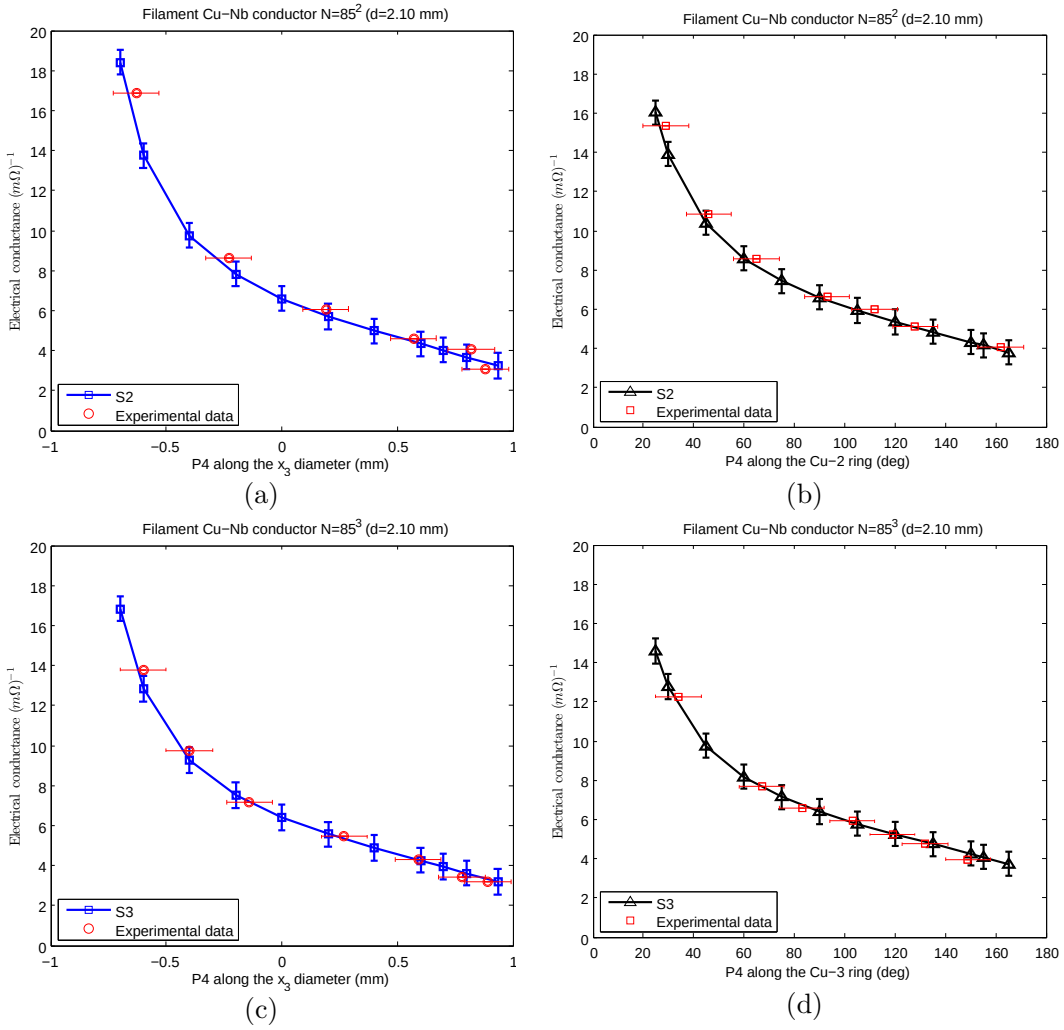

FIGURE 3.7: Experimental transverse conductance compared with model predictions with respect to the positions of P4: (a) P4 along the x_3 diameter for N=85^2; (b) P4 along the Cu-2 ring for N=85^2; (c) P4 along the x_3 diameter for N=85^3; (b) P4 along the Cu-3 ring for N=85^3. The wire diameter d for both N=$85^2/85^3$ is 2.10 mm.

multi-scale modeling demonstrates that current flows along the least resistive path, i.e. within Cu as much as possible, leading to "curved" current lines. On the contrary, when assessed longitudinally, current lines remain parallel to the fibers (Mallick, 2007). In this case, j_L (i.e. j_1) exhibit a uniform distribution in each Cu/Nb component. Therefore, experiments and theory find consistently that the Cu-Nb wires exhibit an anisotropic effective conductivity due to the significant influence of their specific microstructure and architecture.

3.6 Conclusions

This work is focusing on multiscale modeling of the anisotropic electrical conductivity of architectured and nanostructured Cu-Nb composite wires, then this modeling strategy

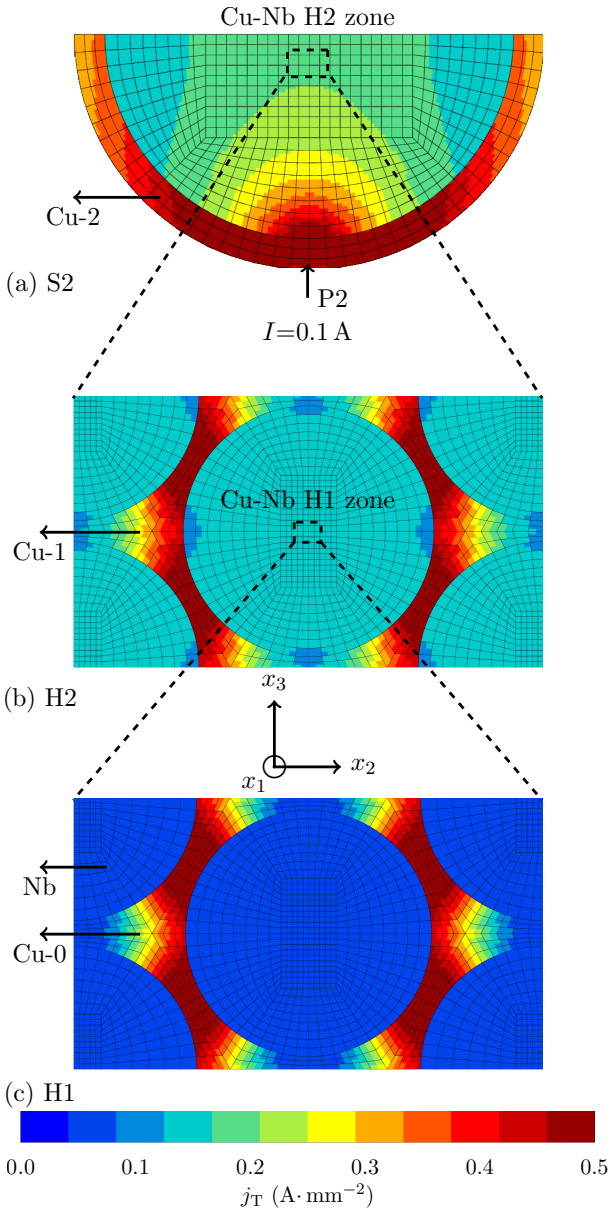

FIGURE 3.8: Transverse current density $j_T = \sqrt{j_2^2 + j_3^2}$ distribution for N=85^2 Cu-Nb Filamentary wires with a diameter of 2.10 mm at (a) the effective scale S2, (b) H2 and (c) H1.

is validated by experimental data for the first time. The main conclusions of this work are the following:

1. *Size effect* is considered in models by the definition of the conductivity of each component in the Cu-Nb wires.

2. *Full field vs. mean field method.* Two homogenization models are applied in this work for the determination of the effective electrical conductivity of the fiber-reinforced microstructure. A full-field GSC scheme and a mean field FEM PH were proposed assuming a random or periodic distribution of Cu-Nb long fibers

respectively. The perfect agreement between the two models reveals a limited influence of fiber distribution on conductivity.

3. *An iterative homogenization approach* is used to predict the effective electrical conductivity up to H2/H3 scale (for N=85^2 and N=85^3 respectively). The effective conductivity estimated by the GSC scheme and PH always almost coincide at all scales.

4. *Anisotropic electrical conductivity characterization.* The anisotropic electrical properties (parallel and perpendicular to the wire direction, i.e. longitudinal and transverse directions) of Cu-Nb wires are determined by experiments.

5. *Model predictions vs. experimental data.* The model predictions are successfully compared with experimental data obtained in this work for both longitudinal and transverse conductivities (i.e. $\widetilde{\sigma}_{\mathrm{L}}$ and $\widetilde{\sigma}_{\mathrm{T}}$). Experiments and theory show consistently that the specific architecture and microstructure of Cu-Nb composites have a significant effect on their anisotropic conductivity (leading to $\widetilde{\sigma}_{\mathrm{L}}/\widetilde{\sigma}_{\mathrm{T}} \approx 1.3$).

It is worth noting that many different physical problems in steady state, such as electrical conductivity, thermal conduction, diffusion and magnetism, share the same constitutive relation between the potential field and its current (Batchelor, 1974; Milton, 2002). In other words, for fiber-reinforced materials (e.g. Cu-Nb wires), the above-mentioned phenomena are equivalent meaning that they can be solved exactly by our hierarchical homogenization strategy.

3.7 Résumé du chapitre en Français

Ce chapitre se concentre sur la modélisation multi-échelles du comportement électrique de fils composites Cu-Nb nanostructurés et architecturés. Après étirage et empilement cumulatif, ce matériaux présente une architecture multi-échelle. Il contient un assemblage de 85^2 ou 85^3 motifs de Nb/Cu (c.-à.-d. fils de Cu-Nb filamentaires, N=85^2 et 85^3 respectivement), avec les plus petites dimensions de l'ordre de $\sim$50 nm. L'effet de taille des constituants élémentaires (nm) est considéré, basé sur le modèle de Dingle (Dingle, 1950; Thilly, 2000). Afin d'étudier le lien entre la conductivité effective et la microstructure, deux méthodes d'homogénéisation sont appliquées : l'une, en champs moyens (le schéma Auto-Cohérent Généralisé, ACG), dans laquelle une microstructure formée de motifs filamentaires répartis aléatoirement est considérée; et l'autre, en champs complets (ici, la méthode des éléments finis, MEF), dans laquelle l'aspect périodique (que nous appelons HP pour Homogénéisation Périodique) de la microstructure expérimentale est pris en compte. Le caractère multi-échelle du matériau est pris en compte par un processus itératif. Ces résultats sont comparés avec les données expérimentales disponibles (Medy, 2016).

Les principales conclusions de ce chapitre sont les suivantes :

1. *L'effet de taille* associé au raffinement de la microstructure est pris en compte dans la définition de la conductivité de chaque composant dans les composites. Par exemple, la conductivité des échantillons massifs du Cu polycristallin est 0,568 $\mu\Omega^{-1}\text{cm}^{-1}$ à 293K, tandis que le modèle de Dingle prédit une conductivité de 0,327 $\mu\Omega^{-1}\text{cm}^{-1}$ pour les canaux longs de Cu de largeur de 50,9 nm.

2. *Champs complets vs. champs moyens.* ACG en champs moyens et HP en champs complets supposent une distribution aléatoire ou périodique de fibres longues respectivement. Les conductivités anisotropes effectives obtenues par les deux méthodes sont en excellent accord, montrant un moindre effet de la distribution des fibres sur ces propriétés.

3. *Une approche d'homogénéisation itérative* est utilisée pour prédire les propriétés effectives électriques jusqu'aux l'échelles H2 et H3 pour N=85^2 et 85^3 respectivement et les conductivités effectives obtenues par ACG et HP sont presque confondus.

4. *Caractérisation de la conductivité électrique anisotrope.* Les réponses des modèles sont en excellent accord à toutes les échelles considérées, permettant des comparaisons supplémentaires avec les données expérimentales. Pour la première fois, les propriétés électriques anisotropes de fils Cu-Nb sont déterminés par la méthode des quatre points grâce à nos partenaires (Medy, 2016).

5. *Prédictions des modèles vs. données expérimentales.* Les prédictions des modèles sont comparées avec succès aux données expérimentales pour les conductivités longitudinales et transversales (c.-à.-d. $\widetilde{\sigma}_{\mathrm{L}}$ et $\widetilde{\sigma}_{\mathrm{T}}$ respectivement). Les expériences et la théorie à la fois montrent que l'architecture et la microstructure des composites Cu-Nb ont un effet significatif sur leur conductivité effective (conduisant à $\widetilde{\sigma}_{\mathrm{L}}/\widetilde{\sigma}_{\mathrm{T}} \approx 1{,}3$).

Dans l'Annexe A, la conductivité de fils de Cu-Nb co-cylindriques (qui contiennent un assemblage de 85^3 motifs de Cu/Nb/Cu) est aussi prédite. Les bons accords entre les données expérimentales et les prédictions des modèles pour différents types de fils Cu-Nb montrent que la modélisation multi-échelles proposée dans ce travail peut être utilisée pour différents matériaux renforcés par des fibres multicouches.

Chapter 4

Multiscale modeling of the elastic behavior of architectured and structured Cu-Nb composite wires

Abstract

This chapter[1] presents a comprehensive study of the effective elastic behavior of this composite material by three multi-scale models accounting for different microstructural contents: two mean-field models and a full-field finite element model. As the specimens exhibit many characteristic scales, several scale transition steps are carried out iteratively from the grain scale to the macro-scale. The general agreement among the model responses allows suggesting the best strategy to estimate the effective behavior of Cu-Nb wires and save computational time. The importance of crystallographical and morphological textures in various cases is discussed. Finally, the models are validated by available experimental data with a good agreement.

[1]This chapter is a paper submitted in July 2016 to the journal "International Journal of Solids and Structures" (still under review, minor corrections are required by the editors). Throughout this thesis, it is cited as Gu et al. (2017).

4.1 Introduction

The present work concentrates on the multiscale modeling of the *anisotropic elastic behavior* of architectured and nanostructured Cu-Nb composite *wires*. Three multiscale methods will be introduced: two mean-field homogenization models (Standard and Generalized Self-Consistent schemes, denoted respectively SSC and GSC hereafter) and a full-field Finite Element Method (FEM) with periodic boundary conditions (denoted PH, for Periodic Homogenization). These models essentially differ by the microstructural information they are based on for the estimation of the effective behavior. Here, the SSC scheme will be used to describe the elastic response of polycrystals made of Cu or Nb grains, but also for the estimation of a random mixture of Cu and Nb phases. The GSC scheme takes into account a specific filament/nanotube Cu/Nb/Cu microstructure. PH assumes a periodic microstructure, and its response will be compared with the ones obtained by SSC and GSC approaches.

The SSC scheme is known as a homogenization theory used to estimate the mechanical behavior of polycrystals. This mean-field homogenization method is based on a statistical description of the microstructure of polycrystalline aggregates. The underlying microstructure, described by Kröner (1978), corresponds to perfect disorder with infinite graduation of size. The development of the SSC model for heterogeneous elasticity goes back to (Hill, 1965b; Budiansky, 1965; Kneer, 1965; Willis, 1977; Kröner, 1978). Later on, the model has been extended to visco-plastic, elasto-plastic, and elasto-visco-plastic properties, e.g. see (Molinari et al., 1987; Ponte-Castañeda and Suquet, 1998; Lebensohn et al., 2011; Yoshida et al., 2011; Vu et al., 2012). Analysis of the intraphase stress and strain heterogeneity obtained by the SSC scheme, and its comparison with full-field reference calculations, can be found e.g. in (Ponte-Castañeda and Suquet, 1998; Brenner et al., 2004; Lebensohn et al., 2011).

The GSC scheme is another mean-field homogenization method taking into account particular morphologies where one phase plays the role of matrix and where the other one is made of multi-layered fibers. This kind of morphology has been first studied by Hashin (1962) who has developed variational bounding methods applied to a Composite Sphere Assembly made of an arrangement of homothetic two-layers spheres. Then, Hashin and Rosen (1964) have applied these variational bounding methods to exhibit bounds for the five independent elastic moduli of the two-dimensional analogue of the Composite Spheres Assembly. Christensen and Lo (1979) have then derived an estimation for the elastic behavior of such sphere or fiber-reinforced composite by considering a representative two-layers concentric sphere/cylinder embedded in a fictitious homogeneous medium representing the Homogeneous Equivalent Medium (HEM). Their method is known as the "three-phase model". Hervé and Zaoui (1993, 1995) have then extended Christensen and Lo (1979)'s approach to multi-coated sphere or fiber-reinforced composite thanks to the "$(n+1)$-phase model". This model is used here to study the elastic behavior of the

Composite Cylinders Assembly (CCA) present at different scales in Fig. 4.1. The GSC scheme has also been extended to visco-elastic behavior (Beurthey and Zaoui, 2000), nonlinear behavior (Zaoui, 1997), diffusion (Caré and Hervé, 2004), thermal conductivity (Hervé, 2002). Interphase effects have also been taken into account in Hashin (2002) and Hervé-Luanco (2014). Application to the conductivity of Cu-Nb wires is presented in Gu et al. (2015).

With the increase in the computational performance and the number of available numerical software products, computational full-field homogenization methods have gained attention. Unlike mean-field approaches (e.g., SSC and GSC schemes), the full-field methods (e.g. based on FEM) applied to Representative Volume Element (RVE) can describe the detailed experimental microstructure and provide the complex stress/strain fields inside the different phases at the expense of increased computational time. Some full-field methods for polycrystalline aggregates were developed by Ghosh et al. (1995, 1996) in terms of a special class of finite element based on Voronoï cells. Making use of such full-field homogenization models, several linear material behaviors were analyzed: the effective thermal conductivity (Flaquer et al., 2007), the effective thermoelastic properties and residual stresses (Wippler et al., 2011), and the effective elastic properties with a statistical description (Kanit et al., 2003; Fritzen et al., 2009; Böhlke et al., 2010). More complex non-linear mechanical behaviors are also studied for Face-Centered Cubic (FCC) and Body-Centered Cubic (BCC) polycrystalline aggregates in many aspects, such as in (Cailletaud et al., 2003; Böhlke et al., 2009; Schneider et al., 2010; Fritzen and Böhlke, 2011; Klusemann et al., 2012). For taking the anisotropic morphological textures into account, three-dimensional Voronoï mesh generation techniques have been proposed (Barbe et al., 2001a; Fritzen et al., 2009; Fritzen and Böhlke, 2011). In addition, (Yaguchi and Busso, 2005; Fritzen et al., 2009; Böhlke et al., 2010) have also compared full-field model results with the previously mentioned mean-field ones for polycrystalline aggregates.

The full-field FEM can also consider a specific periodic microstructure, such as Composite Spheres Assembly in (Llorca et al., 2000; Michel and Suquet, 2009) and CCA in Gu et al. (2015). In this homogenization method, the microstructure unit cell is subjected to periodic boundary conditions (Besson et al., 2009), therefore it is named as PH model in this work. Llorca et al. (2000) compared the three above mentioned models SSC, GSC, and PH for isotropic elastic behaviors of the Composite Spheres Assembly architecture.

Despite a wealth of literature works on polycrystalline elasticity, we have found that the following two points are still missing: 1. No systematic analysis of the simultaneous contributions of morphological and crystallographic textures to the anisotropic elastic properties for Cu and Nb, especially for the specific crystallographic textures encountered in Cu-Nb wires. 2. No application of current homogenization methods to the complex architectures (i.e. CCA) of recent Cu-Nb composites.

Therefore, the objectives of this chapter are twofold: 1. provide a homogenization model for Cu polycrystals and Nb polycrystals taking the crystallographic and morphological textures into account; 2. provide a multi-scale homogenization procedure to model the architectured and nanostructured Cu-Nb composite wires. The outline of the chapter is as follows. The architecture and nano-structure of Cu-Nb composite wires are described in Section 4.2. In order to reproduce the effective elastic behavior of this material, three multi-scale methods, i.e. SSC, GSC and PH are presented in Section 4.3. In Section 4.4, the Cu polycrystals and the Nb polycrystals are considered separately. Then in Section 4.5, several scale transitions of architectured Cu-Nb composites are performed to determine the effective elastic behavior of Cu-Nb wires up to macro-scale. In Section 4.6, the importance of micro-parameters and the best modeling strategies are discussed for various textures and material properties. Finally, the model results are validated by comparison with available experimental data.

4.2 Material description

4.2.1 Elaboration process

The elaboration process of the "Filamentary" Nb/Cu type of Cu-Nb wires has been presented in Section 2.1. In this section, the material processing of the so-called "co-cylindrical" Cu/Nb/Cu composites (Fig. 4.1) will be briefly described.

Cu-Nb nano-composite wires are fabricated via a severe plastic deformation process, based on ADB (series of hot extrusion, cold drawing and bundling stages) according to (Dupouy et al., 1996; Thilly et al., 2002a,b; Dubois, 2010): a Cu wire is inserted into a Nb tube, itself inserted into a Cu tube. The structure is extruded and drawn, then cut into 85 smaller pieces with hexagonal cross section. These pieces are then bundled and inserted into a new Cu tube. The new composite structure is again extruded and drawn. And so on. In the present work, ADB is repeated three times, leading to copper based architectured and nanostructured composite wires which are composed of a multi-scale Cu matrix embedding 85^3 Nb nanotubes containing 85^3 nanofibers, as illustrated in Fig. 4.1.

For a wire with a final diameter[2] of 0.506 mm, Nb nanotubes (average thickness $\delta_{\text{Nb-t}}$=88 nm and total volume fraction $X_{\text{Nb-t}}$=20.8%) are filled with Cu-f copper filaments (diameter $\delta_{\text{Cu-f}}$=130 nm and volume fraction $X_{\text{Cu-f}}$=4.5%), separated by the finest Cu-0 copper channels (width $\delta_{\text{Cu-0}}$=93 nm and volume fraction $X_{\text{Cu-0}}$=17.7%); groups of 85 Cu/Nb/Cu elementary long fibers are separated by Cu-1 copper channels (width $\delta_{\text{Cu-1}}$=360 nm and $X_{\text{Cu-1}}$=9.6%). The width of Cu-2 copper channel is $\delta_{\text{Cu-2}}$=3.9 μm ($X_{\text{Cu-2}}$=19.9%).

[2]Following (Vidal et al., 2007; Thilly et al., 2009), all dimensions are given in the x_2-x_3 cross-section, i.e. perpendicular to the wire axis x_1, see Fig. 4.1 for the coordinate system.

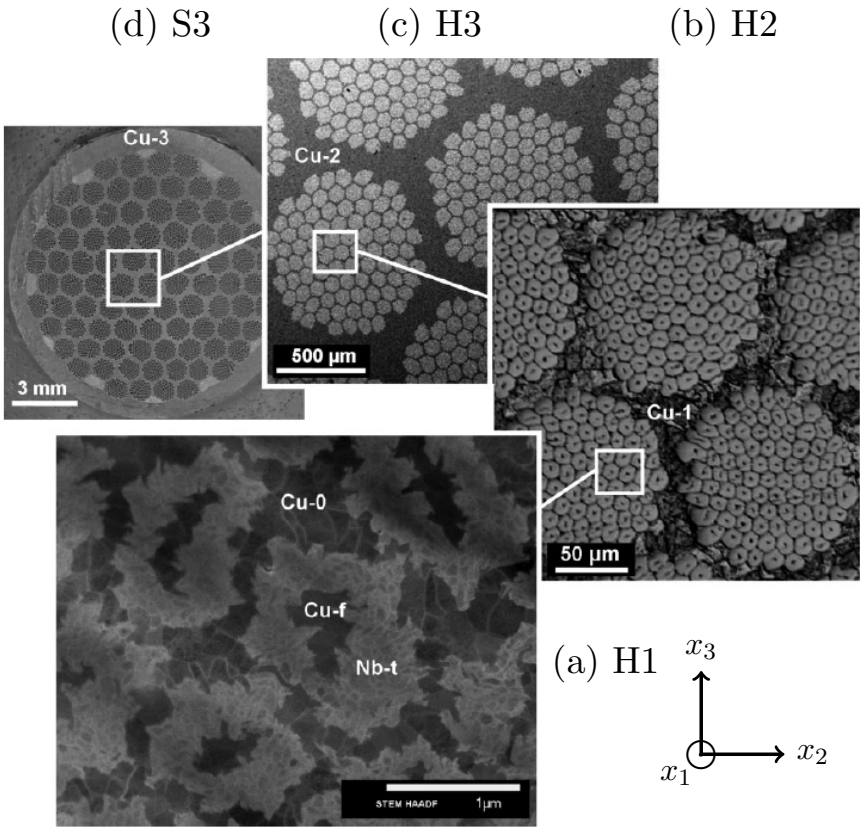

FIGURE 4.1: Successive section views of the Cu/Nb/Cu nano-composite wires (Dubois, 2010; Dubois et al., 2012). (a) Scanning Transmission Electron Microscope image showing details of the Cu/Nb/Cu elementary long fiber sections; (b), (c) and (d) Scanning Electron Microscope images showing intermediate scales and a macroscopic view of the conductor. The diameter of specimen (d) is reduced to 0.506 mm in this work by supplementary cold-drawing.

Finally, the group of 85^3 elementary patterns is embedded in an external Cu-3 copper jacket ($\delta_{\text{Cu-3}}$=21.1 µm and $X_{\text{Cu-3}}$=27.5%).

4.2.2 Morphological and crystallographic textures

The microstructural state of Cu-Nb wires has been studied by Scanning Electron Microscope, Scanning Transmission Electron Microscope and X-ray diffraction by (Vidal et al., 2007; Thilly et al., 2009; Dubois et al., 2010; Dubois, 2010; Dubois et al., 2012). In the present work, we define ℓ as the average grain length along the longitudinal wire axis x_1 and d as the average grain diameter in the transverse x_2-x_3 cross-section. The previous studies have shown that the morphological texture exhibits highly elongated grains along x_1 because of iterative severe plastic extrusion and drawing, therefore we have $\ell \gg d$ for Cu and Nb phases.

Because of the multi-scale structure, different types of copper matrix channels are present in the matrix: (i) Cu channels with a width $\delta_{\text{Cu-i}}$ (i=2,3) larger than a few micrometers

(so-called "large" Cu channels) are mainly composed of grains with a transverse size d=200-400 nm (a typical microstructure of cold-worked material); (ii) On the other hand $\delta_{\text{Cu-i}}$ (i=f,0,1) lies in the sub-micrometer range (so-called "fine" Cu channels), with only a few grains located between the Cu-Nb interfaces: in this case, grain width $d_{\text{Cu-i}}$ varies from $\delta_{\text{Cu-i}}/3$ to $\delta_{\text{Cu-i}}$ (i=f,0,1). In addition, the grain size of Nb tubes $d_{\text{Nb-t}}$ is comparable with their tube width ($d_{\text{Nb-t}} \approx \delta_{\text{Nb-t}}$).

The overall crystallographic texture of a Cu-Nb co-cylindrical composite sample at a diameter of 3.5 mm has been estimated by X-ray diffraction in Dubois (2010). The specimens with smaller diameter 0.506 mm considered in this work are believed to display very similar crystallographic texture, as confirmed by preliminary EBSD results. X-ray diffraction has shown that Cu phases exhibit strong $\langle 111 \rangle$ fiber texture with the remnant $\langle 100 \rangle$ fiber, while a single-component $\langle 110 \rangle$ fiber texture is observed in Nb phases. Due to extrusion and drawing along the wire direction (x_1) in the fabrication process, x_1 is also the symmetry axis of these fibers. In Cu, the volume fractions of $\langle 100 \rangle$ and $\langle 111 \rangle$ components are found to be 37% and 58% respectively (with 5% of an additional random component). In Nb phase, the volume fraction of $\langle 110 \rangle$ fiber is 99% (with 1% random component). The associated texture spread (Full Width at Half Maximum) of individual components are indicated in Table 4.1.

Fiber textures		Volume fractions	FWHM (in *deg*)	
			$\Delta\Phi$	$\Delta\Phi_1$
Cu	$\langle 100 \rangle$	37%	10.1	11.5
	$\langle 111 \rangle$	58%	8.3	10.2
Nb	$\langle 110 \rangle$	99%	6.2	6.8

TABLE 4.1: Overall crystallographic textures and corresponding Full Width at Half Maximum (FWHM) of individual components, for Cu and Nb polycrystals. These fiber textures (symmetry axis x_1) of the Cu-Nb composites were determined by X-ray diffraction (Dubois, 2010). In addition, Cu and Nb contain also 5% and 1% random components respectively.

In the fabrication process, polycrystalline Nb tubes (i.e. Nb-t) are always deformed simultaneously, thus they display the same crystallographic texture. However, the Cu polycrystals are introduced successively at the three steps of ADB, therefore the crystallographic textures are different for each Cu-i ($i = f$, 0, 1, 2 and 3). In the present work, for the sake of simplicity, we consider the same Cu crystallographic textures, as determined from X-ray diffraction in Table 4.1, at all scales of the Cu-Nb wires. In other words, effective elastic behaviors of all the Cu-i ($i = f$, 0, 1, 2 and 3) are assumed to be identical. It will be shown that this approximation is sufficient to predict the elastic behavior for Cu-Nb wires based on the available mechanical data.

From the Orientation Distribution Function described above, we used the software Labo-Tex [3] to generate two sets of 40000 discrete orientations each (one for Cu and one for Nb)

[3] Software for crystallographic textures - http://www.labosoft.com.pl/.

that have been used to generate the microstructure in the three scale transition models. Figure 4.2 shows the obtained Pole Figures and Inverse Pole Figures for both Cu and Nb, using 300 orientations randomly chosen among each of the larger sets of 40000 orientations. The full set of 40000 orientations has been used within the SSC scheme to estimate the effective behavior (section 4.3.1), whereas subsets of 1000 (respectively 100) orientations randomly chosen among the 40000 have been used for parallelepipedic (resp. Voronoï) tessellations (section 4.3.3).

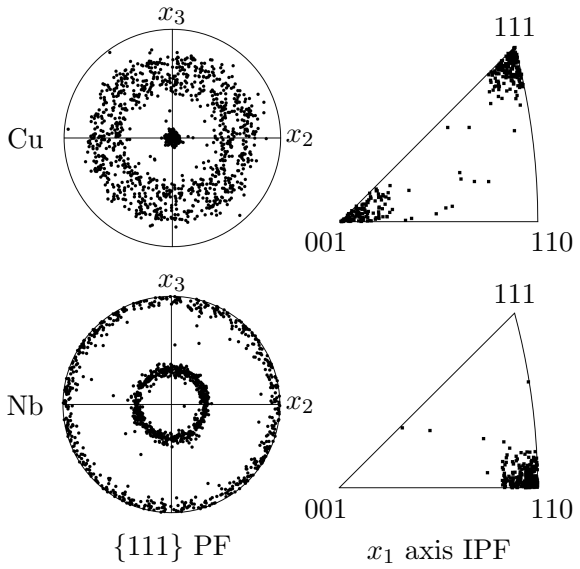

FIGURE 4.2: {111} Pole Figure and x_1 axis Inverse Pole Figure of Cu polycrystals and Nb polycrystals. Grain orientations were generated by LaboTex based on experimental X-ray textures.

4.2.3 Anisotropic elastic properties

The Cu-Nb wires are made of Face-Centered Cubic (FCC) Cu and Body-Centered Cubic (BCC) Nb grains. According to (Epstein and Carlson, 1965; Yosio and Granato, 1966; Carroll, 1965), the cubic elastic constants c_{ij} (Voigt convention) of Cu and Nb single crystals, expressed in a reference frame attached to the cubic crystal lattice, are provided in Table 4.2, and they will be used in H0 for predicting the effective elastic behavior of polycrystalline aggregates. The Zener anisotropy factor Z (Zener, 1948), defined as

$$Z = \frac{2c_{44}}{(c_{11} - c_{12})} , \tag{4.1}$$

is a measure of the elastic anisotropy, having Z=1 for an isotropic material. As shown in Table 4.2, Cu and Nb single crystals exhibit strong anisotropy. The Young's modulus in a $\langle 111 \rangle$ direction is about three times higher (respectively, half smaller) than the one in a $\langle 100 \rangle$ direction in Cu (respectively, Nb) single crystals.

Single crystal	c_{11} (GPa)	c_{12} (GPa)	c_{44} (GPa)	Z
Cu	167.20	120.68	75.65	3.25
Nb	245.60	138.70	29.30	0.55

TABLE 4.2: Cubic elastic constants of Cu and Nb single crystals, expressed in the crystal lattice (Voigt convention).

The components $C_{ijkl}^{(r)}$ of the single crystal elastic moduli $\underset{\sim}{\boldsymbol{C}}^{(r)}$ expressed in a generic global coordinate system can be calculated from the components c_{mnpq} of the independent elastic stiffness $\underset{\sim}{\boldsymbol{c}}$ in the lattice coordinate system

$$C_{ijkl}^{(r)} = Q_{mi}^{(r)} Q_{nj}^{(r)} Q_{pk}^{(r)} Q_{ql}^{(r)} c_{mnpq} \tag{4.2}$$

where $Q_{mi}^{(r)}$ are the components of the rotation matrix $\boldsymbol{Q}^{(r)}$ associated with the crystal orientation r. The corresponding Euler angles $(\psi, \theta, \phi)^{(r)}$ are needed to determine $\boldsymbol{Q}^{(r)}$ (Slaughter, 2002).

Due to ADB processing, the architecture of Cu-Nb wires, morphological and crystallographic textures are axisymmetric with respect to axis x_1. As a result, the effective material behavior of Hi ($i = 0$, 1, 2, 3) is expected to be transversely isotropic. Anisotropic elasticity is then expressed by five independent constants (Hervé and Zaoui, 1995): longitudinal Young's modulus E_1, Poisson's ratio under longitudinal load ν_{12}, longitudinal shear modulus μ_{12}, transverse shear modulus μ_{23}, plane-strain bulk modulus K_{23}. Incidentally, for transverse isotropy, transverse Young's moduli $E_2 \equiv E_3$. In this work, they will be noted as $E_{2,3}$ and can also be derived from the other parameters:

$$E_{2,3} = \frac{4E_1 K_{23} \mu_{23}}{4K_{23}\mu_{23}\nu_{12}^2 + E_1 (K_{23} + \mu_{23})} \tag{4.3}$$

It is also worth noting that $C_{11} = E_1 + 4\nu_{12}^2 K_{23}$, $C_{22} = C_{33} = K_{23} + \mu_{23}$, $C_{12} = C_{13} = 2\nu_{12}K_{23}$, $C_{44} = \mu_{23}$, $C_{55} = C_{66} = \mu_{12}$, $C_{23} = K_{23} - \mu_{23}$ (with $C_{23} = C_{22} - 2C_{44}$ in the case of transverse isotropy), where C_{ij} denotes the components of $\underset{\sim}{\boldsymbol{C}}$ making use of the Voigt notation.

4.3 Homogenization strategies

4.3.1 Mean-field standard self-consistent scheme

The mean-field SSC scheme is used in the present work to estimate the effective elastic property $\underset{\sim}{\widetilde{\boldsymbol{C}}}$ of individual Cu and Nb polycrystals. It is also used to estimate the behavior of a fictitious material in which Cu and Nb grains are randomly mixed all together, with

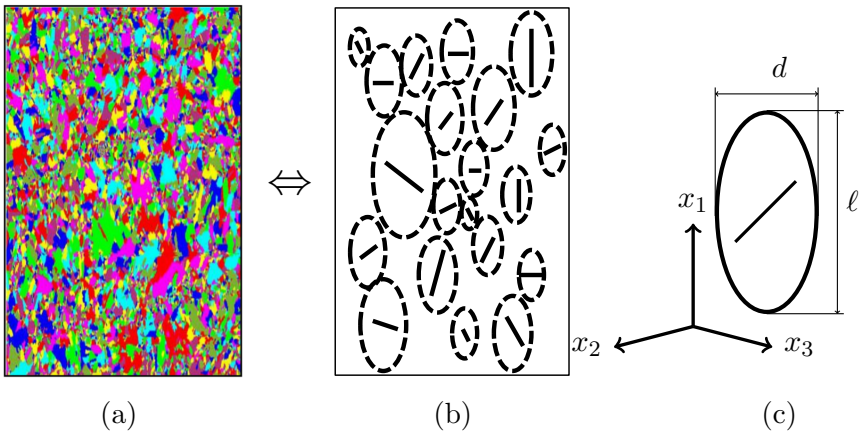

FIGURE 4.3: Schematic geometry of the SSC model: (a) Perfectly disordered mixture of the grains, being similar with the real morphological texture in polycrystals. (b) Statistically equivalent medium composed of randomly mixed *mechanical phases*. A *mechanical phase* is denoted by the set of grains having the same crystal orientation. (c) The overall (mean) shape of all *mechanical phases* is taken ellipsoidal, elongated along direction x_1 and with dimensions $\ell \times d \times d$.

volume fractions and textures introduced above, in order to check the impact of the particular architectured microstructure of our specimens.

Owing to the random character of the microstructure with all grains playing geometrically similar roles, the SSC scheme is especially suited for polycrystals (Kröner, 1978; Castelnau, 2011). The SSC scheme relies on specific microstructure exhibiting a sufficiently irregular mixture of grains and infinite size graduation as illustrated in Fig. 4.3(a). As in (Lebensohn et al., 2011; Castelnau, 2011), one defines a *mechanical phase* (r) as denoting the set of all grains in the microstructure that share the same elastic properties, that is exhibiting the same crystal orientation; those grains have however different shapes and environment. The material can thus be statistically described as an equivalent aggregate filled with mechanical phases of different size and surrounding, and distributed randomly. It is supposed that the phases exhibit, *on average*, an ellipsoidal shape, and therefore the *mean* stress and strain inside those phases can be estimated with the Eshelby inclusion problem; but note that this does not mean that stress and strain are uniform inside individual phases, see e.g. Ponte-Castañeda and Suquet (1998); Brenner et al. (2004). Here, ellipsoids corresponding to the mean grain shape are elongated along the longitudinal direction x_1, with length ℓ and width d, as in Fig. 4.3(c). The associated "grain aspect ratio" ℓ/d statistically defines the morphological texture of the polycrystalline aggregate.

For elastic polycrystals, local and effective constitutive relations read respectively:

$$\underset{\sim}{\boldsymbol{\sigma}}(\underline{\boldsymbol{x}}) = \underset{\approx}{\boldsymbol{C}}(\underline{\boldsymbol{x}}) : \underset{\sim}{\boldsymbol{\varepsilon}}(\underline{\boldsymbol{x}}), \qquad \overline{\underset{\sim}{\boldsymbol{\sigma}}} = \widetilde{\underset{\approx}{\boldsymbol{C}}} : \overline{\underset{\sim}{\boldsymbol{\varepsilon}}} \tag{4.4}$$

with $\underset{\sim}{\widetilde{C}}$ the effective stiffness tensor

$$\underset{\sim}{\widetilde{C}} =< \underset{\sim}{C}(\underline{x}) : \underset{\sim}{A}(\underline{x}) > \tag{4.5}$$

where $\underset{\sim}{A}(\underline{x})$ is the strain localization tensor defined as:

$$\underset{\sim}{\varepsilon}(\underline{x}) = \underset{\sim}{A}(\underline{x}) : \overline{\underset{\sim}{\varepsilon}}, \tag{4.6}$$

and $\overline{\underset{\sim}{\varepsilon}}$ being the macroscopic applied strain. In elastic polycrystals, the local stiffness tensor is a uniform property inside grains. The quantity $\underset{\sim}{C}(\underline{x})$ in Eq.(4.4) can therefore be replaced by the corresponding homogeneous values $\underset{\sim}{C}^{(r)}$ of the considered *mechanical phase* (r) defined previously. Similar substitution can be made in Eq.(4.5) leading to:

$$\underset{\sim}{\widetilde{C}} = \sum_{n=1}^{r} f^{(r)} \underset{\sim}{C}^{(r)} : \underset{\sim}{A}^{(r)} \tag{4.7}$$

where $.^{(r)}$ indicates the average over the volume of phase (r), e.g. $\underset{\sim}{A}^{(r)} = \left\langle \underset{\sim}{A}(\underline{x}) \right\rangle_{(r)}$, and $f^{(r)}$ denotes volume fraction of phase (r).

To estimate the phase-average stress and strain, phase (r) is treated in the SSC scheme as an ellipsoidal inclusion embedded in an homogeneous equivalent medium whose behavior represents that of the polycrystal. According to (Hill, 1965b; Budiansky, 1965; Llorca et al., 2000), tensor $\underset{\sim}{A}^{(r)}$ in phase (r) reads

$$\underset{\sim}{A}^{(r)} = \left\{ \underset{\sim}{I} + \underset{\sim}{S}_{\text{Esh}} : \left[\underset{\sim}{\widetilde{C}} \right]^{-1} : \left(\underset{\sim}{C}^{(r)} - \underset{\sim}{\widetilde{C}} \right) \right\}^{-1}, \tag{4.8}$$

with $\underset{\sim}{I}$ the fourth order unit tensor. The Eshelby tensor $\underset{\sim}{S}_{\text{Esh}}$ depends on $\underset{\sim}{\widetilde{C}}$ and on the aspect ratio ℓ/d. Here, the Eshelby tensor is calculated numerically as detailed in (Brenner et al., 2004). Equations (4.5) and (4.8) lead to an implicit equation for $\underset{\sim}{\widetilde{C}}$ that can be solved with a simple fixed-point method (Kröner, 1978). Finally, from Eq.(4.7), it can be observed that the sole knowledge of the mean (phase average) values $\underset{\sim}{A}^{(r)}$ is sufficient to estimate the overall behavior $\underset{\sim}{\widetilde{C}}$. Therefore, computational time of this mean-field SSC method will be very fast, without having to know the complete field of $\underset{\sim}{A}(\underline{x})$.

4.3.2 Mean-field generalized self-consistent scheme

The "$(n+1)$-phase" GSC scheme (Hervé and Zaoui, 1995) is used here to estimate the overall effective elastic moduli of multi-coated fiber-reinforced composites with a hypothetical random fiber distribution. The GSC scheme was developed by considering at first the "n-layered cylindrical inclusion problem": an n-layered cylindrical inclusion

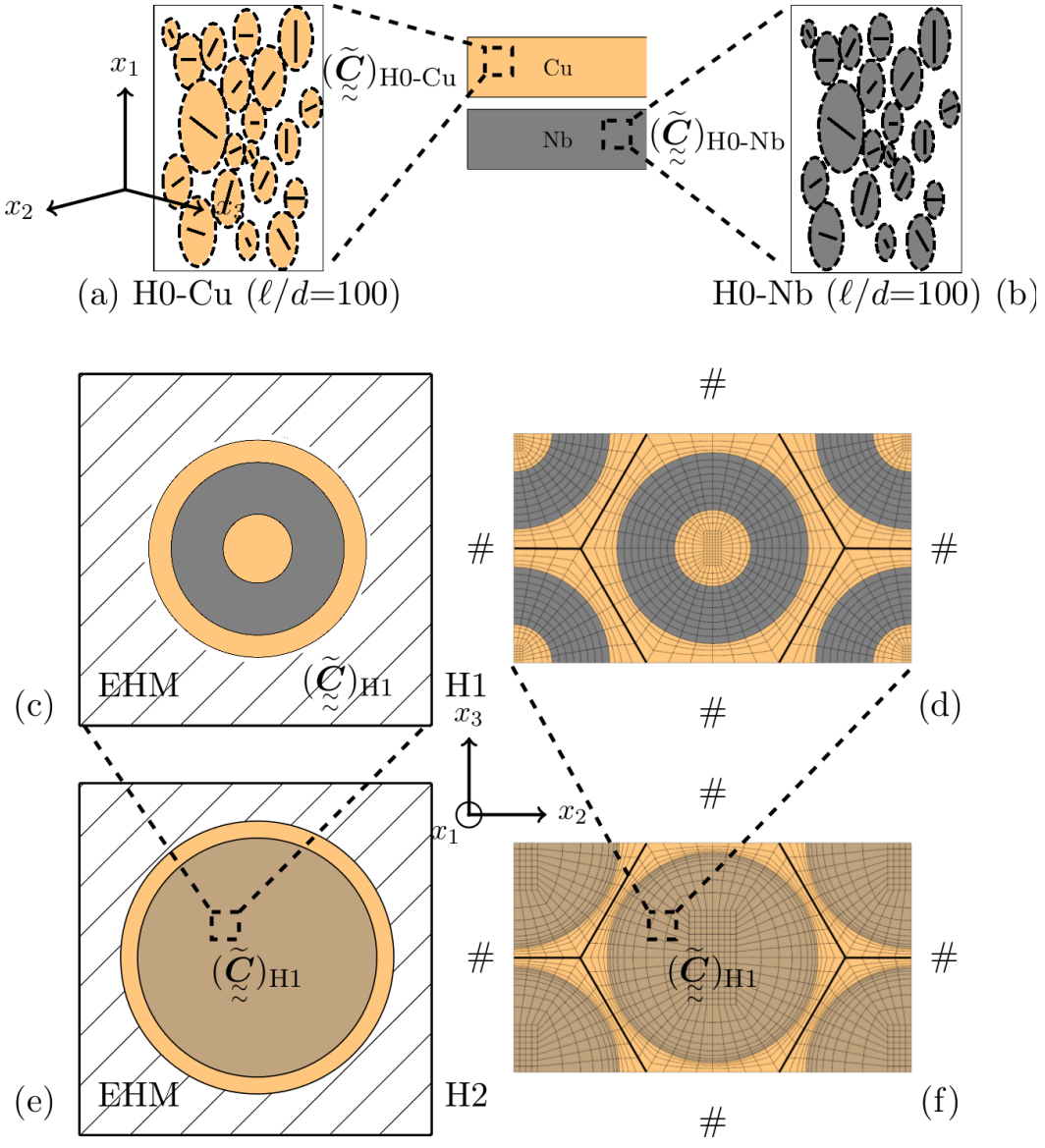

FIGURE 4.4: Multiscale modeling of effective elastic behaviors of Cu-Nb composite wires: (a) Cu polycrystal (at the effective scale H0) with the effective elastic tensor obtained by the SSC scheme (ℓ/d=100); (b) Nb polycrystal (scale H0) with the SSC scheme (ℓ/d=100); (c) Within the GSC scheme, the Cu-Nb n-layered (n = 3 for H1) cylindrical inclusion is surrounded by an infinite Homogeneous Equivalent Medium (HEM); The Cu-Nb CCA (Composite Cylinders Assembly) is assumed to exhibit a random fiber distribution in this model; (d) Cu-Nb CCA of H1 with a periodic distribution assumed by FEM PH model (# denotes the periodic boundary condition); (e) 2-layered cylindrical inclusion for H2 surrounded by an HEM in GSC; (f) Cu-Nb CCA of H2 with a periodic distribution in PH. Yellow stands for Cu, gray for Nb, and brown for Cu-Nb composite.

is embedded in an infinite matrix (i.e. phase $n+1$); each phase is homogeneous, linearly elastic, transversely isotropic with the symmetry axis along the fiber direction x_1. In addition, perfect bonding is assumed requiring the continuity of the stress vector and of the displacement field at the interfaces of different phases. The above-defined specimen is subjected to several different remote boundary conditions in Hervé and Zaoui (1995) (so-called in-plane hydrostatic mode, normal tensile mode, in-plane transverse share mode and anti-plane longitudinal shear mode) aiming to derive the elastic strain and stress fields in each phase. The infinite matrix, phase $n+1$, has been then replaced by an unknown HEM characterized by the effective elastic tensor $\widetilde{\underset{\sim}{C}}$. This tensor is finally determined thanks to a self-consistent energy condition and to the previously solved "n-layered cylindrical inclusion problem" (Christensen and Lo, 1979; Hervé and Zaoui, 1995). In the present work, the effective elastic behavior of the studied Cu-Nb CCA is computed by the GSC scheme with $n = 2$ and $n = 3$, as illustrated in Fig. 4.4(c) and Fig. 4.4(e) for H1 and H2 respectively.

4.3.3 Full-field periodic models

In addition to mean-field SSC and GSC schemes, a full-field FEM PH is proposed here to homogenize the effective elastic behavior of Cu-Nb wires at all scales. An elementary volume V made of heterogeneous material is considered for polycrystalline aggregates (scale H0) in Section 4.3.3.1 and for a specific architecture (scales H1-H3) in Section 4.3.3.2. Periodic boundary conditions are prescribed at its boundary ∂V. The displacement field $\underline{\boldsymbol{u}}$ in V, then takes the following form:

$$\underline{\boldsymbol{u}}\,(\underline{\boldsymbol{x}}\,) = \bar{\underset{\sim}{\varepsilon}}\cdot\underline{\boldsymbol{x}} + \underline{\boldsymbol{v}}\,(\underline{\boldsymbol{x}}\,) \quad \forall \underline{\boldsymbol{x}} \in V \tag{4.9}$$

where the fluctuation $\underline{\boldsymbol{v}}$ is periodic, i.e. it takes the same values at two homologous points on opposite faces of V. Furthermore, the traction vector $\underset{\sim}{\boldsymbol{\sigma}}\cdot\underline{\boldsymbol{n}}$ takes opposite values at two homologous points on opposite faces of V ($\underline{\boldsymbol{n}}$ is the outwards normal vector to ∂V at $\underline{\boldsymbol{x}} \in V$).

Using the Voigt notation, stress and strain fields $\underset{\sim}{\boldsymbol{\sigma}}$ and $\underset{\sim}{\boldsymbol{\varepsilon}}$ are expressed as 6-dimensional vectors: $\underline{\boldsymbol{\sigma}} = (\sigma_{11}, \sigma_{22}, \sigma_{33}, \sigma_{23}, \sigma_{13}, \sigma_{12})$ and $\underline{\boldsymbol{\varepsilon}} = (\varepsilon_{11}, \varepsilon_{22}, \varepsilon_{33}, 2\varepsilon_{23}, 2\varepsilon_{13}, 2\varepsilon_{12})$. In order to determine the symmetric anisotropic tensor $\widetilde{\underset{\sim}{C}}$, six computations are necessary for each statistical realization of the volume element V to find the 21 elastic coefficients (Kanit et al., 2003). Here, we impose successively six macroscopic normal and shear strain boundary conditions over V as follows: $\langle\underline{\boldsymbol{\varepsilon}}\rangle = \underline{\boldsymbol{e_i}}$ where $\underline{\boldsymbol{e_i}}$ denotes the 6-dimensional unit vector, and i varies from 1 to 6. Then six homogenized response stress tensors $\bar{\underline{\boldsymbol{\sigma}}}$ can be determined by numerical homogenization leading to the effective elastic stiffness $\widetilde{\underset{\sim}{C}}$ by using Eq.(4.4).

4.3.3.1 PH adapted for polycrystalline aggregates

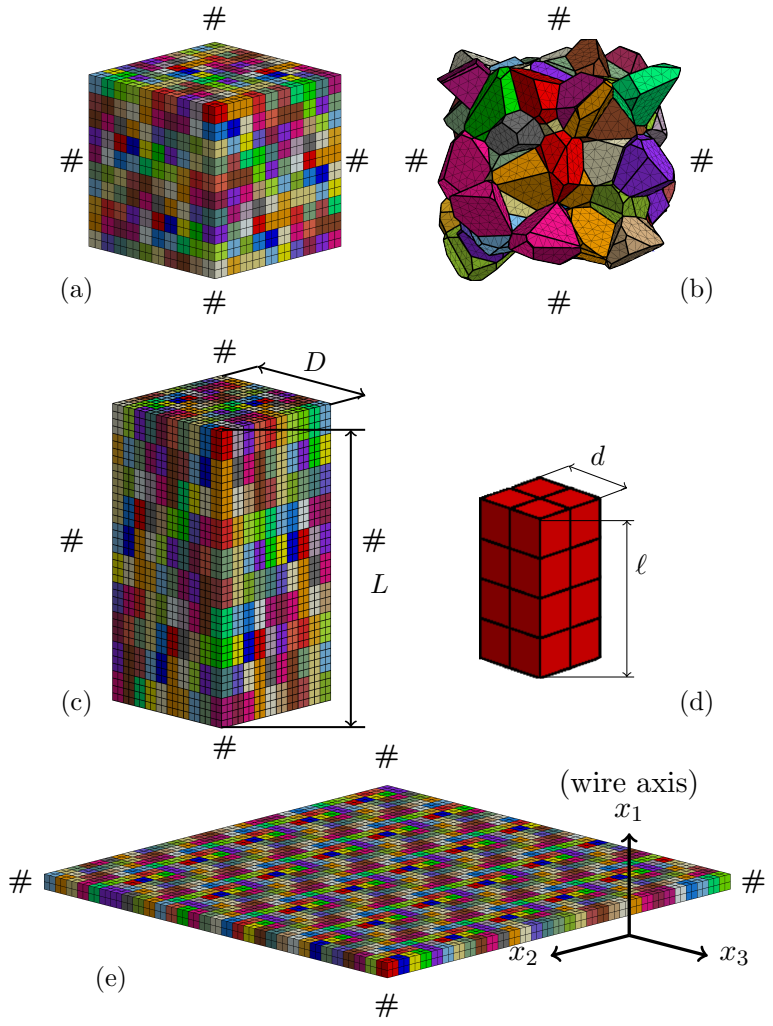

FIGURE 4.5: Meshes of PH models for polycrystalline aggregates: (a) parallelepipedic tessellation of (10 × 10 × 10) 1000 grains with the aspect ratio ℓ/d=1; (b) Voronoï tessellation of 100 grains with ℓ/d=1.00±0.34; (c) parallelepipedic tessellation of (10 × 10 × 10) 1000 grains with L/D=ℓ/d=2, L and D being defined as the length and width of the volume element respectively; tessellations of L/D=ℓ/d=1,2,5,10 and 20 are considered in this work; (d) Individual columnar grain for parallelepipedic tessellations in the case of ℓ/d=2, elongated along the wire direction x_1; (e) parallelepipedic tessellation of (31 × 31) 961 grains with $\ell/d \to \infty$. Periodic boundary conditions, denoted #, are considered.

Unlike mean-field models in which the microstructure is described statistically, FEM PH can account for the real experimental microstructure at scale H0, and it provides the full-field stress/strain fields over V. In the present work, PH is used to study the effect of a specific morphological/crystallographic texture and to compare the results with the ones obtained with mean-field methods.

As illustrated in Fig. 4.5(a), the polycrystalline aggregate (scale H0) is represented by a regular cubic grid made of parallelepipedic grains with the aspect ratio ℓ/d=1. Along

each edge of this three-dimensional tessellation (finite element mesh using c3d20[4]), 10 grains are considered, leading to $10 \times 10 \times 10$=1000 grains per mesh. The used grain orientations (i.e. crystallographic texture) and single crystal properties of Cu and Nb are those given in Section 4.2.2 and Section 4.2.3, and the discrete orientations are spatially randomly distributed among the grains of the parallelepipedic tessellation. Furthermore, this elementary volume is subjected to periodic boundary conditions, Eq.(4.9), in order to take advantage of a smaller RVE than the one with homogeneous boundary conditions (Kanit et al., 2003).

Voronoï tessellation in Fig. 4.5(b) is also used to evaluate the impact of the over-simplified parallelepipedic grain shape in the previous problem. This aggregate (finite element mesh using c3d4[5]) is subjected to periodic boundary conditions, and 100 Voronoï cells are distributed randomly in space. The grain aspect ratio ℓ/d is statistically 1.00 with a 95% confidence interval of ± 0.34. Although more realistic than parallelepipedic grains, Voronoï tessellations still provide a smaller grain size distribution than real polycrystals (Lebensohn et al., 2005).

Due to the fabrication process, Cu and Nb grains are highly elongated along x_1. In order to take this morphological texture into account, a series of parallelepipedic tessellations (c3d20) is considered here in PH. The case L/D=ℓ/d=2, where L and D denote the mesh length and width respectively, is illustrated in Fig. 4.5(c). Several meshes elongated along the wire direction x_1 are used in this work to consider various grain aspect ratios: ℓ/d=2, 5, 10 and 20. The case $\ell/d \to \infty$ is represented by a slice-shaped parallelepipedic tessellation composed of $31 \times 31 = 961$ grains subjected to periodic boundary conditions (Fig. 4.5(e)).

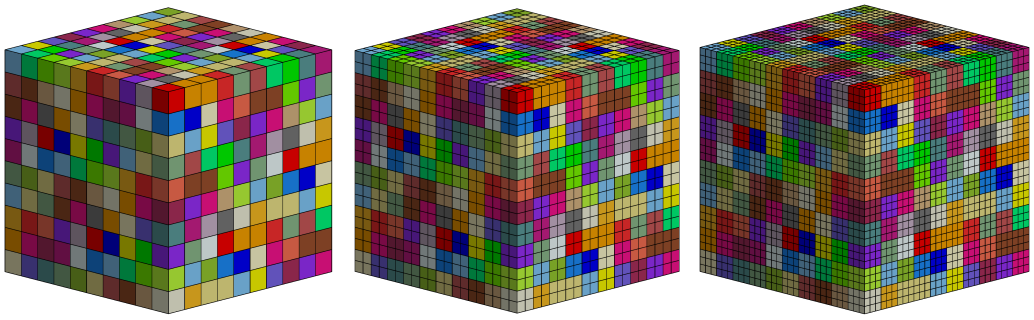

(a) (b) (c)

FIGURE 4.6: Three mesh densities tested by PH: (a) 1, (b) (2×2×2) 8 and (c) (3×3×3) 27 finite element(s) used to mesh one square grain with ℓ/d=1.

The effect of the mesh density (number of elements per grain) is studied in PH for parallelepipedic tessellations of 1000 grains with $\ell/d = 1$ (Fig. 4.6): 1, $2 \times 2 \times 2 = 8$ and $3 \times 3 \times 3 = 27$ finite element(s) are used successively to mesh one square grain. The same grain orientations (as described in Section 4.2.2) and their spatial distributions

[4] c3d20: quadratic hexahedrons with 20 nodes per element
[5] c3d4: linear tetrahedrons with 4 nodes per element

are assigned to these three meshes for Cu polycrystals. The PD [6] of the effective elastic moduli between the first two meshes and between the last two ones are found to be ∼1.8% and ∼0.3% respectively, and the total CPU time for the FE calculation of each realization for the three meshes are 112s, 1472s and 22926s respectively. We choose the second mesh for the purpose of ensuring a sufficient accuracy and avoiding too long computational time.

For parallelepipedic tessellations for which $\ell/d \neq 1$, we take $8\times\ell/d$ elements per grain, as illustrated in Fig.4.5(d) with 16 elements/grain for ℓ/d=2. And for the slice-shaped parallelepipedic tessellation with $\ell/d \to \infty$, 8 elements per grain are used (Fig. 4.5(e)). Doing so, we use the same mesh density as for the case ℓ/d=1. As for Voronoï tessellations, a similar analysis of the effect of mesh density leads us to choose ∼ 500 elements per grain.

When a single realization over the elementary volume V is used, a relatively limited number of grain orientations and grain neighborhoods are accounted for. This leads to a bias in the estimation of the effective properties as explained in (Kanit et al., 2003). The RVE (Hill, 1963) must contain a sufficiently large number of heterogeneities (e.g., grains, inclusions, fibers ...) for the macroscopic properties to be independent on the boundary conditions applied to this volume. Kanit et al. (2003) proposed a statistical strategy to determine the RVE size.

Following this approach, we consider n realizations of the microstructure in a volume with given size. This volume size is then increased to investigate the asymptotic elastic behavior:

$$\overline{Z} = \frac{1}{n}\sum_{i=1}^{n}\widetilde{Z}_i, \qquad D_Z^2 = \frac{1}{n}\sum_{i=1}^{n}(\widetilde{Z}_i - \overline{Z})^2 \tag{4.10}$$

where $\widetilde{Z}_i$ is an apparent elastic modulus obtained for one realization and $\overline{Z}$ is its mean value over n realizations. In addition, the variance D_Z^2 denotes the fluctuations of $\widetilde{Z}_i$.

The number of realizations n is chosen so that the obtained mean value $\overline{Z}$ does not vary any longer up to a given precision when n is increased. This precision (i.e. relative error $\varepsilon_{\text{rela}}$) of the estimation of the effective property $\overline{Z}$ is related to the standard deviation D_Z and the number of realizations n by:

$$\varepsilon_{\text{rela}} = \frac{2D_Z}{\overline{Z}\sqrt{n}}\,. \tag{4.11}$$

Conventionally, if $\varepsilon_{\text{rela}} \leq 1\%$, we suppose that the number of realizations n is sufficiently large for taking into account a good statistical representativity of heterogeneous textures. The RVE is then determined, and the overall effective elastic property is defined by the

[6] Percentage Difference (PD in %): the absolute difference between two values divided by their average.

mean value over n realizations, $\overline{Z}$. In addition, the 95% confidence interval is given by $[\overline{Z} - 2D_Z, \overline{Z} + 2D_Z]$.

For Cu polycrystals, the parallelepipedic tessellations require at least 3 realizations for ensuring $\varepsilon_{\text{rela}} \leq 1\%$ for all of the five independent elastic moduli. Here, the effective elastic tensor of $(\widetilde{\underset{\sim}{C}})_{\text{H0-Cu}}$ are determined over 10 realizations, i.e. a total of 10000 (10×1000) crystallographic orientations were taken into account. This has been done to get a smaller confidence interval, useful when comparing results with those of the SSC scheme. We also choose 10 realizations for the slice-shaped tessellation with $\ell/d \to \infty$.

On the other hand, each realization of the used Voronoï tessellation contains a smaller number of grains (100) than parallelepipedic tessellations. For Cu polycrystal described by Voronoï microstructures, it was found that 30 random realizations are necessary to ensure statistical representativity of the results. Therefore, the number of used Voronoï cells is 3000 (30 × 100). The same number of realization was used for Nb polycrystals.

4.3.3.2 PH adapted for composite cylinders assemblies

When using the analytic mean-field GSC scheme to determine the effective elastic moduli at scales H1 to H3, the long fibers are assumed to be distributed randomly. In order to take into consideration the quasi-periodic fiber distribution observed experimentally (Fig. 4.1) and to investigate the effect of this particular distribution, FEM PH will be also carried out for scales transitions H1 to H3. The section views of the unit cell of H1 and H2, with their meshes (c3d20), are respectively indicated in Fig. 4.4(d) and Fig. 4.4(f). These unit cells are subjected to periodic boundary conditions. They contain all information about the morphological RVE at the effective scales H1 and H2. These meshes are composed of two equivalent long fibers (1+4×1/4 fibers) which are arranged in an hexagonal lattice, and they represent the (idealized) multi-scaled experimental microstructure of the Cu-Nb wires.

This PH model describes an infinite periodic honeycomb microstructure. However, the real architecture of Cu-Nb wires at all scales contains only a finite number (i.e. 85) of long fibers. We have verified with the help of a larger hexagonal structure without periodic boundary conditions that the hypothetical infinity does not significantly affect our results. The mesh density has also been checked for ensuring adapted numerical accuracy.

4.4 Homogenization results at scale H0

In this section, the effective elastic behavior of Cu and Nb polycrystals, i.e. the homogenization scale H0, is considered. Results of the various homogenization schemes presented above will be compared with each other.

As explained above, the anisotropic effective stiffness tensors $(\widetilde{\underset{\sim}{C}})_{\text{H0-Cu}}$ and $(\widetilde{\underset{\sim}{C}})_{\text{H0-Nb}}$ obtained by the SSC scheme and PH are found to be *transversely isotropic* if we compute a statistically sufficiently large equivalent volume (i.e. RVE). It should be noticed that, unlike the homogenized results of PH, the SSC ones display negligible scattering because of the very large number of grain orientations considered.

Five independent effective moduli were used to describe the overall anisotropic elastic behavior of the fiber textured Cu polycrystal and Nb polycrystal. Results for two morphological textures ($\ell/d = 1$, and highly elongated grains) are shown in Table 4.3. In the case of equiaxed grains ($\ell/d = 1$), it is remarkable that all the elastic moduli obtained for the three microstructures, i.e. SSC, parallelepipedic, and Voronoï tessellations, are in a perfect match, with a PD smaller than 4%. There are some visible differences of confidence intervals for PH homogenizations, the ones for parallelepipedic tessellations being about half those for Voronoï tessellations; this might be mainly caused by the computed number of grain orientations considered in these calculations. It can also be observed that results of the SSC scheme fall within the confidence interval of PH, except for $\tilde{\mu}_{12}$ and $\tilde{\mu}_{23}$ for Nb polycrystals where slightly larger differences are found.

Figure 4.7 further illustrates the SSC and PH (using parallelepipedic tessellations) predictions of longitudinal and transverse Young's moduli ($\widetilde{E}_1$ and $\widetilde{E}_{2,3}$) as a function of the grain aspect ratio ℓ/d, for both Cu and Nb polycrystals. Corresponding numerical values of the five independent effective moduli are provided in Table 4.3 for $\ell/d = 100$ (SSC scheme) and $\ell/d \to \infty$ (PH). Again, the agreement between all results is excellent. It can however be noticed that a larger discrepancy is observed for the transverse modulus $\widetilde{E}_{2,3}$ obtained for Nb polycrystals. Additional numerical tests will be performed in Section 4.6.1 to discuss the main factors that contribute to this (small) difference.

Both SSC scheme and PH demonstrate remarkably that, for Cu polycrystals with the double $\langle 100 \rangle$-$\langle 111 \rangle$ fiber texture, aggregates with elongated grains display stiffer effective longitudinal Young's moduli than the ones with equiaxed grains. For $\ell/d > 20$, this tendency becomes saturated, and the elongation of grains along the wire direction x_1 has no more effect on the Young modulus. In contrast, for Nb polycrystals with the single $\langle 110 \rangle$ fiber texture, the effective Young moduli do not depend on the morphological textures. The effects of morphological and crystallographic textures on the effective elastic behavior will be further discussed in Section 4.6.2.

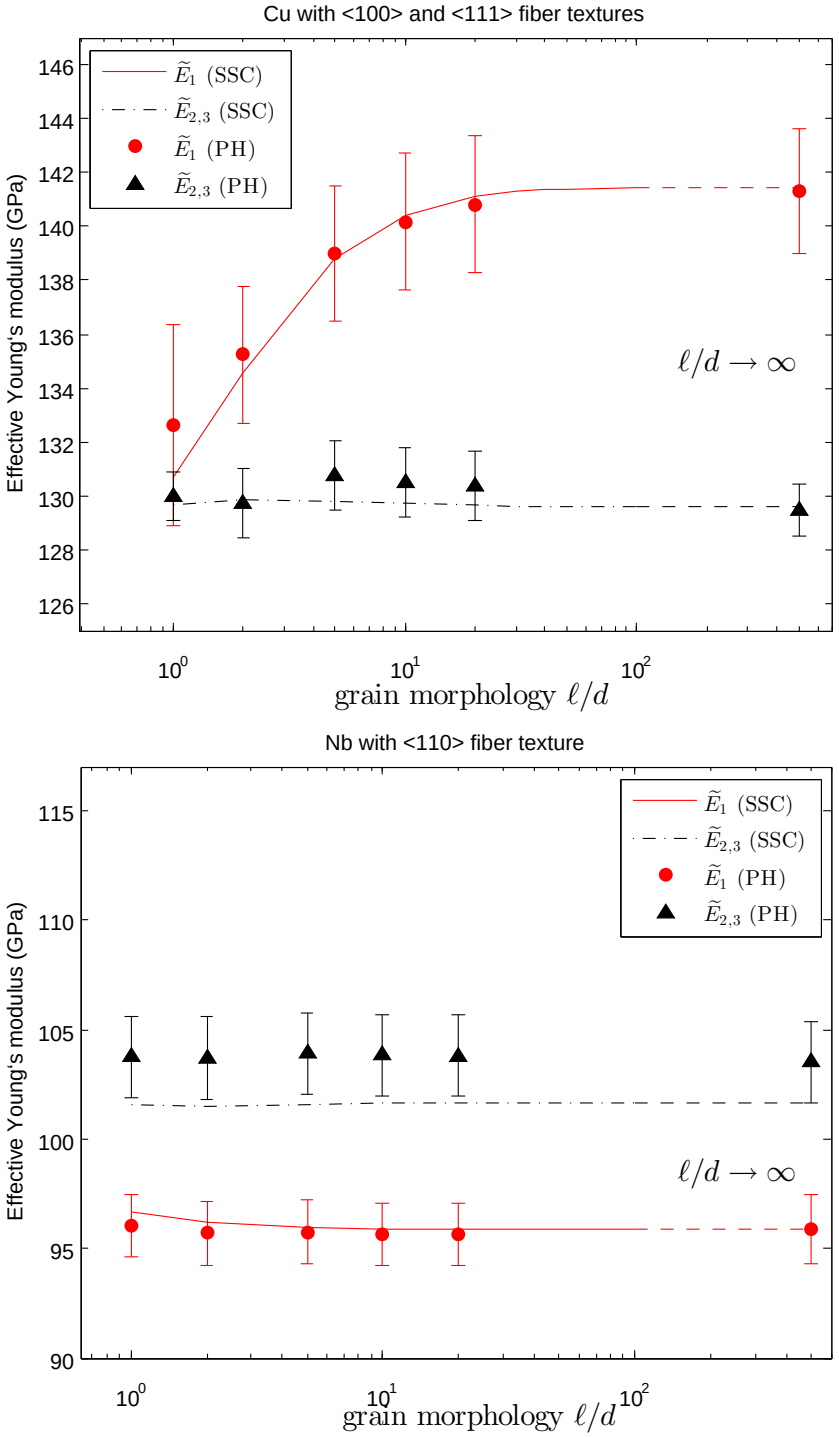

FIGURE 4.7: Effective longitudinal and transverse Young's moduli ($\widetilde{E}_1$ and $\widetilde{E}_{2,3}$ respectively) in terms of the grain aspect ratio ℓ/d. The fiber textured Cu polycrystal and Nb polycrystal are homogenized by the SSC scheme and PH (using parallelepipedic tessellations).

Model	SSC	PH (para)	PH (Voro)	SSC	PH (para)
ℓ/d	1	1	1.00±0.34	100	∞
H0-Cu with a double fiber ⟨100⟩ and ⟨111⟩					
$\widetilde{E}_1$ (GPa)	130.68	132.63±3.72	133.90±8.0	141.45	141.30±2.33
$\widetilde{\nu}_{12}$	0.340	0.338±0.006	0.336±0.012	0.327	0.327±0.004
$\widetilde{K}_{23}$ (GPa)	152.37	152.79±1.08	152.95±2.39	153.88	153.91±0.82
$\widetilde{\mu}_{12}$ (GPa)	47.65	48.30±0.80	49.40±1.80	46.43	46.30±0.52
$\widetilde{\mu}_{23}$ (GPa)	48.20	48.11±0.61	49.17±1.14	46.86	46.80±0.64
H0-Nb with a single fiber ⟨110⟩					
$\widetilde{E}_1$ (GPa)	96.66	96.05±0.70	96.56±1.16	95.85	95.15±0.79
$\widetilde{\nu}_{12}$	0.408	0.410±0.004	0.409±0.005	0.408	0.411±0.003
$\widetilde{K}_{23}$ (GPa)	185.75	184.54±1.22	184.78±2.28	185.65	184.48±1.28
$\widetilde{\mu}_{12}$ (GPa)	39.60	38.36±0.54	38.69±1.23	39.48	38.32±0.62
$\widetilde{\mu}_{23}$ (GPa)	36.88	38.27±0.54	38.44±1.30	37.04	38.26±0.62

TABLE 4.3: Effective transversely isotropic moduli of Cu polycrystals and Nb polycrystals at scale H0 and their 95% confidence intervals. Experimental crystallographic textures and various morphological textures are considered for the SSC scheme and PH. Both parallelepipedic (para) and Voronoï (Voro) tessellations are used for PH.

4.5 Effective behaviors at scales H1 to H3 of architectured Cu-Nb composites

4.5.1 Results for scale H1

The SSC estimate is often advocated to be a good model for polycrystalline aggregates for two reasons: (i) SSC scheme assumes a perfectly disordered mixture of grains which is similar to the real morphological textures in polycrystals; (ii) SSC model can be applied to a statistically large heterogeneous volume composed of a very large number of grain orientations without costing much CPU time. This has been confirmed by our results of the previous section. Therefore, the homogenized anisotropic elastic tensors $(\widetilde{\underset{\sim}{\boldsymbol{C}}})_{\text{H0-Cu}}$ and $(\widetilde{\underset{\sim}{\boldsymbol{C}}})_{\text{H0-Nb}}$ for Cu polycrystals and Nb polycrystals determined by the SSC scheme will be taken here as local constitutive behaviors for the upper scale transitions, as shown in Fig. 4.4(a)(b). Since grains in Cu-Nb wires are highly elongated with $\ell \gg d$, we consider within the SCC scheme a grain aspect ratio ℓ/d=100, believed to be a good approximation of the columnar grains observed in the real microstructure (a larger aspect ratio does not change significantly the elastic properties).

We now proceed to the homogenization of the assembly of 85^1 elementary continuum long fibers (Fig. 4.1(a)), i.e. at scale H1. Both GSC and PH models are applied to the specific CCA made of the co-cylindrical patterns with three layers: Cu-f/Nb-t/Cu-0, with properties at scales H0 provided by the SSC scheme as detailed above. As presented previously in Fig. 4.4(c)(d), GSC scheme and PH assume that the Cu-Nb CCA exhibits a random and a periodic fiber distribution, respectively.

Besides, for the sake of comparison, one can also use for scale H1 the simple SSC scheme, thus assuming a microstructure consisting of the sole random mixture of Cu and Nb grains, i.e. without consideration anymore of the specific architecture of the real specimen. The volume fraction of Cu and Nb phases becomes 51.6% and 48.4%, respectively. This corresponds to the normalized volume fraction of 10.5%, 48.4%, and 41.1% for Cu-f, Nb-t, and Cu-0, respectively (see Section 4.2).

The transversely isotropic effective moduli $(\widetilde{\underset{\sim}{\boldsymbol{C}}})_{\mathrm{H1}}$ of the assembly of 85^1 elementary long fibers (scale H1) are given in Table 4.4. It is remarkable that the GSC scheme and PH provide very close results, and results of the SSC scheme are also in a perfect agreement. The PD between the prediction of these three models is less than only 2%.

Scale	H1			H2			H3		
Model	SSC	GSC	PH	SSC	GSC	PH	SSC	GSC	PH
$\widetilde{E}_1$ (GPa)	117.39	119.62	117.44	123.07	123.64	121.86	128.51	128.56	127.27
$\widetilde{\nu}_{12}$	0.371	0.367	0.371	0.361	0.360	0.363	0.351	0.351	0.353
$\widetilde{K}_{23}$ (GPa)	169.56	168.07	169.56	165.67	165.33	166.51	162.06	162.06	162.89
$\widetilde{\mu}_{12}$ (GPa)	42.53	42.93	42.58	43.40	43.55	43.26	44.27	44.32	44.11
$\widetilde{\mu}_{23}$ (GPa)	41.21	41.77	41.33	42.44	42.64	42.29	43.68	43.75	43.49

TABLE 4.4: Effective transversely isotropic moduli of Cu-Nb wires at scales H1, H2 and H3 (i.e. Homogenization of the assembly of 85^1, 85^2 and 85^3 elementary long fibers respectively), obtained by mean-field SSC (ℓ/d=100) and GSC schemes, and by full-field PH.

4.5.2 Iterative scale transition process up to scale H3

At the effective scale H2 (see Fig. 4.1(b)), we suppose that the 85 continuum cylinders are composed of two layers: (1) the nano-composite Cu-Nb zones containing 85^1 elementary long fibers; (2) the embedding matrix Cu-1. In this work, an iterative process is proposed. The effective tensor of the inner layer for scale H2, $(\underset{\sim}{\boldsymbol{C}}^{(1)})_{\mathrm{H2}}$, is given by the effective tensor $(\widetilde{\underset{\sim}{\boldsymbol{C}}})_{\mathrm{H1}}$ obtained for scale H1. On the other hand, the effective behavior of the second layer for H2, $(\underset{\sim}{\boldsymbol{C}}^{(2)})_{\mathrm{H2}}$, is associated with the effective behavior of Cu polycrystals, $(\widetilde{\underset{\sim}{\boldsymbol{C}}})_{\mathrm{H0\text{-}Cu}}$. The scale transition is then performed by GSC and PH approaches, leading to the effective tensor $(\widetilde{\underset{\sim}{\boldsymbol{C}}})_{\mathrm{H2}}$ for the assembly of 85^2 elementary long fibers.

The same iterative process will be repeated up to scale H3 using GSC and PH approaches, allowing to estimate $(\widetilde{\underset{\sim}{\boldsymbol{C}}})_{\mathrm{H3}}$, the effective elasticity of 85^2 Cu-Nb composite zone of H2 embedded by Cu-2. Moreover, as mentioned in Section 4.5.1, regardless of the specific filament/nanotube microstructure, the SSC scheme can also be used to predict $(\widetilde{\underset{\sim}{\boldsymbol{C}}})_{\mathrm{H2}}$ and $(\widetilde{\underset{\sim}{\boldsymbol{C}}})_{\mathrm{H3}}$, considering the true volume fractions of Cu-Nb phases for scales H2 and H3, the crystallographic and morphological (ℓ/d=100) texture, but discarding the material architecture.

The effective moduli of H2 and H3 are indicated in Table 4.4. As before, SSC, GSC, and PH homogenizations exhibit very close results at all the effective scales considered, the maximal PD among them being as small as ∼1.5%. This result will receive further attention in Section 4.6.3.

4.6 Discussion

4.6.1 SSC and PH predictions at scale H0

In this section, we investigate the factors that contribute to the deviation of the SSC scheme from PH for Cu polycrystals and Nb polycrystals, i.e. considering scale H0. Then in Section 4.6.2, the role of morphological and crystallographic textures on the effective elastic behavior will be discussed.

The effective elastic tensors $(\widetilde{\underset{\sim}{C}})_{\text{H0-Cu}}$ and $(\widetilde{\underset{\sim}{C}})_{\text{H0-Nb}}$ were determined in Section 4.4 for the double ⟨100⟩-⟨111⟩ fiber textured Cu polycrystal and the single ⟨110⟩ Nb polycrystal. Both mean-field SSC scheme and full-field PH were applied, and an excellent agreement of model responses were found. However, a larger PD was found for $\widetilde{E}_{2,3}$ in the case of Nb polycrystals (see Fig. 4.7), a deviation that seems larger than for all other investigated moduli. For a better understanding of the deviation between the SSC scheme and PH, additional numerical tests have been performed.

First of all, we exchanged the crystallographic textures : the experimental ⟨110⟩ fiber texture of Nb is taken as a fictitious crystallographic texture for Cu polycrystals. Similarly, the double ⟨100⟩-⟨111⟩ fiber components of Cu are taken to build a fictitious polycrystal of Nb. The predictions for the longitudinal and transverse Young's moduli ($\widetilde{E}_1$ and $\widetilde{E}_{2,3}$ respectively) are plotted in Fig. 4.8 as a function of the grain aspect ratio ℓ/d for these fictitious textures.

As before, it is observed that, despite the large difference of the Zener anisotropy factor Z between Cu and Nb, SSC and PH models provide very similar results, for all the considered grain aspect ratio ℓ/d and crystallographic textures. However, one sees that a larger discrepancy is now observed for the $\widetilde{E}_{2,3}$ modulus of Cu polycrystals, with the fictitious ⟨110⟩ fiber texture. These differences arise mainly because these models do not take into account exactly the same grain topology: perfectly disordered mixture of grains for the SSC scheme and regular parallelepipedic grains of PH. Grain size graduation is also infinite for the SSC scheme, whereas grains all have the same size for the parallelepipedic tessellations; grain size distribution of the Voronoï tessellation is narrow. Combining Table 4.3, Fig. 4.7 and Fig. 4.8, it can be concluded that the effective properties of sharp ⟨110⟩ fiber textures are more sensitive to microstructure details than double ⟨100⟩-⟨111⟩ textures.

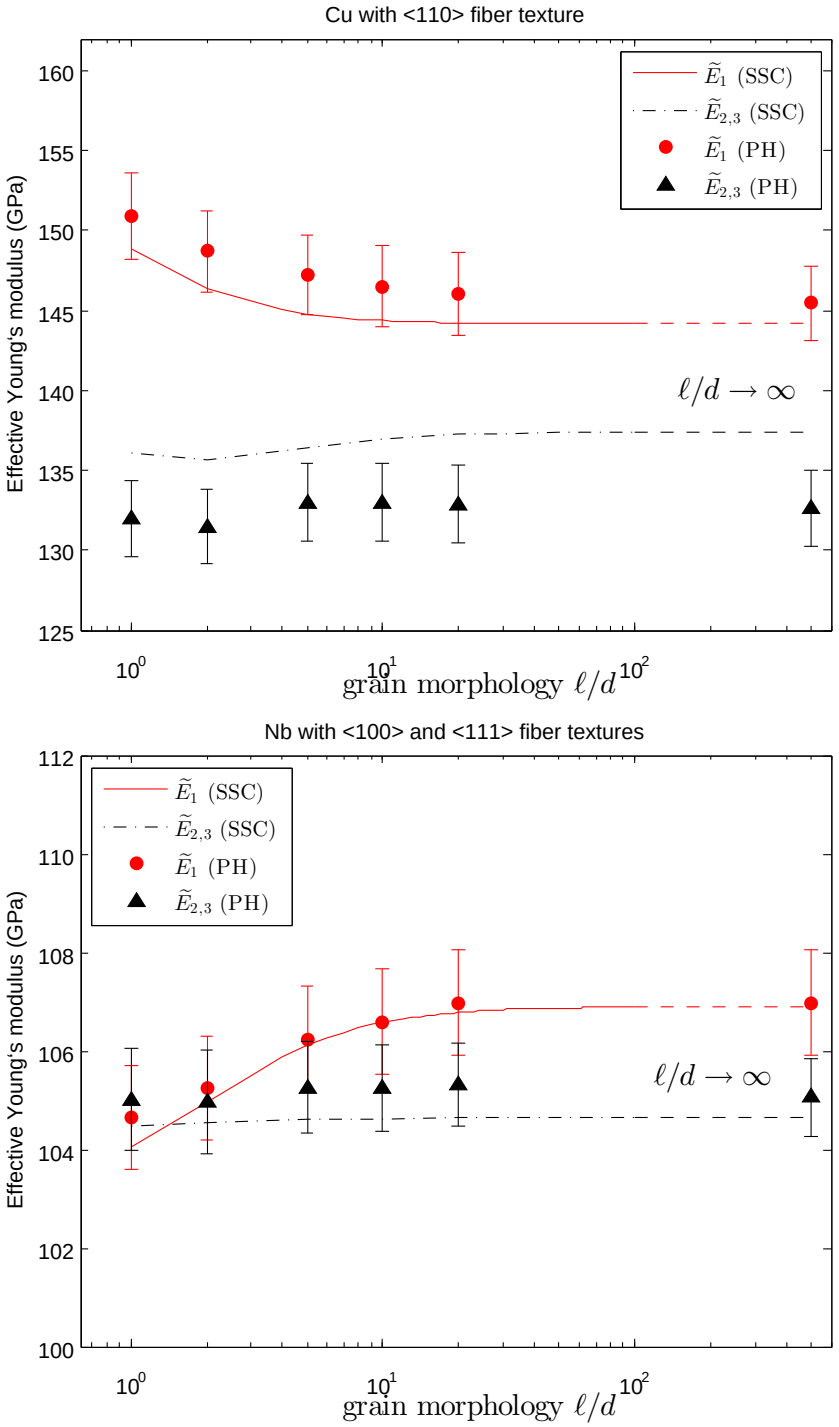

FIGURE 4.8: Effective longitudinal and transverse Young's moduli ($\widetilde{E}_1$ and $\widetilde{E}_{2,3}$ respectively) in terms of the grain aspect ratio ℓ/d, obtained by SSC and PH (using parallelepipedic tessellations). Cu polycrystal and Nb polycrystal are textured by fictitious $\langle 110 \rangle$ and $\langle 100 \rangle$-$\langle 111 \rangle$ fibers respectively.

4.6.2 Anisotropy induced by morphological and crystallographic textures

In the preceding section, the SSC scheme has been shown to provide almost identical results than PH for various morphological and crystallographic textures. Thanks to its high numerical efficiency, the SSC scheme will now be used to explore the role of micro-parameters, such as morphological and crystallographic textures.

Fig. 4.9 shows predictions of the SSC scheme for the effective longitudinal and transverse Young's moduli ($\widetilde{E}_1$ and $\widetilde{E}_{2,3}$ respectively) as functions of the grain aspect ratio ℓ/d, for Cu polycrystals and Nb polycrystals with a *random* (i.e. isotropic) crystallographic texture. Results are compared with the ones obtained for experimental fiber textures of Fig. 4.7. For Nb polycrystals, it can be observed that grain morphology only has a small effect on the effective behavior, for both random and $< 110 >$ crystallographic textures. For Cu, the effect of grain morphology depends on the texture. It has only a small influence for a random texture, but it affects significantly (by about 10%) $\widetilde{E}_1$ for the experimental $< 100 > - < 111 >$ texture.

To be more quantitative, Thomsen coefficients (Thomsen, 1986) are used for characterizing the transverse isotropy. These dimensionless parameters are a combination of the components of the elastic stiffness matrix

$$\begin{aligned} \epsilon &= \frac{C_{33} - C_{11}}{2C_{11}}\,, \\ \delta &= \frac{(C_{13} + C_{66})^2 - (C_{11} - C_{66})^2}{2C_{11}(C_{11} - C_{66})}\,, \\ \gamma &= \frac{C_{44} - C_{66}}{2C_{66}}\,, \end{aligned} \tag{4.12}$$

where index 1 indicates the symmetry axis (x_1). For isotropic elasticity, the three Thomsen parameters are strictly equal to 0. Conversely, the elastic mechanical behavior exhibits more anisotropy with larger absolute values of ϵ, δ and γ. Note also that the absolute value of these parameters is usually much less than 1. Fig. 4.10 illustrates these parameters obtained for $(\underset{\sim}{\widetilde{\boldsymbol{C}}})_{\mathrm{H0}}$ using the SSC scheme in terms of ℓ/d for the Cu and Nb polycrystals with experimental fiber textures. It can be again observed that the behavior of the $\langle 110 \rangle$ fiber textured Nb is much less sensitive to grain morphology than the $\langle 100 \rangle$-$\langle 111 \rangle$ Cu. For the latter one, the anisotropy is weak for equiaxed grain shape (ℓ/d=1), and increases significantly with the grain aspect ratio.

The Cu polycrystals and Nb polycrystals with double $\langle 100 \rangle$-$\langle 111 \rangle$ fiber textures have been studied previously. We now proceed to predict the effective elastic properties of *perfect*[7] $\langle 100 \rangle$ fiber textured aggregates and *perfect* $\langle 111 \rangle$ ones separately for the propose of comparison. An analytic solution for this homogenization problem has been derived

[7] A texture component is *perfect* when its spread FWHM vanishes, i.e. here all {100} planes lie exactly parallel or perpendicular to x_1 axis.

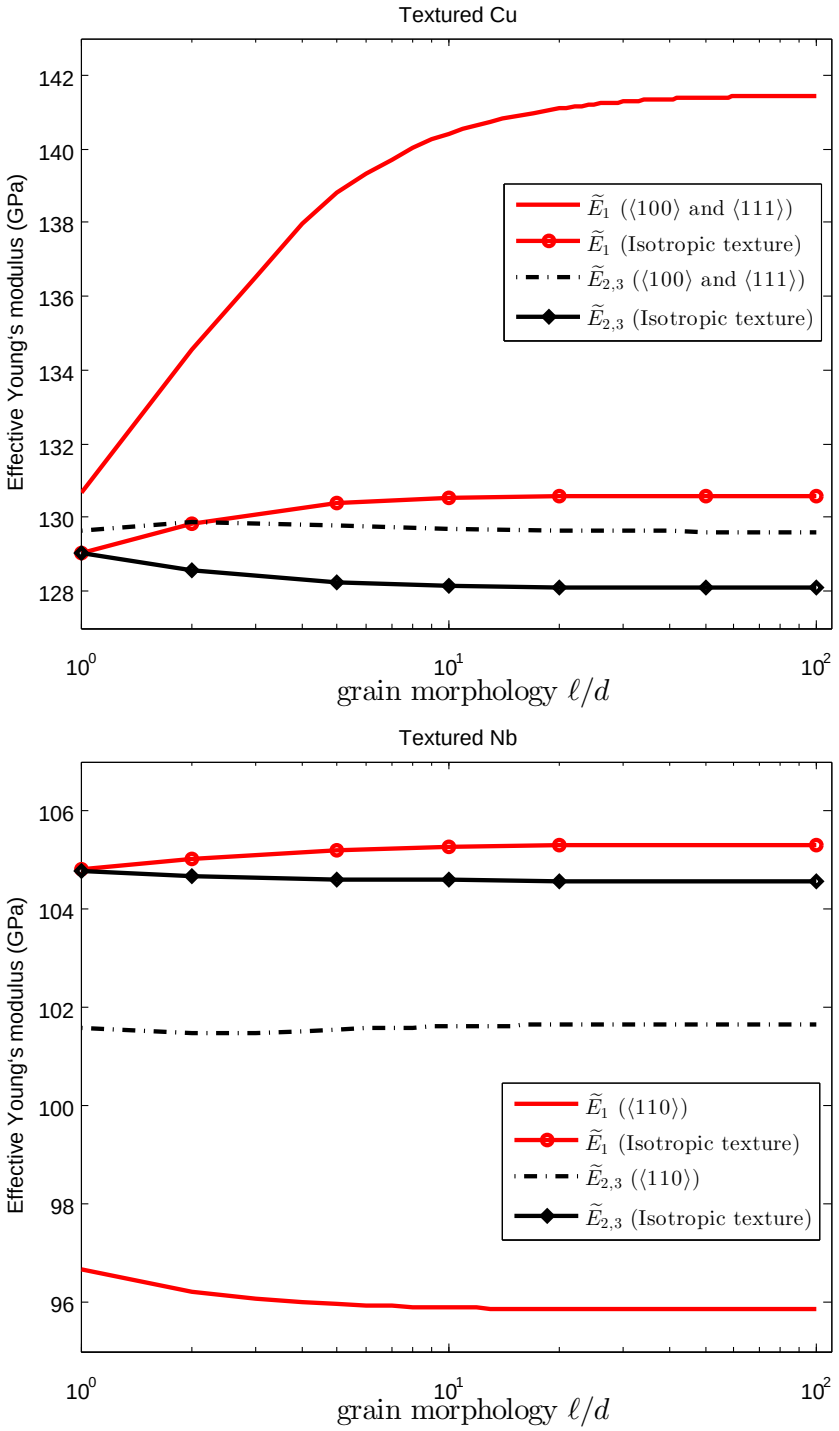

FIGURE 4.9: Effective longitudinal and transverse Young's moduli ($\widetilde{E}_1$ and $\widetilde{E}_{2,3}$ respectively) in terms of the grain aspect ratio ℓ/d predicted by the SSC scheme. Cu polycrystal and Nb polycrystal with experimental fiber textures are compared with the ones with a random (isotropic) texture.

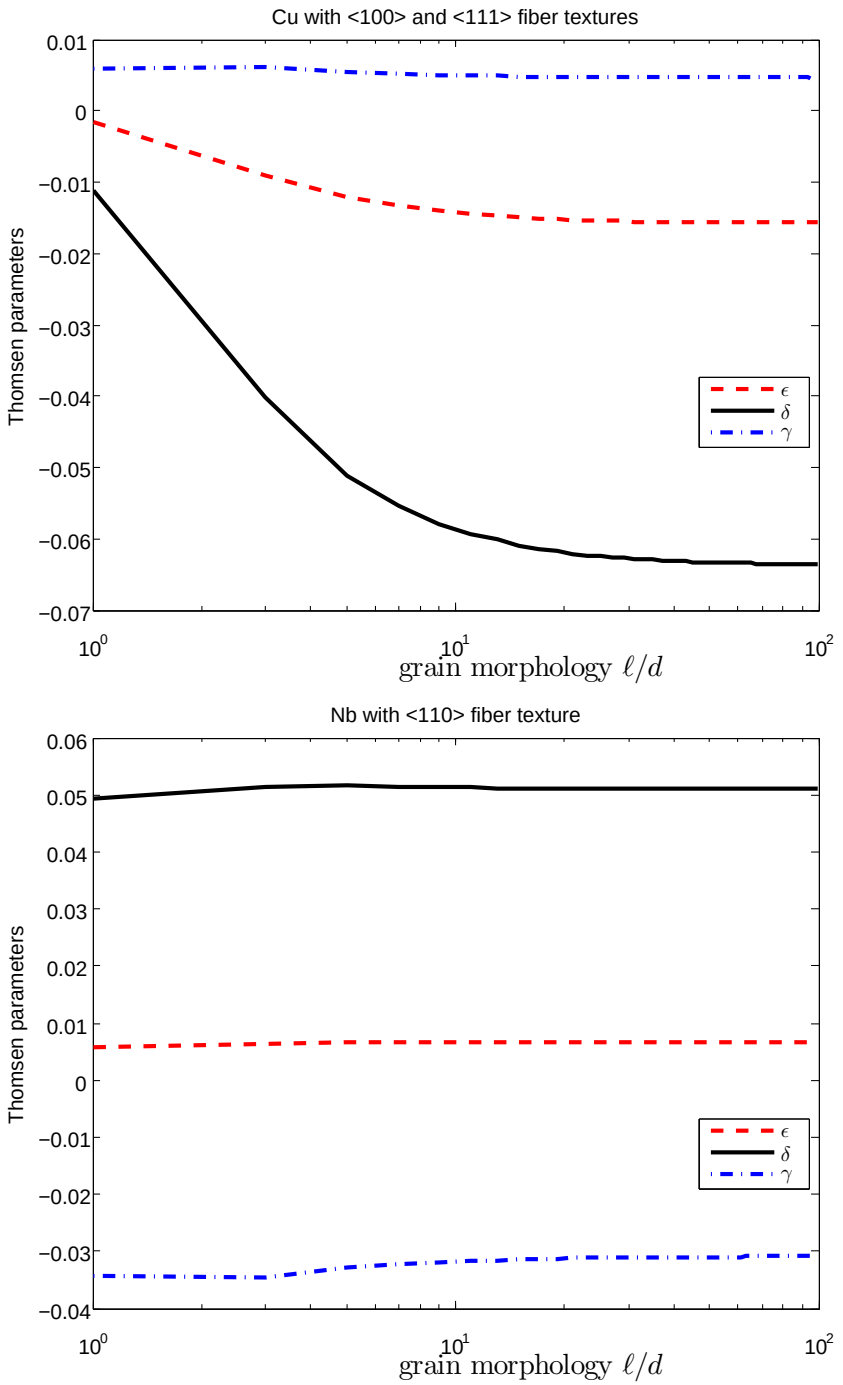

FIGURE 4.10: Thomsen parameters in terms of the grain aspect ratio ℓ/d, obtained with the SSC scheme. Experimental fiber textures are used for Cu and Nb polycrystals.

by Walpole (1985), for cubic polycrystalline aggregates: for ⟨100⟩, $\widetilde{E}_1$=66.03 GPa, $\widetilde{E}_{2,3} \in [87.54, 105.79]$ GPa; for ⟨111⟩, $\widetilde{E}_1$=191.49 GPa, $\widetilde{E}_{2,3} \in [129.82, 160.93]$ GPa). Fig. 4.11 illustrates the effective Young's moduli ($\widetilde{E}_1$ and $\widetilde{E}_{2,3}$) obtained by the SSC scheme for Cu polycrystals with various morphological textures. These results, of course, are consistent with the analytical solution of Walpole. It can be noted that $\widetilde{E}_1$ and $\widetilde{E}_{2,3}$ are significantly different for both texture components. Moreover, it can be observed that, although $\widetilde{E}_1$ is insensitive to the grain aspect ratio for both individual ⟨100⟩ and ⟨111⟩ texture components, it become sensitive to the aspect ratio when the two components are mixed together (see Fig. 4.7). In contrast $\widetilde{E}_{2,3}$ decreases with the aspect ratio for both individual texture components, but becomes rather insensitive to it when they are mixed together.

For sake of comparison, we have also computed the effective elastic parameters for Nb polycrystal with the perfect ⟨100⟩ fiber texture and the perfect ⟨111⟩ one: $\widetilde{E}_1$=145.14 GPa, $\widetilde{E}_{2,3}$=117.69 GPa for ⟨100⟩ and $\widetilde{E}_1$=83.35 GPa, $\widetilde{E}_{2,3}$=95.89 GPa for ⟨111⟩. It is found that these results (which are in agreement with Walpole (1985) estimations: $\widetilde{E}_1$=145.48 GPa, $\widetilde{E}_{2,3} \in [113.62, 121.38]$ GPa for ⟨100⟩ and $\widetilde{E}_1$=83.24 GPa, $\widetilde{E}_{2,3} \in [93.21, 98.28]$ GPa for ⟨111⟩) are only slightly sensitive to the grain aspect ratio. Note also that the difference in $\widetilde{E}_1$ and $\widetilde{E}_{2,3}$ for both texture components is less than for Cu, indicating a smaller effective anisotropy.

For Cu polycrystals, both effective Young's moduli ($\widetilde{E}_1$ and $\widetilde{E}_{2,3}$) and Thomsen parameters depend on the grain aspect ratio ℓ/d in the range of $1 \leqslant \ell/d < 20$ irrespective of the fiber textures. However, this dependency saturates with increasingly elongated grains along the wire direction x_1. A similar feature has also been observed for Ni alloy directionally solidified polycrystalline aggregates in Yaguchi and Busso (2005). In contrast, the effect of the grain aspect ratio ℓ/d on the stiffness coefficients of Nb polycrystal is non-zero but rather small.

Concerning the effect of crystallographic texture, we have obtained different $\widetilde{E}_1$ values for different textures, for Cu polycrystals: 66.03 GPa for perfect single fiber ⟨100⟩, ∼ 146 GPa for ⟨110⟩ (mean value between ℓ/d=1 and $\ell/d \to \infty$), and 191.49 GPa for perfect ⟨111⟩. The PD between the first two moduli and the last two ones are significant, i.e. 75% and 26% respectively. For Nb polycrystals, $\widetilde{E}_1$ was found to be 145.14 GPa for a perfect single ⟨100⟩ texture, ∼ 96 GPa for single ⟨110⟩, and 83.35 GPa for perfect single ⟨111⟩. Thus, the PD between the first two ones and the last two ones are less than for Cu (40% and 15% respectively), but still significant.

In summary, it was found that crystallographic textures play an important role in the effective elastic moduli of Cu and Nb polycrystals. The combination of crystallographic and morphological texture effects is not straightforward. For example, grains average morphology has strictly no effect on $\widetilde{E}_1$ for Cu with a ⟨100⟩ or a ⟨111⟩ perfect texture, but is responsible for a 10% variation for the sharp ⟨100⟩-⟨111⟩ experimental texture.

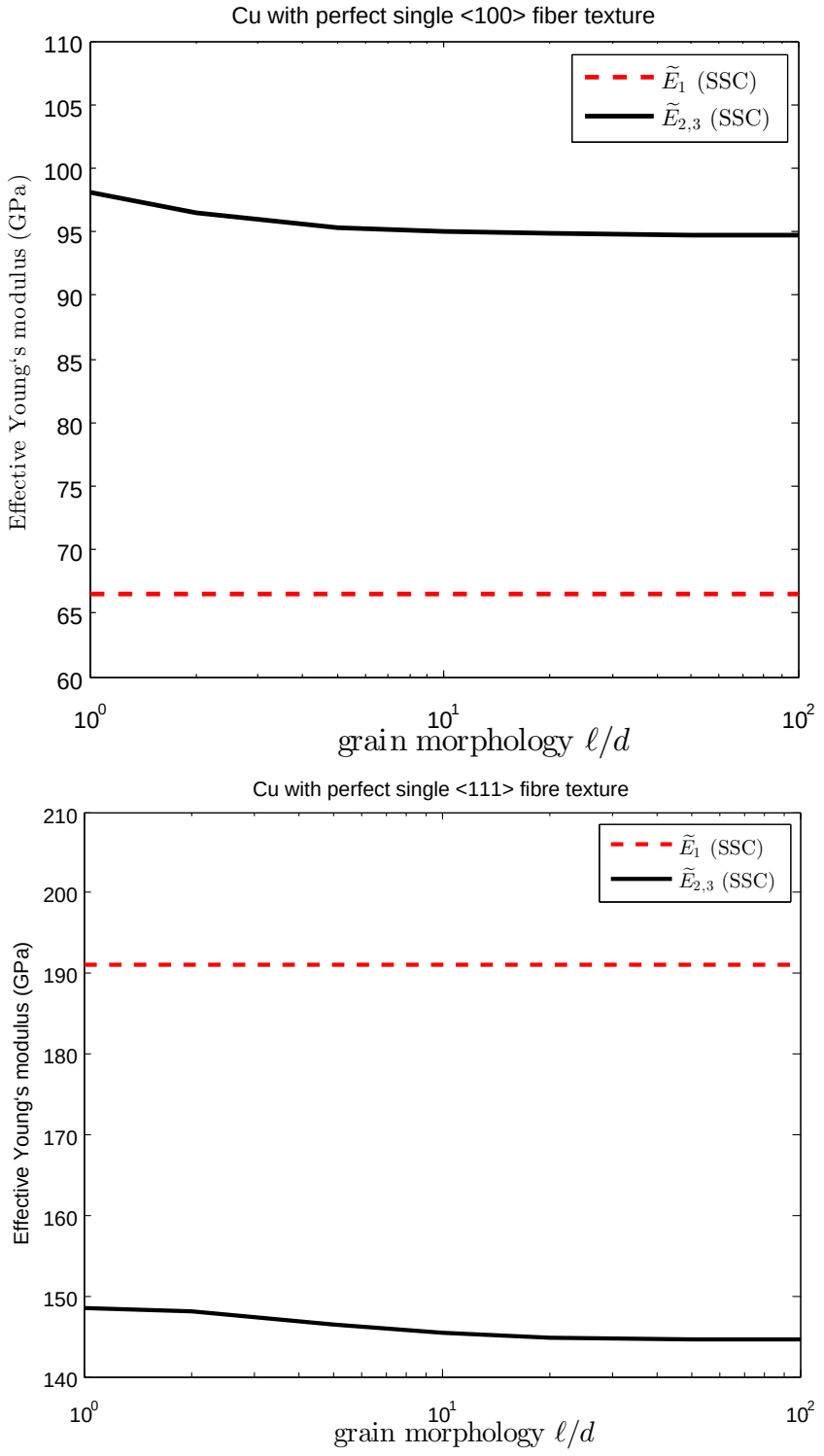

FIGURE 4.11: Effective longitudinal and transverse Young's moduli ($\widetilde{E}_1$ and $\widetilde{E}_{2,3}$ respectively) of perfect single-component $\langle 100 \rangle$ and perfect single-component $\langle 111 \rangle$ fiber textured Cu by the SSC scheme in terms of ℓ/d.

With the experimental textures, grain morphology has a much smaller effect on Nb that on Cu polycrystals. These results highlight the necessity of accounting for the correct grain morphology and orientation when modelling the effective behavior at the different scales. A comparison to experimental data is provided in the section 4.6.4.

4.6.3 Modeling Strategies for Cu-Nb wires

In section 4.5, three homogenization models were applied to perform the scale transitions up to scales H1, H2 and H3 for the architectured Cu-Nb nano-composite wires. The SSC scheme assumes a random mixture of Cu and Nb phases; the GSC scheme and PH both take into account the specific CCA microstructure with random and periodic distribution, respectively. As shown in Table 4.4, the three models provide very close results at H1, H2 and H3 scales, in spite of the very different approximations of geometry.

This good match is likely due to the relatively small elastic contrast between Cu and Nb elastic behavior. For instance, the effective longitudinal Young's moduli ratio between Cu polycrystals and Nb polycrystals, $(\widetilde{E}_1)_{\text{H0-Cu}}/(\widetilde{E}_1)_{\text{H0-Nb}}$, is about 1.5 (Table 4.3). Conversely, as shown by Llorca et al. (2000), considerable deviations between SSC, GSC and PH models are obtained when the contrast is enlarged. The Young's modulus obtained by the SSC scheme can be twice stiffer than the one obtained by GSC/PH model, for an epoxy matrix reinforced with steel spheres. In that case, the Young's modulus of the spheres and of the matrix differ by a ratio of $E_{\text{spheres}}/E_{\text{matrix}} = 60$. For such a large contrast, the architectures and microstructures play a noticeable role on the effective elastic properties.

As a conclusion, the SSC scheme is demonstrated to be an efficient homogenization model for Cu-Nb wires, because of small elastic contrast between Cu phases and Nb phases.

4.6.4 Structural problem S3 and experimental comparison

As illustrated in Fig. 4.1(d), a real Cu-Nb wire can be seen as a single cylinder-shaped structure S3 at macro-scale. In Thilly et al. (2007, 2009), the S3 sample was locally thinned to obtain a reduced gauge section below $0.14\,\text{mm}^2$ over several millimeters long, as shown in Fig. 4.12(a). This polishing allows X-rays to probe directly the nano-composite interior (i.e. so-called effective H3 zone) of the wire that would be otherwise screened by the external Cu-3 jacket. It is worth noting that the polished H3 zone is now containing less than 85^3 elementary fibers, but the material property, such as $(\widetilde{\widetilde{\boldsymbol{C}}})_{\text{H3}}$, is supposed not to be modified thanks to the quasi-periodic microstructure. With this reduced S3 sample, multiple load-unload in-situ tensile tests were conducted (Thilly et al., 2007), and the experimental longitudinal Young's modulus $(\tilde{E}_1)_{\text{S3}}$ was determined. Obtained result (131.2 GPa, uncertainty $\sim 5\%$) is shown in Table 4.5.

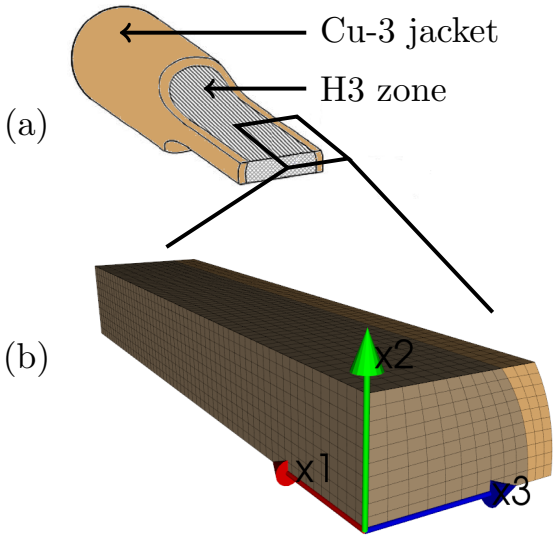

FIGURE 4.12: Structural problem S3: (a) Schematic view of half of the S3 sample with a reduced section. On such a sample geometry, multiple load-unload in-situ tensile tests were performed under X-rays by Thilly et al. (2007, 2009). (b) 1/8th mesh of the reduced S3 sample.

The X-ray diffraction response of this reduced specimen has been investigated in (Thilly et al., 2007, 2009). By analysing the shift of $\{hkl\}$ Bragg peaks, X-ray diffraction provides information about the mean elastic strain within the diffracting volume. The diffracting volume is constituted by all grains fulfilling Bragg conditions, i.e. exhibiting an $\{hkl\}$ plane perpendicular to the diffraction vector, i.e. perpendicular to the bisectrix of the incident and diffracted beams. As (i) only a small proportion of grains fulfil Bragg conditions and (ii) diffracting grains exhibit a specific crystallographic direction, the diffraction volume does not provide a RVE. Thilly et al. (2007, 2009) took advantage of the strong crystallographic texture of the specimen for their analysis (see Table 4.1 and figure 4.2). For Cu, the $\langle 111\rangle$-$\langle 100\rangle$ fibers lead to a significant proportion of $\{220\}$ and $\{111\}$ planes respectively parallel and perpendicular to the wire axis x_1. Performing diffraction on these lattice planes allows estimating the mean elastic strain, within the corresponding diffraction volumes, along the specimen transverse and longitudinal directions, respectively. For Nb, the strong $\langle 110\rangle$ fibers leads to a significant proportion of $\{220\}$ planes parallel or perpendicular to the wire, allowing estimating transverse and longitudinal mean elastic strains for the corresponding diffraction volumes. Table 4.5 reports results obtained for the case corresponding to a pure elastic response of the specimen, where transverse lattice strains on both Cu and Nb phases have been normalised by the applied effective tensile stress. Uncertainty on $(\varepsilon_e)_T/(\overline{\sigma}_{11})_{S3}$ is estimated as $\pm 5\%$ (fit uncertainty of experimental data).

In addition, Thilly et al. (2006) has performed neutron diffraction experiments on specimens similar to S3, i.e. on wires containing 55^4 Nb/Cu-0 elementary long fibers, instead of 85^3 Cu-f/Nb-t/Cu-0 fibers. However, this specimen exhibits similar Cu/Nb volume

fractions and textures to the previous "co-cylindrical" wires. Diffraction on Cu{111}, Cu{220}, and Nb{110} planes along different directions of the diffraction vector allows estimating the ratio $(\varepsilon_e)_T/(\varepsilon_e)_L$ between transverse and longitudinal strains, for both Cu and Nb phases, still for the corresponding diffraction volumes. In Thilly et al. (2009), uncertainties on the "fine" Cu channels (i.e. Cu-f, Cu-0 and Cu-1), the "large" Cu channels (i.e. Cu-2 and Cu-3), and the Nb-t, are estimated to be ±25%, ±13% and ±10% respectively. In our model, no distinction is made between fine and large Cu, treated as a single mechanical phase. These uncertainties are reported in Table 4.5.

	Experimental data	Modeling
$(\widetilde{E}_1)_{S3}$ (GPa)	131.2 ±5%	130.6
$(\varepsilon_e^{\{220\}Cu})_T/(\overline{\sigma}_{11})_{S3}$ (GPa^{-1})	-2.2E-3 ±5%	-2.4E-3
$(\varepsilon_e^{\{110\}Nb})_T/(\overline{\sigma}_{11})_{S3}$ (GPa^{-1})	-4.0E-3 ±5%	-3.9E-3
$(\varepsilon_e^{\{220\}Cu})_T/(\varepsilon_e^{\{111\}Cu})_L$	-0.34 ±13 − 25%	-0.32
$(\varepsilon_e^{\{110\}Nb})_T/(\varepsilon_e^{\{110\}Nb})_L$	-0.62 ±10%	-0.51

TABLE 4.5: Comparison of experimental data with modeling results for macroscopic longitudinal stiffness $(\widetilde{E}_1)_{S3}$, the ratio of transverse (i.e. along x_2-x_3 plane) elastic strain of reflection planes of individual Cu/Nb phase to the macroscopic stress $(\varepsilon_e)_T/(\overline{\sigma}_{11})_{S3}$ and the ratio of the transverse elastic strain to the longitudinal one $(\varepsilon_e)_T/(\varepsilon_e)_L$.

These data are now used to validate the multi-scale model presented above. Fig. 4.12(b) indicates 1/8th of the thinned S3 sample (length L) with its mesh (c3d20). For saving CPU time, symmetric boundary conditions are applied: U_1 (displacement field along x_1) is fixed at the middle plane x_1=0; U_2 is fixed at the bottom plane x_2=0 and U_3 is fixed at the left border plane x_3=0. The elastic properties of the inner Cu-Nb composites zone of H3 and the external polycrystalline Cu-3 jacket are assigned to $(\underset{\sim}{\widetilde{C}})_{H3}$ (Table 4.4) and $(\underset{\sim}{\widetilde{C}})_{H0\text{-}Cu}$ (Table 4.3 with ℓ/d=100) respectively. A normal tensile displacement U_1 is prescribed on the terminal section (x=L) of this S3 specimen. From the computed axial force, longitudinal stiffness $(\widetilde{E}_1)_{S3}$ is obtained, in excellent agreement with the data (Table 4.5).

For a comparison with diffraction data, one need to (i) compute the mean stress acting on H3, (ii) compute the corresponding stress concentration within the grains, by means of the SC scheme, and then (iii) isolate the diffraction volume and calculate the mean elastic strain along the direction of the different diffraction vectors. Obtained results are indicated in Table 4.5, with again an excellent match to all available data. From these experimental comparison, one can conclude that the proposed model not only predict the correct effective behavior, but also provide a good estimation of the stress and strain distributions within Cu and Nb grains; the mechanical scale transition is thus well captured.

4.7 Conclusions

This work is focusing on multiscale modeling of the elastic behavior of architectured and nanostructured Cu-Nb composite wires. After accumulative drawing and bundling, the nano-composite Cu-Nb material exhibits a multiscale architecture. It contains an assembly of 85^3 continuous and parallel Nb nanotubes and Cu nanofibers, with the smallest dimensions on the order of 50 nm. At the smallest scale (i.e. on the level of grains), Cu-Nb nano-composite is composed of Cu polycrystals and Nb polycrystals. The Cu phase displays a double $\langle 100 \rangle$-$\langle 111 \rangle$ crystallographic fiber texture, while a sharp single-component $\langle 110 \rangle$ fiber is seen in Nb. The morphological texture is characterized by highly elongated grains along the wire axis.

As the specimens exhibit several characteristic scales, the elastic behavior of these composite wires has been modeled by various homogenization methods: the SSC scheme assuming a random mixture of Cu or/and Nb phases, a FEM full-field model assuming a periodic microstructure (i.e. PH) and the GSC scheme taking into account the specific filament/nanotube microstructure. In the end, several scale transition steps were carried out iteratively in a hierarchical process to obtain the effective macro-scale elastic tensor.

The main conclusions of this work are the following:

1. *Morphological texture effect.* For the double ∼60% $\langle 111 \rangle$ and ∼40% $\langle 100 \rangle$ fiber textures, Cu polycrystal with elongated grains displays stiffer longitudinal Young's moduli than the one with spherical/square grains. Furthermore, the parameters characterizing the anisotropy of the elastic properties are found to be higher for elongated copper grains. In contrast, the effective elastic properties of the $\langle 110 \rangle$ Nb polycrystal only poorly depend on the morphological texture.

2. *Full field vs. mean field method.* Regarding the effective behavior of the Cu polycrystals and Nb polycrystals separately, a good agreement is found between full-field FEM (PH) and SSC model up to only 3% deviation for all considered crystallographic and morphological textures. In addition, parallelepipedic tessellations provide very similar results as Voronoï ones.

3. *Morphological vs. crystallographic texture effect.* Crystallographic texture plays an important role in the effective elastic moduli of Cu and Nb polycrystals. Conversely, the morphological texture only slightly affects these effective moduli, except for some special crystallographic texture cases, such as the double $\langle 100 \rangle$-$\langle 111 \rangle$ fiber.

4. *Effective behavior at scale H1.* The three homogenization schemes (i.e. SSC, GSC, and PH) provide very close results (differences smaller than 1.5%) due to limited contrast of elastic properties in the Cu and Nb phases. Therefore mean-field methods turn out to be more efficient than the full-field method PH for scale

H1. In spite of the absence of precise description of the microstructure, the SSC scheme delivers a good estimation of elastic properties.

5. *An iterative homogenization approach* is used to predict the elastic effective properties up to scale H3, and the elastic moduli estimated by the SSC scheme, the GSC scheme, and PH always almost coincide. In the end, the real structure used in the in-situ X-rays experiments by Thilly et al. (2007, 2009) is computed. A very good agreement has been obtained between available experimental results and the numerical estimation for the effective longitudinal Young's modulus and for the elastic strain of reflection planes of Cu/Nb phase separately.

4.8 Résumé du chapitre en Français

Ce chapitre se concentre sur la modélisation multi-échelles du comportement élastique de fils composites Cu-Nb nanostructurés et architecturés. Ces matériaux contiennent un assemblage de 85^3 nanotubes de Nb et nanofibres de Cu (fils de Cu-Nb co-cylindriques), avec les plus petites dimensions de l'ordre de ∼50 nm. À la plus petite échelle (c'est-à-dire au niveau des grains), ces fils nano-composite Cu-Nb sont composés de Cu polycristallin et de Nb polycristallin. Les phases de Cu présentent une double-texture de fibre cristallographique ⟨100⟩-⟨111⟩, tandis qu'une texture de fibre unique ⟨110⟩ est constatée dans Nb. La texture morphologique est caractérisée par des grains fortement allongés le long de l'axe du fil.

Comme les spécimens présentent plusieurs échelles caractéristiques, le comportement élastique de ces fils composites est modélisé par plusieurs méthodes d'homogénéisation multi-échelles : le schéma Auto-Cohérent Standard (ACS) en champs moyens supposant un mélange aléatoire des phases de Cu ou/et de Nb, la méthode des éléments finis (MEF) en champs complets supposant une microstructure périodique (que nous appelons HP pour Homogénéisation Périodique), et le schéma Auto-Cohérent Généralisé (ACG) en champs moyens prenant en compte la microstructure spécifique des filaments/nanotubes. Puis, plusieurs étapes de transition d'échelle sont réalisées de façon itérative dans un processus hiérarchique pour obtenir le tenseur élastique effectif macroscopique. Enfin, ces résultats sont comparés avec les données expérimentales disponibles ex-situ et in-situ (Thilly et al., 2006, 2007, 2009).

Les principales conclusions de ce chapitre sont les suivantes :

1. *L'effet de texture morphologique.* Pour la double-texture de fibre ∼60% ⟨111⟩ et ∼40% ⟨100⟩, le module longitudinal de Cu polycristallin avec les grains fortement allongés est plus rigide que celui des grains sphériques/carrés. En outre, les paramètres caractérisant l'anisotropie des propriétés élastiques se trouvent être plus élevés pour les grains de cuivre allongés. En revanche, les propriétés effectives élastiques du polycristal de Nb ⟨110⟩ dépendent peu de la texture morphologique.

2. *Champs complets vs. champs moyens.* Concernant le comportement effectif de polycristaux de Cu et de Nb séparément, MEF (HP) en champs complets et ACS en champs moyens sont en bon accord, avec au maximum 3% d'écart pour toutes les textures cristallographiques et morphologiques considérées. En outre, les tessellations parallélépipédiques prédisent les résultats très similaires à ceux de mosaiques de Voronoï.

3. *L'effet de texture morphologique vs. cristallographique.* La texture cristallographique joue un rôle important dans les modules élastiques effectifs des polycristaux de Cu et de Nb. À l'inverse, la texture morphologique affecte légèrement ces modules

effectifs, sauf certains cas spéciaux de texture cristallographique, par exemple, la double-texture de fibre ⟨100⟩-⟨111⟩.

4. *Comportement effectif à l'échelle H1.* Les trois schémas d'homogénéisation (c'est-à-dire ACS, ACG et HP) prédisent les résultats très proches (écarts inférieurs à 1,5%) en raison du contraste limité des propriétés élastiques des phases de Cu et Nb. Par conséquent, les méthodes en champs moyens sont plus efficaces que la méthode en champs complets à l'échelle H1. En dépit de l'absence de description précise de la microstructure, ACS offre une bonne estimation des propriétés élastiques.

5. *Une approche d'homogénéisation itérative* est utilisée pour prédire les propriétés effectives élastiques jusqu'à l'échelle H3, et les modules élastiques obtenus par ACS, ACG et HP sont presque confondus. Enfin, la structure réelle utilisée dans les expériences in-situ de diffraction des rayons X par Thilly et al. (2007, 2009) est calculée. Un très bon accord a été obtenu entre les données expérimentales disponibles, i.e. l'estimation numérique du module de Young longitudinal effectif et la déformation élastique individuelle des plans de diffraction de Cu/Nb.

Chapter 5

Multiscale modeling of the elasto-plastic behavior and comparison with neutron diffraction experiments

Abstract

This chapter presents a comprehensive study of the effective elasto-plastic behavior of Cu-Nb composite wires by using two different approaches to model the microstructural features: full-field finite elements and mean-field modeling. As the specimens exhibit many characteristic length scales, several scale transition steps are carried out iteratively from the grain scale to the macro-scale. The general agreement of the model responses allows us to determine the best strategy to estimate reliably the effective elasto-plastic behavior of Cu-Nb wires and save computational time. Taking into account a realistic field of residual stresses, model predictions are validated by available ex-situ tests and in-situ neutron diffraction experimental data with an excellent agreement. Experiments and theory find consistently that plastic activity occurs in Cu $\langle 100 \rangle$ orientated grains at a higher macroscopic stress than in Cu $\langle 111 \rangle$ grains, when the wire is deformed under tension along the wire direction.

5.1 Introduction

Predicting the elasto-plastic behavior of polycrystalline Cu-Nb composites is a complex matter, particularly if these materials are fabricated by severe plastic deformations leading to: (1) specific crystallographic/morphological textures; (2) microstructural features which exhibit anisotropy and induce size effect; and (3) initial residual stresses.

This chapter concentrates on the multiscale modeling of the *anisotropic elasto-plastic behavior* of architectured and nanostructured Cu-Nb composite *wires*. Two multiscale models will be introduced: a mean-field homogenization model, i.e. the so-called β-model and a full-field Finite Element Method (FEM) with periodic boundary conditions (denoted PH, for Periodic Homogenization). These models essentially differ by the microstructural information they are based on for the estimation of the effective behavior. Here, the β-model will be used to describe the elasto-plastic behavior of polycrystals made of Cu or Nb grains, but also for the estimation of a random mixture of Cu and Nb phases. Meanwhile, FEM PH assumes a periodic microstructure and its response will be compared with the one obtained by the mean-field approach. In addition, the constitutive (visco-)plastic laws for the single crystal will be described by using Méric-Cailletaud's model (Méric et al., 1991).

Considering the dislocation movement for strain hardening of a single crystal, a dislocation-based constitutive formulation has been in the literature proposed, e.g. see Tabourot et al. (1997); Kubin et al. (2008); Devincre et al. (2008); Groh et al. (2009) for BCC (Body-Centered Cubic) and FCC (Face-Centered Cubic). In these models, all parameters have a physical meaning which can be determined by experiments or other theoretical methods, such as dislocation dynamics (Tabourot et al., 1997; Groh et al., 2009). Moreover, among many others, known as Méric-Cailletaud's model, is more phenomenological and uses a combination of kinematic and isotropic hardening for each slip system (Méric et al., 1991; Besson et al., 2009). This model is used for the crystal plastic predictions of metallic alloys, particularly for FCC Cu polycrystals (Méric et al., 1994; Šiška et al., 2006; Musienko et al., 2007; Gérard, 2008).

The mean-field methods were initially developed for heterogeneous linear thermal-elasticity, such as the Standard Self-Consistent scheme (denoted SSC), according to Kröner (1978); François et al. (1998); Castelnau (2011). Later on, this method has been extended to visco-plastic, elasto-plastic and elasto-visco-plastic nonlinear properties (Ponte-Castañeda and Suquet, 1998). In addition, in order to improve the accuracy of nonlinear calculations and to investigate the higher-order statistical information inside grains, a second moment method is developed from the above-mentioned nonlinear mean-field methods (Masson et al., 2000; Lebensohn et al., 2011; Doghri et al., 2011). Based on the Berveiller and Zaoui (1978) model for isotropic nonlinear behavior of equiaxed aggregates, the β-model was proposed for anisotropic behavior of multi-axial aggregates (Cailletaud, 1992;

Forest and Pilvin, 1996; Sai et al., 2006; Martin et al., 2014; Coudon et al., 2017). β-model assumes a purely elastic (instead of an elasto-plastic) intergranular interactions which make it very efficient numerically. Such a treatment leads to an overestimation of these interactions and a too stiff polycrystalline behavior (Masson and Zaoui, 1999), therefore an accommodation variable β is introduced to correct this error.

Unlike the mean-field approaches, full-field methods (e.g. based on FEM) applied to Representative Volume Element (RVE) can describe the detailed experimental microstructure and provide the complex stress/strain fields inside the different phases at the expense of increased computational time. The elasto-(visco-)plastic effective behavior of FCC and BCC polycrystalline aggregates can be studied by FEM in many aspects, as mentioned in Barbe et al. (2001b,c); Fritzen and Böhlke (2011). In addition, in order to accelerate CPU time, another full-field method, named as Fast Fourier Transform (FFT), is developed for both linear and nonlinear polycrystalline behaviors (Lebensohn et al., 2012; Kanjarla et al., 2012).

The scale transition for elasto-(visco-)plastic heterogeneous materials with a random or complex microstructure, e.g. Composite Cylinders Assembly (denoted CCA, present at different scales in Fig. 2.2) is a challenge for homogenization models. In this regard, considerable attention has been paid, such as: the above-mentioned full-field FEM (Williams and Pindera, 1997), macroscopic model with phenomenological parameters identified (Haddadi et al., 2006), FE^2 multiscale approach (Feyel and Chaboche, 2000; Geers et al., 2010), and TFA (Transformation Field Analysis)/NTFA (Nonuniform Transformation Field Analysis) (Franciosi and Berbenni, 2008; Fritzen and Böhlke, 2011; Michel and Suquet, 2016).

Despite a wealth of literature works on elasto-(visco-)plasticity, we have found that the following three points are still missing: 1. No systematic analysis of anisotropic behavior for Cu/Nb polycrystals by elasto-plastic homogenization models, especially for the specific crystallographic/morphological textures encountered in Cu-Nb wires; 2. No application of current nonlinear homogenization methods to the complex architectures (i.e. CCA) of recent Cu-Nb wires; 3. No experimental comparison for the recent obtained in-situ neutron diffraction data for Cu-Nb wires.

Therefore, the objectives of this chapter are threefold: 1. provide a homogenization model for individual Cu/Nb polycrystals taking the crystallographic/morphological textures of Cu-Nb wires into account; 2. provide a multi-scale homogenization procedure to model the architectured and nanostructured Cu-Nb composite wires, taking into account the initial residual stresses; 3. provide a quantitative understanding of the load dependence of crystal lattice neutron diffraction evolution during uniaxial loading test for Cu-Nb wires.

The outline of the chapter is as follows. The architecture/microstructure of Cu-Nb composite wires and their corresponding mechanical properties are described in Section 5.2.

In order to reproduce the effective elasto-plastic behavior of this material, two multi-scale methods, namely, β-model and PH are presented in Section 5.3. In Section 5.4, the Cu polycrystals are isolated and homogenized. Then in Section 5.5, several scale transitions of architectured Cu-Nb composites are performed to determine the effective elasto-plastic behavior of Cu-Nb wires up to macro-scale. In Section 5.6, the best modeling strategies are proposed. Finally, the model results are validated by comparison with available experimental data.

5.2 Material description

In this chapter, two N=85^2 Cu-Nb Filamentary wires (see Fig. 2.2) with a final diameter [1] 0.29 mm and 2.10 mm are studied which are used for ex-situ and in-situ tensile experiments respectively. These wires are obtained from initial specimens with a diameter of 4.50 mm by supplementary cold-drawing. The volume fraction $f^{(i)}$ of each component (i.e. Nb, Cu-0, Cu-1 and Cu-2) is not changed by hot-extrusion nor cold-drawing and they can be determined by the initial dimensions of Nb cylinder and Cu jacket. The theoretical value of channel width, $\delta^{(i)}$, can be estimated by assuming that all the perfect and concentric components (i.e. Nb cylinder and Cu tube) are deformed in a homothetic way by the material processing (Vital, 2006). These theoretical $\delta^{(i)}$ are confirmed by SEM (Scanning Electron Microscope) observations (Medy, 2016). Table 5.1 indicates the volume fraction $f^{(i)}$ and theoretical channel width $\delta^{(i)}$ in two diameter cases: 0.29 mm and 2.10 mm.

Component		Nb	Cu-0	Cu-1	Cu-2
Volume fraction $f^{(i)}$		44.7%	15.2%	17.5%	22.6%
sample diameter 0.29 mm					
Channel width $\delta^{(i)}$		1.94 μm	310 nm	3.09 μm	17.65 μm
sample diameter 2.10 mm					
Channel width $\delta^{(i)}$		13.74 μm	2.19 μm	21.97 μm	124.48 μm
Fiber textures	$\langle 111 \rangle$	-	70%	90%	81%
	$\langle 100 \rangle$	-	30%	10%	19%
	$\langle 110 \rangle$	100%	-	-	-
Yield stress σ_y		> 2 GPa[2]	350 MPa		

TABLE 5.1: Volume fraction $f^{(i)}$, channel width $\delta^{(i)}$, crystallographic textures and yield stresses σ_y of individual component for Cu and Nb polycrystals in Cu-Nb wires, obtained from Medy (2016). The two samples with different diameters are assumed to exhibit the same textures and σ_y in each component.

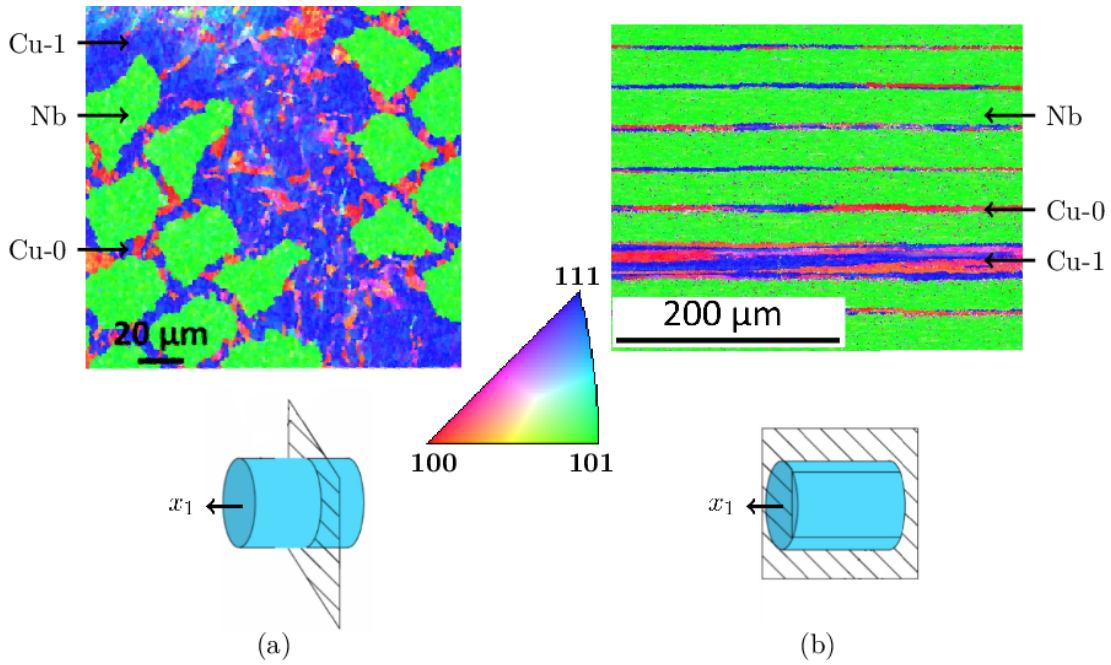

FIGURE 5.1: EBSD orientation map combining the Cu and Nb phases (Nb appears in green due to the strong ⟨110⟩ fiber texture) at the H1 scale (specimen diameter 4.50 mm): (a) the cross section perpendicular to the wire direction x_1; (b) the cross section parallel to x_1. Inverse pole figure (x_1 axis) coloring according to the cubic crystal system.

5.2.1 Crystallographic and morphological textures

The crystallographic texture of a Cu-Nb Filamentary wire (N=85[2]) at a diameter of 4.50 mm has been investigated by EBSD at all scales by Medy (2016). Fig. 5.1(a) illustrates the EBSD orientation map on the cross-section perpendicular to the wire axis x_1 at the effective scale H1. The Cu components exhibit strong ⟨111⟩ fiber texture with the remnant ⟨100⟩ fiber, while a single ⟨110⟩ texture is observed in Nb fibers. Due to extrusions and drawings along the wire direction in ADB processing, x_1 is also the symmetry axis of theses fibers. The crystallographic textures of each component are given in Table 5.1. Noting that the associated texture spread is estimated to be 10.0° ± 3.0° by EBSD (FWHM, for Full Width at Half Maximum). The specimens with smaller diameter 2.10 and 0.29 mm studied in this work are believed to display very similar similar crystallographic texture, as confirmed by preliminary EBSD results. From the Orientation Distribution Function described above, two sets of 10000 discrete orientations (one for Cu and one for Nb) are created by LaboTex [3]. They will be used to generate the microstructure in the full-field/mean-field scale transition models (see Section 5.3).

[1]Following (Thilly et al., 2002a; Medy, 2016), all dimensions are given in the x_2-x_3 cross-section, i.e. perpendicular to the wire axis x_1, see Fig. 2.2 for the coordinate system.

[2]Only for Nb fibers in Cu-Nb wires instead of bulk specimens of Nb, see Section 5.2.2 for explanations.

[3]Software for crystallographic textures - http://www.labosoft.com.pl/.

In the present work, we define ℓ as the average grain length along the longitudinal wire axis x_1 and d as the average grain diameter in the transverse x_2-x_3 cross-section. As illustrated in Fig. 5.1(b), the morphological texture exhibits highly elongated grains along x_1 because of iterative severe plastic extrusion and drawing, therefore $\ell \gg d$ for both Cu and Nb components (Medy, 2016).

5.2.2 Yield stresses

Because of the multi-scale structure, different types of copper matrix channels are present (Thilly et al., 2009): (1) Cu channels with δ larger than a few micrometers (so-called "large" Cu channels) which are composed of grains with a transverse size $d \sim 1\,\mu$m together with remaining smaller grains with d=200-400 nm (a typical grain size in cold-worked Cu); (2) On the other hand, the so-called "fine" Cu channels lie in the sub-micrometer range, with only a few grains located between the Cu/Nb interfaces: in this case, grain width d varies from $\delta/3$ to δ, e.g. Cu-0 in the specimens with a diameter of 0.29 mm (δ=310 nm, see Table 5.1). According to Vidal et al. (2007); Thilly et al. (2009), the yield stresses σ_y of the highly hardened large Cu channels can be estimated as 350 MPa. Furthermore, the fine Cu-0 channels (i.e. δ=310 nm) may display a higher σ_y up to 500 MPa due to the size effect (Thilly et al., 2009). For the sake of simplicity, all Cu components here are assumed to exhibit the same σ_y=350 MPa, as shown in Table 5.1. A higher σ_y of Cu-0 will not change significantly the model results, as the volume fraction of fine Cu-0 is small (∼15%).

The bulk specimens of hardened polycrystalline Nb display a $\sigma_y \sim 1.4$ GPa (Dupouy et al., 1995). On the other hand, the grain size of Nb fibers in Cu-Nb wires d_{Nb} is comparable with their fiber width ($d_{\mathrm{Nb}} \approx \delta_{\mathrm{Nb}}$) according to Thilly et al. (2009). Involving the size effect, Dubois et al. (2012) argued that σ_y of Nb fibers is much higher (>2 GPa) than the ones of Cu channels. Several tensile tests of Cu-Nb wires were performed along the wire direction x_1 up to macroscopic material failure, and plastic strain has not been seen for Nb fibers (Vital, 2006; Dubois, 2010). Therefore in this work, Nb is assumed to remain elastic for the small-strain mechanical tests considered.

5.2.3 Initial residual stresses

Due to ADB processing, residual stresses are initially introduced in composite Cu-Nb wires, as observed by X-ray diffraction (Vital, 2006). The longitudinal initial residual stresses $(\sigma_{\mathrm{res}})_{11}$ along the wire direction x_1 are determined in a Cu-Nb wire containing N=55^4 elementary Cu/Nb fibers (specimen diameter 1.49 mm): an axial compression ∼-100 MPa for the large Cu channels ($\delta \geqslant 1\,\mu$m) and a tension ∼250 MPa for Nb. However, $\underset{\sim}{\boldsymbol{\sigma}}_{\mathrm{res}}$ measurements have not been reported for the N=85^2 Cu-Nb Filamentary

wires studied in this work (Medy, 2016). The chosen values of $\underset{\sim}{\boldsymbol{\sigma}}_{\text{res}}$ will be discussed later in Section 5.6.3.

Furthermore, in a thermo-elastic like homogenization problem, $\underset{\sim}{\boldsymbol{\sigma}}_{\text{res}}$ are generated by the stress-free strain (or "eigenstrain") $\underset{\sim}{\boldsymbol{\varepsilon}}_0$ in each individual component (Castelnau, 2011). $\underset{\sim}{\boldsymbol{\varepsilon}}_0$ in Cu-Nb composite wires can be estimated by Eq. (B.6) which is used for polycrystalline aggregates where $\underset{\approx}{\boldsymbol{C}}^{(r)}$ and $\underset{\approx}{\widetilde{\boldsymbol{C}}}$ indicate the effective elastic tensor of individual Cu/Nb component and of overall Cu-Nb wires respectively. In addition, elastic properties $\underset{\approx}{\boldsymbol{C}}$ of Cu-Nb wires are determined by SSC scheme (Gu et al., 2017).

5.3 Hierarchical homogenization strategy

5.3.1 Constitutive equations for the single crystal

The Cu-Nb wires are made of FCC Cu and BCC Nb grains. In addition, Nb polycrystals exhibit a high yield stress leading to an elastic behavior (Section 5.2.2). This section briefly presents the elasto-visco-plastic single crystal model used in this work for the Cu components. It has been developed in the framework of crystal plasticity theory (Méric et al., 1991) (i.e. Méric-Cailletaud's model), and used for metallic alloys. It is presented here in its small perturbation version, which uses an additive decomposition of the elastic and the viscoplastic strain rates. The resolved shear stress τ^s acting on a particular slip system (s) is given by Schmid's law:

$$\tau^s = \underset{\sim}{\boldsymbol{\sigma}}^{(r)} : \underset{\sim}{\boldsymbol{m}}^s \tag{5.1}$$

where $\underset{\sim}{\boldsymbol{\sigma}}^{(r)}$ is the stress tensor in a crystal phase (r) and $\underset{\sim}{\boldsymbol{m}}^s$ is the orientation tensor attributed to the slip system (s):

$$\underset{\sim}{\boldsymbol{m}}^s = \frac{1}{2}(\underline{\boldsymbol{l}}^s \otimes \underline{\boldsymbol{n}}^s + \underline{\boldsymbol{n}}^s \otimes \underline{\boldsymbol{l}}^s) \tag{5.2}$$

with $\underline{\boldsymbol{n}}^s$ and $\underline{\boldsymbol{l}}^s$ being the "slip plane" normal vector and the "slip direction" vector in this plane, respectively. Here, we have 12 octahedral systems for FCC Cu. The resolved shear stress τ^s is related to corresponding shear rate $\dot{\gamma}^s$ via a power law expression:

$$\dot{\gamma}^s = \left\{ \frac{|\tau^s - X^s| - R^s}{K} \right\}^n \text{sign}(\tau^s - X^s), \quad \text{with } \{a\} = \max(a, 0)\,. \tag{5.3}$$

For each slip system, internal variables are introduced to describe the hardening of the material: isotropic hardening variables R^s and kinematic hardening variables X^s. In addition, n and K are the parameters controlling viscosity. The non-linear evolution rule for isotropic hardening involves an interaction matrix $\boldsymbol{h}$ which represents self-hardening

(diagonal terms) and latent hardening (non-diagonal terms):

$$R^s = R_0 + Q\sum_u h_{su}[1 - exp(-bv^u)], \quad \text{with } \dot{v}^u = |\dot{\gamma}^u|\,, \tag{5.4}$$

then the form of non-linear kinematic hardening is adopted:

$$X^s = C\alpha^s, \text{with } \dot{\alpha}^s = \dot{\gamma}^s - D|\dot{\gamma}^s|\alpha^s\,. \tag{5.5}$$

Here, R_0 in Eq.(5.4) denotes the initial critical resolved shear stress (CRSS). Noting that Q, b, C, D in above equations are material parameters for isotropic and kinematic hardening. The choice of isotropic/kinematic hardening and model parameters will be discussed in Section 5.4.1 for Cu polycrystals. In addition, the hardening variables α^s in Eq.(5.5) are initialized as 0. Finally, plastic deformation $\underset{\sim}{\boldsymbol{\varepsilon}}_{\mathrm{p}}^{(r)}$ in a crystal phase (r) is the result of slip processes on all slip systems:

$$\dot{\underset{\sim}{\boldsymbol{\varepsilon}}}_{\mathrm{p}}^{(r)} = \sum_{s=1}^{12} \dot{\gamma}^s \underset{\sim}{\boldsymbol{m}}^s\,. \tag{5.6}$$

5.3.2 Mean-field β-model

According to Lebensohn et al. (2011); Castelnau (2011); Gu et al. (2017), the mean-field SSC scheme is advocated to be a good candidate to estimate the effective elastic property of individual Cu and Nb polycrystals. The SSC scheme is also used to estimate the behavior of a fictitious material in which Cu and Nb grains are randomly mixed together, with volume fractions, textures and initial residual stresses described above, in order to check the impact of the particular architectured microstructure of Cu-Nb wires.

In the present work, we introduce a fast computational scale transition model, i.e. the so-called β-model which is an extension of SSC scheme to investigate the elasto-plasticity of Cu-Nb wires (Cailletaud, 1992; Forest and Pilvin, 1996; Sai et al., 2006; Martin et al., 2014; Coudon et al., 2017). The scale transition interaction equation of β-model is proposed as follows (see the detailed derivations in Appendix B):

$$\underset{\sim}{\boldsymbol{\sigma}}^{(r)} = \underset{\sim\sim}{\boldsymbol{B}}^{(r)} : \left[\overline{\underset{\sim}{\boldsymbol{\sigma}}} + \underset{\sim\sim}{\boldsymbol{L}}_{\mathrm{C}}^{*} : \left(\widetilde{\underset{\sim}{\boldsymbol{\beta}}} - \underset{\sim}{\boldsymbol{\beta}}^{(r)}\right)\right] + \underset{\sim}{\boldsymbol{\sigma}}_{\mathrm{res}}^{(r)} \tag{5.7}$$

where $\underset{\sim\sim}{\boldsymbol{B}}^{(r)}$ and $\underset{\sim}{\boldsymbol{\sigma}}_{\mathrm{res}}^{(r)}$ denote respectively the stress localization tensor (for the purely elastic problem) and initial residual stresses in phase (r). In addition, the accommodation tensor $\underset{\sim\sim}{\boldsymbol{L}}_{\mathrm{C}}^{*}$ is expressed as:

$$\underset{\sim\sim}{\boldsymbol{L}}_{\mathrm{C}}^{*} = \widetilde{\underset{\sim\sim}{\boldsymbol{C}}} : \left(\underset{\sim\sim}{\boldsymbol{I}} - \underset{\sim\sim}{\boldsymbol{S}}_{\mathrm{Esh}}\right) \tag{5.8}$$

with $\underset{\sim}{\underset{\sim}{\boldsymbol{I}}}$ the fourth order identity tensor and $\underset{\sim}{\underset{\sim}{\boldsymbol{S}}}_{\text{Esh}}$ the Eshelby tensor. Here, $\underset{\sim}{\underset{\sim}{\boldsymbol{S}}}_{\text{Esh}}$ depends on $\underset{\sim}{\underset{\sim}{\widetilde{\boldsymbol{C}}}}$ (instead of elasto-plastic tensor $\underset{\sim}{\underset{\sim}{\widetilde{\boldsymbol{L}}}}$) and on the morphological texture ℓ/d. β-model can save a lot CPU time compared with other elasto-plastic mean-field models (refer to Section B.4 for the computational efficiency of β-model); the price to pay being the calibration of the scale transition coefficients. The accommodation variables $\underset{\sim}{\boldsymbol{\beta}}$ are given as follows associated with plastic strain $\underset{\sim}{\boldsymbol{\varepsilon}}_{\text{p}}$:

$$\dot{\underset{\sim}{\boldsymbol{\beta}}}^{(r)} = \dot{\underset{\sim}{\boldsymbol{\varepsilon}}}_{\text{p}}^{(r)} - \underset{\sim}{\underset{\sim}{\boldsymbol{D}}} : \underset{\sim}{\boldsymbol{\beta}}^{(r)} \|\dot{\underset{\sim}{\boldsymbol{\varepsilon}}}_{\text{p}}^{(r)}\| \tag{5.9}$$

where $\|\dot{\underset{\sim}{\boldsymbol{\varepsilon}}}_{\text{p}}^{(r)}\|$ denotes the equivalent overall plastic strain rate. Analogous to $\underset{\sim}{\boldsymbol{\varepsilon}}_{\text{p}}^{(r)}$, $\dot{\underset{\sim}{\boldsymbol{\beta}}}^{(r)}$ variables are initialized as $\underset{\sim}{\mathbf{0}}$ before loading. Moreover, $\underset{\sim}{\underset{\sim}{\boldsymbol{D}}}$ denotes a fourth order phenomenological constant tensor to be calibrated. It is determined by comparing the model responses between β-model and the reference full-field FEM. In this work, the following form is considered for $\underset{\sim}{\underset{\sim}{\boldsymbol{D}}}$, as proposed by Sai et al. (2006); Martin et al. (2014) for the anisotropic elasto-plastic properties of multi-axial aggregates:

$$\underset{\sim}{\underset{\sim}{\boldsymbol{D}}} = \begin{pmatrix} D_{11} & D_{12} & D_{12} & & & & \\ D_{12} & D_{33} & D_{23} & & & & \\ D_{12} & D_{23} & D_{33} & & & & \\ & & & D_{44} & & & \\ & & & & D_{55} & & \\ & & & & & D_{55} & \end{pmatrix} . \tag{5.10}$$

In the material frame, using the deviatoric property of the accommodation variable, i.e. trace($\dot{\underset{\sim}{\boldsymbol{\beta}}}^{(r)}$)=0, the following additional condition is enforced (Sai et al., 2006) according to Eq. (5.9):

$$D_{11} = D_{33} + D_{23} - D_{12} \, . \tag{5.11}$$

We thus have five interdependent coefficients D_{ij} to be determined. With this form of $\underset{\sim}{\underset{\sim}{\boldsymbol{D}}}$, it will be found that β-model predictions fit satisfactorily the results obtained by the FEM reference for the anisotropic behavior of polycrystalline aggregates (Section 5.4.3).

Furthermore, to ensure the homogenization condition $\overline{\underset{\sim}{\boldsymbol{\sigma}}} = \langle \underset{\sim}{\boldsymbol{\sigma}}^{(r)} \rangle$, $\widetilde{\underset{\sim}{\boldsymbol{\beta}}}$ is given by (according to Eq. (5.7)):

$$\widetilde{\underset{\sim}{\boldsymbol{\beta}}} = \langle \underset{\sim}{\underset{\sim}{\boldsymbol{L}}}_{\text{C}}^{*-1} : \underset{\sim}{\underset{\sim}{\boldsymbol{B}}}^{(r)} : \underset{\sim}{\underset{\sim}{\boldsymbol{L}}}_{\text{C}}^{*} : \underset{\sim}{\boldsymbol{\beta}}^{(r)} \rangle \, . \tag{5.12}$$

5.3.3 Full-field periodic models

In addition to the mean-field β-model, a full-field FEM PH is proposed here to compute the effective elasto-plastic behavior of Cu-Nb wires at all scales. An elementary volume V made of heterogeneous material is considered for polycrystalline aggregates (scale H0) in Section 5.3.3.1 and for a specific architecture (scale H1 and H2) in Section 5.3.3.2.

Periodic boundary conditions are prescribed at the boundary ∂V. The displacement field $\underline{\boldsymbol{u}}$ in V, then takes the following form:

$$\underline{\boldsymbol{u}}(\underline{\boldsymbol{x}}) = \underset{\sim}{\overline{\varepsilon}} \cdot \underline{\boldsymbol{x}} + \underline{\boldsymbol{v}}(\underline{\boldsymbol{x}}) \quad \forall \underline{\boldsymbol{x}} \in V \tag{5.13}$$

where the fluctuation $\underline{\boldsymbol{v}}$ is periodic, i.e. it takes the same values at two homologous points on opposite faces of V. Furthermore, the traction vector $\underset{\sim}{\boldsymbol{\sigma}} \cdot \underline{\boldsymbol{n}}$ takes opposite values at two homologous points on opposite faces of V ($\underline{\boldsymbol{n}}$ is the outwards normal vector to ∂V).

5.3.3.1 PH adapted for polycrystalline aggregates

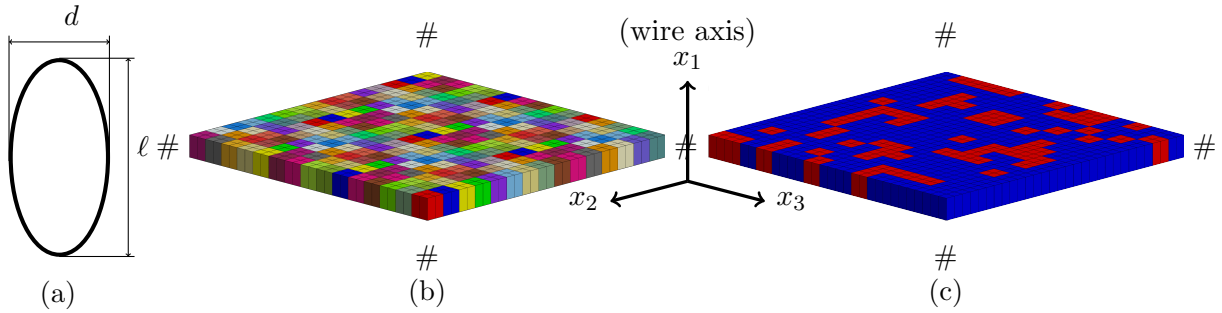

FIGURE 5.2: Meshes of PH models for H0 polycrystalline aggregates: (a) The overall shape of a single grain elongated along direction x_1 with dimensions $\ell \times d \times d$; (b) Parallelepipedic tessellation of (15×15) 225 grains with the aspect ratio $\ell/d \to \infty$; (c) Orientation distribution in the tessellation mesh (b), blue stands for $\langle 111 \rangle$ fiber texture and red for $\langle 100 \rangle$. Periodic boundary conditions, denoted #, are considered.

Unlike mean-field models in which the microstructure is described statistically, FEM PH can account for a realistic microstructure at H0, and it provides the full stress/strain fields over V. In the present work, PH is used to study the elasto-plasticity of polycrystalline Cu and its model response will be taken as a reference for the identification of the phenomenological parameters $\underset{\sim}{\boldsymbol{D}}$ in the mean-field β-model (Section 5.3.2).

As illustrated in Fig. 5.1(b), Cu grains are highly elongated along x_1 due to material processing. In order to take this morphological texture into account, a slice-shaped parallelepipedic tessellation (finite element mesh using c3d20r elements [4]) was proposed in Gu et al. (2017), as shown in Fig. 5.2(b). This tessellation is composed of $15 \times 15 (=225)$ regularly arranged square grains, and it is subjected to periodic boundary conditions (Eq.(5.13)) for taking advantage of a smaller RVE than the one with homogeneous boundary conditions (Kanit et al., 2003). In addition, the single crystal constitutive law of Cu is given in Section 5.3.1. Furthermore, the 225 grain orientations are randomly chosen among the full set of 10000 (see orientation sets in Section 5.2.1), and the discrete orientations are spatially randomly distributed among the grains of the parallelepipedic

[4] c3d20r: reduced quadratic hexahedrons with 20 nodes and 8 Gauss points per element

tessellation. Fig. 5.2(c) indicates the ⟨111⟩ and ⟨100⟩ fiber texture distributions, this figure is analogous to EBSD orientation map (see Fig. 5.1). The mesh density has also been checked for ensuring adapted numerical accuracy and avoiding too long computational time.

PH Voronoï tessellations of Coudon et al. (2017) was also used to evaluate the impact of the over-simplified parallelepipedic grain shape in previous problem. It was found that the deviations of homogenized stress/strain between the parallelepipedic and Voronoï tessellations are always smaller than 5% based on different boundary conditions.

5.3.3.2 PH adapted for composite cylinders assemblies

We now proceed to predict the effective elasto-plastic behavior of the specific CCA microstructure of Cu-Nb composites (i.e. H1 and H2). As the specimens exhibit many characteristic scales, one of the model challenges is to account for the nonlinear behavior in the different scale transitions. As mentioned in Section 5.1, this scale transition can be performed for elasto-(visco-)plastic heterogeneous materials with a complex and random microstructure in various ways. In the present work for H1 and H2, macroscopic model of Haddadi et al. (2006) can provide an accurate homogenized behavior, however this macroscopic and phenomenological model cannot investigate the intergranular interactions; FE^2 (Feyel and Chaboche, 2000; Geers et al., 2010) approach will cost a long CPU time despite applying parallel computational techniques; TFA/NTFA are promising models (Franciosi and Berbenni, 2008; Fritzen and Böhlke, 2011; Michel and Suquet, 2016), however they are not yet available for successive scale transition steps, needed for Cu-Nb wires.

Here, in order to achieve the elasto-plastic H1/H2 with a reasonable CPU time, a combination of the mean-field β-model and full-field FEM PH is used. Taking into account the CCA architecture with the quasi-periodic distribution observed experimentally (Fig. 2.2(a) and Fig. 2.2(b)), the section views of the unit cell of H1 and H2, with their meshes (c3d20r elements), are respectively indicated in Fig. 5.3(a) and Fig. 5.3(b). These unit cells are subjected to periodic boundary conditions. These meshes are composed of two equivalent long fibers (1+4×1/4 fibers) which are arranged in an hexagonal lattice, and they represent the (idealized) multi-scaled experimental microstructure of the Cu-Nb wires.

Nb will be assigned to an effective elastic tensor $(\widetilde{\underset{\sim}{C}})_{\text{H0-Nb}}$ which is determined by H0 SSC scheme with the full set of 10000 crystallographic orientations (see Section 5.2.1) considered. On the other hand, the elasto-plastic β-model (Section 5.3.2) for the homogenization of polycrystalline Cu-0 component will be associated with the local constitutive behavior of Cu-0 envelope at H1, as illustrated in Fig. 5.3 (a). This approach is called

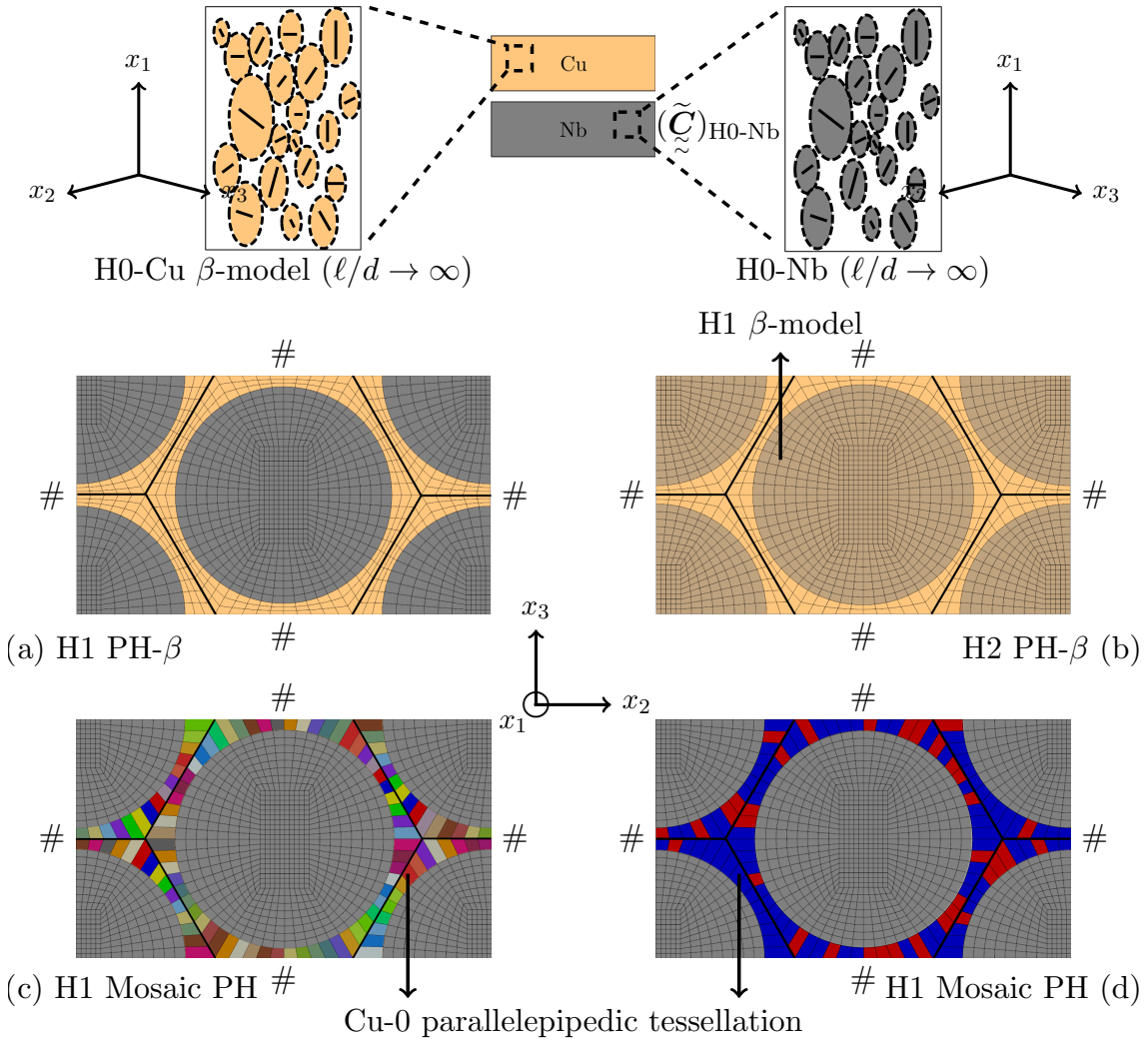

FIGURE 5.3: Multiscale modeling of effective elasto-plastic behaviors of Cu-Nb composite wires: (a) PH-β at H1, i.e. FEM PH model with polycrystalline Nb/Cu component assigned to the effective H0-Nb elastic tensor and H0-Cu-0 β-model respectively; (b) PH-β at H2; (c) Mosaic PH at H1 with crystal plastic Cu-0 parallelepipedic tessellation; (d) Crystallographic textures distribution in (c) the H1 Mosaic PH, blue for $\langle 111 \rangle$ fiber texture and red for $\langle 100 \rangle$. Periodic boundary conditions, denoted #, are considered. Yellow stands for Cu, gray for Nb, brown for Cu-Nb composite.

as PH-β model throughout this work, the iterative modeling strategies of PH-β up to H2 (Fig. 5.3(b)) will be further discussed in Section 5.5.3.

Inspired from the parallelepipedic tessellation of Fig. 5.2(b), another so-called H1 Mosaic PH model is proposed as shown in Fig. 5.3(c) for validating the newly introduced elasto-plastic PH-β model. The FE mesh (c3d20r elements) of the Mosaic PH is composed of elastic Nb fibers and elasto-plastic Cu-0 channels. Again, the structure is subjected to periodic boundary conditions. In these Cu-0 channels, individual grains are considered, instead of polycrystalline aggregates as in the PH-β approaches. Here the 120 FE elements located in the channels represent 120 grains, with crystal orientations representing the crystal textures. Therefore, the parallelepipedic tessellation of

Cu-0 channels takes the crystallographic/morphological textures and single crystal constitutive law into account, as mentioned in Section 5.3.3.1. Analogous to Fig. 5.2(c), the experimental crystallographic textures (i.e. randomly distributed ⟨111⟩ and ⟨100⟩ fiber) accounted in model are shown in Fig. 5.3(d). According to Section 5.2.2, the Cu grain transverse size d varies between from $\delta/3$ to δ where δ denotes Cu-0 channel width from experimental observation (Fig. 5.1(a)). Thus $d{=}\delta/2$ is chosen to construct the mesh of the Mosaic PH model.

Note that PH model describes an infinite periodic honeycomb microstructure. However, the real architecture of Cu-Nb wires at all scales contains only a finite number (i.e. 85) of long fibers. Simulations of a larger hexagonal structure without periodic boundary conditions confirm that the hypothetical infinity does not significantly affect our results. Furthermore, the effect of mesh density for H1/H2 will be studied further in Section 5.5.2.

5.3.3.3 Statistical representative volume element

When a single realization over the elementary volume V (e.g. H0 polycrystalline aggregate in Fig. 5.2(b)) is used, a relatively limited number of grain orientations and grain neighborhoods are accounted for. This leads to a bias in the estimation of the effective properties as explained in (Kanit et al., 2003; Gu et al., 2017). The RVE must contain a sufficiently large number of heterogeneities (e.g., grains, inclusions, fibers etc.) for the macroscopic properties to be independent on the boundary conditions applied to this volume. Kanit et al. (2003) proposed a statistical strategy to determine the RVE size for elastic moduli.

In this work, we extend this approach to elasto-plasticity by considering n realizations of the microstructure in a volume with given size. This volume size is then increased to investigate the asymptotic elasto-plastic stress/strain:

$$\overline{Z}(t) = \frac{1}{n}\sum_{i=1}^{n}\widetilde{Z}_i(t), \qquad D_Z(t)^2 = \frac{1}{n}\sum_{i=1}^{n}[\widetilde{Z}_i(t) - \overline{Z}(t)]^2 \tag{5.14}$$

where $\widetilde{Z}_i(t)$ is an apparent elasto-plastic stress/strain obtained for one realization and $\overline{Z}(t)$ is its mean value over n realizations at a given time t during loading. In addition, the variance $D_Z(t)^2$ denotes the fluctuations of $\widetilde{Z}_i(t)$. The number of realizations n is chosen so that the obtained mean value $\overline{Z}(t)$ does not vary any longer up to a given precision when n is increased. This precision (i.e. relative error $\varepsilon_{\text{rela}}(t)$) of the estimation of the effective property $\overline{Z}(t)$ is related to the standard deviation $D_Z(t)$ and the number of realizations n by:

$$\varepsilon_{\text{rela}}(t) = \frac{2D_Z(t)}{\overline{Z}(t)\sqrt{n}}\,. \tag{5.15}$$

Conventionally, if at any time t during the loading, $\varepsilon_{\text{rela}}(t) \leq 1.5\%$, we suppose that the number of realizations n is sufficiently large for taking into account a good statistical representativity of heterogeneous textures. The RVE is then determined, and the overall effective elasto-plastic property is defined by the mean value over n realizations, $\overline{Z}(t)$. In addition, the 95% confidence interval is given by $[\overline{Z}(t) - 2D_Z(t), \overline{Z}(t) + 2D_Z(t)]$.

5.4 Homogenization at scale H0

5.4.1 Single crystal model parameters

Elasticity					
	c_{11} (GPa)	c_{12} (GPa)	c_{44} (GPa)		
Cu	167.2	120.7	75.7		
Nb	245.6	138.7	29.3		
	$\widetilde{E}_1$ (GPa)	$\widetilde{\nu}_{12}$	$\widetilde{K}_{23}$ (GPa)	$\widetilde{\mu}_{12}$ (GPa)	$\widetilde{\mu}_{23}$ (GPa)
$(\underset{\sim}{\widetilde{\boldsymbol{C}}})_{\text{H0-Nb}}$	95.9	0.408	185.7	39.5	37.0

Single crystal plasticity						
Isotropic hardening			Kinematic hardening		Viscosity	
Q (MPa)	b	R_0 (MPa)	C (MPa)	D	K (MPa$\cdot$ s$^{1/n}$)	n
6.0	15.0	118.0	4500.0	600.0	2.0	15.0
h_1		h_2	h_3	h_4	h_5	h_6
1.0		4.4	4.75	4.75	4.75	5.0

$\underset{\sim}{\boldsymbol{D}}$ in β-model ($D_{11} = D_{33} + D_{23} - D_{12}$, other components are zero)					
D_{11}	D_{12}	D_{23}	D_{33}	D_{44}	D_{55}
200	200	185	215	70	240

TABLE 5.2: Model parameters used in this work for elasticity, single crystal plasticity and β-model.

In order to estimate the effective behavior of polycrystalline Cu and Nb separately, i.e. the homogenization at H0 scale, Table 5.2 provides the cubic elastic constants $\underset{\sim}{\boldsymbol{c}}$ of FCC Cu and BCC Nb single crystals which are expressed in a reference frame attached to the cubic crystal lattice (Voigt convention). The single crystal elastic moduli $\underset{\sim}{\boldsymbol{C}}^{(r)}$ expressed in a generic global coordinate system can be calculated from $\underset{\sim}{\boldsymbol{c}}$ by applying a rotation. Then the effective elastic tensor $(\underset{\sim}{\widetilde{\boldsymbol{C}}})_{\text{H0}}$ of individual polycrystalline Cu/Nb component is determined by SSC scheme in this work (Appendix B.1). Due to ADB processing, the architecture of Cu-Nb wires, morphological and crystallographic textures are quasi-axisymmetric with respect to x_1. As a result, the effective material behavior of Hi ($i = 0$, 1, 2) is expected to be *transversely isotropic*. The five elastic moduli (refer to Gu et al. (2017)) in $(\underset{\sim}{\widetilde{\boldsymbol{C}}})_{\text{H0}}$ are reported in Table 5.2 for the Nb with a single $\langle 110 \rangle$ fiber texture, aggregates with elongated grains $\ell/d \to \infty$.

In this section, we concentrate on the estimation of the effective elasto-plastic behavior of Cu polycrystals (i.e. H0-Cu). The parameters of Méric-Cailletaud's model (Section

5.3.1) are chosen in such a way that the model response fits the experimental stress-strain curve of specimen for various boundary conditions. Several authors have studied the parameter identification of the recrystallized OFHC Cu (grain size $\sim 100\,\mu m$) for this model: Cu bicrystals in cyclic tension-compression with $\bar{\varepsilon}^{min,max}=\pm 0.1\%$ and $\pm 0.5\%$ (Méric et al., 1994); Cu polycrystals in tensile test with $\bar{\varepsilon}^{max}$ up to 10% and in cyclic loading with $\bar{\varepsilon}^{min,max}=\pm 0.5\%$ (Šiška et al., 2006; Musienko et al., 2007); Textured Cu polycrystals in cyclic loading with $\bar{\varepsilon}^{min,max}=\pm 1.0\%$ (Gérard, 2008).

In the present work, Q, b, C, D and $\boldsymbol{h}$ from Musienko et al. (2007) are used to describe the isotropic and the kinematic hardening for each slip system at the same time. The model responses are found to match satisfactorily with the uniaxial tensile tests for highly hardened OFHC Cu. Furthermore, this parameter combination is also believed to be applicable to cyclic loading where not only isotropic hardening but also kinematic hardening play a role. This is confirmed by preliminary experimental comparison with the data of cyclic tensions with "Bauschinger effect" (Thilly et al., 2009). In addition, the simulation results will not change significantly (PD [5] <5%) by using the combination from Gérard (2008).

Recrystallized OFHC Cu studied in Musienko et al. (2007) exhibit a yield stress σ_y ~10 MPa. In contrast, highly hardened Cu channels of Cu-Nb wires display a σ_y up to 350 MPa (Section 5.2.2). In single crystal plasticity models, apparent aggregate yield stresses σ_y are introduced by setting the CRSS R_0:

$$\sigma_y = M R_0 \tag{5.16}$$

where M denotes the Taylor factor and equals to 3.06 assuming that all the grains in the aggregate deformed uniformly (Stoller and Zinkle, 2000). In order to take the specific $\langle 111\rangle$-$\langle 100\rangle$ fiber textures into account, M=2.97 (i.e. R_0=118 MPa) is chosen in such a way that the σ_y obtained by H0-Cu fits 350 MPa. For the sake of simplicity, R_0 of Cu-0, Cu-1, Cu-2 are chosen as the same value disregarding the small crystallographic texture differences among these components (see Section 5.2.1).

In the case of quasi-static mechanical tests (strain rate $\dot{\varepsilon} < 10^{-2}\,s^{-1}$) at 293 K, strain rate sensitivity of OFHC Cu is negligible (Meyers et al., 1995; Lu et al., 2001). Thus in this work, the parameters controlling viscosity K and n are chosen as $2.0\,MPa\cdot s^{1/n}$ and 15.0 respectively. Throughout this work, let $\dot{\varepsilon}$ equal to $5\times 10^{-5}\,s^{-1}$ in simulations (being the same with the one in ex-situ tests). All the single crystal model parameters are summarized in Table 5.2.

[5] Percentage Difference (PD in %): the absolute difference between two values divided by their average.

5.4.2 H0 results of FEM PH

In this section, the effective elasto-plastic behavior will be predicted by the full-field FEM PH for the polycrystalline Cu components which exhibit a double $\langle 111\rangle$-$\langle 100\rangle$ fiber with $\ell/d \to \infty$. The PH model responses will be taken as a reference for parameter identification of β-model (see Section 5.4.3).

As explained above, the effective behavior of Cu-Nb wires at all scales is expected to be *transversely isotropic*. In order to predict the anisotropic elasto-plastic model responses, four strain directions are subjected successively to RVE as loading conditions:

1. $\langle\varepsilon_{11}\rangle$=2% for the Longitudinal Tensile test (denoted as LT hereafter);
2. $\langle\varepsilon_{22}\rangle$=2% or $\langle\varepsilon_{33}\rangle$=2% for the Transverse Tensile test (TT);
3. $\langle\varepsilon_{23}\rangle$=1.5% for the Transverse Shear test (TS);
4. $\langle\varepsilon_{12}\rangle$=1.5% or $\langle\varepsilon_{31}\rangle$=1.5% for the Longitudinal Shear test (LS).

In Fig. 5.4, the volume average stress-strain curves of polycrystalline Cu-0 (i.e. H0-Cu-0) are plotted successively for the above-mentioned loading conditions: $\overline{\sigma}_{11}$-$\overline{\varepsilon}_{11}$ for the LT test; $\overline{\sigma}_{22,33}$-$\overline{\varepsilon}_{22,33}$ for the TT test; $\overline{\sigma}_{23}$-$\overline{\varepsilon}_{23}$ for the TS test; $\overline{\sigma}_{12,31}$-$\overline{\varepsilon}_{12,31}$ for the LS test. Similar transverse tensile responses along x_2 and x_3 directions (i.e. TT test loaded by $\langle\varepsilon_{22}\rangle$ or $\langle\varepsilon_{33}\rangle$) are expected. However, their deviations are non-negligible (PD$\sim$5%) when considering single realizations due to the limited crystallographic orientations considered, in other words, the 225 grains do not constitute a statistical RVE. In order to take the transverse isotropy into account in each realization, results of TT test is determined by the average model responses along x_2 and x_3 directions. The LS test (loaded by $\langle\varepsilon_{12}\rangle$ and $\langle\varepsilon_{31}\rangle$) is performed in the same way.

In order to investigate the heterogeneities of model responses for both stress and strain, Fig. 5.5 shows the average elasto-plastic behavior of $\langle 100\rangle$ and $\langle 111\rangle$ fiber texture components separately (denoted as H0-Cu-$\langle 100\rangle$ and H0-Cu-$\langle 111\rangle$ respectively). To ensure a statistically sufficiently large equivalent volume (i.e. RVE, see Section 5.3.3.3), 20 realizations are performed for PH to estimate the H0-Cu behavior for the four loading conditions, i.e. a total of 4500 (20×225) crystallographic orientations are taken into account. 95% confidence intervals of the average stress $\overline{\underset{\sim}{\boldsymbol{\sigma}}}$ obtained by these 20 realizations are also plotted in Fig. 5.4 and Fig. 5.5. It is worth noting that, for the sake of clarity, strain uncertainties are only predicted at the ultimate load state (e.g. Fig. 5.5(c)).

5.4.3 Parameter identification of β-model

H0-Cu-0 results obtained by the reference full-field FEM PH will be compared with the ones of mean-field β-model, allowing the identification of the phenomenological tensor

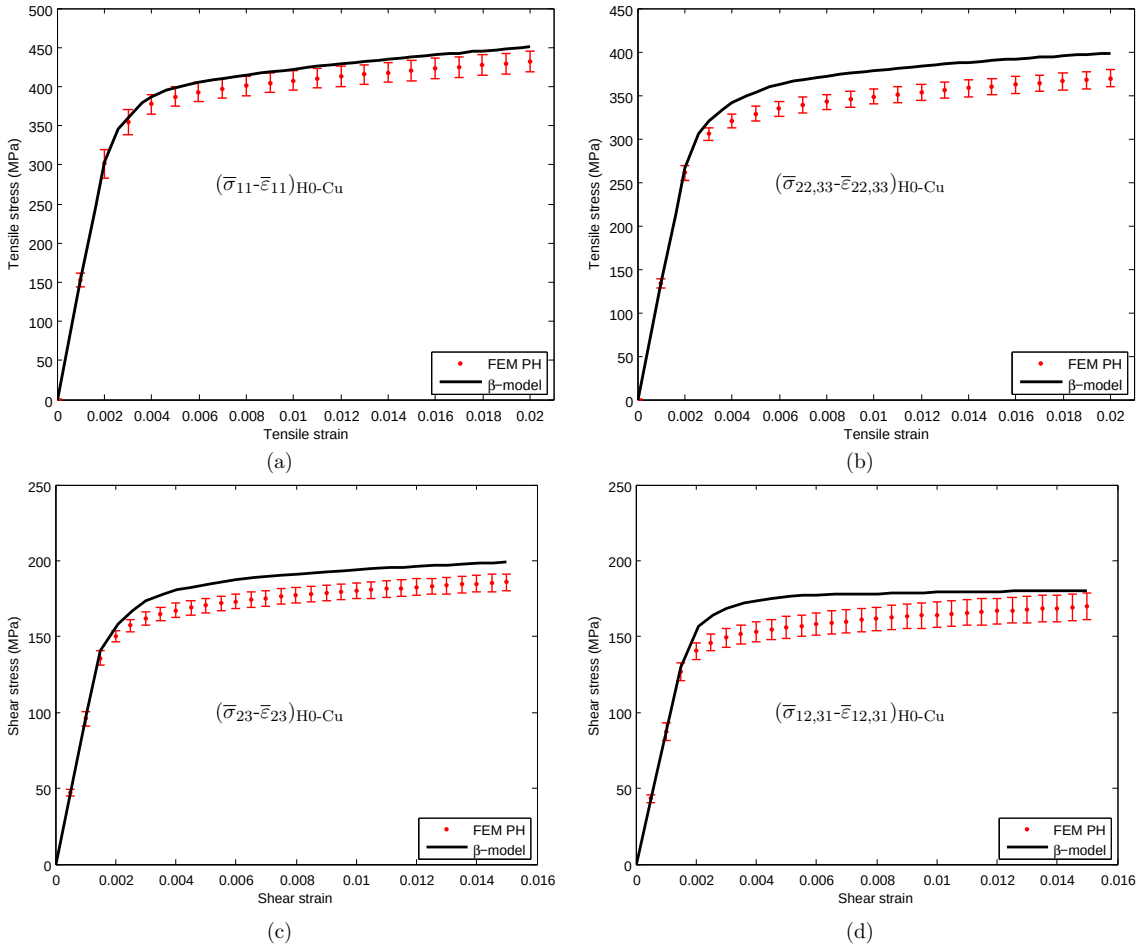

FIGURE 5.4: Effective elasto-plastic behavior of polycrystalline Cu-0 (i.e. H0-Cu-0) predicted by FEM PH and β-model for the: (a) Longitudinal Tensile (LT) test, (b) Transverse Tensile (TT) test, (c) Tranverse Shear (TS) test and (d) Longitudinal Shear (LS) test. See Section 5.4.2 for the conventions of loading condition.

$\underset{\sim\sim}{\boldsymbol{D}}$ (as mentioned in Section 5.3.2). It is found that we can calibrate D_{11}, D_{12}, D_{23} and D_{33} in the LT or TT tests for fitting β-model to the reference. Moreover, D_{44} and D_{55} control respectively TS and LS tests. It should be noticed that, D_{44} and D_{55} can be identified as a unique value. In contrast, the combination of D_{11}, D_{12}, D_{23} and D_{33} is not unique; here D_{11} is chosen as a similar magnitude of D_{55}, leading to the determination of the other components. All the non-zero components in $\underset{\sim\sim}{\boldsymbol{D}}$ are reported in Table 5.2.

As illustrated in Fig. 5.4 and Fig. 5.5, it is remarkable that the PH and the β-model responses at H0 are in a good agreement, not only for the effective polycrystalline behavior, but also for the average behavior of each individual fiber texture components. All these results demonstrate that the fast computational β-model is an efficient homogenization tool for H0. It should be noticed that, unlike the homogenized results of PH, the β-model results display negligible scatting because of the very large number of grain orientations considered (i.e. 4500 orientations, the same as the total number

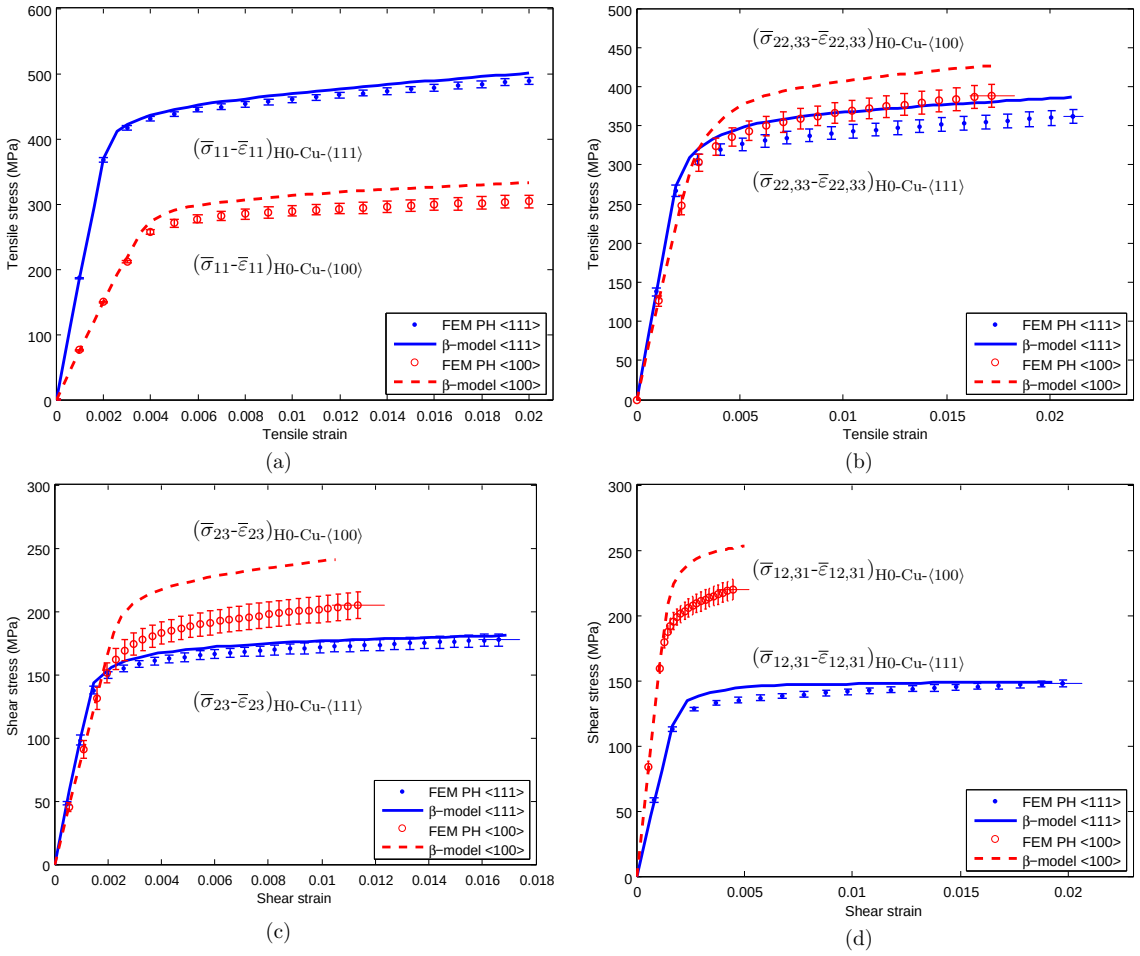

FIGURE 5.5: Individual behavior of $\langle 100\rangle$ and $\langle 111\rangle$ fiber texture of H0-Cu-0 predicted by FEM PH and β-model in the: (a) LT test, (b) TT test, (c) TS test and (d) LS test. Blue stands for the stress-strain curve of $\langle 111\rangle$ fiber texture and red for $\langle 100\rangle$.

of grains considered in PH). On the other hand, we find that the mean-field β-model overestimate hardening compared with the reference, especially for the $\langle 100\rangle$ fiber (see Fig. 5.5). The PD between these models is up to $\sim 15\%$. We have verified that different D_{ij} combinations will not reduce this deviation. Therefore, it is believed this error is mainly caused by the assumption of Kröner (1961) despite the correction by β variables (see B.3 and B.4).

The Cu-i (i=0,1,2) components exhibit different crystallographic textures (Table 5.1). Based on the previous $\underset{\sim}{\boldsymbol{D}}$ for H0-Cu-0, $\underset{\sim}{\boldsymbol{D}}$ can be slightly modified for various components. However, limited improvements are found by using $\underset{\sim}{\boldsymbol{D}}$ calibrated for Cu-1 or Cu-2 with PD<2%, compared with the results using directly $\underset{\sim}{\boldsymbol{D}}$ for H0-Cu-0. For the sake of simplicity, the same $\underset{\sim}{\boldsymbol{D}}$ are chosen throughout this work, as the β-model and the reference FEM PH responses are still in good agreements at H0 scale.

Finally, PH and β-model find consistently that in the LT test, plastic activity occurs in $\langle 100\rangle$ oriented grains at a higher $\overline{\varepsilon}_{11}$ than in $\langle 111\rangle$ ones, as illustrated in Fig. 5.5(a).

This result will receive further attention in experimental comparison (Section 5.6.3).

5.5 H1 and H2 scale transitions for architectured Cu-Nb composites

5.5.1 H1 results

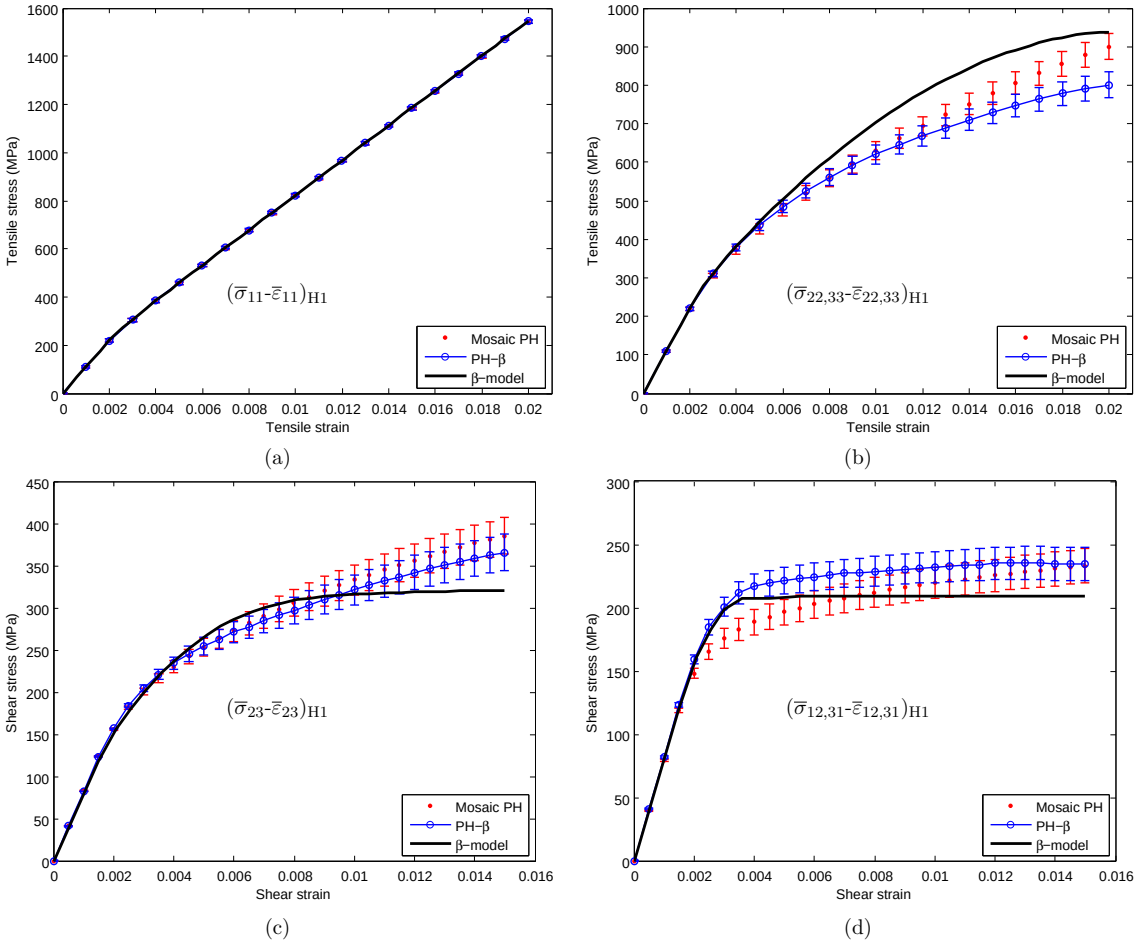

FIGURE 5.6: Effective elasto-plastic behavior at the scale H1 predicted by Mosaic PH, PH-β and β-model for the: (a) LT test, (b) TT test, (c) TS test and (d) LS test.

Section 5.4 dealt with the effective elasto-plastic behavior of polycrystalline Cu (i.e. H0-Cu). The mean-field β-model has been proved to be an efficient homogenization tool based on the comparison with the full-field FEM PH. We now proceed to the homogenization of the assembly of 85^1 elementary continuum long fibers (Fig. 2.2(a)), i.e. H1. Two full-field models, i.e. PH-β and Mosaic PH (Section 5.3.3.2) will be applied to the specific CCA microstructure made of the filamentary patterns with two layers: Nb/Cu-0. As illustrated in Fig. 5.3(a), in the PH-β model, the Cu-0 matrix and the Nb filaments will be assigned to the H0-Cu-0 β-model (Section 5.4) and $(\underset{\sim}{\widetilde{\boldsymbol{C}}})_{\text{H0-Nb}}$ (Table

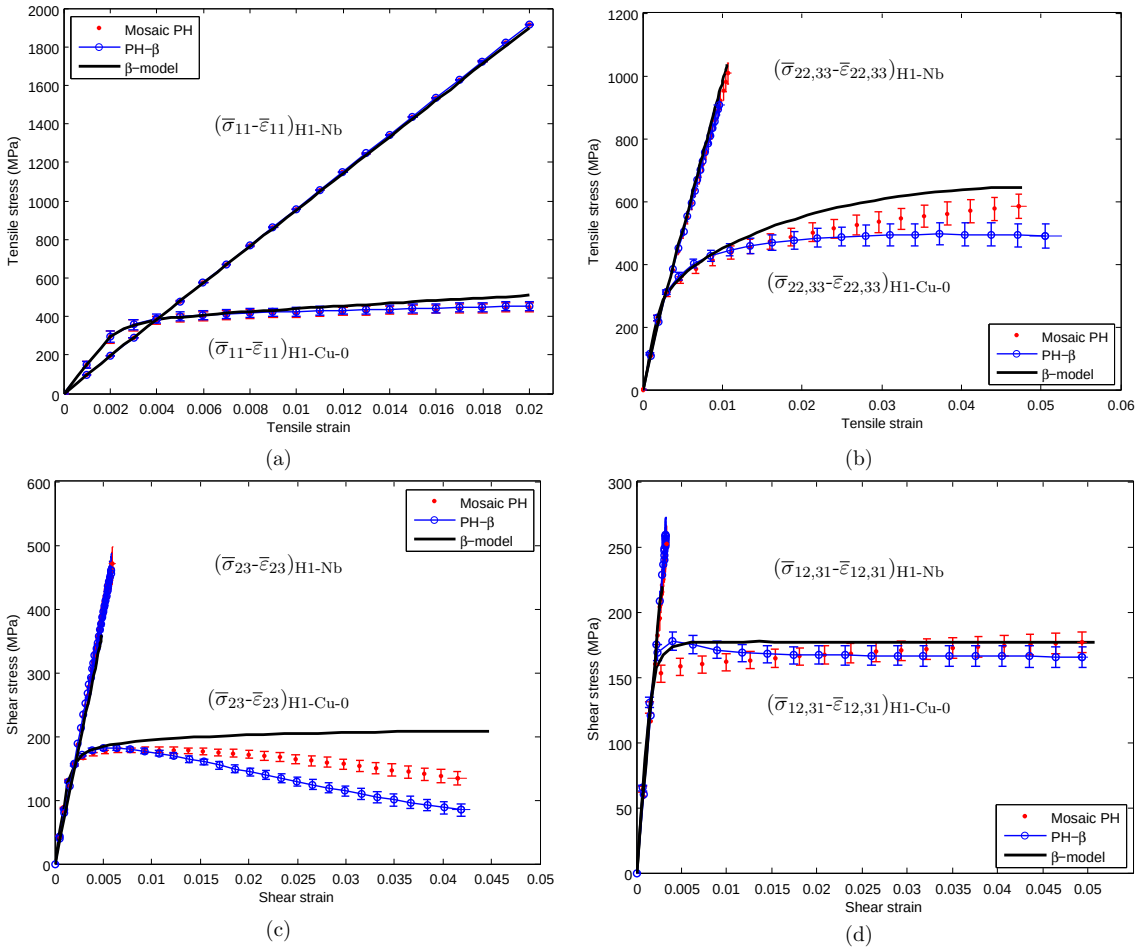

FIGURE 5.7: Individual behavior of Cu-0 and Nb component at H1 predicted by Mosaic PH, PH-β and β-model for the: (a) LT test, (b) TT test, (c) TS test and (d) LS test.

5.2) respectively. In order to validate the models at H1, another Mosaic PH model (Fig. 5.3(c)) will be used. Both PH-β and Mosaic PH assume the Cu-Nb CCA exhibits a periodic distribution. Besides, for saving computational time, one can also use for scale H1 the simple mean-field β-model (denoted H1 β-model hereafter), thus assuming a microstructure consisting of the sole random mixture of Cu and Nb phases. In other words, H1 β-model considers the true volume fractions of Cu-Nb phases for scale H1 (i.e. 25.4% for Cu-0 and 74.6% for Nb), the crystallographic/morphological textures and initial residual stresses, but discards the material architecture.

The statistical RVE for the four loading conditions (i.e. the LT, TT, TS, LS tests) requires 20 realizations for the Mosaic PH model, i.e. 2400 (20×120) crystallographic orientations of Cu-0 considered. Similarly, 20 realizations are performed for the H1 PH-β where in each realization, 120 crystallographic orientations are used in the H0-Cu-0 β-model. In addition, the same RVE size is taken into account for the H1 β-model.

As illustrated in Fig. 5.6, the effective transverse isotropic elasto-plastic behavior of H1 is predicted by the three homogenization models for various loading conditions. For

investigating the heterogeneities of the H1 model responses, Fig. 5.7 shows the average stress and strain of each individual component (denoted as H1-Cu-0 and H1-Nb). The uncertainties of stress/strain obtained by Mosaic PH and PH-β models are also plotted in Fig. 5.6 and Fig. 5.7. It is remarkable that all three models provide generally close results for both effective behavior and the responses of individual components. The deviations among models will receive further attention in Section 5.5.2.

5.5.2 Deviations of model responses at H1

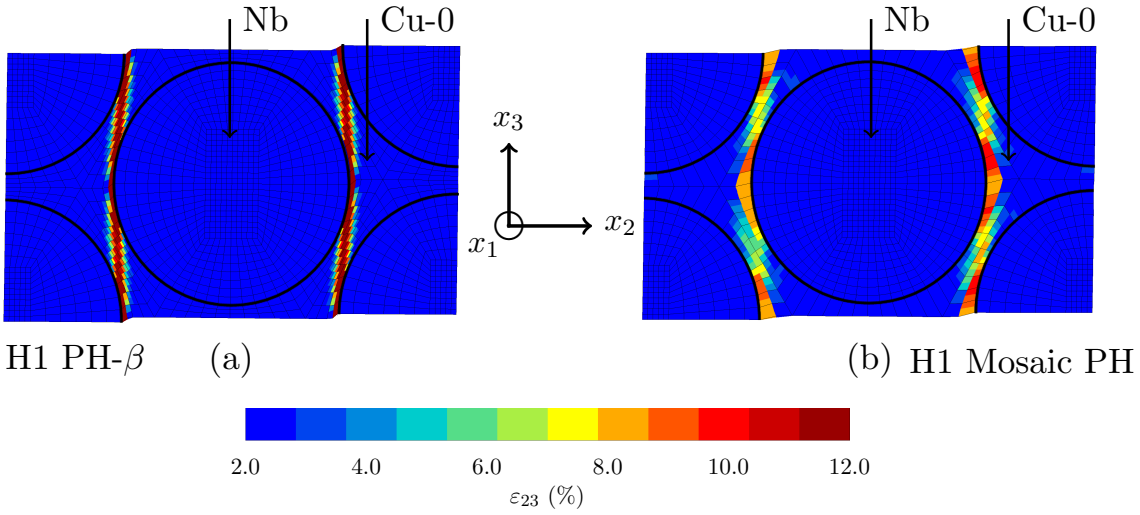

FIGURE 5.8: ε_{23} distribution of (a) the PH-β model and (b) the Mosaic PH at the scale H1 with an effective transverse shear $(\overline{\varepsilon}_{23})_{\text{H1}}$=1.5% imposed in the TS test.

In the previous section, the two full-field Mosaic PH, PH-β and the mean-field β-model are generally in good agreement at H1. However, deviations of these models up to ∼15% is still observed, e.g. in the TS test at H1 (see Fig. 5.6(c) and Fig. 5.7(c)). In this section, we investigate the factors that contribute to the deviations for homogenization of the specific CCA microstructure.

In Fig. 5.7(c) for the TS test, softening of $(\overline{\sigma}_{23})_{\text{H1-Cu-0}}$ is found with the prescribed $(\overline{\varepsilon}_{23})_{\text{H1-Cu-0}}$ for the two full-field models. On the other hand, this softening is not seen for the mean-field β-model responses. To investigate this phenomenon, the ε_{23} strain profile predictions of PH-β and Mosaic PH are presented in Fig. 5.8(a) and Fig. 5.8(b) respectively with the overall H1 CCA imposed by $(\overline{\varepsilon}_{23})_{\text{H1}}$=1.5% in the TS test. This figure demonstrates a strong strain localization in Cu-0 components. We have also verified that higher mesh density leads to a stronger strain localization and stronger $(\overline{\sigma}_{23})_{\text{H1-Cu-0}}$ softening for the full-field models.

Moreover, the H1/H2 model responses depend directly on H0 model results. At H0, β-model overestimates hardening compared with the reference FEM PH (e.g. Fig. 5.5(a)), leading to similar deviations such as in Fig.5.7(a). In addition, disregarding the specific

H1/H2 architecture in the mean-field β-model (see Section 5.5) is believed to be another main factor contributing to the model response deviations.

5.5.3 Iterative scale transition process up to H2

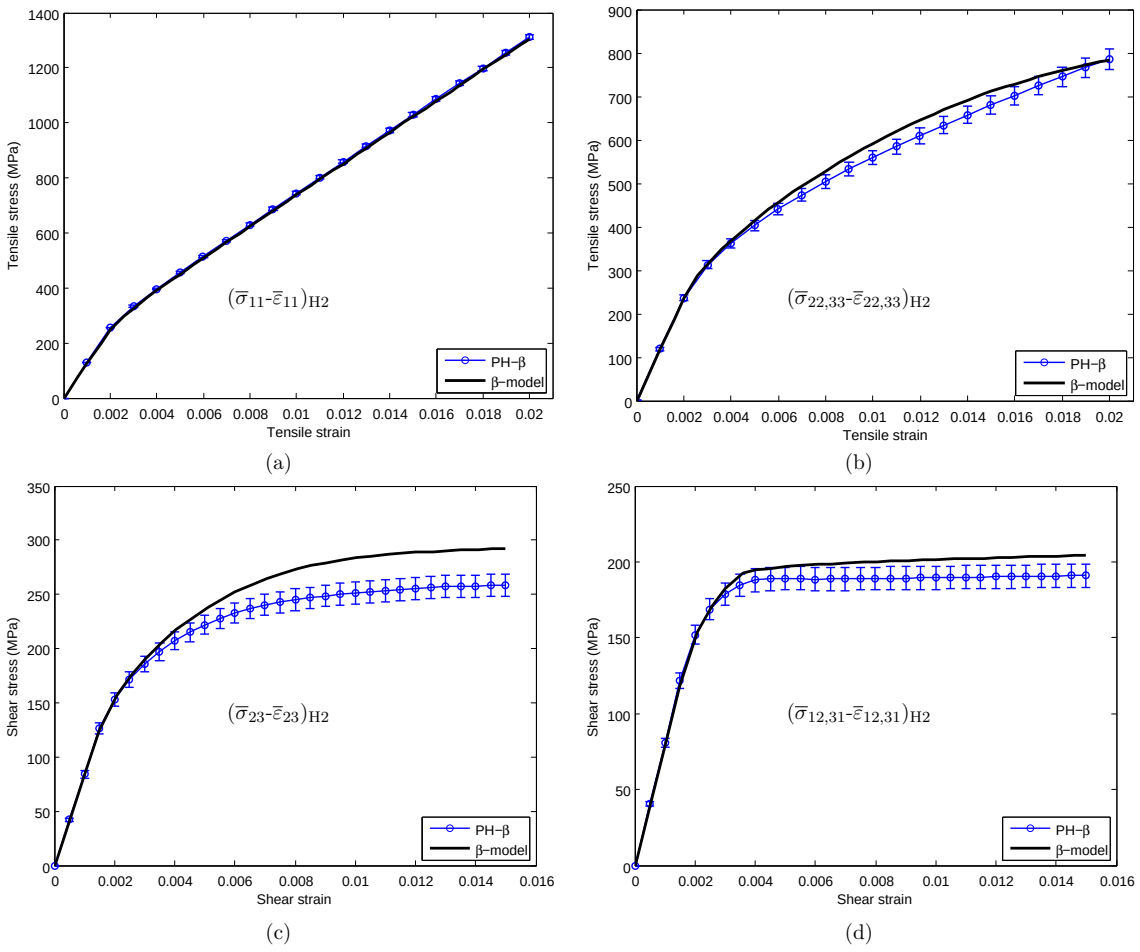

FIGURE 5.9: Effective elasto-plastic behavior at the scale H2 predicted by PH-β and β-model for the: (a) LT test, (b) TT test, (c) TS test and (d) LS test.

At the effective scale H2 (see Fig. 2.2(b)), we suppose that 85 continuum cylinders are composed of two layers: (1) the effective Cu-Nb composite zones containing 85[1] elementary long fibers (i.e. H1 zone); (2) the embedding matrix Cu-1. The main challenge of this work is to account for the elasto-plastic behavior at the different scale transitions. To circumvent this limitation, we propose using the two following multi-scale approaches: PH-β and three-phase H2 β-model.

It was found in Section 5.5.1 that the simple two-phase H1 β-model correctly predicts the elasto-plastic behavior at H1 compared with the reference full-field models. Therefore, the full-field PH-β at H2 takes the two-phase H1 β model and H0-Cu-1 β-model as the local behavior in the H1 Cu-Nb zone and Cu-1 envelope respectively, as illustrated in Fig. 5.3(b). The scale transition is then performed by PH-β approaches, leading

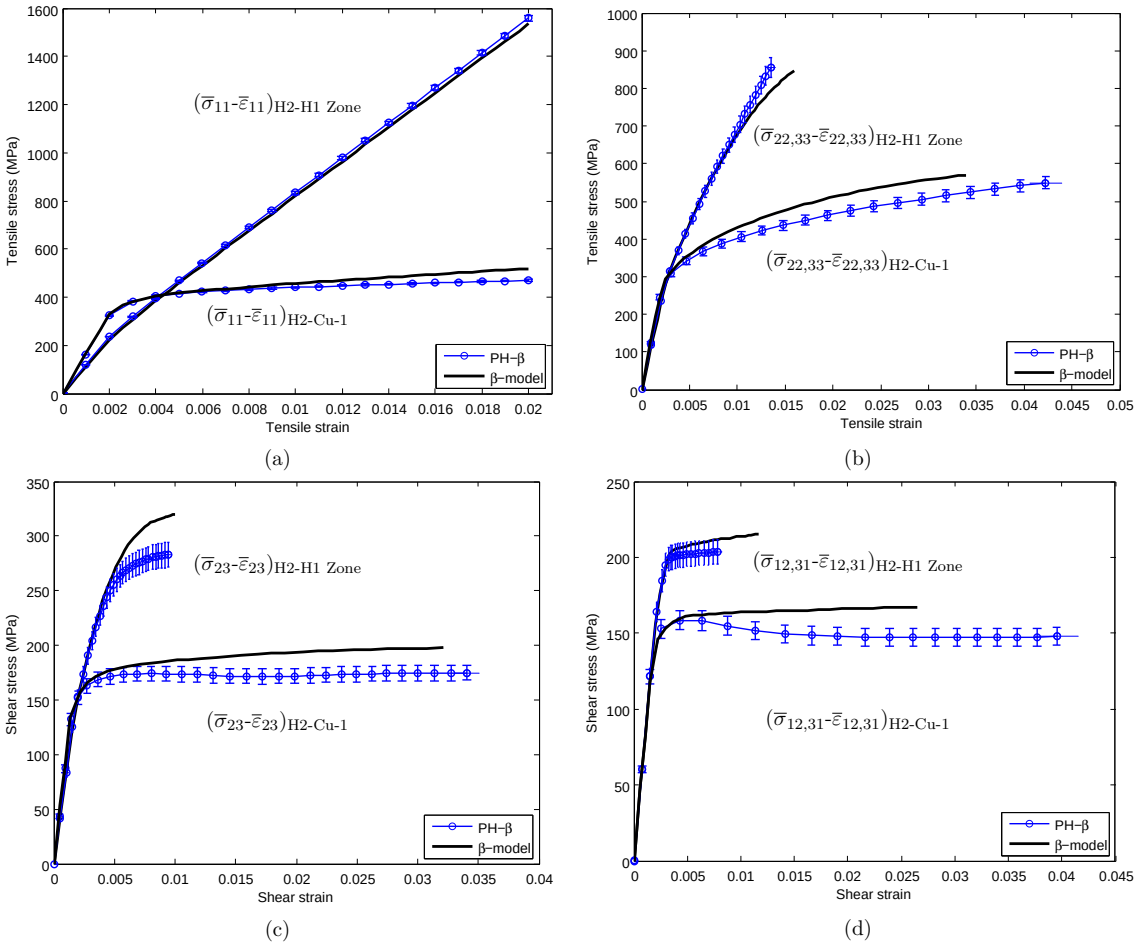

FIGURE 5.10: Individual behavior of the H1 Cu-Nb composite zone and Cu-1 component at H2 predicted by PH-β and β-model for the: (a) LT test, (b) TT test, (c) TS test and (d) LS test.

to the effective elasto-plastic behavior for the assembly of 85^2 elementary long fibers. Moreover, as mentioned in Section 5.5.1, the three-phase (i.e. Nb, Cu-0 and Cu-1) H2 β-model can be used to predict the effective H2 elasto-plasticity without considering anymore the specific architecture of the real specimen.

The effective behavior at H2 and the individual H1 zone/Cu-1 responses are plotted in Fig. 5.9 and Fig. 5.10 respectively for various loading conditions. For avoiding a too long CPU time in each realization of H2 PH-β, 240 crystallographic orientations in H1 β-model (120 for Cu-0 and 120 for Nb) and 120 orientations in H0-Cu-1 β-model are used. In order to ensure statistical RVE, 20 realizations are performed for H2 PH-β. The same number of crystallographic orientations is also considered for H2 β-model. The full-field PH-β and mean-field β-model still provide close results at H2. The PD between them is $\sim$ 15%, and the main factors that contribute to these deviations are believed to be similar to H1 (analyzed in Section 5.5.2).

5.6 Modeling strategies and experimental comparison

The focus of the present work is to develop a multi-scale modeling to predict the mechanical behavior of Cu-Nb wires. At first in Section 5.6.1, a modeling strategy up to the H2 scale is presented. Then in Section 5.6.2, (1) the ex-situ tensile test and (2) the in-situ neutron diffraction tensile test (Medy, 2016) will be briefly described. In Section 5.6.3, the structural problem S2 will be considered for experimental comparison to demonstrate predictive capabilities of our models. Finally, these models will provide a quantitative understanding of the stress and related elastic strain evolution during uniaxial loading test.

5.6.1 Modeling strategies for Cu-Nb wires

In Section 5.5, three homogenization models were applied to perform the scale transitions up to H1/H2 for the architectured Cu-Nb nano-composite wires. The β-model assumes a random mixture of Cu and Nb phases; the Mosaic PH and PH-β both take into account the specific CCA microstructure with periodic distribution. As shown in Fig. 5.6, Fig. 5.7, Fig. 5.9 and Fig. 5.10, these models provide close results (PD $\sim$15%) at the H1 and H2 scales, in spite of the very different approximations of geometry. Furthermore, the total CPU time of the β-model, Mosaic PH and PH-β is on the order of 1:100:1000 respectively with the same conditions considered. As a conclusion, the β-model is demonstrated to be an efficient homogenization model for Cu-Nb wires.

5.6.2 Ex-situ and in-situ neutron diffraction tensile experiments

Due to the high hardness of Cu-Nb wires (Thilly et al., 2002a), slip between the specimen and the grips was often observed during tensile tests (Vital, 2006; Medy, 2016), leading to a difficulty in strain measurement for the ex-situ experiments. In order to determine the strain along x_1 with a high accuracy, we applied an optical method that employs tracking and image registration techniques at Centre des Matériaux Mines ParisTech. Fig. 5.11(a) shows the experimental data of a tensile test carried out with a N=85^2 Cu-Nb Filamentary wire (diameter 0.29 mm). Uniaxial tensile test along the wire direction x_1 was performed with a strain rate $\dot{\varepsilon} \approx 5\times10^{-5}\,\mathrm{s}^{-1}$ at 293 K.

This test was performed as follows: (1) specimens were prepared by painting black speckle patterns on a white background; (2) digital images were recorded by one fixed CCD camera during tensile tests; (3) changes in images (i.e. strains) were determined by 2D DIC methods (Digital Image Correlation, e.g. mentioned in Pan et al. (2009)). The data processing of 2D DIC leads to an uncertainty $< \pm0.02\%$ for the longitudinal strain. This uncertainty is not plotted in Fig. 5.11(a) due to its small value. In addition, the stresses are computed from the tensile force and their uncertainties are estimated

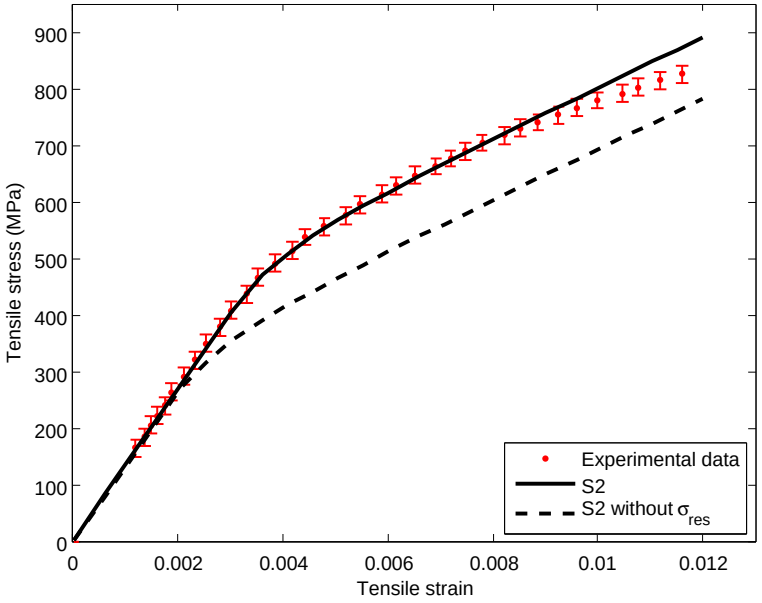

FIGURE 5.11: Comparison of experimental data with model predictions for N=85[2] Cu-Nb Filamentary wires: (a) Ex-situ tensile test $(\overline{\sigma}_{11}\text{-}\overline{\varepsilon}_{11})_{S2}$ (sample diameter: 0.29 mm); (b) In-situ neutron diffraction tensile test (sample diameter: 2.10 mm), macroscopic longitudinal stress $(\sigma_{11})_{S2}$ vs. longitudinal mean elastic trains of individual $\langle 111\rangle$ Cu, $\langle 100\rangle$ Cu and $\langle 110\rangle$ Nb fiber textures, i.e. $(\varepsilon_e^{\langle 111\rangle Cu})_L$, $(\varepsilon_e^{\langle 100\rangle Cu})_L$ and $(\varepsilon_e^{\langle 110\rangle Nb})_L$. The dashed line in (a) shows the model prediction without taking into account the initial residual stresses.

as ±15 MPa which is caused by stress relaxation during tensile tests. Moreover, as illustrated in Fig. 5.11(a) for the Cu-Nb wire, the macroscopic longitudinal Young's modulus E_1 and yield stress σ_y along the wire direction x_1 are found respectively to be ∼140 GPa and ∼650 MPa (refer to Thilly et al. (2009) for yield criterion).

Besides the ex-situ tensile tests, an in-situ neutron diffraction tensile experiment was also performed by Medy (2016) on the N=85[2] Cu-Nb Filamentary wires with a diameter of 2.10 mm at 6T1 diffractometer of Orphée-LLB (CEA Saclay, France). The strain rate $\dot{\varepsilon}$ was $10^{-5}\,s^{-1}$ and the temperature was 293 K. The detailed information on the setup can be found in Medy (2016). By analyzing the shift of $\{hkl\}$ Bragg peaks, neutron diffraction provides information about the mean elastic strain within the diffracting volume. The diffraction volume is constituted by all grains fulfilling Bragg conditions, i.e. exhibiting an $\{hkl\}$ plane perpendicular to diffraction vector $\underline{\boldsymbol{g}}$. Medy (2016) took advantage of the strong crystallographic texture (see Table 5.1) of the specimen for the analysis: for Cu, the double $\langle 100\rangle$ and $\langle 111\rangle$ fibers lead to respectively a significant proportion of $\{200\}$ and $\{111\}$ planes perpendicular to the wire axis x_1; similarly for Nb, the strong $\langle 110\rangle$ fibers lead $\{220\}$ planes perpendicular to x_1. Taking the diffraction vector $\underline{\boldsymbol{g}} \,/\!/\, x_1$ and performing diffraction on these lattice planes allow to estimate the longitudinal mean elastic strain, i.e. $(\varepsilon_e^{\langle 111\rangle Cu})_L$, $(\varepsilon_e^{\langle 100\rangle Cu})_L$ and $(\varepsilon_e^{\langle 110\rangle Nb})_L$, within the corresponding diffraction volumes, for individual $\langle 100\rangle$ Cu, $\langle 111\rangle$ Cu and $\langle 110\rangle$ Nb fibers respectively. Fig. 5.11(b) reports the above-mentioned individual fiber texture lattice evolution during in-situ experiments in terms of the applied tensile stress $(\overline{\sigma}_{11})_{S2}$. The uncertainty of $(\varepsilon_e)_L$ is estimated as about ±0.05%, as determined by peak fitting. In addition, stress relaxation during the in-situ experiment leads to an uncertainty of ±15 MPa for the applied tensile stress $(\overline{\sigma}_{11})_{S2}$ (refer to Medy (2016) for the detailed estimation of stress/strain uncertainty and their exact values).

It is worth noting that stress-free strains $\underset{\sim}{\boldsymbol{\varepsilon}}_0$ exist, as mentioned in Section 5.2.3. However, the exact $\underset{\sim}{\boldsymbol{\varepsilon}}_0$ values of the studied Cu-Nb wires remain unknown due to the lack of the $\{hkl\}$ Bragg peak reference position (Medy, 2016). The lattice strain data of individual fiber textures are thus initialized as zero, as shown in Fig. 5.11(b).

5.6.3 Structural problem S2

As illustrated in Fig. 2.2(c), a real Cu-Nb wire can be seen as a single cylinder-shaped structure S2 at macro-scale. The structural problem S2 will be solved by FEM to compute: (1) the effective elasto-plastic behavior $(\sigma_{11}$-$\varepsilon_{11})_{S2}$; (2) the mean elastic strain ε_e along the direction of the diffraction vector $\underline{\boldsymbol{g}}$ for each individual fiber texture. A cylinder-shaped FE mesh (c3d20r elements) is used here for the structural problem S2, readers can refer to Fig. 4.12(b) for a similar mesh with two layers. The elasto-plastic properties of the inner Cu-Nb H2 zone and the external polycrystalline Cu-2 jacket are assigned to H2 β-model (Section 5.5.3) and H0-Cu-2 β-model (Section 5.4)

respectively. A normal tensile displacement is prescribed on the two terminal sections of this S2 specimen. From the computed axial force, the effective S2 behavior $(\sigma_{11}\text{-}\varepsilon_{11})_{S2}$ is obtained.

Component	Nb	Cu-i (i=0,1,2)
$(\sigma_{res})_{11}$	+250 MPa	-200 MPa
$(\varepsilon_0)_{11}$	0.26%	-0.12%
$(\varepsilon_0)_{22,33}$	-0.104%	0.040%

TABLE 5.3: Initial residual stresses σ_{res} and stress-free strain ε_0 of individual component for Cu and Nb polycrystals. These values are chosen in such a way that model results fit statistically experimental data. The initial residual stresses σ_{res} are along the wire direction x_1: Nb in tension and Cu in compression. Here, the two samples with different diameters are assumed to exhibit the same σ_{res} and ε_0 in each component.

It is worth noting that both initial residual stress $\underset{\sim}{\boldsymbol{\sigma}}_{res}$ and yield stress σ_y^{Cu} of Cu components play a significant role for the apparent yield stress of Cu-Nb wires, as shown by the model response without considering $\underset{\sim}{\boldsymbol{\sigma}}_{res}$ in Fig. 5.11(a). However, the exact values of $\underset{\sim}{\boldsymbol{\sigma}}_{res}$ for the N=85[2] Cu-Nb Filamentary wires are not known yet. In the present work, $(\sigma_{res})_{11}$ in the Nb phases is assumed to be +250 MPa in tension which is chosen as the same value of the N=55[4] type of Cu-Nb wires (mentioned in Section 5.2.3). To ensure macroscopic equilibrium of Cu-Nb wires, i.e. $(\overline{\underset{\sim}{\boldsymbol{\sigma}}})_{S2}=\underset{\sim}{\mathbf{0}}$ or $(\overline{\underset{\sim}{\boldsymbol{\sigma}}}_{res})_{S2}=\underset{\sim}{\mathbf{0}}$, we estimate $(\sigma_{res})_{11}$=-200 MPa for Cu components. In addition, $\underset{\sim}{\boldsymbol{\sigma}}_{res}$ in transverse directions and in shear directions are assumed to be zero. It will be shown that this approximation is sufficient to predict the elasto-plastic behavior for Cu-Nb wires based on the available mechanical data performed by tensile load along x_1. Furthermore, stress-free strain $\underset{\sim}{\boldsymbol{\varepsilon}}_0$ can be computed based on the chosen $\underset{\sim}{\boldsymbol{\sigma}}_{res}$ (Section 5.2.3). All the related nonzero components in $\underset{\sim}{\boldsymbol{\sigma}}_{res}$ and $\underset{\sim}{\boldsymbol{\varepsilon}}_0$ are reported in Table 5.3. Taking $\underset{\sim}{\boldsymbol{\sigma}}_{res}$ into account, model response display a good agreement with the ex-situ tensile data, as illustrated in Fig. 5.11(a).

Nevertheless, some arguments in Medy (2016) suggest that $(\sigma_{res})_{11}$ in large Cu channels may not be as high as -200 MPa, as seen from preliminary neutron diffraction tests. Therefore, an axial compression value of -100 MPa for Cu components will also be used. In this case, a tension +125 MPa for Nb is determined to fulfill a zero macroscopic $\underset{\sim}{\boldsymbol{\sigma}}_{res}$. It is found in this case, if we let σ_y=450 MPa for Cu components, the S2 homogenization display the same results with the ones using the parameters in Table 5.1, Table 5.2 and Table 5.3. This confirms the formula proposed in Vidal et al. (2009): the sum of σ_y^{Cu} and $|(\sigma_{res}^{Cu})_{11}|$ equal to a constant in Cu-Nb wires, here $\sigma_y^{Cu}+|(\sigma_{res})_{11}^{Cu}| \approx 550$MPa. Further X-ray/neutron diffraction experiments for investigating $(\sigma_{res})_{11}$ are still in preparation to determine more precisely the $(\sigma_y)^{Cu}$.

According to Upadhyay et al. (2016); Gu et al. (2017), a comparison with diffraction data requires to (1) compute the mean stresses acting on H2 zone and Cu-2 as a function of tensile strain; (2) compute the corresponding stress and strain concentration within the

grains, by means of β-model in H2 zone and Cu-2 separately; (3) isolate the diffraction volume and calculate the mean elastic strain along the direction of diffraction vector $\underline{\boldsymbol{g}}$; (4) gather the mean elastic strains for all individual fiber textures. In order to do experimental comparison, the mean elastic strains of model prediction are initialized as zero. Obtained results are shown in Fig. 5.11(b), with again an excellent match to all available data.

From these comparisons with experimental results for Cu-Nb wires, one can conclude that the proposed elasto-plastic models not only predict the correct effective behavior, but also provide a good estimation of the stress and strain distributions within Cu and Nb grains; the mechanical scale transition is thus well captured. The deviations between experiment and theory are believed to be caused by the following reasons: (1) Approximations in β-model compared with the reference full-field models; (2) Disregarding different crystallographic textures of the studied wires with different diameters (Section 5.2.1).

Furthermore, both experiments and theory show that plastic activity occurs in $\langle 100 \rangle$ oriented grains at a higher macroscopic stress than in $\langle 111 \rangle$ grains in tensile loading along the wire direction. A similar phenomenon is observed for Cu polycrystals at H0 (see Fig. 5.5(a) in Section 5.4.3).

5.7 Conclusions

This work focuses on multiscale modeling of the elasto-plastic behavior of architectured and nanostructured Cu-Nb composite wires. The main conclusions of this work are the following:

1. *Hierarchical homogenization strategy.* As the specimens exhibit several characteristic scales, an iterative scale transition elasto-plastic homogenization approach is proposed considering the specific texture and architecture of Cu-Nb wires.

2. *Full field vs. mean field method.* In order to investigate the links between the effective material behavior and the wire microstructure, full-field finite element homogenization is first carried out. A mean-field β-model is then proposed for saving computational time and performing iterative scale transition steps. It is found the full-field and mean-field model responses are in a good agreement.

3. *Model responses vs. ex-situ/in-situ experimental data.* Mechanical modeling is experimentally validated by both macroscopic tensile tests and in-situ neutron diffraction data where the mean elastic strains are measured in the individual copper and niobium phases.

4. *Plastic activity in different Cu/Nb phases.* In Cu-Nb wires, polycrystalline Cu exhibits a double $\langle 100 \rangle$-$\langle 111 \rangle$ fiber texture. Experiments and theory find consistently that plastic activity occurs in $\langle 100 \rangle$ oriented grains at a higher macroscopic stress than in $\langle 111 \rangle$ grains in tensile loading along the wire direction.

5. *Initial residual stresses.* Multi-scale modeling in this work considers the initial residual stresses which is related to material processing as measured from the experiments. Initial residual stresses show a significant effect on yield stresses of Cu-Nb wires.

5.8 Résumé du chapitre en Français

Ce chapitre se concentre sur la modélisation multi-échelles du comportement élasto-plastique de fils composites Cu-Nb nanostructurés et architecturés. Ces matériaux contiennent un assemblage de 85^2 motifs de Nb/Cu-0 (c.-à.-d. fils de Cu-Nb filamentaires, N=85^2) et les matrices multi-échelles de Cu (c.-à.-d. Cu-1 et Cu-2). À la plus petite échelle (c.-à.-d. au niveau des grains), ces fils composites Cu-Nb sont composés de Cu polycristallin et de Nb polycristallin. Les textures cristallographiques et morphologiques de chaque composante individuelle de Nb/Cu-i (i=0,1,2) sont caractérisées par EBSD dans Medy (2016). Les phases de Cu présentent une double-texture de fibre ⟨100⟩-⟨111⟩, tandis qu'une texture de fibre unique ⟨110⟩ est constatée dans Nb. La texture morphologique est caractérisée par des grains fortement allongés le long de l'axe du fil.

Afin de modéliser *le comportement élasto-plastique anisotrope* de fils Cu-Nb, l'un des défis est de tenir compte la non-linéarité aux différentes transitions d'échelle. Deux modèles multi-échelles sont appliqués ici : la méthode des éléments finis (MEF) en champs complets supposant une microstructure périodique (que nous appelons HP pour Homogénéisation Périodique); la règles en β en champs moyens prenant en compte un mélange aléatoire des phases de Cu ou/et de Nb. Pour étudier les liens entre le comportement effectif élasto-plastique et la microstructure, le modèle HP est d'abord appliqué. La règle en β est ensuite proposé pour économiser du temps de calcul et pour réaliser la transition des échelles itératives en tenant compte l'élasto-plasticité. En outre, le modèle de Méric-Cailletaud (Méric et al., 1991) est choisi pour décrire la loi élasto-visco-plastique à l'échelle du monocristal. Ce travail prend en compte également les contraintes résiduelles initiales créées par l'élaboration des matériaux et mesurées expérimentalement par Vital (2006). Les comparaisons des réponses de modèle nous permettent de déterminer la meilleure stratégie de modélisation multi-échelles pour déterminer le comportement effectif élasto-plastique de fils Cu-Nb de manière fiable. Enfin, les résultats sont aussi comparés avec les données expérimentales ex-situ/in-situ disponibles dans Medy (2016).

Les principales conclusions de ce chapitre sont les suivantes :

1. *Stratégie d'homogénéisation hiérarchique.* Comme les spécimens présentent plusieurs échelles caractéristiques, une approche itérative d'homogénéisation elasto-plastique est proposée en tenant compte de la texture et de l'architecture spécifiques de fils Cu-Nb.

2. *Champs complets vs. champs moyens.* On trouve que les réponses des modèles en champs complets (c.-à.-d. HP) et en champs moyens (c.-à.-d. la règle en β) sont en bon accord avec des écarts ∼15%.

3. *Réponses des modèles vs. données expérimentales ex-situ/in-situ.* La modélisation est validée expérimentalement à la fois par des essais de traction macroscopique

et des données de diffraction in-situ des neutrons où les déformations élastiques moyennes dans les phases individuelles de Cu ou de Nb sont mesurées.

4. *Activités plastiques dans différentes phases de Cu/Nb.* Les expériences in-situ et les calculs numériques montrent tous les deux que l'activité plastique se produit dans les grains orientés $\langle 100 \rangle$ à une contrainte macroscopique plus élevée que dans les grains orientés $\langle 111 \rangle$. En revanche, on constate que Nb polycristallin avec une seule texture de fibre $\langle 110 \rangle$ ne présente pas de plasticité.

5. *Contraintes résiduelles initiales.* La modélisation multi-échelles montre que les contraintes résiduelles initiales affectent significativement la limite d'élasticité de fils Cu-Nb.

Pour les fils Cu-Nb filamentaires $N{=}85^2$ étudiés dans ce chapitre, on suppose que les différentes composantes de Cu présentent une limite d'élasticité similaire ($\sim$350 MPa). Cependant, les "canaux fins" de Cu-0 (largeur des canaux $\delta{=}310$ nm) dans le conducteur de diamètre 0,29 mm montrent probablement une limite d'élasticité 500 MPa en raison de *l'effet de taille* (Thilly et al., 2009). Cet effet n'est pas encore considéré, car la fraction volumique de Cu-0 est relativement faible ($\sim$15%). On pense cependant que l'effet de taille doit être pris en compte pour d'autres types de fils de Cu-Nb (par exemple, fils filamentaires N=85^3) qui contiennent une fraction volumique plus grande de Cu fin, avec une largeur nanométrique des canaux.

Chapter 6

Conclusions and opportunities

6.1 Conclusions

Nanostructured and architectured copper niobium composite wires are excellent candidates for winding coils used for the generation of very intense pulsed magnetic fields (>90T) as they combine both high strength and high electrical conductivity. The accumulative drawing and bundling process used to elaborate these Cu-Nb wires leads to severe plastic deformations of the composite material and generates a multiscale, architectured and nanostructured microstructure with a pronounced fiber crystallographic texture and elongated grain shapes along the wire axis. This thesis is aiming at modeling the effective electrical conductivity and elasto-plastic mechanical behavior of the composite wires, based on multi-scale approaches. In order to investigate the link between the effective material behavior and the wire microstructure, several homogenization schemes, either based on mean-field or full-field methods, have been applied. The different methods account for different microstructural content and thus estimate the microstructural features of importance for the measured behavior. Mean-field approaches, assuming a random microstructure, are based on the Self-Consistent scheme (standard or generalized versions) for conductivity and elastic homogenizations. As for the elasto-plastic behavior, the so-called β-model has been used thanks to its high computational efficiency and its ability for scale transitions; this model has been extended to polycrystals with initial residual stress field. Mean-field results are systematically compared with a Finite Element approach assuming a periodic microstructure. As specimens exhibit many characteristic scales, ranging from nanometers up to millimeters, an iterative scale transition strategy has been developed to bridge the wire scale (mm) with the grain scale (nm). Model results have been compared with available experimental data such as longitudinal and transverse effective conductivities, overall mechanical response, as well as X-ray and neutron diffraction during in-situ specimen deformation. The main results are summarized as follows:

Concerning the electrical conductivity:

- The effective longitudinal conductivity (i.e. the homogenized conductivity along the wire direction) can be estimated with a great accuracy.
- The effective transverse conductivity predicted by the full-field and mean-field approaches are in very good match with each other. This result provides an accurate estimation of the behavior at the largest scale, obtained by iterative scale transition steps.
- When accounting for size effects (mean free path of electrons), the predicted conductivities are in very good agreement with experimental data. The effect of wire diameter is well captured.
- The obtained ratio between effective longitudinal and transverse conductivities is $\sim$1.3 due to the specific fiber-reinforced microstructure of Cu-Nb wires.

Concerning the elasto-plastic behavior:

- At all scales, mean-field and full-field models predict very similar (deviation $<3\%$) effective elastic behavior. The crystallographic texture plays an important role in the effective elastic moduli of Cu-Nb wires. Morphological texture has a significant influence on the elastic properties for the double $\langle 111 \rangle$-$\langle 100 \rangle$ fiber texture observed in Cu, but its effect is less pronounced for the single $\langle 110 \rangle$ fiber of Nb.
- The elasto-plastic response predicted by the β-model has been compared with full-field reference solutions. A good agreement is obtained at all scales (deviation $\sim$15%). Taking into account a realistic field of residual stresses, the predicted elasto-plastic response is found in good agreement with the experimental effective behavior but also with neutron diffraction data during in-situ mechanical test for which the elastic strains are measured for individual copper and niobium phases.
- Experiments and theory find consistently that plastic activity occurs in $\langle 100 \rangle$ orientated grains at a higher macroscopic stress than in $\langle 111 \rangle$ grains, when the wire is deformed under tension along the wire direction.

The general agreement among the model responses allows suggesting the best strategy to estimate reliably the effective electrical and elasto-plastic behavior of Cu-Nb wires, and save computational time.

6.2 Future work and opportunities

The present work can be continued along the following directions:

- *Temperature effect of electrical problems:* Cu-Nb wires are used in winding coils for generation of intense pulsed magnetic fields (>90 T) at 77K, while the present work has been limited to room temperature 293K in Chapter 3. Therefore, theory and experiment should be extended taking various temperatures into account.

- *Size effect:* For the N=85^2 Cu-Nb Filamentary wires studied in Chapter 5, the various Cu components are assumed to exhibit a similar yield stress (i.e. 350 MPa). However, "fine" Cu-0 channels (channel width δ=310 nm) in the conductor with a diameter of 0.29 mm probably display a higher yield stress up to 500 MPa due to size effect (Thilly et al., 2009). This effect was not considered in this chapter, because the volume fraction of Cu-0 is relatively small (∼15%). On the other hand, size effect need to be taken into account for other types of Cu-Nb wires (e.g. N=85^3 Cu-Nb Filamentary wires) which contains a larger volume fraction of Cu with nanoscale channel width.

- *Initial residual stresses:* The measurement of residual stresses needs to be carried out carefully by X-ray/neutron diffraction for the Cu-Nb Filamentary wires studied in Chapter 5. Furthermore, simulations of material processing should also help studying quantitatively the residual stresses in different directions. This is important point, as we have shown that the initial residual stress state significantly affect the wire behavior.

- *Various loading conditions:* In order to fully validate the mechanical models, ex-situ/in-situ experiments could be performed for various loading conditions, such as the TT (Transverse Tensile) test and torsion. In addition, one could for example perform compression tests along the transverse direction on specimens machined by FIB-SEM.

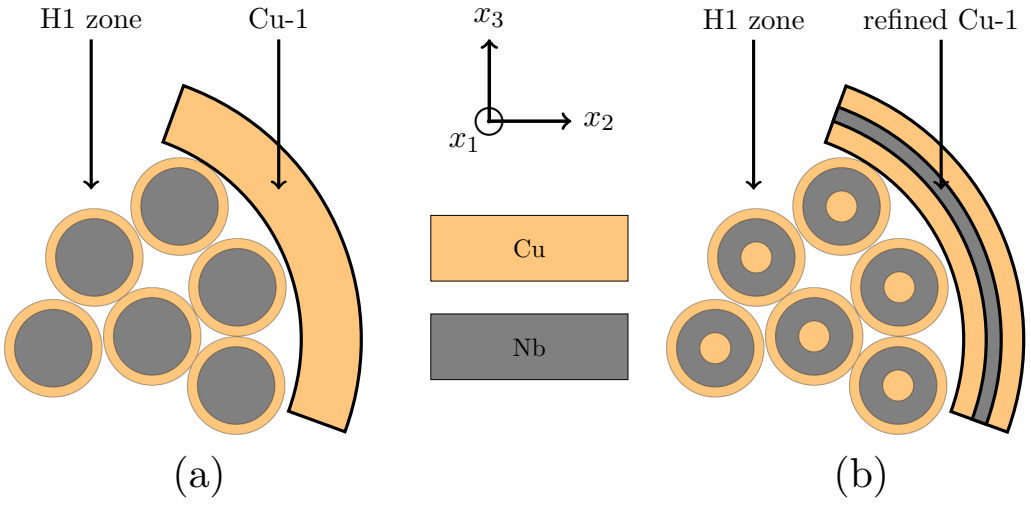

FIGURE 6.1: (a) Cu-Nb Filamentary wires in Thilly (2000); Medy (2016); (b) Strategy of material improvement for Cu-Nb wires proposed in this work.

Finally, the theoretical models can be used to optimize the microstructure parameters in the fabrication process of Cu-Nb wires. According to Thilly (2000), the effective longitudinal electrical conductivity and longitudinal yield stress play an important role in magnetic field generation for winding coils. Thus, there two properties should be improved.

Different types of Cu channels are present in Cu-Nb wires. In Chapter 4 and Chapter 5, we denote (1) the Cu channels with a width δ larger than a few micrometers by "large" Cu (i.e. Cu-L); (2) the Cu channels with a width δ in the sub-micrometer range by "fine" Cu (i.e. Cu-F). Cu-L exhibits typical highly hardened Cu property with a conductivity of $\sim 0.568\,\mu\Omega^{-1}\mathrm{cm}^{-1}$ (at 293 K) and a yield stress of $\sim$350 MPa; On the other hand, due to size effect, Cu-F (e.g δ=500 nm) exhibits a conductivity of $\sim 0.537\,\mu\Omega^{-1}\mathrm{cm}^{-1}$ and a yield stress of $\sim$450 MPa. In addition, Nb channels displays a high yield stress (typically > 2 GPa) while a low conductivity $0.060\,\mu\Omega^{-1}\mathrm{cm}^{-1}$.

The effective longitudinal conductivity $\widetilde{\sigma}_{\mathrm{L}}$ of Cu-Nb wires can be determined by the rule of mixture (Section 3.4.1):

$$\widetilde{\sigma}_{\mathrm{L}} = f^{(\text{Cu-L})}\,\sigma_{\mathrm{L}}^{(\text{Cu-L})} + f^{(\text{Cu-F})}\,\sigma_{\mathrm{L}}^{(\text{Cu-F})} + f^{(\text{Nb})}\,\sigma_{\mathrm{L}}^{(\text{Nb})} \tag{6.1}$$

where $f^{(i)}$ denotes volume fraction of each component. In order to increase $\widetilde{\sigma}_{\mathrm{L}}$, it is possible to reduce the volume fraction $f^{(\text{Nb})}$ of Nb, as its conductivity is negligible compared with Cu-L and Cu-F. The effective yield stress can be estimated by homogenization models, as shown in Chapter 5. We have verified that the effective longitudinal yield stress can be increased by reducing $f^{(\text{Cu-L})}$, as Cu-L exhibit lower yield stress compared with the other two components. Therefore, the effective electrical and mechanical property could be improved by increasing $f^{(\text{Cu-F})}$.

Fig. 6.1(a) shows the Cu-Nb Filamentary wires at the H2 scale; the H1 zone contains 85 Nb/Cu elementary fibers. As illustrated in Fig. 6.1(b), a strategy of material improvement is proposed. In order to reduce the $f^{(\text{Nb})}$, the Nb/Cu elementary fibers in Fig. 6.1(a) are replaced by Cu/Nb/Cu fibers (similar to the "co-cylindrical" wires in Dubois (2010), see also Fig. 4.1). In addition, the Cu-L (e.g. Cu-1 here) could be refined by an Nb envelope leading to a three layered Cu-F/Nb/Cu-F microstructure, instead of a Cu-L envelope. In this way, volume fraction $f^{(\text{Cu-L})}$ of Cu-L can be reduced. Further quantitative predictions are still in preparation.

6.3 Conclusions en Français

Les fils composites nanostructurés et architecturés cuivre-niobium sont d'excellents candidats pour la génération de champs magnétiques intenses (>90T); en effet, ces fils allient une limite élastique élevée et une excellente conductivité électrique. Les fils Cu-Nb multi-échelles sont fabriqués par étirage et empilement cumulé (une technique de déformation plastique sévère), conduisant à une microstructure multi-échelle, architecturée et nanostructurée présentant une texture cristallographique de fibre prononcée et des formes de grains fortement allongées le long de l'axe du fil. Cette thèse présente une étude du comportement électrique et élasto-plastique de ce matériau composite, basée sur des approches multi-échelles. Afin d'étudier le lien entre le comportement effectif et la microstructure du fil, plusieurs méthodes d'homogénéisation sont appliquées, qui peuvent être séparées en deux types principaux : méthodes en champs moyens et en champs complets. Les différentes méthodes prennent en compte différents contenus microstructuraux et estiment ainsi l'importance des microstructures et des architectures pour le comportement de fils Cu-Nb. Les approches en champs moyens, en supposant une microstructure aléatoire, sont basées sur le schéma Auto-Cohérent (version standard ou généralisée) pour l'homogénéisation électrique ou élastique. Concernant le comportement élasto-plastique, le modèle dit en β est utilisé en raison de son efficacité numérique; ce modèle est étendu aux polycristaux avec un champ initial de contraintes résiduelles. Les résultats obtenus par les méthodes en champs moyens sont systématiquement comparés à une approche par éléments finis, supposant une microstructure périodique. Comme les spécimens présentent plusieurs échelles caractéristiques, plusieurs étapes de transition d'échelle sont effectuées itérativement de l'échelle de grain (nm) jusqu'à l'échelle macroscopique (mm). Enfin, les résultats des modèles sont comparés aux données expérimentales disponibles, telles que les conductivités effectives longitudinale et transversale, la réponse mécanique macroscopique, ainsi que la diffraction des rayons X et des neutrons lors de la déformation in-situ de l'échantillon. Les principaux résultats sont les suivants :

Concernant la conductivité électrique :

- La conductivité longitudinale effective (c'est-à-dire, la conductivité homogénéisée le long de la direction du fil) peut être estimée avec une grande précision.
- Les conductivités transversales effectives prédites par les approches en champs complets et en champs moyens sont en très bon d'accord. Ce résultat permet d'obtenir une estimation précise du comportement macroscopique par des étapes itératives de transition d'échelle.
- En prenant en compte l'effet de taille associé au libre parcours moyen des électrons, du au raffinement de la microstructure, les conductivités prédites sont en très bon

accord avec les données expérimentales. L'effet du diamètre du fil est correctement reproduit par le modèle.

- Le rapport obtenu entre les conductivités effectives longitudinale et transversale est de ∼1.3 en raison de la microstructure spécifique de fils Cu-Nb qui est renforcée par des fibres longues.

Concernant le comportement élasto-plastique :

- À toutes les échelles, les modèles en champs moyens et en champs complets prédisent un comportement élastique effectif très similaire (l'écart <3%). On trouve que la texture cristallographique joue un rôle important dans les modules élastiques effectifs. La texture morphologique a une influence significative sur les propriétés élastiques pour la double-texture de fibre ⟨111⟩-⟨100⟩ observée dans Cu; son effet est cependant moins prononcé pour la fibre unique ⟨110⟩ de Nb.
- Le comportement elasto-plastique prédit par la règle en β est comparé aux solutions de référence en champs complets. Un bon d'accord est alors obtenu à toutes les échelles (l'écart ∼15%). En prenant en compte un champ réaliste de contraintes résiduelles initiales, on trouve un bon accord entre la prédiction des modèles et les données expérimentales, i.e. non seulement pour le comportement en traction, mais aussi pour les déformations élastiques moyennes par phase individuelle de Cu ou Nb mesurées in-situ par diffraction de neutrons.
- En appliquant une traction le long de la direction longitudinale des fils Cu-Nb, les expériences in-situ et la théorie montrent que l'activité plastique se produit dans les grains orientés ⟨100⟩ à une contrainte macroscopique plus élevée que dans les grains orientés ⟨111⟩.

L'accord général parmi les réponses des modèles permet de suggérer la meilleure stratégie pour estimer de manière fiable les comportements électrique et élasto-plastique des fils Cu-Nb tout en limitant le temps de calcul.

6.4 Perspectives

Ce travail peut se poursuivre dans les directions suivantes :

- *L'effet de la température sur la conductivité électrique :* Les fils Cu-Nb sont utilisés dans les bobines pour la génération de champs magnétiques intenses (>90 T) à 77K, alors que ce travail a été limité à la température ambiante. Par conséquent, les théories et les expériences devraient être étendues en tenant compte des différentes températures.

- *L'effet de taille :* Pour les fils Cu-Nb Filamentaires N=85^2 étudiés dans Chapitre 5, on suppose que les différentes composantes de Cu présentent une même limite d'élasticité, ~ 350 MPa. Cependant, les canaux du Cu-0 "fin" (largeur des canaux δ=310 nm) dans le conducteur avec un diamètre de 0,29 mm présentent probablement une limite d'élasticité plus élevée de ~ 500 MPa en raison de l'effet de taille (Thilly et al., 2009). Cet effet n'a pas été pris en compte dans ce chapitre, car la fraction volumique de Cu-0 est relativement faible ($\sim$15%). D'autre part, l'effet de taille doit être pris en compte pour d'autres types de fils Cu-Nb (par exemple, fils Cu-Nb Filamentaires N=85^3) qui contiennent une plus grande fraction volumique de Cu avec une largeur nanométrique des canaux .

- *Contraintes résiduelles initiales :* La mesure des contraintes résiduelles doit être effectuée par la diffraction des rayons X/neutrons pour les fils Cu-Nb étudiés dans Chapitre 5. En outre, la simulation du procédé de fabrication peut être effectuée pour prédire quantitativement les contraintes résiduelles dans différentes directions. C'est un point important, car nous avons montré que les contraintes résiduelles initiales affectent fortement le comportement effectif du fil.

- *Différentes conditions de chargement :* Les expériences ex-situ/in-situ pourraient être effectuées pour différentes conditions de chargement, par exemple, une traction transversale ou une torsion, afin de valider complètement les modèles mécaniques. En outre, on pourrait, par exemple, effectuer des tests de compression le long de la direction transversale sur des échantillons usinés par "FIB-SEM".

Les modèles micromécaniques peuvent être utilisés pour optimiser les paramètres de la microstructure dans le processus de fabrication de fils Cu-Nb. Selon Thilly (2000), la conductivité électrique longitudinale effective et la limite d'élasticité longitudinale effective jouent un rôle important dans la génération de champ magnétique pour les bobines. Ainsi, ces deux propriétés devraient être améliorées simultanément.

Différents types des canaux de Cu sont présents dans les fils Cu-Nb. Dans Chapitre 4 et Chapitre 5, nous appelons (1) Cu "large" (Cu-L) les canaux de Cu présentant une largeur δ supérieure à quelques micromètres, et (2) Cu "fin" (Cu-F) les canaux de Cu présentant une largeur δ plus petite que le micromètre. Cu-L présente les propriétés typiques du Cu travaillé à froid, avec une conductivité de $\sim 0.568\,\mu\Omega^{-1}\mathrm{cm}^{-1}$ (à 293 K) et une limite d'élasticité de $\sim$350 MPa; D'autre part, en raison de l'effet de taille, Cu-F (ex. pour δ=500 nm) présente une conductivité de $\sim 0.537\,\mu\Omega^{-1}\mathrm{cm}^{-1}$ et une limite d'élasticité de $\sim$450 MPa. En outre, les canaux de Nb présentent toujours une limite d'élasticité haute (généralement > 2 GPa) ainsi qu'une faible conductivité de $0.060\,\mu\Omega^{-1}\mathrm{cm}^{-1}$.

La conductivité longitudinale effective $\widetilde{\sigma}_{\mathrm{L}}$ de fils Cu-Nb peut être déterminée par la loi des mélanges (Section 3.4.1):

$$\widetilde{\sigma}_{\mathrm{L}} = f^{(\text{Cu-L})}\,\sigma_{\mathrm{L}}^{(\text{Cu-L})} + f^{(\text{Cu-F})}\,\sigma_{\mathrm{L}}^{(\text{Cu-F})} + f^{(\text{Nb})}\,\sigma_{\mathrm{L}}^{(\text{Nb})}$$

où $f^{(i)}$ représente la fraction volumique de chaque composante. Pour augmenter $\widetilde{\sigma}_{\mathrm{L}}$, il est possible de réduire la fraction de volume $f^{(\mathrm{Nb})}$ de Nb, car sa conductivité est négligeable par rapport à celles de Cu-L et Cu-F. Nous avons vérifié que la limite d'élasticité longitudinale effective peut être augmenter en réduisant $f^{(\mathrm{Cu\text{-}L})}$, car Cu-L présente une limite d'élasticité inférieure à celle des deux autres composantes. Par conséquent, les propriétés électrique et mécanique effectives pourrait être améliorée en augmentant $f^{(\mathrm{Cu\text{-}F})}$.

Fig. 6.1(a) montre les fils "Filamentaires" de Cu-Nb à l'échelle H2; la zone d'H1 contient des 85 fibres élémentaires de Nb/Cu. Comme illustré dans Fig. 6.1(b), une stratégie d'amélioration des matériaux est proposée. Afin de réduire le $f^{(\mathrm{Nb})}$, les fibres élémentaires de Nb/Cu dans la Fig. 6.1(a) sont remplacés par des fibres Cu/Nb/Cu (similaire aux fils "co-cylindriques" de Dubois (2010), voir aussi Fig. 4.1). En outre, le Cu-L (par exemple, Cu-1 ici) pourrait être raffiné par une enveloppe du Nb conduisant à une microstructure Cu-F/Nb/Cu-F à trois couches, au lieu d'une seule enveloppe du Cu-L. De cette façon, la fraction volumique $f^{(\mathrm{Cu\text{-}L})}$ de Cu-L peut être réduite. D'autres prévisions quantitatives sont encore en préparation.

Appendix A

Modélisation multi-échelle du comportement électrique de nano composites Cu-Nb

This paper (Gu et al., 2015) has been published in "Matériaux & Thechniques".

It deals with the homogenization of the electrical conductivity for the co-cylindrical Cu-Nb wires which contain 85^3 Cu/Nb/Cu elementary fibers (e.g. see Fig. 4.1). It should be noted that, in Chapter 3, the effective electrical conductivity of the Filamentary Cu-Nb wires (i.e. containing 85^2 and 85^3 Nb/Cu elementary fibers, as illustrated in Fig. 3.1) has been studied. The good agreements between experimental data and model predictions for various types of Cu-Nb wires demonstrate that multiscale modeling proposed in this work can be used for different multi-coated fiber-reinforced materials.

In addition, the detailed derivations of the effective conductivity by the GSC scheme are also shown in this appendix.

Matériaux & Techniques **103**, 309 (2015)

DOI: 10.1051/mattech/2015033
www.mattech-journal.org

Matériaux & Techniques

Modélisation multi-échelle du comportement électrique de nano-composites Cu-Nb

T. Gu[1,2], E. Herve-Luanco[2], H. Proudhon[2], L. Thilly[3], J.-B. Dubois[3], F. Lecouturier[4], O. Castelnau[1] et S. Forest[2]

Reçu le 28 février 2015, accepté le 29 juin 2015

Résumé – Les fils composites nanostructurés et architecturés cuivre-niobium, qui sont de bons candidats pour la génération de champs magnétiques intenses, allient une limite d'élasticité élevée et une excellente conductivité électrique. Ils sont élaborés par co-déformation d'un assemblage composite Cu-Nb. La microstructure, multi-échelle, est formée de 85^3 motifs élémentaires de Cu-Nb de taille caractéristique nanométrique. Afin d'étudier le lien entre la conductivité électrique effective et la microstructure, deux méthodes d'homogénéisation sont appliquées : l'une, en champs moyens (modèle auto-cohérent généralisé), dans laquelle une microstructure formée de motifs co-cylindriques répartis aléatoirement est considérée, et l'autre, en champs complets (éléments finis), dans laquelle l'aspect périodique de la microstructure expérimentale est pris en compte. Les effets de la taille des constituants élémentaires (nm), de la température, ainsi que de la densité de dislocations, sur la conductivité locale sont considérés. Le caractère multi-échelle du matériau est pris en compte grâce à un processus itératif. Les conductivités effectives longitudinale et transversale obtenues avec les deux méthodes sont en excellent accord, montrant un moindre effet de la distribution des fibres sur ces propriétés. Ces résultats reproduisent également les données expérimentales disponibles.

Mots clés : Composites architecturés / matériaux polycristallins / méthodes d'homogénéisation / modélisation multi-échelle / conductivité électrique

Abstract – Multiscale modeling of the electrical behavior of Cu-Nb nanocomposites. Nanostructured and architectured copper niobium composite wires are very good candidates for the generation of very high magnetic fields as they combine both high strength and high electrical conductivity. They are fabricated by co-deformation of a Cu-Nb composite assembly. A multiscale microstructure formed by 85^3 Cu-Nb elementary patterns with dimensions of the order of nanometers, is obtained. In order to investigate the link between the effective electrical conductivity and the wire microstructure, two homogenization methods are applied: first, using a mean field theory (generalized self-consistent model) in which a microstructure formed by co-cylindrical long fibers with a random distribution is considered, and second a full field method (Finite Elements) in which the periodic character of the experimental microstructure is taken into account. The size effect of components (nm), temperature, and dislocation density are taken into account into the definition of the local conductivity. The multiscale character of the material is taken into consideration through an iterative process. The longitudinal and transverse effective conductivities obtained by both methods perfectly match with each other, showing the limited influence of the effect of fiber distribution for this behavior. Results also compare well with the available experimental data.

Key words: Multiscale composites / polycrystalline materials / homogenization methods / multiscale modeling / electrical conductivity

[1] Laboratoire PIMM, CNRS UMR 8006, Arts & Métiers ParisTech, 151 Bd de l'hopital, 75013 Paris, France
Tang.GU@ensam.eu
[2] Centre des matériaux, CNRS UMR 7633, Mines ParisTech, BP 87, 91003 Evry Cedex, France
[3] Institut Pprime, UPR 3346, CNRS, University of Poitiers, ISAE-ENSMA, SP2MI, Boulevard Marie et Pierre Curie, BP 30179, 86962 Futuroscope Chasseneuil Cedex, France
[4] Laboratoire National des Champs Magnétiques Intenses, UPR 3228 CNRS-UPS-INSA-UJF, 143 avenue de Rangueil, 31400 Toulouse, France

Article publié par EDP Sciences

1 Introduction

Les travaux présentés ici concernent l'étude de fils conducteurs composites nanostructurés à base de cuivre-niobium (Cu-Nb), qui sont de bons candidats pour la réalisation de bobines permettant la génération des champs magnétiques très intenses (>90 T). Ces champs magnétiques sont devenus un outil expérimental et industriel essentiel [1–3]. Pour les produire, les fils conducteurs constituant les bobines doivent allier une limite d'élasticité et une conductivité électrique élevées [4]. Dans [5], un conducteur présentant une contrainte maximale de 1.9 GPa à 77 K a été obtenu, pour une conductivité de 1.72 $\mu\Omega^{-1}\,cm^{-1}$.

Les conducteurs nano-composites continus Cu-Nb sont élaborés par un procédé de déformation plastique sévère, basé sur des cycles successifs d'extrusion à chaud, d'étirage à froid et d'empilements [4]. Comme illustré dans la figure 1, ce procédé d'élaboration conduit à la formation d'une structure multi-échelle complexe de la matrice de cuivre et la nanostructuration des renforts de niobium. Il en résulte une nanostructuration du matériau composite, qui a un effet important sur les propriétés du conducteur, lui permettant d'atteindre les propriétés recherchées.

La figure 1 présente la microstructure multi-échelle des fils Cu-Nb (microstructure appelée "co-cylindriques" dans [7]) : à l'échelle du Zoom 1, les nanotubes de niobium (Nb-t) sont séparés par de fins canaux de cuivre (Cu-0), et ils contiennent un filament de cuivre (Cu-f). On définit l'échelle effective du Zoom 1 par l'assemblage de 85 de ces motifs élémentaires. Sur le Zoom 2, des canaux de Cu (Cu-1) entourent 85 motifs élémentaires décrits dans le Zoom 1. Au niveau du Zoom 3, le fil est constitué de 85^3 motifs de Cu-f/Nb-t/Cu-0 de taille caractéristique nanométrique, et séparés par les canaux de cuivre Cu-1, Cu-2. Le Zoom 4 correspond à la microstructure du Zoom 3 entourée d'un cylindre de Cu-3, reproduisant ainsi la structure expérimentale de la dernière étape d'élaboration (échelle macroscopique). En raison du processus d'élaboration itératif, tous les nanotubes de Nb ont subi la même déformation, et présentent donc des microstructures et des tailles caractéristiques similaires. Concernant le Cu, les régions Cu-f et Cu-0 sont introduites lors de la toute première étape d'élaboration, alors que Cu-1, Cu-2, et Cu-3 sont introduits successivement ; les microstructures et les tailles caractéristiques de ces constituants sont donc différentes (voir le Tab. 1).

Les études réalisées précédemment sur ces matériaux concernent le procédé d'élaboration [8, 9], la caractérisation des matériaux [10, 11], la stabilité thermique [12], la modélisation atomistique des interfaces [13] et les propriétés mécaniques [14,15]. En outre, la conductivité électrique a été étudiée expérimentalement et théoriquement par Thilly [5] et Dubois [7] dans la direction longitudinale, i.e. selon l'axe du fil.

Dans ce travail, nous présentons une modélisation multi-échelle de la conductivité électrique effective du fil, en tenant compte de son aspect anisotrope. Le modèle Auto-Cohérent Généralisé (ACG, Sect. 2.1), initialement développé pour prédire le comportement élastique effectif [16–18], puis modifié par Joannes et Hervé-Luanco [19] pour les phénomènes de diffusion dans les composites à fibres longues n-phases isotropes transverses, est appliqué ici au cas de la conductivité électrique. Ce modèle considère une répartition aléatoire des motifs élémentaires. Un second modèle, basé sur la méthode des Eléments Finis et prenant en compte le caractère périodique de la microstructure expérimentale (HP dans Sect. 2.2), mais plus lourd au niveau numérique, est également appliqué [20–22]. Dans [5], les effets de la taille des constituants (nm), de la température, et de la densité de dislocations sur la conductivité locale sont pris en compte à l'aide de la loi de Dingle (Sect. 3.1). Les résultats théoriques et numériques obtenus, dans lesquels le caractère multi-échelle du matériau est pris en compte grâce à un processus itératif (Sect. 3.2), sont comparés à des mesures expérimentales (Sect. 4).

2 Modélisation de la conductivité électrique effective des composites

2.1 Modèle auto-cohérent généralisé

La figure 1 présente la disposition des fils de nanocomposite Cu-Nb à différents échelles. Sur le Zoom 1, les fils co-cylindriques apparaissent avec trois couches : Cu-f/Nb-t/Cu-0. Le modèle Auto-Cohérent Généralisé (ACG) [19] considère qu'ils sont distribués aléatoirement. Ce schéma est développé de la manière suivante : d'abord le problème élémentaire d'une inclusion constituée de n phases co-cylindriques dans une matrice homogène, défini sur la figure 2, est résolu ; puis la matrice est remplacée par le Milieu Homogène Équivalent (MHE), dont la conductivité effective $\widetilde{\boldsymbol{\sigma}}$ sera déterminée par une condition d'auto-cohérence (Fig. 3a).

2.1.1 Problème cylindrique n-phase

Nous commençons par présenter le problème élémentaire d'une inclusion dans une matrice homogène (problème cylindrique n-phase). Une inclusion cylindrique de n couches est noyée dans une matrice infinie (phase $n+1$), chaque phase étant supposée homogène et isotrope transverse (l'axe de symétrie est ici confondu avec la direction longitudinale des fibres longues). Des systèmes de coordonnées cartésiennes (x_1, x_2, x_3) et cylindriques (r, θ, z), de même origine, sont utilisés dans cette étude. L'axe z est ici identique à l'axe x_1, et il est aligné avec la direction longitudinale des fibres longues (Fig. 2).

Comme dans Hervé et Zaoui [18], sur la figure 2, la phase i se situe dans la couronne limitée par les deux cylindres concentriques de rayon R_{i-1} et R_i ($i \in [1, n+1]$ avec $R_0 = 0$, $R_{n+1} \to \infty$). Dans la phase i, $\sigma_L^{(i)}$ et $\sigma_T^{(i)}$ sont respectivement les conductivités longitudinale et

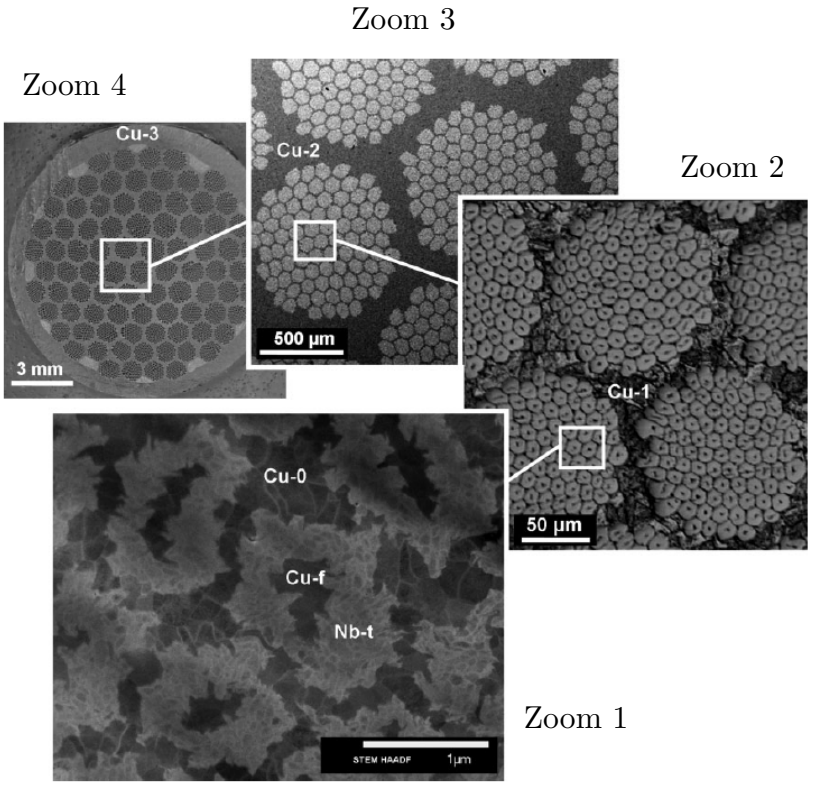

Fig. 1. Microstructure multi-échelle des conducteurs nano-composites Cu-Nb. Zoom 4, 3 et 2 : observations par Microscopie Électronique à Balayage (MEB), Zoom 1 : observation par Microscopie Électronique en Transmission (MET) [6,7].

Fig. 1. Multi-scale microstructure of Cu-Nb nano-composite conductor. Zoom 4, 3 and 2: micrographs obtained by Scanning Electron Microscopy (SEM), Zoom 1: obtained by Transmission Electron Microscopy (TEM) [6, 7].

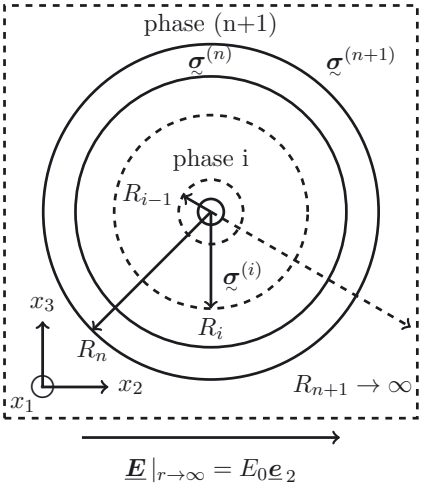

Fig. 2. Problème cylindrique n-phase (conduction électrique transversale).

Fig. 2. n-layered cylindrical problem (transverse electrical conduction).

transversale. On écrit la conductivité isotrope transverse sous la forme du tenseur d'ordre deux suivant :

$$\underset{\sim}{\boldsymbol{\sigma}}^{(i)} = \sigma_T^{(i)} \left(\underline{\boldsymbol{e}}_r \otimes \underline{\boldsymbol{e}}_r + \underline{\boldsymbol{e}}_\theta \otimes \underline{\boldsymbol{e}}_\theta\right) + \sigma_L^{(i)}\, \underline{\boldsymbol{e}}_1 \otimes \underline{\boldsymbol{e}}_1,$$

Tableau 1. Dimensions théoriques $\delta^{(i)}$ dans le cas des diamètres $d = 0.506$ et 2.064 mm, avec les conductivités locales $\sigma^{(i)}$ ($\mu\Omega^{-1}\,\mathrm{cm}^{-1}$) à 293 K et la fraction volumique $f^{(i)}$ de chaque phase i.

Table 1. Theoretical dimensions $\delta^{(i)}$ in the case of diameters $d = 0.506$ and 2.064 mm, with the corresponding local conductivity $\sigma^{(i)}$ ($\mu\Omega^{-1}\,\mathrm{cm}^{-1}$) at 293 K and volume fraction $f^{(i)}$ of each phase i.

phase i	$f^{(i)}$	$d = 0.506$ mm		$d = 2.064$ mm	
		$\delta^{(i)}$	$\sigma^{(i)}$	$\delta^{(i)}$	$\sigma^{(i)}$
Nb-t	23.8%	83 nm	0.057	338 nm	0.060
Cu-f	4.5%	110 nm	0.424	450 nm	0.533
Cu-0	16.5%	71 nm	0.372	289 nm	0.513
Cu-1	13.7%	492 nm	0.536	2006 nm	0.560
Cu-2	18.0%	5.58 μm	0.565	22.8 μm	0.568
Cu-3	23.4%	31.6 μm	0.568	129 μm	0.568
Cu massif		∞	0.568	∞	0.568
Nb massif		∞	0.060	∞	0.060

avec $\otimes$ le produit tensoriel. La loi de comportement dans la phase i obéit à la loi d'Ohm :

$$\underline{\boldsymbol{j}}^{(i)} = -\underset{\sim}{\boldsymbol{\sigma}}^{(i)} \cdot \boldsymbol{\nabla}\, \Phi^{(i)} = \underset{\sim}{\boldsymbol{\sigma}}^{(i)} \underline{\boldsymbol{E}}^{(i)} \qquad (1)$$

où Φ, $\underline{\boldsymbol{j}}$ et $\underline{\boldsymbol{E}}^{(i)}$ représentent respectivement le potentiel électrique (V), la densité de courant électrique (A m^{-2})

et le champ électrique (V m^{-1}). On fait l'hypothèse d'un régime quasi-statique, d'où :

$$\mathrm{div}(\underline{\boldsymbol{j}}) = 0. \tag{2}$$

À partir des équations (1) et (2), on obtient l'équation d'équilibre de $\Phi^{(i)}$ dans la phase i :

$$-\sigma_T^{(i)}\frac{\partial^2\Phi^{(i)}}{\partial^2 r} - \frac{\sigma_T^{(i)}}{r}\left[\frac{\partial^2\Phi^{(i)}}{r\partial\theta^2} + \frac{\partial\Phi^{(i)}}{\partial r}\right] - \sigma_L^{(i)}\frac{\partial^2\Phi^{(i)}}{\partial x_1^2} = 0. \tag{3}$$

Nous nous intéressons dans un premier temps à la conduction électrique *transversale*. Pour cela, un champ électrique à distance est appliqué sur la surface de l'échantillon ($r = R_{n+1}$ avec $r \to \infty$) selon la direction transversale x_2 (voir Fig. 2)

$$\underline{\boldsymbol{E}}\,|_{r\to\infty} = E_0\underline{\boldsymbol{e}}_2. \tag{4}$$

Le potentiel électrique solution dans la phase i qui satisfait à la fois l'équation d'équilibre (3) et la condition aux limites (4) est proposé sous la forme :

$$\Phi^{(i)}(r,\theta) = \left(A_i r + B_i\frac{R_{i-1}^2}{r}\right)\cos\theta \tag{5}$$

où A_i and B_i sont les constantes à déterminer. Afin d'éviter un problème de singularité en $r = 0$, la valeur $B_1 = 0$ est choisie, sans perte de généralité. La densité de courant électrique correspondante selon la direction normale $\underline{\boldsymbol{r}}$ est alors donnée par :

$$j_r^{(i)}(r,\theta) = -\sigma_T^{(i)}\left(A_i - B_i\frac{R_{i-1}^2}{r^2}\right)\cos\theta. \tag{6}$$

Les interfaces ($r = R_i$) étant supposées parfaites, le potentiel électrique Φ et la densité de courant normale j_r doivent vérifier la condition de continuité à l'interface :

$$\begin{cases}\Phi^{(i)}(R_i,\theta) = \Phi^{(i+1)}(R_i,\theta)\\ j_r^{(i)}(R_i,\theta) = j_r^{(i+1)}(R_i,\theta).\end{cases} \tag{7}$$

Pour déterminer la valeur des constantes A_i et B_i du problème cylindrique n-phase, Hervé et Zaoui [17] ont proposé d'utiliser les "matrices de transfert" $\boldsymbol{J_i}$ sur les interfaces ($r = R_i$). La continuité en $r = R_i$ devient alors :

$$\boldsymbol{J_i}\,(R_i)\cdot\boldsymbol{W_i} = \boldsymbol{J_{i+1}}\,(R_i)\cdot\boldsymbol{W_{i+1}} \tag{8}$$

avec $\boldsymbol{W_i}$ désignant $(A_i\ B_i)^T$, et $\boldsymbol{J_i}$ est la matrice suivante :

$$\boldsymbol{J_i}\,(r) = \begin{pmatrix} r & \dfrac{R_{i-1}^2}{r}\\ -\sigma_T^{(i)} & \sigma_T^{(i)}\dfrac{R_{i-1}^2}{r^2}\end{pmatrix}. \tag{9}$$

Définissons les matrices $\boldsymbol{N}$ et $\boldsymbol{Q}$ à partir des matrices $\boldsymbol{J_i}$:

$$\boldsymbol{N^{(i)}} = \boldsymbol{J_{i+1}^{-1}}\,(R_i)\cdot\boldsymbol{J_i}\,(R_i) \quad\text{et}\quad \boldsymbol{Q^{(k)}} = \prod_{i=k}^{1}\boldsymbol{N^{(i)}}.$$

L'équation (8) est réécrite sous la forme :

$$\boldsymbol{W_{i+1}} = \boldsymbol{N^{(i)}}\cdot\boldsymbol{W_i}, \quad \boldsymbol{W_{k+1}} = \boldsymbol{Q^{(k)}}\,\boldsymbol{W_1}. \tag{10}$$

Tous les coefficients A_k, B_k ($k \in [1,n]$) peuvent alors être calculés :

$$\begin{cases}A_k = \dfrac{Q_{11}^{(k-1)}}{Q_{11}^{(n)}}A_{n+1}\\ B_k = \dfrac{Q_{21}^{(k-1)}}{Q_{11}^{(n)}}A_{n+1}\end{cases} \tag{11}$$

avec $A_{n+1} = -E_0$. La densité de courant électrique $\underline{\boldsymbol{j}}^{(i)}$ et le potentiel $\Phi^{(i)}$ sont maintenant déterminés dans toutes les phases $i (i \in [1,n])$.

Dans le cas de la conduction électrique *longitudinale*, l'équation d'équilibre (3) se met sous la forme suivante dans chaque phase :

$$\Phi^{(i)} = -E_0 x_1, \tag{12}$$

pour des conditions aux limites homogènes au contour : $\underline{\boldsymbol{j}}\,|_{r\to\infty}\cdot\underline{\boldsymbol{e}}_r = 0$ sur la surface latérale du cylindre et $\Phi = -E_0 x_1$ sur les deux sections extrêmes, avec E_0 un champ électrique constant. On obtient alors une densité de courant homogène par phase, contrairement au cas transversal.

2.1.2 Schéma autocohérent généralisé

Afin de déterminer la conductivité effective $\widetilde{\boldsymbol{\sigma}}$ du composite Cu-Nb, le problème cylindrique n-phase résolu précédemment est utilisé avec une phase $(n+1)$ inconnue représentant le MHE, et une condition d'auto-cohérence (qui peut être une condition énergétique telle que celle utilisée par Christensen et Lo [23] ou une condition portant sur les moyennes de champs [24], ces deux conditions étant équivalentes). Cette démarche a été suivie par Joannes et Hervé-Luanco [19] et conduit, dans le cas de la conductivité *transversale*, à $B_{n+1} = 0$ et, par voie de conséquence à $Q_{12}^{(n)} = 0$, entrainant :

$$\widetilde{\sigma}_T = \sigma_T^{(n+1)} = \frac{\sigma_T^{(n)}[R_n^2 Q_{11}^{(n-1)} - R_{n-1}^2 Q_{21}^{(n-1)}]}{R_n^2 Q_{11}^{(n-1)} + R_{n-1}^2 Q_{21}^{(n-1)}}. \tag{13}$$

Dans le cas de la conductivité *longitudinale*, la condition d'auto-cohérence conduit à :

$$\widetilde{\sigma}_L = \sum f^{(i)}\,\sigma_L^{(i)} \tag{14}$$

avec $f^{(i)}$ la fraction volumique de la phase i. On remarquera que cette dernière expression n'est autre que la loi des mélanges sur les conductivités. Il s'agit en fait de la solution exacte pour toutes les microstructures formées de fils parallèles, quel que soit l'assemblage de ces fils.

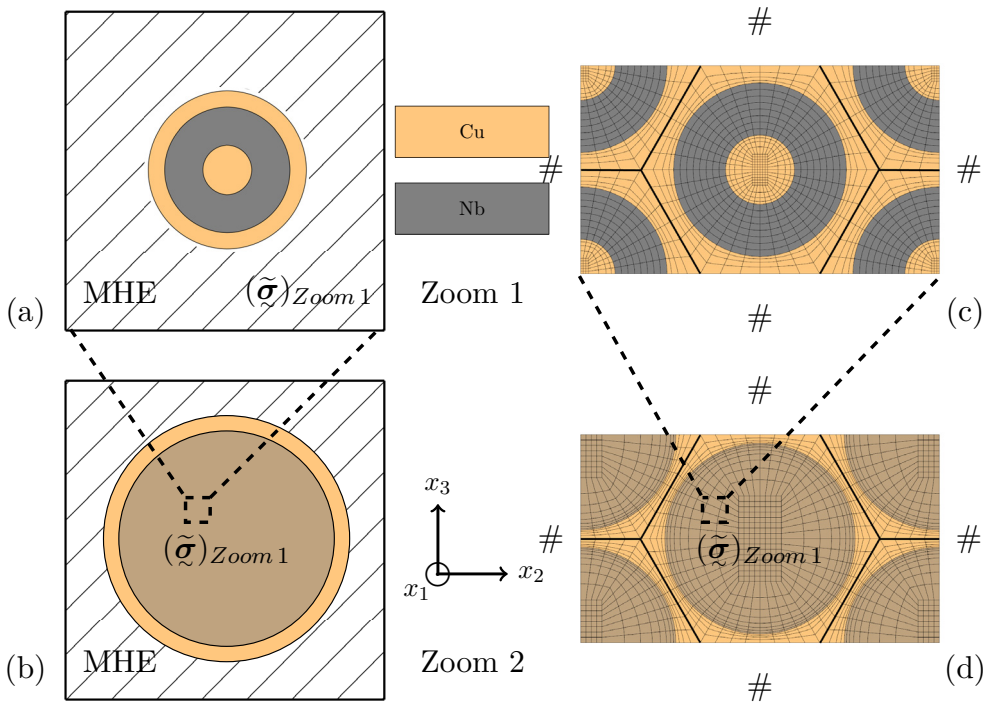

Fig. 3. Modélisation multi-échelle de la conductivité effective du Zoom 1 (a et c) au Zoom 2 (b et d). (a, b) : processus itératif par modèle Auto-Cohérent Généralisé (ACG) ; (c, d) : Homogénéisation Périodique (HP) avec les maillages de la méthode des éléments finis (MEF).

Fig. 3. Multi-scale modeling of the effective conductivity from the Zoom 1 (a and c) to the Zoom 2 (b and d). (a, b): the iterative process by the Generalized Self-Consistent model (GSC); (c, d): Periodic Homogenization (PH) with the finite element method (FEM).

2.2 Homogénéisation périodique

Le modèle analytique ACG présenté ci-dessus suppose que les fibres longues sont distribuées aléatoirement (Fig. 3a). Afin de tenir compte de la distribution quasi-périodique observée expérimentalement (Fig. 1), résultant du processus d'élaboration, et d'étudier l'effet de cette distribution particulière, le problème périodique a été résolu. Pour cela, nous avons considéré une cellule élémentaire soumise à des conditions aux limites périodiques, et le problème (que nous appelons HP pour Homogénéisation Périodique) a été résolu par la méthode des éléments finis [20–22]. La périodicité de la cellule de base et des conditions aux limites permettent de déterminer la conductivité effective $\widetilde{\sigma}$ du MHE correspondant, i.e. infini et périodique.

La cellule de base considérée dans le modèle HP, ainsi que le maillage utilisé (éléments quadratiques à 20 nœuds, c3d20), sont indiqués sur la figure 3c. La cellule de base contient toute l'information morphologique du Volume Élémentaire Représentatif (VER). Elle contient deux fibres longues ($1 + 4 \times 1/4$ fibres) disposées sur un réseau hexagonal, et elle représente la microstructure expérimentale (idéalisée) des nano-composites Cu-Nb sur le Zoom 1. Ces calculs HP sont basés sur des conditions aux limites et des microstructures périodiques. Or la microstructure réelle ne l'est pas, notamment car chaque Zoom ne contient finalement qu'un nombre limité de motifs élémentaires (85). Nous avons vérifié à l'aide de calculs EF sur de plus grandes structures avec conditions aux limites non périodiques que cette hypothèse de périodicité ne modifiait guère les résultats.

Sous conditions aux limites périodiques, le potentiel Φ dans le volume V s'écrit de la manière suivante :

$$\Phi = \langle \boldsymbol{\nabla}\, \Phi \rangle \cdot \underline{\boldsymbol{x}} + t, \quad \forall \underline{\boldsymbol{x}} \in V \tag{15}$$

où $\langle \underline{\boldsymbol{a}} \rangle$ désigne la moyenne volumique :

$$\langle \underline{\boldsymbol{a}} \rangle = \frac{1}{V} \int_V \underline{\boldsymbol{a}}\, \mathrm{d}V. \tag{16}$$

Dans l'équation (15), t est la fluctuation périodique, i.e. deux points homologues sur des faces opposées de V ont la même valeur de t. En outre, le scalaire $\underline{\boldsymbol{j}} \cdot \underline{\boldsymbol{n}}$ prend des valeurs opposées en deux points homologues ($\underline{\boldsymbol{n}}$ étant le vecteur normal de ∂V en $\underline{\boldsymbol{x}}$).

Afin de déterminer les deux composantes de la conductivité électrique, on applique successivement, comme conditions aux limites sur V, le champ électrique $\underline{\boldsymbol{E}}$ suivant : $\langle \boldsymbol{\nabla}\, \Phi \rangle = E_0 \underline{\boldsymbol{e_1}}$ pour la conductivité *longitudinale*, et $\langle \boldsymbol{\nabla}\, \Phi \rangle = E_0 \underline{\boldsymbol{e_2}}$ (ou $E_0 \underline{\boldsymbol{e_3}}$) pour la conductivité *transversale*. Puis, la densité de courant moyenne $\langle \underline{\boldsymbol{j}} \rangle$ est déterminée par homogénéisation numérique, afin d'obtenir la conductivité effective HP à partir de la condition suivante :

$$\langle \boldsymbol{\nabla}\, \Phi \rangle = \widetilde{\sigma} \cdot \langle \underline{\boldsymbol{j}} \rangle . \tag{17}$$

3 Application à la conductivité effective des nano-composites Cu-Nb

3.1 Comportement local

Les phases Cu et Nb évoquées ci-dessus sont en réalité elles-mêmes constituées de grains nanométriques (polycristaux). Cependant, ces deux métaux étant de structure cristalline cubique, la conductivité à l'échelle des grains est isotrope (Sivardière [25]), et donc, du point de vue de la conductivité, les phases polycristallines de Cu et Nb peuvent être considérées comme homogènes, les propriétés effectives de ces polycristaux étant identiques à celle des grains constitutifs. Ainsi, les conductivités longitudinale $\sigma_L^{(i)}$ et transversale $\sigma_T^{(i)}$ sont égales, pour Cu et pour Nb.

En outre, Thilly [5] a montré que la température T, la densité de dislocations β et l'effet de taille (largeur des canaux) peuvent avoir un effet significatif sur la conductivité électrique locale des nano-composites Cu-Nb. La conductivité d'échantillons massifs de Cu et de Nb a été mesurée, en fonction de T et β, dans [5]. Il a ainsi été montré que, à température ambiante (293 K), dans le cas des conducteurs fortement écrouis de diamètre $d \in (0.5, 2.5)$ mm, la densité de dislocations β influence peu la conductivité. Cela correspond au cas de fortes densités de dislocation, probablement saturantes, estimées à $\beta \sim 10^{16}$ m^{-2} dans les canaux larges, et de l'ordre de 10^{12} à 10^{13} m^{-2} dans les canaux fins. Pour ces échantillons massifs, les valeurs de conductivité sont, à 293 K : $\sigma_{\text{massif}} = 0.568$ $\mu\Omega^{-1}\,\text{cm}^{-1}$ pour Cu, et 0.060 $\mu\Omega^{-1}\,\text{cm}^{-1}$ pour Nb (voir aussi le Tab. 1). Les composites Cu-Nb étudiés ici présentent des densités de dislocations similaires, associées aux grandes déformations à froid, et donc l'effet de β ne sera pas pris en compte dans la suite.

Concernant l'effet de taille, nous utilisons l'expression issue de Ashcroft et Mermin [26] et Thilly [5] qui relie la conductivité du matériau au libre parcours moyen ℓ des électrons :

$$\ell_{\text{Cu}}(T) = 66\ \sigma_{\text{massif}-\text{Cu}}(T) \tag{18a}$$

$$\ell_{\text{Nb}}(T) = 87\ \sigma_{\text{massif}-\text{Nb}}(T) \tag{18b}$$

(avec σ_{massif} en $\mu\Omega^{-1}\,\text{cm}^{-1}$ et ℓ en nm). Ici, σ_{massif} et ℓ dépendent de la température, et le libre parcours moyen ℓ des électrons est défini comme la distance moyenne que ces derniers peuvent parcourir entre deux collisions. Initialement, Dingle [27] a étudié les effets de taille dans la diffusion des électrons. Il a modélisé la conductivité d'un fil fin, infiniment long, et de diamètre δ, et s'est donc intéressé à la façon dont la conductivité longitudinale est affectée par les dimensions transversales du fil, en raison de la diffusion des électrons aux surfaces/interfaces. Deux cas extrêmes, $\delta \gg \ell$ et $\delta \ll \ell$, ont été considérés. En modifiant le modèle de Dingle [27] and Thilly [5] obtient les équations suivantes en fonction des rapports δ/ℓ :

$$\frac{\sigma}{\sigma_{\text{massif}}} = \frac{\delta}{\ell} - \frac{3}{8}\left(\frac{\delta}{\ell}\right)^2 \left[\ln\left(\frac{\ell}{\delta}\right) + 1.059\right] \text{ pour } \delta < 0.467\ell, \tag{19a}$$

$$\frac{\sigma}{\sigma_{\text{massif}}} = \left(1 + \frac{\ell}{\delta}\right)^{-1} \qquad \text{pour } \delta \in [0.467\ell, 3\ell[\,, \tag{19b}$$

$$\frac{\sigma}{\sigma_{\text{massif}}} = 1 - \frac{3}{4}\frac{\ell}{\delta} \qquad \text{pour } \delta > 3\ell. \tag{19c}$$

Le choix de l'une de ces trois équations pour le calcul de la conductivité locale $\sigma^{(i)}$ d'une phase i se fait en fonction du rapport $\delta^{(i)}/\ell$, où $\delta^{(i)}$ est la dimension théorique des différentes phases i des conducteurs Cu-Nb (Fig. 4). Les valeurs de $\delta^{(i)}$ peuvent être estimées en supposant que toutes les phases forment des cylindres ou des tubes parfaits et concentriques déformés de manière homothétique lors de l'étirage du composite [7]. Le diamètre extérieur d du fil considéré, ainsi que la fraction volumique $f^{(i)}$ des composants doivent être pris en compte. La fraction volumique, qui n'est pas modifiée par l'étape d'étirage, est déterminée à partir des dimensions initiales des tubes et fils de Cu et Nb introduits dans le procédé. Nous désignons par $e_{\text{Nb}-\text{t}}$ l'épaisseur des tubes de niobium, $d_{\text{Cu}-\text{f}}$ le diamètre des filaments de cuivre, et $d_{\text{Cu}-\text{i}}$ la largeur des canaux de la matrice multi-échelle de cuivre, avec $i = 0, 1, 2, 3$. Ainsi, $\delta^{(i)} = d_{\text{Cu}-0}$ pour la phase Cu-0, $\delta^{(i)} = d_{\text{Cu}-\text{f}}$ pour Cu-f, et $\delta^{(i)} = e_{\text{Nb}-\text{t}}$ pour les tubes de Nb. Ces valeurs sont reportées dans le Tableau 1. Dans ce travail, nous considérons une série des conducteurs nano-composites Cu-Nb contenant 85^3 motifs élémentaires et étirés aux diamètres $d = 0.506, 0.592, 0.640, 0.692, 0.748, 0.875, 1.023, 1.511, 1.634$ et 2.064 mm [7]. Le Tableau 1 indique la dimension $\delta^{(i)}$ dans la phase i, la fraction volumique $f^{(i)}$ et les conductivités locales $\sigma^{(i)}$ à 293 K correspondantes, calculées par les equations (18) et (19), pour le plus grand ($d = 2.064$ mm) et le plus petit ($d = 0.506$ mm) diamètre.

3.2 Homogénéisation multi-échelle

Une fois la conductivité locale $\sigma^{(i)}$ dans chaque phase i déterminée (Sect. 3.1), le modèle Auto-Cohérent Généralisé (Fig. 3a) ainsi que le modèle Homogénéisation Périodique (Fig. 3c) sont tous les deux appliqués à l'échelle du Zoom 1, en considérant une microstructure de motifs co-cylindriques avec trois couches, Cu-f/Nb-t/Cu-0. Avec ces deux modèles, nous obtenons des conductivités effectives $\widetilde{\underline{\sigma}}$ pratiquement confondues, l'écart relatif entre les deux estimations étant ∼0.5 %.

À l'échelle du Zoom 2, les fibres longues sont composées de deux couches : (1) les nano-composites Cu-Nb qui contiennent 85 motifs parallèles issus du Zoom 1, et (2) la matrice de Cu-1. Similairement au cas du Zoom 1, les approximations de la géométrie de ACG et HP sont illustrées dans les figures 3b et 3d : répartition aléatoire pour ACG, et périodique pour HP. Dans le processus itératif, la conductivité de la couche interne du

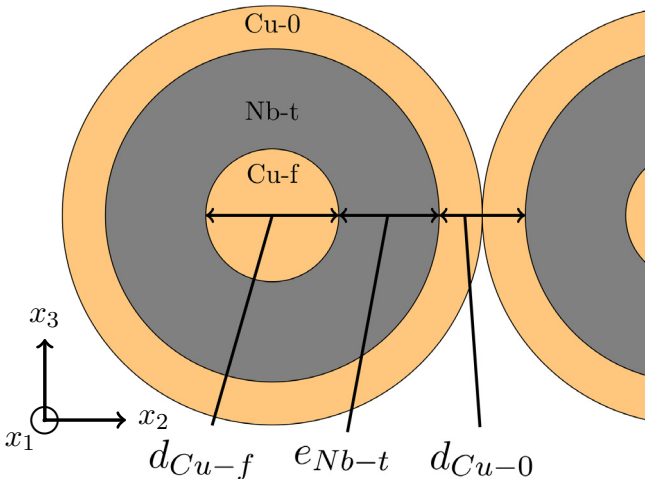

Fig. 4. Largeur théorique des canaux δ : sur le Zoom 1, $e_{\mathrm{Nb-t}}$ désigne l'épaisseur des tubes de niobium, $d_{\mathrm{Cu-f}}$ le diamètre des filaments de cuivre, d_{Cu-0} la largeur des canaux de cuivre.

Fig. 4. Theoretical channel width δ: on the Zoom 1, $e_{\mathrm{Nb-t}}$ denotes the thickness of the niobium tubes, $d_{\mathrm{Cu-f}}$ the diameter of the copper filaments, $d_{\mathrm{Cu-0}}$ copper channel width.

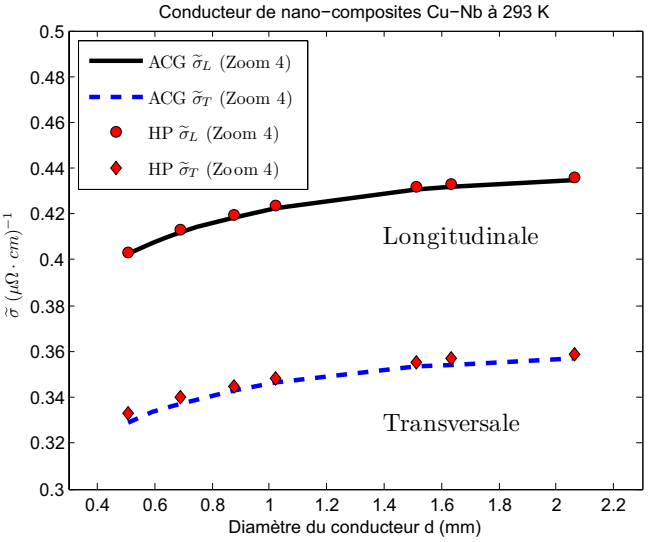

Fig. 5. Conductivités effectives longitudinale et transversale en fonction du diamètre du conducteur, pour les fils de nano-composites Cu-Nb sur le Zoom 4 (i.e. à l'échelle macroscopique) à 293 K, obtenues par le modèle Auto-Cohérent Généralisé (ACG, traits continus) et par Homogénéisation Périodique (HP, points).

Fig. 5. Effective longitudinal and transverse conductivities with respect to the conductor diameter, for nano-composite Cu-Nb wires on Zoom 4 (i.e. at the macroscopic scale) at 293 K*, obtained with the Generalized Self-Consistent model (GSC, continuous lines) and the Periodic Homogenization model (PH, points).*

Zoom 2 $(\underset{\sim}{\boldsymbol{\sigma}}^{(1)})_{\mathrm{Zoom\,2}}$ est donnée par la conductivité effective obtenue sur le Zoom 1 $(\widetilde{\underset{\sim}{\boldsymbol{\sigma}}})_{\mathrm{Zoom\,1}}$. D'autre part, la conductivité de la deuxième couche du Zoom 2 est donnée par la conductivité locale de Cu-1, i.e. $(\underset{\sim}{\boldsymbol{\sigma}}^{(2)})_{\mathrm{Zoom\,2}} = (\underset{\sim}{\boldsymbol{\sigma}})_{\mathrm{Cu-1}}$. Ainsi, une procédure de calcul multi-échelle est mise en place pour les modèles ACG et HP, comme illustré sur les figures 3a−3c et 3b−3d. Les conductivités effectives sur le Zoom 2 $(\widetilde{\underset{\sim}{\boldsymbol{\sigma}}})_{\mathrm{Zoom\,2}}$ ainsi obtenues avec les deux modèles sont encore pratiquement confondues. Le même processus itératif est répété jusqu'à échelle macroscopique (Zoom 4), permettant d'estimer les conductivités à toutes les échelles $(\widetilde{\underset{\sim}{\boldsymbol{\sigma}}})_{\mathrm{Zoom\,i}}$ avec $i = 2, 3, 4$:

$$\left.\begin{array}{l}(\underset{\sim}{\boldsymbol{\sigma}}^{(1)})_{\mathrm{Zoom}\,i} = (\widetilde{\underset{\sim}{\boldsymbol{\sigma}}})_{\mathrm{Zoom}\,(i-1)} \\ (\underset{\sim}{\boldsymbol{\sigma}}^{(2)})_{\mathrm{Zoom}\,i} = (\underset{\sim}{\boldsymbol{\sigma}})_{\mathrm{Cu-}(i-1)}\end{array}\right\} \Rightarrow (\widetilde{\underset{\sim}{\boldsymbol{\sigma}}})_{\mathrm{Zoom}\,i} \Rightarrow \ldots (\widetilde{\underset{\sim}{\boldsymbol{\sigma}}})_{\mathrm{macro}}. \quad (20)$$

La figure 5 illustre les résultats sur le Zoom 4 à 293 K : les traits continus reportent les résultats obtenus avec le modèle analytique ACG et les points ceux du modèle par éléments finis HP. Il est remarquable de constater que les deux conductivités effectives, longitudinale $\widetilde{\sigma}_L$ et transversale $\widetilde{\sigma}_T$, obtenues avec les deux modèles, sont quasiment confondues, pour tous les diamètres du conducteur d. Le faible écart entre ces deux prédictions s'explique par le fait que (i) le contraste entre la conductivité des deux phases reste faible pour Cu-Nb, et (ii) les deux modèles prennent en compte la présence d'une phase jouant le rôle de matrice. La diminution de la conductivité $\widetilde{\underset{\sim}{\boldsymbol{\sigma}}}$ avec la réduction du diamètre d est due à la réduction des largeurs des canaux δ associée à l'étirage (effet de taille).

4 Comparaison expérimentale

Dubois [7] a déterminé expérimentalement la conductivité longitudinale effective $\widetilde{\sigma}_L$ sur la même série de conducteurs nano-composites Cu-Nb par la méthode des quatre pointes [28] : un courant continu d'intensité j est injecté entre deux pointes et une mesure de tension est réalisée entre deux autres pointes placées entre les pointes d'injection de courant. La conductivité transversale n'a pas encore pu être mesurée (travail en cours) ; il s'agit en effet d'une mesure plus délicate, en raison du faible diamètre des fils, mais aussi de sa microstructure composite avec une peau en Cu (Cu-3) entourant le fil.

L'incertitude sur la mesure de conductivité est de l'ordre de 5 % pour les échantillons composites dans la direction longitudinale $\widetilde{\sigma}_L$ et pour les échantillons massifs σ_{massif}. Les résultats des modèles ACG et HP étant directement dépendants de la valeur de la conductivité σ_{massif} de chacune des phases polycristallines Cu et Nb, l'incertitude de mesure sur σ_{massif} entraîne une incertitude sur les prédictions du modèle, également de l'ordre de ± 5 %.

La comparaison avec les données expérimentales est illustrée sur la figure 6. Rappelons que la conductivité longitudinale obtenue par le modèle Auto-Cohérent Généralisé (ACG) est ici confondue avec les résultats du modèle périodique (HP) ; en effet, la conductivité longitudinale, dont la valeur exacte est donnée par la loi des mélanges, ne dépend pas du caractère périodique de la microstructure. La figure 6 montre que les résultats des modèles théoriques sont en très bon accord avec les données expérimentales, pour tous les diamètres considérés. Ce résultat provient d'une prise en compte

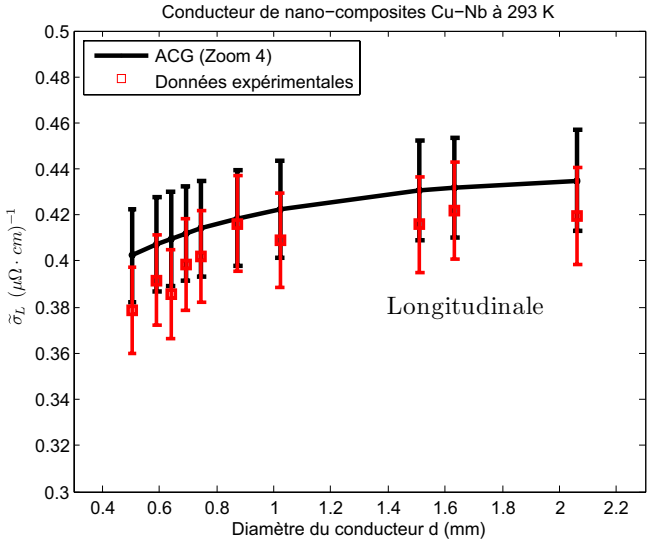

Fig. 6. Conductivité effective longitudinale obtenue avec le modèle ACG (Auto-Cohérent Généralisé, trait continu), et comparée aux données expérimentales (points), en fonction du diamètre du conducteur, pour les fils de nano-composites Cu-Nb sur le Zoom 4 (échelle macroscopique) à 293 K. L'incertitude sur la mesure de la conductivité des échantillons massifs (∼5 %) entraîne une incertitude du même ordre sur les résultats du modèle ACG.

Fig. 6. Effective longitudinal conductivity obtained with the GSC model (Generalized Self-Consistent scheme, continuous line), compared with experimental data (points), for various conductor diameters, for nano-composite Cu-Nb wires on the Zoom 4 (macroscopic scale) at 293 K. *Uncertainties on the measurement of resistivity on bulk specimen (∼5%) leads to an uncertainty of a similar magnitude on model results.*

pertinente (i) de la conductivité locale et (ii) des transitions des échelles dans les modèles utilisés.

5 Conclusions et perspectives

En prenant en compte les effets de taille (ou largeur des canaux δ), la température T et la densité de dislocations β à l'aide de la loi Dingle modifiée, nous avons déterminé la conductivité locale $\sigma^{(i)}$ dans chaque phase i. Par un processus itératif, le caractère multi-échelle est pris en compte dans le modèle analytique ACG et dans les calculs par éléments finis HP. Les conductivités effectives $\widetilde{\boldsymbol{\sigma}}$ obtenues par ACG et HP sont parfaitement confondues dans les directions longitudinale et transversale.

Au niveau de l'approximation de la géométrie, nous avons considéré une microstructure formée de motifs co-cylindriques répartis aléatoirement par ACG et périodiquement par HP. Les résultats sur ces deux modélisations sont pratiquement confondus sur tous les zooms. Ce résultat suggère que la distribution des fibres longues joue un rôle mineur sur la conductivité effective $\widetilde{\boldsymbol{\sigma}}$ du conducteur Cu-Nb, dans la direction transversale. Dans la direction longitudinale, il est rappelé que la solution exacte est indépendante du caractère périodique de la microstructure. Ces résultats justifient pleinement l'emploi du modèle ACG en champs moyens pour l'estimation de la conductivité effective, qui permet un gain de temps de calculs très significatif par rapport aux calculs par Eléments Finis. Les conductivités effectives $\widetilde{\boldsymbol{\sigma}}$ déterminées par ACG et HP sont également en bon accord avec les données expérimentales disponibles dans la direction longitudinale.

Ce travail se poursuit actuellement selon les directions suivantes :

1. La méthode classique des quatre pointes ne permet de mesurer que la conductivité longitudinale. Il reste donc à effectuer les mesures de conductivité tranversale pour une validation complète des modèles. Les comparaisons expérimentales à plusieurs températures T seront aussi importantes pour la validation des modèles.
2. Dans ce travail, nous avons utilisé des valeurs théoriques pour les largeurs des canaux δ. Les observations expérimentales montrent cependant une certaine fluctuation de ces largeurs, probablement associées à des hétérogénéités de déformation lors des étapes de mise en forme. Une évaluation plus fine des largeurs effective est en cours pour affiner les prédictions, puisque la largeur des canaux influence sur la conductivité locale.
3. Basée sur les résultats obtenus en conductivité, une approche similaire est en cours afin d'estimer les propriétés élastiques et plastiques, afin de positionner le comportement modélisé de ces fils Cu-Nb sur des cartes d'Ashby, et, à terme, pouvoir en tirer les paramètres microstructuraux importants en vue d'une optimisation du matériau et/ou du procédé d'élaboration.

Remerciements. Les auteurs remercient l'ANR pour le financement du projet METAFORES ANR-12-BS09-0002.

Références

[1] J. Béard, J. Billette, P. Frings, M. Suleiman, F. Lecouturier, *J. Low Temperature Phys.* **170** (2013) 442-446
[2] National Research Council, High Magnetic Field Science and Its Application in the United States : Current Status and Future Directions, The National Academies Press, 2013
[3] L. Frydman, *J. Magnetic Resonance* **242** (2014) 256-264
[4] L. Thilly, F. Lecouturier, Les nanosciences 2 : Nanomatériaux et nanochimie, chapter Applications des nanomatériaux : mécanique : bobines hauts champs, Ed. Belin, coll. Echelles, 2006, pp. 650-658
[5] L. Thilly, Exploration théorique et expérimentale de fils nanocomposites continus présentant des propriétés extrêmes de conductivite électrique et de limite élastique, Ph.D. thesis, Institut National des Sciences Appliquées de Toulouse, 2000
[6] J.B. Dubois, L. Thilly, P.-O. Renault, F. Lecouturier, *Adv. Eng. Mater.* **14** (2012) 998-1003

[7] J.B. Dubois, Conducteurs nanocomposites métalliques élaborés par déformation plastique sévère : formation et stabilité thermo-mécanique des nanostructures, propriétés induites, Ph.D. thesis, Université de Poitiers, 2010
[8] K. Spencer, F. Lecouturier, L. Thilly, J.D. Embury, *Adv. Eng. Mater.* **6** (2004) 290-297
[9] L. Thilly, F. Lecouturier, J. Von Stebut, *Acta Materialia* **50** (2002) 5049-5065
[10] L. Thilly, M. Véron, O. Ludwig, F. Lecouturier, *Mater. Sci. Eng. A* **309** (2001) 510-513
[11] V. Vidal, L. Thilly, F. Lecouturier, P.-O. Renault, *Scripta Materialia* **57** (2007) 245-248
[12] J.B. Dubois, L. Thilly, P.-O. Renault, F. Lecouturier, M. Di Michiel, *Acta Materialia* **58** (2010) 6504-6512
[13] M.J. Demkowicz, L. Thilly, *Acta Materialia* **59** (2011) 7744-7756
[14] L. Thilly, P.-O. Renault, S. Van Petegem, S. Brandstetter, B. Schmitt, H. Van Swygenhoven, V. Vidal, F. Lecouturier, *Appl. Phys. Lett.* **90** (2007) 241907
[15] L. Thilly, S. Van Petegem, P.-O. Renault, F. Lecouturier, V. Vidal, B. Schmitt, H. Van Swygenhoven, *Acta Materialia* **57** (2009) 3157-3169
[16] Z. Hashin, D. Bagchi, B.W. Rosen, Non-linear behavior of fiber composite laminates, NASA (NASA-CR-1974), 1974
[17] E. Hervé, A. Zaoui, *Int. J. Eng. Sci.* **31** (1993) 1-10
[18] E. Hervé, A. Zaoui, *Int. J. Eng. Sci.* **33** (1995) 1419-1433
[19] S. Joannes, E. Hervé-Luanco, Multiscale modeling of transport phenomena for materials with n-layered embedded fibres : an analytical and numerical-based approach, Publication in progress.
[20] J. Besson, G. Cailletaud, J.-L. Chaboche, S. Forest, *Nonlinear mechanics of materials*, Springer, 2009, Vol. 167
[21] S. Forest, G. Cailletaud, D. Jeulin, F. Feyel, I. Galliet, V. Mounoury, S. Quilici, *Mécanique & industries* **3** (2002) 439-456
[22] T. Kanit, S. Forest, I. Galliet, V. Mounoury, D. Jeulin, *Int. J. Solids Struct.* **40** (2003) 3647-3679
[23] R.M. Christensen, K.H. Lo, *J. Mech. Phys. Solids* **27** (1979) 315-330
[24] E Hervé, *Int. J. Solids Struct.* **39** (2002) 1041-1058
[25] J. Sivardière, Symétrie et propriétés physiques – Du principe de Curie aux brisures de symétrie, EDP Sciences, 2008
[26] N.W. Ashcroft, N.D. Mermin, Solid State Physics, Saunders College, 1976
[27] R.B. Dingle, *Proc. Roy. Soc. London. Ser. A. Math. Phys. Sci.* **201** (1950) 545-560
[28] Commission Electrotechnique Internationale, Méthode de mesure de la résistivité des matériaux métalliques, Technical report, Publication CEI 468, 1974

Appendix B

Derivation of mean-field β-model

B.1 Standard thermo-elastic self-consistent scheme

In polycrystals, the local elastic stiffness tensor $\underset{\sim}{\boldsymbol{C}}(\underline{\boldsymbol{x}})$ is a uniform property inside grains. The quantity $\underset{\sim}{\boldsymbol{C}}(\underline{\boldsymbol{x}})$ can therefore be replaced by the corresponding homogeneous values $\underset{\sim}{\boldsymbol{C}}^{(r)}$ of the considered *mechanical phase* (r). As in (Lebensohn et al., 2011; Castelnau, 2011), one defines the phase (r) as denoting the set of all grains in the microstructure that share the same elastic properties and exhibit the same crystal orientation; those grains have however different shapes and environment. Local and effective thermo-elastic constitutive relation writes respectively:

$$\underset{\sim}{\boldsymbol{\varepsilon}}^{(r)} = \underset{\sim}{\boldsymbol{C}}^{(r)-1} : \underset{\sim}{\boldsymbol{\sigma}}^{(r)} + \underset{\sim}{\boldsymbol{\varepsilon}}_0^{(r)}, \quad \overline{\underset{\sim}{\boldsymbol{\varepsilon}}} = \widetilde{\underset{\sim}{\boldsymbol{C}}}^{-1} : \overline{\underset{\sim}{\boldsymbol{\sigma}}} + \widetilde{\underset{\sim}{\boldsymbol{\varepsilon}}}_0 \tag{B.1}$$

where $.^{(r)}$ indicates the average over the volume of phase (r), e.g. $\underset{\sim}{\boldsymbol{\varepsilon}}^{(r)} = \left\langle \underset{\sim}{\boldsymbol{\varepsilon}}(\underline{\boldsymbol{x}}) \right\rangle_{(r)}$. In addition, $\underset{\sim}{\boldsymbol{\varepsilon}}_0^{(r)}$ denotes the uniform stress-free strain associated with temperature changes in thermo-elasticity. In this work, $\underset{\sim}{\boldsymbol{\varepsilon}}_0^{(r)}$ are initially presented in composite materials (e.g. Cu-Nb wires) to generate the residual stresses. According to Castelnau (2011), it can be shown that the effective elastic tensor $\widetilde{\underset{\sim}{\boldsymbol{C}}}$ and the effective stress-free strain $\widetilde{\underset{\sim}{\boldsymbol{\varepsilon}}}_0$ reads:

$$\widetilde{\underset{\sim}{\boldsymbol{C}}}^{-1} = \langle \underset{\sim}{\boldsymbol{C}}^{(r)-1} : \underset{\sim}{\boldsymbol{B}}^{(r)} \rangle \,, \quad \widetilde{\underset{\sim}{\boldsymbol{\varepsilon}}}_0 = \langle \underset{\sim}{\boldsymbol{\varepsilon}}_0^{(r)} : \underset{\sim}{\boldsymbol{B}}^{(r)} \rangle \tag{B.2}$$

with $\underset{\sim}{\boldsymbol{B}}^{(r)}$ denotes the stress localization tensor of the purely elastic problem. To estimate the phase-average stress and strain, phase (r) is treated in SSC scheme as an ellipsoidal inclusion embedded in an HEM whose behavior represents that of the polycrystal. Eshelby's inclusion formalism Eshelby (1957) is used to describe the interaction between each phase and the aggregates. According to (François et al., 1998; Qu and

Cherkaoui, 2006; Nemat-Nasser and Hori, 2013), $\underset{\sim}{\underset{\sim}{\boldsymbol{B}}}^{(r)}$ is derived as:

$$\underset{\sim}{\underset{\sim}{\boldsymbol{B}}}^{(r)} = \underset{\sim}{\underset{\sim}{\boldsymbol{C}}}^{(r)} : \left[\underset{\sim}{\underset{\sim}{\boldsymbol{I}}} + \underset{\sim}{\underset{\sim}{\boldsymbol{S}}}_{\text{Esh}} : \widetilde{\underset{\sim}{\underset{\sim}{\boldsymbol{C}}}}^{-1} : \left(\underset{\sim}{\underset{\sim}{\boldsymbol{C}}}^{(r)} - \widetilde{\underset{\sim}{\underset{\sim}{\boldsymbol{C}}}}\right)\right]^{-1} : \widetilde{\underset{\sim}{\underset{\sim}{\boldsymbol{C}}}}^{-1}. \tag{B.3}$$

with $\underset{\sim}{\underset{\sim}{\boldsymbol{I}}}$ the fourth order identity tensor and $\underset{\sim}{\underset{\sim}{\boldsymbol{S}}}_{\text{Esh}}$ the Eshelby tensor. In addition, $\underset{\sim}{\underset{\sim}{\boldsymbol{S}}}_{\text{Esh}}$ is calculated as function of $\widetilde{\underset{\sim}{\underset{\sim}{\boldsymbol{C}}}}$ and morphology of the spheroid $\ell \times d \times d$ (Mura, 1987; Suvorov and Dvorak, 2002).

Moreover, if we compute a statistically sufficiently large equivalent volume (i.e. RVE), we will found:

$$\langle \underset{\sim}{\underset{\sim}{\boldsymbol{B}}}^{(r)} \rangle = \underset{\sim}{\underset{\sim}{\boldsymbol{I}}} \tag{B.4}$$

The phase average stress $\underset{\sim}{\boldsymbol{\sigma}}^{(r)}$ is expressed by a scale transition rule:

$$\underset{\sim}{\boldsymbol{\sigma}}^{(r)} = \underset{\sim}{\underset{\sim}{\boldsymbol{B}}}^{(r)} : \overline{\underset{\sim}{\boldsymbol{\sigma}}} + \underset{\sim}{\boldsymbol{\sigma}}_{\text{res}}^{(r)} \tag{B.5}$$

with $\overline{\underset{\sim}{\boldsymbol{\sigma}}}$ and $\underset{\sim}{\boldsymbol{\sigma}}_{\text{res}}^{(r)}$ being the macroscopic applied stress and initial residual stresses in phase (r) respectively. In the initial state before loading (i.e. t <0), the macroscopic stress $\overline{\underset{\sim}{\boldsymbol{\sigma}}} = \underset{\sim}{\mathbf{0}}$ to ensure equilibrium. This leads to $\overline{\underset{\sim}{\boldsymbol{\varepsilon}}}$=$\widetilde{\underset{\sim}{\boldsymbol{\varepsilon}}}_0$ and $\underset{\sim}{\boldsymbol{\sigma}}^{(r)}$=$\underset{\sim}{\boldsymbol{\sigma}}_{\text{res}}^{(r)}$ by using Equations (B.1) and (B.5) respectively. Based on the initial stress-strain state, $\underset{\sim}{\boldsymbol{\sigma}}_{\text{res}}^{(r)}$ can be written as follows (Brenner et al., 2004):

$$\underset{\sim}{\boldsymbol{\sigma}}_{\text{res}}^{(r)} = \left(\underset{\sim}{\underset{\sim}{\boldsymbol{C}}}^{(r)-1} + \underset{\sim}{\underset{\sim}{\boldsymbol{C}}}^{*-1}\right)^{-1} : \left(\widetilde{\underset{\sim}{\boldsymbol{\varepsilon}}}_0 - \underset{\sim}{\boldsymbol{\varepsilon}}_0^{(r)}\right) \tag{B.6}$$

where the effective stress-free strain $\overline{\underset{\sim}{\boldsymbol{\varepsilon}}}_0$ is given in Eq. B.2. In addition, the "Hill's constraint tensor" $\underset{\sim}{\underset{\sim}{\boldsymbol{C}}}^*$ is introduced for simplifying deviations:

$$\underset{\sim}{\underset{\sim}{\boldsymbol{C}}}^* = \widetilde{\underset{\sim}{\underset{\sim}{\boldsymbol{C}}}} : \left(\underset{\sim}{\underset{\sim}{\boldsymbol{S}}}_{\text{Esh}}^{-1} - \underset{\sim}{\underset{\sim}{\boldsymbol{I}}}\right). \tag{B.7}$$

At t >0, it is worth noting that $\underset{\sim}{\boldsymbol{\varepsilon}}^{(r)} \neq \underset{\sim}{\boldsymbol{\varepsilon}}_0^{(r)}$. Based on Eq. B.1:

$$\underset{\sim}{\boldsymbol{\varepsilon}}^{(r)} = \underset{\sim}{\underset{\sim}{\boldsymbol{C}}}^{(r)-1} : \underset{\sim}{\boldsymbol{\sigma}}_{\text{res}}^{(r)} + \underset{\sim}{\boldsymbol{\varepsilon}}_0^{(r)} \tag{B.8}$$

where $\underset{\sim}{\boldsymbol{\sigma}}_{\text{res}}^{(r)}$ can be calculated in Eq. B.6. Thus before loading, local strain $\underset{\sim}{\boldsymbol{\varepsilon}}^{(r)}$ contains (1) the stress-free strain $\underset{\sim}{\boldsymbol{\varepsilon}}_0^{(r)}$ and (2) another elastic strain due to the equilibrium of aggregates.

B.2 Hill's elasto-plastic homogenization model

(Hill, 1965a; Turner and Tomé, 1994; Zecevic and Knezevic, 2015) introduced an incremental self-consistent homogenization model for the elasto-plastic behavior of polycrystalline aggregates. The linearized local and effective rate-independent constitutive relations are written respectively:

$$\dot{\underset{\sim}{\boldsymbol{\sigma}}}^{(r)} = \underset{\sim\sim}{\boldsymbol{L}}^{(r)} : \dot{\underset{\sim}{\boldsymbol{\varepsilon}}}^{(r)}, \qquad \dot{\overline{\underset{\sim}{\boldsymbol{\sigma}}}} = \widetilde{\underset{\sim\sim}{\boldsymbol{L}}} : \dot{\overline{\underset{\sim}{\boldsymbol{\varepsilon}}}} \tag{B.9}$$

where $\dot{\underset{\sim}{\boldsymbol{\sigma}}}$ and $\dot{\underset{\sim}{\boldsymbol{\varepsilon}}}$ are the stress and strain rate and $\underset{\sim\sim}{\boldsymbol{L}}$ the elasto-plastic stiffness tensor. Similarly to the elastic SSC scheme, in Hill's model, stress equilibrium is solved for one phase embedded in the HEM using the Eshelby formalism. The stress rate and strain rate are related through the following interaction equation:

$$\begin{cases} \dot{\overline{\underset{\sim}{\boldsymbol{\sigma}}}} - \dot{\underset{\sim}{\boldsymbol{\sigma}}}^{(r)} = -\underset{\sim\sim}{\boldsymbol{L}}^{*} : \left(\dot{\overline{\underset{\sim}{\boldsymbol{\varepsilon}}}} - \dot{\underset{\sim}{\boldsymbol{\varepsilon}}}^{(r)} \right) , \\ \\ \quad \underset{\sim\sim}{\boldsymbol{L}}^{*} = \widetilde{\underset{\sim\sim}{\boldsymbol{L}}} : \left(\underset{\sim\sim}{\boldsymbol{S}}_{\mathrm{Esh}}^{-1} - \underset{\sim\sim}{\boldsymbol{I}} \right) . \end{cases} \tag{B.10}$$

Here, it is worth noting that the Eshelby tensor $\underset{\sim\sim}{\boldsymbol{S}}_{\mathrm{Esh}}$ is determined by the effective elasto-plastic instantaneous moduli $\widetilde{\underset{\sim\sim}{\boldsymbol{L}}}$ and the grain aspect ratio ℓ/d. In this elasto-plastic model, the total strain rate $\dot{\underset{\sim}{\boldsymbol{\varepsilon}}}$ is decomposed into elastic strain rate $\dot{\underset{\sim}{\boldsymbol{\varepsilon}}}_{\mathrm{e}}$ and plastic strain rate $\dot{\underset{\sim}{\boldsymbol{\varepsilon}}}_{\mathrm{p}}$. The local and effective relations are written as follow

$$\dot{\underset{\sim}{\boldsymbol{\varepsilon}}}^{(r)} = \dot{\underset{\sim}{\boldsymbol{\varepsilon}}}_{\mathrm{e}}^{(r)} + \dot{\underset{\sim}{\boldsymbol{\varepsilon}}}_{\mathrm{p}}^{(r)}, \qquad \dot{\overline{\underset{\sim}{\boldsymbol{\varepsilon}}}} = \dot{\widetilde{\underset{\sim}{\boldsymbol{\varepsilon}}}}_{\mathrm{e}} + \dot{\widetilde{\underset{\sim}{\boldsymbol{\varepsilon}}}}_{\mathrm{p}} . \tag{B.11}$$

In addition, the stress rate $\dot{\underset{\sim}{\boldsymbol{\sigma}}}$ is computed by Hooke's law:

$$\dot{\underset{\sim}{\boldsymbol{\sigma}}}^{(r)} = \underset{\sim\sim}{\boldsymbol{C}}^{(r)} : \dot{\underset{\sim}{\boldsymbol{\varepsilon}}}_{\mathrm{e}}^{(r)}, \qquad \dot{\overline{\underset{\sim}{\boldsymbol{\sigma}}}} = \widetilde{\underset{\sim\sim}{\boldsymbol{C}}} : \dot{\widetilde{\underset{\sim}{\boldsymbol{\varepsilon}}}}_{\mathrm{e}} \tag{B.12}$$

where $\widetilde{\underset{\sim}{\boldsymbol{\varepsilon}}}_{\mathrm{e}}$ ($\neq \overline{\underset{\sim}{\boldsymbol{\varepsilon}}}_{\mathrm{e}}$) denotes the macroscopic elastic strain response by the applied $\overline{\underset{\sim}{\boldsymbol{\sigma}}}$. Similarly, $\widetilde{\underset{\sim}{\boldsymbol{\varepsilon}}}_{\mathrm{p}}$ in Eq.(B.11) is the plastic response. In order to take the initial residual stresses into account, the local strain $\underset{\sim}{\boldsymbol{\varepsilon}}^{(r)}$ of Eq.(B.11) is initialized as stress-free strain $\underset{\sim}{\boldsymbol{\varepsilon}}_{0}^{(r)}$. Then the incremental self-consistent scheme will find macroscopic equilibrium itself (see Eq.(B.8) for $\underset{\sim}{\boldsymbol{\varepsilon}}^{(r)}$ before loading), as mentioned in Turner and Tomé (1994).

The following derivations of Hill's elasto-plastic model will be used for the so-called β-model. Multiplying Eq.(B.10) by $\underset{\sim}{\boldsymbol{S}}_{\text{Esh}} : \widetilde{\underset{\sim}{\boldsymbol{L}}}^{-1}$:

$$
\begin{aligned}
&\underset{\sim}{\boldsymbol{S}}_{\text{Esh}} : \widetilde{\underset{\sim}{\boldsymbol{L}}}^{-1} : \dot{\underset{\sim}{\boldsymbol{\sigma}}}^{(r)} = \underset{\sim}{\boldsymbol{S}}_{\text{Esh}} : \widetilde{\underset{\sim}{\boldsymbol{L}}}^{-1} : \dot{\underset{\sim}{\boldsymbol{\sigma}}} + \left(\underset{\sim}{\boldsymbol{I}} - \underset{\sim}{\boldsymbol{S}}_{\text{Esh}}\right) : \left(\dot{\underset{\sim}{\boldsymbol{\varepsilon}}} - \dot{\underset{\sim}{\boldsymbol{\varepsilon}}}^{(r)}\right) \\
&\Leftrightarrow \\
&\underset{\sim}{\boldsymbol{S}}_{\text{Esh}} : \widetilde{\underset{\sim}{\boldsymbol{L}}}^{-1} : \dot{\underset{\sim}{\boldsymbol{\sigma}}}^{(r)} = \\
&\underset{\sim}{\boldsymbol{S}}_{\text{Esh}} : \widetilde{\underset{\sim}{\boldsymbol{L}}}^{-1} : \dot{\underset{\sim}{\boldsymbol{\sigma}}} + \left(\underset{\sim}{\boldsymbol{I}} - \underset{\sim}{\boldsymbol{S}}_{\text{Esh}}\right) : \left(\widetilde{\underset{\sim}{\boldsymbol{C}}}^{-1} : \dot{\underset{\sim}{\boldsymbol{\sigma}}} + \dot{\underset{\sim}{\boldsymbol{\varepsilon}}}_{\text{p}} - \underset{\sim}{\boldsymbol{C}}^{(r)-1} : \dot{\underset{\sim}{\boldsymbol{\sigma}}}^{(r)} - \dot{\underset{\sim}{\boldsymbol{\varepsilon}}}_{\text{p}}^{(r)}\right) \\
&\Leftrightarrow \\
&\left[\underset{\sim}{\boldsymbol{S}}_{\text{Esh}} : \widetilde{\underset{\sim}{\boldsymbol{L}}}^{-1} + \left(\underset{\sim}{\boldsymbol{I}} - \underset{\sim}{\boldsymbol{S}}_{\text{Esh}}\right) : \underset{\sim}{\boldsymbol{C}}^{(r)-1}\right] : \dot{\underset{\sim}{\boldsymbol{\sigma}}}^{(r)} = \\
&\left[\underset{\sim}{\boldsymbol{S}}_{\text{Esh}} : \widetilde{\underset{\sim}{\boldsymbol{L}}}^{-1} + \left(\underset{\sim}{\boldsymbol{I}} - \underset{\sim}{\boldsymbol{S}}_{\text{Esh}}\right) : \widetilde{\underset{\sim}{\boldsymbol{C}}}^{-1}\right] : \dot{\underset{\sim}{\boldsymbol{\sigma}}} + \left(\underset{\sim}{\boldsymbol{I}} - \underset{\sim}{\boldsymbol{S}}_{\text{Esh}}\right) : \left(\dot{\underset{\sim}{\boldsymbol{\varepsilon}}}_{\text{p}} - \dot{\underset{\sim}{\boldsymbol{\varepsilon}}}_{\text{p}}^{(r)}\right)
\end{aligned}
$$

Eq.(B.10) can be rewritten taking Equations (B.11) and (B.12) into account:

$$
\dot{\underset{\sim}{\boldsymbol{\sigma}}}^{(r)} = \underset{\sim}{\boldsymbol{a}}_{\text{L}}^{(r)-1} : \left[\widetilde{\underset{\sim}{\boldsymbol{a}}}_{\text{L}} : \dot{\underset{\sim}{\boldsymbol{\sigma}}} + \left(\underset{\sim}{\boldsymbol{I}} - \underset{\sim}{\boldsymbol{S}}_{\text{Esh}}\right) : \left(\dot{\underset{\sim}{\boldsymbol{\varepsilon}}}_{\text{p}} - \dot{\underset{\sim}{\boldsymbol{\varepsilon}}}_{\text{p}}^{(r)}\right)\right] \tag{B.13}
$$

where we define

$$
\begin{aligned}
\underset{\sim}{\boldsymbol{a}}_{\text{L}}^{(r)} &= \underset{\sim}{\boldsymbol{S}}_{\text{Esh}} : \widetilde{\underset{\sim}{\boldsymbol{L}}}^{-1} + \left(\underset{\sim}{\boldsymbol{I}} - \underset{\sim}{\boldsymbol{S}}_{\text{Esh}}\right) : \underset{\sim}{\boldsymbol{C}}^{(r)-1}, \\
\widetilde{\underset{\sim}{\boldsymbol{a}}}_{\text{L}} &= \underset{\sim}{\boldsymbol{S}}_{\text{Esh}} : \widetilde{\underset{\sim}{\boldsymbol{L}}}^{-1} + \left(\underset{\sim}{\boldsymbol{I}} - \underset{\sim}{\boldsymbol{S}}_{\text{Esh}}\right) : \widetilde{\underset{\sim}{\boldsymbol{C}}}^{-1}.
\end{aligned} \tag{B.14}
$$

B.3 Kröner's assumption

In this formulation, Kröner (1961) treated $\underset{\sim}{\boldsymbol{\varepsilon}}_{\text{p}}$ as a stress-free strain, and assumed the accommodation to be purely elastic. This leads to $\underset{\sim}{\boldsymbol{L}}^{*}$ in Eq. B.10 replaced by $\widetilde{\underset{\sim}{\boldsymbol{C}}} : \left(\underset{\sim}{\boldsymbol{S}}_{\text{Esh}}^{-1} - \underset{\sim}{\boldsymbol{I}}\right)$, where $\underset{\sim}{\boldsymbol{S}}_{\text{Esh}}$ is calculated with respect to $\widetilde{\underset{\sim}{\boldsymbol{C}}}$ instead of $\widetilde{\underset{\sim}{\boldsymbol{L}}}$. Thus $\underset{\sim}{\boldsymbol{a}}_{\text{L}}^{(r)}$ and $\widetilde{\underset{\sim}{\boldsymbol{a}}}_{\text{L}}$ in Eq.(B.14) become:

$$
\begin{aligned}
\underset{\sim}{\boldsymbol{a}}_{\text{L}}^{(r)} &= \underset{\sim}{\boldsymbol{S}}_{\text{Esh}} : \widetilde{\underset{\sim}{\boldsymbol{C}}}^{-1} + \left(\underset{\sim}{\boldsymbol{I}} - \underset{\sim}{\boldsymbol{S}}_{\text{Esh}}\right) : \underset{\sim}{\boldsymbol{C}}^{(r)-1}, \\
\widetilde{\underset{\sim}{\boldsymbol{a}}}_{\text{L}} &= \widetilde{\underset{\sim}{\boldsymbol{C}}}^{-1}.
\end{aligned} \tag{B.15}
$$

Substituting Eq.(B.15) in Eq.(B.13)

$$
\dot{\underset{\sim}{\boldsymbol{\sigma}}}^{(r)} = \underset{\sim}{\boldsymbol{B}}^{(r)} : \left[\dot{\underset{\sim}{\boldsymbol{\sigma}}} + \underset{\sim}{\boldsymbol{L}}_{\text{C}}^{*} : \left(\dot{\underset{\sim}{\boldsymbol{\varepsilon}}}_{\text{p}} - \dot{\underset{\sim}{\boldsymbol{\varepsilon}}}_{\text{p}}^{(r)}\right)\right] \tag{B.16}
$$

where $\underset{\sim}{\underset{\sim}{\boldsymbol{B}}}^{(r)}$ is the stress localization tensor of elastic problem (see Eq.(B.3)) and the tensor $\underset{\sim}{\underset{\sim}{\boldsymbol{L}}}^{*}_{\mathrm{C}}$ is expressed as follow

$$\underset{\sim}{\underset{\sim}{\boldsymbol{L}}}^{*}_{\mathrm{C}} = \underset{\sim}{\underset{\sim}{\widetilde{\boldsymbol{C}}}} : \left(\underset{\sim}{\underset{\sim}{\boldsymbol{I}}} - \underset{\sim}{\underset{\sim}{\boldsymbol{S}}}_{\mathrm{Esh}}\right) \tag{B.17}$$

with $\underset{\sim}{\underset{\sim}{\boldsymbol{L}}}^{*}_{\mathrm{C}} = \underset{\sim}{\underset{\sim}{\boldsymbol{C}}}^{*} : \underset{\sim}{\underset{\sim}{\boldsymbol{S}}}_{\mathrm{Esh}}$ based on Eq.(B.7). Moreover, the computations of Eshelby tensor $\underset{\sim}{\underset{\sim}{\boldsymbol{S}}}_{\mathrm{Esh}}$ will receive further attention in Section B.4 for both Kröner's elasto-plastic homogenization model (Kröner, 1961) and β-model.

The interaction in Eq.(B.16) is purely elastic due to Kröner's assumption, which can be shown to result in a too stiff behavior and the internal stresses significantly overestimated (Masson and Zaoui, 1999). Compared with Hill's model of Section B.2, the nonlinearity of the operator multiplying the difference between global and local plastic strain tensors is not introduced. Nevertheless, this assumption can be taken as a new starting point for an alternative approach, i.e. the β-model, where the nonlinearity is transferred to the term that represents heterogeneity.

B.4 β-model

B.4.1 β-model with heterogeneous local elastic behavior

According to (Cailletaud, 1992; Forest and Pilvin, 1996; Sai et al., 2006; Besson et al., 2009; Martin et al., 2014; Coudon et al., 2017), the heuristic β-model is proposed, introducing an interphase accommodation variable $\underset{\sim}{\boldsymbol{\beta}}^{(r)}$ to replace the local plastic strain $\underset{\sim}{\boldsymbol{\varepsilon}}_{\mathrm{p}}^{(r)}$ in Eq.(B.16). In small-strain loading conditions, i.e. with negligible microstructure evolution, $\underset{\sim}{\underset{\sim}{\boldsymbol{B}}}^{(r)}$ and $\underset{\sim}{\underset{\sim}{\boldsymbol{L}}}^{*}_{\mathrm{C}}$ in Eq. B.16 are constants. By integrating Eq.(B.16), the scale transition interaction equation is obtained with considering both the elastic local heterogeneity and the plastic one:

$$\underset{\sim}{\boldsymbol{\sigma}}^{(r)} = \underset{\sim}{\underset{\sim}{\boldsymbol{B}}}^{(r)} : \left[\overline{\underset{\sim}{\boldsymbol{\sigma}}} + \underset{\sim}{\underset{\sim}{\boldsymbol{L}}}^{*}_{\mathrm{C}} : \left(\underset{\sim}{\widetilde{\boldsymbol{\beta}}} - \underset{\sim}{\boldsymbol{\beta}}^{(r)}\right)\right] + \underset{\sim}{\boldsymbol{\sigma}}^{(r)}_{\mathrm{res}}, \tag{B.18}$$

here $\underset{\sim}{\underset{\sim}{\boldsymbol{B}}}^{(r)}$, $\underset{\sim}{\underset{\sim}{\boldsymbol{L}}}^{*}_{\mathrm{C}}$ and $\underset{\sim}{\boldsymbol{\sigma}}^{(r)}_{\mathrm{res}}$ are still given by Equations (B.3), (B.17) and (B.6) respectively. In Eq. (B.18), $\underset{\sim}{\boldsymbol{\sigma}}^{(r)}$ is initialized as $\underset{\sim}{\boldsymbol{\sigma}}^{(r)}_{\mathrm{res}}$ before loading, to take the initial residual stresses into account. Analogous to $\underset{\sim}{\boldsymbol{\varepsilon}}_{\mathrm{p}}^{(r)}$, the $\underset{\sim}{\boldsymbol{\beta}}^{(r)}$ variables are also initialized as $\underset{\sim}{\mathbf{0}}$. In the elastic regime without plastic activities, Eq.(B.18) can be reduced to Eq.(B.5).

Furthermore, it should be noted that in the β-model (or Kröner's elasto-plastic model), $\underset{\sim}{\underset{\sim}{\boldsymbol{S}}}_{\mathrm{Esh}}$ is computed by using the effective elastic tensor $\underset{\sim}{\underset{\sim}{\widetilde{\boldsymbol{C}}}}$ (instead of $\underset{\sim}{\underset{\sim}{\widetilde{\boldsymbol{L}}}}$) in the HEM and the grain aspect ratio ℓ/d. In this way, the CPU time of β-model can be saved, as $\underset{\sim}{\underset{\sim}{\boldsymbol{S}}}_{\mathrm{Esh}}$ needs just one calculation. In contrast, Hill's model (Section B.2) must calculate $\underset{\sim}{\underset{\sim}{\boldsymbol{S}}}_{\mathrm{Esh}}$ during the whole load due to the various $\underset{\sim}{\underset{\sim}{\widetilde{\boldsymbol{L}}}}$.

Inspired from the kinematic hardening evolution rule of Lemaitre and Chaboche (1994), a time-independent non-linear evolution equation is used with respect to plastic strain:

$$\dot{\underset{\sim}{\boldsymbol{\beta}}}^{(r)} = \dot{\underset{\sim}{\boldsymbol{\varepsilon}}}_{\mathrm{p}}^{(r)} - \underset{\sim}{\underset{\sim}{\boldsymbol{D}}} : \underset{\sim}{\boldsymbol{\beta}}^{(r)} \| \dot{\underset{\sim}{\boldsymbol{\varepsilon}}}_{\mathrm{p}}^{(r)} \| \tag{B.19}$$

where $\underset{\sim}{\underset{\sim}{\boldsymbol{D}}}$ denotes a constant phenomenological tensor to be calibrated in order to correct the errors caused by the assumption of Kröner (1961) $\underset{\sim}{\underset{\sim}{\widetilde{\boldsymbol{L}}}}=\underset{\sim}{\underset{\sim}{\widetilde{\boldsymbol{C}}}}$. The form of $\underset{\sim}{\underset{\sim}{\boldsymbol{D}}}$ and its identification are shown in Section 5.3.2 and Section 5.4 respectively. In addition, the equivalent overall plastic strain rate is expressed as:

$$\| \dot{\underset{\sim}{\boldsymbol{\varepsilon}}}_{\mathrm{p}}^{(r)} \| = \sqrt{\frac{2}{3} (\dot{\varepsilon}_{\mathrm{p}}^{(r)})_{ij} (\dot{\varepsilon}_{\mathrm{p}}^{(r)})_{ij}} \, . \tag{B.20}$$

As mentioned in Section B.1, $\langle \underset{\sim}{\boldsymbol{\sigma}}_{\mathrm{res}}^{(r)} \rangle = \underset{\sim}{\mathbf{0}}$ due to the aggregate equilibrium in the initial state. Moreover, reminding that the homogenization condition $\overline{\underset{\sim}{\boldsymbol{\sigma}}} = \langle \underset{\sim}{\boldsymbol{\sigma}}^{(r)} \rangle$ must be ensured, this leads to the determination of the effective accommodation variable $\underset{\sim}{\widetilde{\boldsymbol{\beta}}}$ by combining Equations (B.18) and (B.4):

$$\underset{\sim}{\widetilde{\boldsymbol{\beta}}} = \langle \underset{\sim}{\underset{\sim}{\boldsymbol{L}}}_{\mathrm{C}}^{*-1} : \underset{\sim}{\underset{\sim}{\boldsymbol{B}}}^{(r)} : \underset{\sim}{\underset{\sim}{\boldsymbol{L}}}_{\mathrm{C}}^{*} : \underset{\sim}{\boldsymbol{\beta}}^{(r)} \rangle \, . \tag{B.21}$$

B.4.2 β-model with homogeneous local elastic behavior

The previous section presents a new extension of β-model taking into account the heterogeneous local elasticity (Ausias et al., 2007; Coudon et al., 2017) and initial residual stresses $\underset{\sim}{\boldsymbol{\sigma}}_{\mathrm{res}}^{(r)}$. In this section, we recall the relation between this new extension and the earlier versions of β-model, e.g. Sai et al. (2006); Martin et al. (2014).

According to the earlier versions, it is assumed that the main source of mechanical heterogeneity is plasticity more than elasticity (Cailletaud, 1992; Besson et al., 2009). In other words, the polycrystalline aggregates exhibit a homogeneous local elastic law: $\underset{\sim}{\underset{\sim}{\boldsymbol{C}}}^{(r)}=\underset{\sim}{\underset{\sim}{\boldsymbol{C}}}=\underset{\sim}{\underset{\sim}{\widetilde{\boldsymbol{C}}}}$. In this case, the stress localization tensor $\underset{\sim}{\underset{\sim}{\boldsymbol{B}}}^{(r)}$ in Eq.(B.3) becomes $\underset{\sim}{\underset{\sim}{\boldsymbol{I}}}$. In addition, $\underset{\sim}{\widetilde{\boldsymbol{\beta}}}$ is derived as $\langle \underset{\sim}{\boldsymbol{\beta}}^{(r)} \rangle$, i.e. $\overline{\underset{\sim}{\boldsymbol{\beta}}}$, based on Eq.(B.21). Therefore, Eq.(B.18) can be simplified as follows assuming $\underset{\sim}{\boldsymbol{\sigma}}_{\mathrm{res}}^{(r)}=\underset{\sim}{\mathbf{0}}$:

$$\underset{\sim}{\boldsymbol{\sigma}}^{(r)} = \overline{\underset{\sim}{\boldsymbol{\sigma}}} + \underset{\sim}{\underset{\sim}{\boldsymbol{L}}}_{\mathrm{C}}^{*} : \left(\overline{\underset{\sim}{\boldsymbol{\beta}}} - \underset{\sim}{\boldsymbol{\beta}}^{(r)} \right) \tag{B.22}$$

where $\underset{\sim}{\underset{\sim}{\boldsymbol{L}}}_{\mathrm{C}}^{*}$ and $\underset{\sim}{\boldsymbol{\beta}}^{(r)}$ are given by Equations (B.17) and (B.19) respectively.

In particular, if the phenomenological tensor $\underset{\sim}{\underset{\sim}{\boldsymbol{D}}}$ in Eq.(B.19) vanishes, we get $\underset{\sim}{\boldsymbol{\beta}}^{(r)} = \underset{\sim}{\boldsymbol{\varepsilon}}_{\mathrm{p}}^{(r)}$ and therefore $\overline{\underset{\sim}{\boldsymbol{\beta}}} = \overline{\underset{\sim}{\boldsymbol{\varepsilon}}}_{\mathrm{p}}$. In this case, the β-model reduces to Kröner's elasto-plastic homogenization model (Kröner, 1961):

$$\underset{\sim}{\boldsymbol{\sigma}}^{(r)} = \overline{\underset{\sim}{\boldsymbol{\sigma}}} + \underset{\sim}{\underset{\sim}{\boldsymbol{L}}}_{\mathrm{C}}^{*} : \left(\overline{\underset{\sim}{\boldsymbol{\varepsilon}}}_{\mathrm{p}} - \underset{\sim}{\boldsymbol{\varepsilon}}_{\mathrm{p}}^{(r)} \right) \, . \tag{B.23}$$

Bibliography

Ashcroft, N. W. and Mermin, N. D. (2010). Solid state physics (saunders college, philadelphia, 1976). *Appendix N*.

Ausias, G., Thuillier, S., Omnes, B., Wiessner, S., and Pilvin, P. (2007). Micromechanical model of TPE made of polypropylene and rubber waste. *Polymer*, 48(11):3367–3376.

Badinier, G., Sinclair, C., Allain, S., and Bouaziz, O. (2014). The Bauschinger effect in drawn and annealed nanocomposite Cu–Nb wires. *Materials Science and Engineering: A*, 597:10–19.

Barbe, F., Decker, L., Jeulin, D., and Cailletaud, G. (2001a). Intergranular and intragranular behavior of polycrystalline aggregates. part 1: FE model. *International journal of plasticity*, 17(4):513–536.

Barbe, F., Decker, L., Jeulin, D., and Cailletaud, G. (2001b). Intergranular and intragranular behavior of polycrystalline aggregates. Part 1: FE model. *International journal of plasticity*, 17(4):513–536.

Barbe, F., Forest, S., and Cailletaud, G. (2001c). Intergranular and intragranular behavior of polycrystalline aggregates. Part 2: Results. *International Journal of Plasticity*, 17(4):537–563.

Batchelor, G. (1974). Transport properties of two-phase materials with random structure. *Annual Review of Fluid Mechanics*, 6(1):227–255.

Béard, J., Billette, J., Frings, P., Suleiman, M., and Lecouturier, F. (2013). Special coils development at the national high magnetic field laboratory in toulouse. *Journal of Low Temperature Physics*, 170(5-6):442–446.

Behzad, T. and Sain, M. (2007). Measurement and prediction of thermal conductivity for hemp fiber reinforced composites. *Polymer Engineering & Science*, 47(7):977–983.

Berveiller, M. and Zaoui, A. (1978). An extension of the self-consistent scheme to plastically-flowing polycrystals. *Journal of the Mechanics and Physics of Solids*, 26(5-6):325–344.

Besson, J., Cailletaud, G., Chaboche, J., and Forest, S. (2009). *Non-linear mechanics of materials*, volume 167. Springer.

Beurthey, S. and Zaoui, A. (2000). Structural morphology and relaxation spectra of viscoelastic heterogeneous materials. *European Journal of Mechanics-A/Solids*, 19(1):1–16.

Beyerlein, I. J., Mayeur, J. R., Zheng, S., Mara, N. A., Wang, J., and Misra, A. (2014). Emergence of stable interfaces under extreme plastic deformation. *Proceedings of the national academy of sciences*, 111(12):4386–4390.

Böhlke, T., Fritzen, F., Joechen, K., and Tsotsova, R. (2009). Numerical methods for the quantification of the mechanical properties of crystal aggregates with morphologic and crystallographic texture. *International Journal of Material Forming*, 2(1):915–917.

Böhlke, T., Jöchen, K., Kraft, O., Löhe, D., and Schulze, V. (2010). Elastic properties of polycrystalline microcomponents. *Mechanics of Materials*, 42(1):11–23.

Brenner, R., Castelnau, O., and Badea, L. (2004). Mechanical field fluctuations in polycrystals estimated by homogenization techniques. *Proceedings of the Royal Society of London. Series A: Mathematical, Physical and Engineering Sciences*, 460(2052):3589–3612.

Budiansky, B. (1965). On the elastic moduli of some heterogeneous materials. *Journal of the Mechanics and Physics of Solids*, 13(4):223–227.

Cailletaud, G. (1992). A micromechanical approach to inelastic behaviour of metals. *International Journal of Plasticity*, 8(1):55–73.

Cailletaud, G., Forest, S., Jeulin, D., Feyel, F., Galliet, I., Mounoury, V., and Quilici, S. (2003). Some elements of microstructural mechanics. *Computational Materials Science*, 27(3):351–374.

Caré, S. and Hervé, E. (2004). Application of a n-phase model to the diffusion coefficient of chloride in mortar. *Transport in Porous Media*, 56(2):119–135.

Carroll, K. (1965). Elastic Constants of Niobium 4.2 to 300 K. *Journal of Applied Physics*, 36(11):3689–3690.

Castelnau, O. (2011). Mechanical behavior of polycrystalline materials. In Thomas, O., Ponchet, A., Forest, S., et al., editors, *Mechanics of Nano-objects*, chapter 5, pages 301–322. Presses des MINES, Paris.

Chan, J. (1994). Four-point probe manual. *Microfabrication Laboratory, University of California at Berkeley, Spring*.

Christensen, R. and Lo, K. (1979). Solutions for effective shear properties in three phase sphere and cylinder models. *Journal of the Mechanics and Physics of Solids*, 27(4):315–330.

Coudon, F., Cailletaud, G., and Cormier, J. (2017). Mean-field modeling of the anisotropic behavior of directionally solidified superalloys. In preparation for "International Journal of Plasticity".

Devincre, B., Hoc, T., and Kubin, L. (2008). Dislocation mean free paths and strain hardening of crystals. *Science*, 320(5884):1745–1748.

Dingle, R. (1950). The electrical conductivity of thin wires. In *Proceedings of the Royal Society of London A: Mathematical, Physical and Engineering Sciences*, volume 201, pages 545–560. The Royal Society.

Doghri, I., Brassart, L., Adam, L., and Gérard, J.-S. (2011). A second-moment incremental formulation for the mean-field homogenization of elasto-plastic composites. *International Journal of Plasticity*, 27(3):352–371.

Dubois, J. (2010). *Conducteurs nanocomposites métalliques élaborés par déformation plastique sévère : formation et stabilité thermo-mécanique des nanostructures, propriétés induites*. PhD thesis, Université de Poitiers.

Dubois, J., Thilly, L., Renault, P., and Lecouturier, F. (2012). Cu–Nb nanocomposite wires processed by severe plastic deformation: Effects of the multi-scale microstructure and internal stresses on elastic-plastic properties. *Advanced Engineering Materials*, 14(11):998–1003.

Dubois, J., Thilly, L., Renault, P., Lecouturier, F., and Di Michiel, M. (2010). Thermal stability of nanocomposite metals: In situ observation of anomalous residual stress relaxation during annealing under synchrotron radiation. *Acta Materialia*, 58(19):6504–6512.

Dupouy, F., Askenazy, S., Peyrade, J., and Legat, D. (1995). Composite conductors for high pulsed magnetic fields. *Physica B: Condensed Matter*, 211(1):43–45.

Dupouy, F., Snoeck, E., Casanove, M., Roucau, C., Peyrade, J., and Askenazy, S. (1996). Microstructural characterization of high strength and high conductivity nanocomposite wires. *Scripta materialia*, 34(7):1067–1073.

Epstein, S. and Carlson, O. (1965). The elastic constants of nickel-copper alloy single crystals. *Acta Metallurgica*, 13(5):487–491.

Eshelby, J. D. (1957). The determination of the elastic field of an ellipsoidal inclusion, and related problems. In *Proceedings of the Royal Society of London A: Mathematical, Physical and Engineering Sciences*, volume 241, pages 376–396. The Royal Society.

Feyel, F. and Chaboche, J.-L. (2000). FE2 multiscale approach for modelling the elastoviscoplastic behaviour of long fibre SiC/Ti composite materials. *Computer methods in applied mechanics and engineering*, 183(3):309–330.

Flaquer, J., Ríos, A., Martín-Meizoso, A., Nogales, S., and Böhm, H. (2007). Effect of diamond shapes and associated thermal boundary resistance on thermal conductivity of diamond-based composites. *Computational Materials Science*, 41(2):156–163.

Forest, S. and Pilvin, P. (1996). Modelling the cyclic behaviour of two-phase single crystal nickel-base superalloys. In *IUTAM Symposium on micromechanics of plasticity and damage of multiphase materials*, pages 51–58. Springer.

Franciosi, P. and Berbenni, S. (2008). Multi-laminate plastic-strain organization for non-uniform tfa modeling of poly-crystal regularized plastic flow. *International Journal of Plasticity*, 24(9):1549–1580.

François, D., Pineau, A., Zaoui, A., Zaoui, A., Zaoui, A., and Physicist, F. (1998). *Mechanical behaviour of materials*. Springer.

Fritzen, F. and Böhlke, T. (2011). Nonuniform transformation field analysis of materials with morphological anisotropy. *Composites Science and Technology*, 71(4):433–442.

Fritzen, F., Böhlke, T., and Schnack, E. (2009). Periodic three-dimensional mesh generation for crystalline aggregates based on Voronoi tessellations. *Computational Mechanics*, 43(5):701–713.

Frydman, L. (2014). High magnetic field science and its application in the united states: A magnetic resonance perspective. *Journal of Magnetic Resonance*, 242:256–264.

Fuchs, K. (1938). The conductivity of thin metallic films according to the electron theory of metals. In *Mathematical Proceedings of the Cambridge Philosophical Society*, volume 34, pages 100–108. Cambridge Univ Press.

Geers, M. G., Kouznetsova, V. G., and Brekelmans, W. (2010). Multi-scale computational homogenization: Trends and challenges. *Journal of computational and applied mathematics*, 234(7):2175–2182.

Gérard, C. (2008). *Mesures de champs et identification de modèles de plasticité cristalline*. PhD thesis, Université Paris-Nord-Paris XIII.

Ghosh, S., Lee, K., and Moorthy, S. (1995). Multiple scale analysis of heterogeneous elastic structures using homogenization theory and Voronoi cell finite element method. *International Journal of Solids and Structures*, 32(1):27–62.

Ghosh, S., Lee, K., and Moorthy, S. (1996). Two scale analysis of heterogeneous elastic-plastic materials with asymptotic homogenization and Voronoi cell finite element model. *Computer Methods in Applied Mechanics and Engineering*, 132(1):63–116.

Groh, S., Marin, E., Horstemeyer, M., and Zbib, H. (2009). Multiscale modeling of the plasticity in an aluminum single crystal. *International Journal of Plasticity*, 25(8):1456–1473.

Gu, T., Castelnau, O., Forest, S., Hervé-Luanco, E., Lecouturier, F., Proudhon, H., and Thilly, L. (2017). Multiscale modeling of the elastic behavior of architectured and nanostructured Cu–Nb composite wires. *International Journal of Solids and Structures*, 121:148 – 162.

Gu, T., Hervé-Luanco, E., Proudhon, H., Thilly, L., Dubois, J.-B., Lecouturier, F., Castelnau, O., and Forest, S. (2015). Modélisation multi-échelle du comportement électrique de nano-composites Cu-Nb. *Matériaux & Techniques*, 103(3):309.

Haddadi, H., Bouvier, S., Banu, M., Maier, C., and Teodosiu, C. (2006). Towards an accurate description of the anisotropic behaviour of sheet metals under large plastic deformations: modelling, numerical analysis and identification. *International Journal of Plasticity*, 22(12):2226–2271.

Halperin, B., Aeppli, G., Ando, Y., Aronson, M., Basov, D., Budinger, T., Dimeo, R., Gore, J., Hunte, F., Lau, C., et al. (2013). High magnetic field science and its application in the united states: Current status and future directions. *National Academy of Sciences: Washington, DC*.

Hansen, B., Carpenter, J., Sintay, S., Bronkhorst, C., McCabe, R., Mayeur, J., Mourad, H., Beyerlein, I., Mara, N., Chen, S., et al. (2013). Modeling the texture evolution of Cu/Nb layered composites during rolling. *International journal of plasticity*, 49:71–84.

Hashin, Z. (1962). The elastic moduli of heterogeneous materials. *Journal of Applied Mechanics*, 29(1):143–150.

Hashin, Z. (2002). Thin interphase/imperfect interface in elasticity with application to coated fiber composites. *Journal of the Mechanics and Physics of Solids*, 50(12):2509–2537.

Hashin, Z. and Rosen, B. W. (1964). The elastic moduli of fiber-reinforced materials. *Journal of Applied Mechanics*, 31(2):223–232.

Hasselman, D. and Johnson, L. F. (1987). Effective thermal conductivity of composites with interfacial thermal barrier resistance. *Journal of Composite Materials*, 21(6):508–515.

Heringhaus, F., Schneider-Muntau, H.-J., and Gottstein, G. (2003). Analytical modeling of the electrical conductivity of metal matrix composites: application to Ag–Cu and Cu–Nb. *Materials Science and Engineering: A*, 347(1):9–20.

Hervé, E. (2002). Thermal and thermoelastic behaviour of multiply coated inclusion-reinforced composites. *International Journal of Solids and Structures*, 39(4):1041–1058.

Hervé, E. and Zaoui, A. (1993). N-layered inclusion-based micromechanical modelling. *International Journal of Engineering Science*, 31(1):1–10.

Hervé, E. and Zaoui, A. (1995). Elastic behaviour of multiply coated fibre-reinforced composites. *International Journal of Engineering Science*, 33(10):1419–1433.

Hervé-Luanco, E. (2014). Elastic behavior of composites containing multi-layer coated particles with imperfect interface bonding conditions and application to size effects and mismatch in these composites. *International Journal of Solids and Structures*, 51(15):2865–2877.

Hervé-Luanco, E. and Joannès, S. (2016). Multiscale modelling of transport phenomena for materials with n-layered embedded fibres. part I: Analytical and numerical-based approaches. *International Journal of Solids and Structures*, 97:625–636.

Hill, R. (1963). Elastic properties of reinforced solids: some theoretical principles. *Journal of the Mechanics and Physics of Solids*, 11(5):357–372.

Hill, R. (1965a). Continuum micro-mechanics of elastoplastic polycrystals. *Journal of the Mechanics and Physics of Solids*, 13(2):89–101.

Hill, R. (1965b). A self-consistent mechanics of composite materials. *Journal of the Mechanics and Physics of Solids*, 13(4):213–222.

Huang, Q., Lilley, C. M., Bode, M., and Divan, R. (2008). Surface and size effects on the electrical properties of Cu nanowires. *Journal of Applied Physics*, 104(2):023709.

Islam, M. R. and Pramila, A. (1999). Thermal conductivity of fiber reinforced composites by the fem. *Journal of Composite Materials*, 33(18):1699–1715.

Joannès, S. and Hervé-Luanco, E. (2016). Multiscale modelling of transport phenomena for materials with n-layered embedded fibres. part II: Investigation of fibre packing effects. *International Journal of Solids and Structures*, 97:566–574.

Kanit, T., Forest, S., Galliet, I., Mounoury, V., and Jeulin, D. (2003). Determination of the size of the representative volume element for random composites: statistical and numerical approach. *International Journal of solids and structures*, 40(13):3647–3679.

Kanjarla, A., Lebensohn, R., Balogh, L., and Tomé, C. (2012). Study of internal lattice strain distributions in stainless steel using a full-field elasto-viscoplastic formulation based on fast fourier transforms. *Acta Materialia*, 60(6):3094–3106.

Kitaoka, Y., Tono, T., Yoshimoto, S., Hirahara, T., Hasegawa, S., and Ohba, T. (2009). Direct detection of grain boundary scattering in damascene Cu wires by nanoscale four-point probe resistance measurements. *Applied Physics Letters*, 95(5):052110.

Klusemann, B., Svendsen, B., and Vehoff, H. (2012). Investigation of the deformation behavior of Fe–3% Si sheet metal with large grains via crystal plasticity and finite-element modeling. *Computational Materials Science*, 52(1):25–32.

Kneer, G. (1965). Über die Berechnung der Elastizitätsmoduln vielkristalliner Aggregate mit Textur. *physica status solidi (b)*, 9(3):825–838.

Kröner, E. (1961). On the plastic deformation of polycrystals. *Acta Metallurgica*, 9(2):155–161.

Kröner, E. (1978). Self-consistent scheme and graded disorder in polycrystal elasticity. *Journal of Physics F: Metal Physics*, 8(11):2261.

Kubin, L., Devincre, B., and Hoc, T. (2008). Modeling dislocation storage rates and mean free paths in face-centered cubic crystals. *Acta materialia*, 56(20):6040–6049.

Lebensohn, R., Castelnau, O., Brenner, R., and Gilormini, P. (2005). Study of the antiplane deformation of linear 2-D polycrystals with different microstructures. *International journal of solids and structures*, 42(20):5441–5459.

Lebensohn, R., Ponte-Castañeda, P., Brenner, R., and Castelnau, O. (2011). Full-field vs. homogenization methods to predict microstructure–property relations for polycrystalline materials. In *Computational Methods for Microstructure-Property Relationships*, pages 393–441. Springer.

Lebensohn, R. A., Kanjarla, A. K., and Eisenlohr, P. (2012). An elasto-viscoplastic formulation based on fast fourier transforms for the prediction of micromechanical fields in polycrystalline materials. *International Journal of Plasticity*, 32:59–69.

Lee, S.-B., LeDonne, J., Lim, S., Beyerlein, I., and Rollett, A. (2012). The heterophase interface character distribution of physical vapor-deposited and accumulative roll-bonded Cu–Nb multilayer composites. *Acta Materialia*, 60(4):1747–1761.

Lemaitre, J. and Chaboche, J.-L. (1994). *Mechanics of solid materials*. Cambridge university press.

Lim, S. and Rollett, A. (2009). Length scale effects on recrystallization and texture evolution in Cu layers of a roll-bonded Cu–Nb composite. *Materials Science and Engineering: A*, 520(1):189–196.

Liu, H.-D., Zhao, Y.-P., Ramanath, G., Murarka, S., and Wang, G.-C. (2001). Thickness dependent electrical resistivity of ultrathin ($<$ 40 nm) Cu films. *Thin Solid Films*, 384(1):151–156.

Llorca, J., Elices, M., and Termonia, Y. (2000). Elastic properties of sphere-reinforced composites with a mesophase. *Acta materialia*, 48(18):4589–4597.

Lu, L., Li, S., and Lu, K. (2001). An abnormal strain rate effect on tensile behavior in nanocrystalline copper. *Scripta Materialia*, 45(10):1163–1169.

Lu, L., Shen, Y., Chen, X., Qian, L., and Lu, K. (2004). Ultrahigh strength and high electrical conductivity in copper. *Science*, 304(5669):422–426.

Mallick, P. K. (2007). *Fiber-reinforced composites: materials, manufacturing, and design*. CRC press.

Martin, G., Ochoa, N., Sai, K., Hervé-Luanco, E., and Cailletaud, G. (2014). A multiscale model for the elastoviscoplastic behavior of directionally solidified alloys: Application to FE structural computations. *International Journal of Solids and Structures*, 51(5):1175–1187.

Masson, R., Bornert, M., Suquet, P., and Zaoui, A. (2000). An affine formulation for the prediction of the effective properties of nonlinear composites and polycrystals. *Journal of the Mechanics and Physics of Solids*, 48(6):1203–1227.

Masson, R. and Zaoui, A. (1999). Self-consistent estimates for the rate-dependentelastoplastic behaviour of polycrystalline materials. *Journal of the Mechanics and Physics of Solids*, 47(7):1543–1568.

Mayeur, J., Beyerlein, I., Bronkhorst, C., and Mourad, H. (2015). Incorporating interface affected zones into crystal plasticity. *International journal of plasticity*, 65:206–225.

Mayeur, J., Beyerlein, I., Bronkhorst, C., Mourad, H., and Hansen, B. (2013). A crystal plasticity study of heterophase interface character stability of cu/nb bicrystals. *International Journal of Plasticity*, 48:72–91.

Medy, J.-R. (2016). *Evaluation des effets de taille et d'architecture sur les propriétés mécaniques et électriques de fils composites métalliques cuivre/niobium fabriqués par déformation plastique sévère*. PhD thesis, Université de Poitiers.

Méric, L., Cailletaud, G., and Gaspérini, M. (1994). FE calculations of copper bicrystal specimens submitted to tension-compression tests. *Acta metallurgica et materialia*, 42(3):921–935.

Méric, L., Poubanne, P., and Cailletaud, G. (1991). Single crystal modeling for structural calculations: part 1—model presentation. *Journal of Engineering Materials and Technology*, 113(1):162–170.

Meyers, M. A., Andrade, U. R., and Chokshi, A. H. (1995). The effect of grain size on the high-strain, high-strain-rate behavior of copper. *Metallurgical and materials transactions A*, 26(11):2881–2893.

Michel, J. and Suquet, P. (2009). Nonuniform transformation field analysis: a reduced model for multiscale nonlinear problems in solid mechanics. *Multiscale Modelling in*

Solid Mechanics-Computational Approaches, edited by U. Galvanetto and F. Aliabadi Imperial College Press (Imperial College Press, London., 2009), pages 159–206.

Michel, J.-C. and Suquet, P. (2016). A model-reduction approach in micromechanics of materials preserving the variational structure of constitutive relations. *Journal of the Mechanics and Physics of Solids*, 90:254–285.

Milton, G. W. (2002). The theory of composites. *The Theory of Composites, by Graeme W. Milton, pp. 748. ISBN 0521781256. Cambridge, UK: Cambridge University Press, May 2002.*, page 748.

Misra, A. and Hoagland, R. (2007). Plastic flow stability of metallic nanolaminate composites. *Journal of materials science*, 42(5):1765–1771.

Misra, A. and Thilly, L. (2010). Structural metals at extremes. *MRS Bull*, 35(12):965–976.

Molinari, A., Canova, G., and Ahzi, S. (1987). A self consistent approach of the large deformation polycrystal viscoplasticity. *Acta Metallurgica*, 35(12):2983–2994.

Mura, T. (1987). *Micromechanics of defects in solids*. Springer Science & Business Media.

Musienko, A., Tatschl, A., Schmidegg, K., Kolednik, O., Pippan, R., and Cailletaud, G. (2007). Three-dimensional finite element simulation of a polycrystalline copper specimen. *Acta materialia*, 55(12):4121–4136.

Nemat-Nasser, S. and Hori, M. (2013). *Micromechanics: overall properties of heterogeneous materials*. Elsevier.

NormeInternationale, C. E. (1974). Méthode de mesure de la résistivité des matériaux métalliques. Technical report, Publication CEI 468.

Pan, B., Qian, K., Xie, H., and Asundi, A. (2009). Two-dimensional digital image correlation for in-plane displacement and strain measurement: a review. *Measurement science and technology*, 20(6):062001.

Ponte-Castañeda, P. and Suquet, P. (1998). Nonlinear composites. *Advances in applied mechanics*, 34(998):171–302.

Qu, J. and Cherkaoui, M. (2006). *Fundamentals of micromechanics of solids*. Wiley Hoboken.

Sai, K., Cailletaud, G., and Forest, S. (2006). Micro-mechanical modeling of the inelastic behavior of directionally solidified materials. *Mechanics of Materials*, 38(3):203–217.

Sambles, J., Elsom, K., and Preist, T. (1982). The resistivity of thin wires. *Journal of Physics F: Metal Physics*, 12(6):1169.

Schneider, Y., Bertram, A., Böhlke, T., and Hartig, C. (2010). Plastic deformation behaviour of Fe–Cu composites predicted by 3D finite element simulations. *Computational Materials Science*, 48(3):456–465.

Schulgasser, K. (1976a). On the conductivity of fiber reinforced materials. *Journal of Mathematical Physics*, 17(3):382–387.

Schulgasser, K. (1976b). Relationship between single-crystal and polycrystal electrical conductivity. *Journal of Applied Physics*, 47(5):1880–1886.

Šiška, F., Forest, S., Gumbsch, P., and Weygand, D. (2006). Finite element simulations of the cyclic elastoplastic behaviour of copper thin films. *Modelling and Simulation in Materials Science and Engineering*, 15(1):S217.

Sivardière, J. (2008). *Symétrie et propriétés physiques – Du principe de Curie aux brisures de symétrie*. EDP Sciences.

Slaughter, W. (2002). *The linearized theory of elasticity*. Springer Science & Business Media.

Smits, F. (1958). Measurement of sheet resistivities with the four-point probe. *Bell System Technical Journal*, 37(3):711–718.

Sondheimer, E. H. (2001). The mean free path of electrons in metals. *Advances in physics*, 50(6):499–537.

Spencer, K., Lecouturier, F., Thilly, L., and Embury, J. (2004). Established and emerging materials for use as high-field magnet conductors. *Advanced Engineering Materials*, 6(5):290–297.

Steinhögl, W., Schindler, G., Steinlesberger, G., and Engelhardt, M. (2002). Size-dependent resistivity of metallic wires in the mesoscopic range. *Physical Review B*, 66(7):075414.

Steinhögl, W., Schindler, G., Steinlesberger, G., Traving, M., and Engelhardt, M. (2005). Comprehensive study of the resistivity of copper wires with lateral dimensions of 100 nm and smaller. *Journal of Applied Physics*, 97(2):023706.

Stoller, R. and Zinkle, S. (2000). On the relationship between uniaxial yield strength and resolved shear stress in polycrystalline materials. *Journal of Nuclear Materials*, 283:349–352.

Suvorov, A. P. and Dvorak, G. J. (2002). Rate form of the Eshelby and Hill tensors. *International Journal of Solids and Structures*, 39(21):5659–5678.

Tabourot, L., Fivel, M., and Rauch, E. (1997). Generalised constitutive laws for f.c.c. single crystals. *Materials Science and Engineering: A*, 234:639–642.

Tavman, I. and Akinci, H. (2000). Transverse thermal conductivity of fiber reinforced polymer composites. *International Communications in Heat and Mass Transfer*, 27(2):253–261.

Thilly, L. (2000). *Exploration theorique et experimentale de fils nanocomposites continus presentant des proprietes extremes de conductivite electrique et de limite elastique*. PhD thesis, l'Institut national des sciences appliquees de Toulouse.

Thilly, L., Lecouturier, F., and Von Stebut, J. (2002a). Size-induced enhanced mechanical properties of nanocomposite copper/niobium wires: nanoindentation study. *Acta Materialia*, 50(20):5049–5065.

Thilly, L., Renault, P., Van Petegem, S., Brandstetter, S., Schmitt, B., Van Swygenhoven, H., Vidal, V., and Lecouturier, F. (2007). Evidence of internal Bauschinger test in nanocomposite wires during in situ macroscopic tensile cycling under synchrotron beam. *Applied physics letters*, 90(24):241907.

Thilly, L., Renault, P., Vidal, V., Lecouturier, F., Van Petegem, S., Stuhr, U., and Van Swygenhoven, H. (2006). Plasticity of multiscale nanofilamentary Cu/Nb composite wires during in situ neutron diffraction: Codeformation and size effect. *Applied physics letters*, 88(19):191906.

Thilly, L., Van Petegem, S., Renault, P., Lecouturier, F., Vidal, V., Schmitt, B., and Van Swygenhoven, H. (2009). A new criterion for elasto-plastic transition in nanomaterials: Application to size and composite effects on Cu–Nb nanocomposite wires. *Acta Materialia*, 57(11):3157–3169.

Thilly, L., Veron, M., Ludwig, O., and Lecouturier, F. (2001). Deformation mechanism in high strength Cu/Nb nanocomposites. *Materials Science and Engineering: A*, 309:510–513.

Thilly, L., Veron, M., Ludwig, O., Lecouturier, F., Peyrade, J., and Askénazy, S. (2002b). High-strength materials: in-situ investigations of dislocation behaviour in Cu-Nb multifilamentary nanostructured composites. *Philosophical Magazine A*, 82(5):925–942.

Thomsen, L. (1986). Weak elastic anisotropy. *Geophysics*, 51(10):1954–1966.

Turner, P. and Tomé, C. (1994). A study of residual stresses in Zircaloy-2 with rod texture. *Acta metallurgica et Materialia*, 42(12):4143–4153.

Upadhyay, M., Van Petegem, S., Panzner, T., Lebensohn, R., and Van Swygenhoven, H. (2016). Study of lattice strain evolution during biaxial deformation of stainless steel using a finite element and fast fourier transform based multi-scale approach. *Acta Materialia*, 118:28–43.

Vidal, V., Thilly, L., Lecouturier, F., and Renault, P. (2007). Cu nanowhiskers embedded in Nb nanotubes inside a multiscale Cu matrix: The way to reach extreme mechanical properties in high strength conductors. *Scripta materialia*, 57(3):245–248.

Vidal, V., Thilly, L., Van Petegem, S., Stuhr, U., Lecouturier, F., Renault, P.-O., and Van Swygenhoven, H. (2009). Plasticity of nanostructured Cu–Nb-based wires: Strengthening mechanisms revealed by in situ deformation under neutrons. *Scripta Materialia*, 60(3):171–174.

Vital, V. (2006). *Optimisation des propriétés mécaniques des conducteurs nanofilamentaires Cu/X (X=Nb ou Ta) par l'étude des mécanismes élémentaires de déformation.* PhD thesis, Docteur de l'Institut National des Sciences Appliquées de Toulouse.

Vu, Q. H., Brenner, R., Castelnau, O., Moulinec, H., and Suquet, P. (2012). A self-consistent estimate for linear viscoelastic polycrystals with internal variables inferred from the collocation method. *Model. Simul. Mater. Sci. Engin.*, 20(2):024003.

Walpole, L. (1985). Evaluation of the elastic moduli of a transversely isotropic aggregate of cubic crystals. *Journal of the Mechanics and Physics of Solids*, 33(6):623–636.

Williams, T. and Pindera, M.-J. (1997). An analytical model for the inelastic axial shear response of unidirectional metal matrix composites. *International journal of plasticity*, 13(3):261–289.

Willis, J. (1977). Bounds and self-consistent estimates for the overall properties of anisotropic composites. *Journal of the Mechanics and Physics of Solids*, 25(3):185–202.

Wippler, J., Fünfschilling, S., Fritzen, F., Böhlke, T., and Hoffmann, M. (2011). Homogenization of the thermoelastic properties of silicon nitride. *Acta Materialia*, 59(15):6029–6038.

Yaguchi, M. and Busso, E. (2005). On the accuracy of self-consistent elasticity formulations for directionally solidified polycrystal aggregates. *International journal of solids and structures*, 42(3):1073–1089.

Yoshida, K., Brenner, R., Bacroix, B., and Bouvier, S. (2011). Micromechanical modeling of the work-hardening behavior of single-and dual-phase steels under two-stage loading paths. *Materials Science and Engineering: A*, 528(3):1037–1046.

Yosio, H. and Granato, A. V. (1966). Anharmonicity in noble metals; higher order elastic constants. *Phys. Rev.*, 144:411–419.

Zaoui, A. (1997). *Structural morphology and constitutive behaviour of microheterogeneous materials.* Springer.

Zecevic, M. and Knezevic, M. (2015). A dislocation density based elasto-plastic self-consistent model for the prediction of cyclic deformation: Application to AA6022-T4. *International Journal of Plasticity*, 72:200–217.

Zener, C. (1948). *Elasticity and anelasticity of metals.* University of Chicago press.

MODÉLISATION MULTI-ÉCHELLE DU COMPORTEMENT ÉLECTRIQUE ET ÉLASTO-PLASTIQUE DE FILS COMPOSITES CU-NB NANOSTRUCTURÉS ET ARCHITECTURÉS

RESUME : Les fils composites nanostructurés et architecturés cuivre-niobium sont de candidats excellents pour la génération de champs magnétiques intenses (>90T); en effet, ces fils allient une limite élastique élevée et une excellente conductivité électrique. Les fils Cu-Nb multi-échelles sont fabriqués par étirage et empilement cumulatif (une technique de déformation plastique sévère), conduisant à une microstructure multi-échelle, architecturée et nanostructurée présentant une texture cristallographique de fibres forte et des formes de grains allongées le long de l'axe du fil. Cette thèse présente une étude compréhensive du comportement électrique et élasto-plastique de ce matériau composite, elle est divisée en trois parties: modélisation multi-échelle électrique, élastique et élasto-plastique. Afin d'étudier le lien entre le comportement effective et la microstructure du fil, plusieurs méthodes d'homogénéisation sont appliquées, qui peuvent être séparées en deux types principaux: la méthode en champs moyens et en champs complets. Comme les spécimens présentent plusieurs échelles caractéristiques, plusieurs étapes de transition d'échelle sont effectuées itérativement de l'échelle de grain à la macro-échelle. L'accord général parmi les réponses de modèle permet de suggérer la meilleure stratégie pour estimer de manière fiable le comportement électrique et élasto-plastique des fils Cu-Nb et économiser le temps de calcul. Enfin, les modèles sont validés par les données expérimentales avec un bon accord.

Mots clés : comportement électrique et élasto-plastique, matériaux architecturé, approche multi-échelle, microstructure, homogénéisation

MULTISCALE MODELING OF THE ELECTRICAL AND ELASTO-PLASTIC BEHAVIOR OF ARCHITECTURED AND NANOSTRUCTURED CU-NB COMPOSITE WIRES

ABSTRACT : Nanostructured and architectured copper niobium composite wires are excellent candidates for the generation of intense pulsed magnetic fields (>90T) as they combine both high strength and high electrical conductivity. Multi-scaled Cu-Nb wires are fabricated by accumulative drawing and bundling (a severe plastic deformation technique), leading to a multiscale, architectured and nanostructured microstructure exhibiting a strong fiber crystallographic texture and elongated grain shapes along the wire axis. This thesis presents a comprehensive study of the effective electrical and elasto-plastic behavior of this composite material. It is divided into three parts: electrical, elastic and elasto-plastic multiscale modeling. In order to investigate the link between the effective material behavior and the wire microstructure, several homogenization methods are applied which can be separated into two main types: mean-field and full-field theories. As the specimens exhibit many characteristic scales, several scale transition steps are carried out iteratively from the grain scale to the macro-scale. The general agreement among the model responses allows suggesting the best strategy to estimate reliably the effective electrical and elasto-plastic behavior of Cu-Nb wires and save computational time. Finally, the models are validated by experimental data with a good agreement.

Keywords : electrical and elasto-plastic behavior, architectured material, multi-scale approach, microstructure, homogenization

ARTS ET MÉTIERS ParisTech

ParisTech INSTITUT DES SCIENCES ET TECHNOLOGIES PARIS INSTITUTE OF TECHNOLOGY